UNIVERSITÀ
degli STUDI
di CATANIA

Dipartimento
di Fisica
e Astronomia
"Ettore Majorana"

PhD programme in physics

Marika Rasà

(Anti)deuteron production in and out of jets in p–Pb collisions at $\sqrt{s_{\mathrm{NN}}} = 5.02$ TeV with the ALICE detector at the LHC

PhD thesis

Supervisor:
Prof. P. La Rocca

Tutored by:
Dr. C. Pinto

---

academic year 2023/2024

“Pick up a pen, start writing!
I wanna talk about what I have learned
The hard-won wisdom I have earned”

[One Last Time - Christopher Jackson,
Lin-Manuel Miranda & Original
Broadway Cast of "Hamilton"]

"Science would not be contained,
he would argue. It would not be revealed
according to Man’s agenda,
but according to its own"

[The First King of Shannara, Terry Brooks]

Abstract

Heavy-ion collisions at ultra-relativistic energies are one of the fundamental tools to explore the extreme conditions of the nuclear matter. In fact, in these collisions, a deconfined state of quarks and gluons, namely the Quark-Gluon Plasma (QGP), is created. This state of matter is relevant not only in nuclear physics, but also in astrophysics. In fact, it is established that some μs after the Big Bang, our universe was in this state of matter, and also the QGP is a candidate to explain the core of neutron stars and other compact astrophysical objects.

In heavy-ion collisions a large number of particles are produced: from hadrons (among which pions, kaons and protons are the most abundantly produced) to composite objects such as light nuclei (d, t, ^{3}He, ^{4}He) and hypernuclei, along with their antiparticles. The production rate at the CERN Large Hadron Collider (LHC) for deuterons is approximately one every one thousand p–Pb collisions, while for ^{3}He is even lower, one every one million events. Hence, the study of the production of light (anti)nuclei is particularly challenging. Moreover, the production mechanism of light (anti)nuclei, despite the abundance of experimental results, is still a highly debated topic in the scientific community. In fact, if we consider the energy scale in which the hadronization process happens, $\Lambda_{\text{QCD}} \sim 200$ MeV, the QCD perturbative approach can not be applied. For this reason, the production of light (anti)nuclei is described with some phenomenological models. In particular, it is possible to identify two different classes of models: the Statistical Hadronization Model and the baryon coalescence.

With the current experimental results, both models qualitatively re-

produce the data, even if some tensions are present in selected results. In particular, while for the deuteron production the models do not have enough discrimination power, for the ^{3}He case the data are not precise enough. Then, in order to discriminate between the two models, novel experimental observables are needed. One innovative approach is to study the production of light (anti)nuclei in and out of jets. In fact, as predicted by the coalescence model, an enhanced nucleus production is expected in jets, due to the nucleons proximity in the phase space.

The production of nuclei in jets has been studied in pp collision by the ALICE experiment at CERN. In fact, even if the detector is specifically designed in order to study and characterize the QGP, its excellent particle identification capabilities allow the studies on light (anti)nucleus production. In particular, deuteron, triton, ^{3}He, ^{4}He and their respective antiparticles have been identified in pp, p–Pb, Xe–Xe and Pb–Pb collisions at different energies, exploiting the information from the Inner Tracking System (ITS), Time Projection Chamber (TPC) and Time-Of-Flight (TOF) detectors.

In this work, the (anti)deuteron and antiproton production in and out of jets in p–Pb collisions at $\sqrt{s_{\rm NN}} = 5.02$ TeV is presented. With the obtained transverse momentum distributions, the coalescence parameter in and out of jets, which is related to the probability to form a deuteron via coalescence, is evaluated. The experimental results show an enhanced deuteron coalescence probability in jets, as predicted by the coalescence model. The experimental data are also compared with both the values obtained in pp collisions and with the expectations from the coalescence model. The results are then discussed in the knowledge of the current theoretical framework. To further understand the experimental results, the deuteron-over-proton ratio in both pp and p–Pb collisions in and out of jets is evaluated, and the obtained results are coherent with the coalescence picture.

The presented results contribute in a deeper understanding on the production of light (anti)nuclei. This information is not only crucial in the field of QCD, in order to understand how this object are formed, but also in the astrophysical field. In fact, these measurements can be used as an input for studies in the search of dark matter via the measurement of light (anti)nuclei in space, carried out from the AMS-02 and GAPS experiments.

Contents

Chapter 1

QCD and high-energy hadronic collisions

The study of high-energy hadronic collisions is a fundamental tool to investigate the property of the nuclei and the Equation of State (EoS) of the hadronic matter. In fact, in such collisions, high temperature and energy density condition are achieved: in this environment, the hadronic matter undergoes a phase transition where the Quark Gluon Plasma (QGP), a state of deconfined quarks and gluons, is formed.

1.1 Introduction

In particle physics, the Quantum ChromoDynamics (QCD) is the theory that describes the strong force. The development of this theory started in the first half of 1900, with the attempt to describe the force that binds the nucleons into the nucleus after Chadwick's discovery of the neutron [1]. Despite the different attempts to develop such theory through the years, the developed models were not able to describe the presence of Δ resonances and kaons, recently discovered hadronic states. Only with the *Eightfold way*, a theory developed by Gell-Mann [2] and Ne'eman [3], the first successful results were achieved. In this model, the hadrons are grouped into *mesons* and *baryons*, and they are classified accordingly to their hypercharge Y, defined as the sum of baryonic and strangeness num-

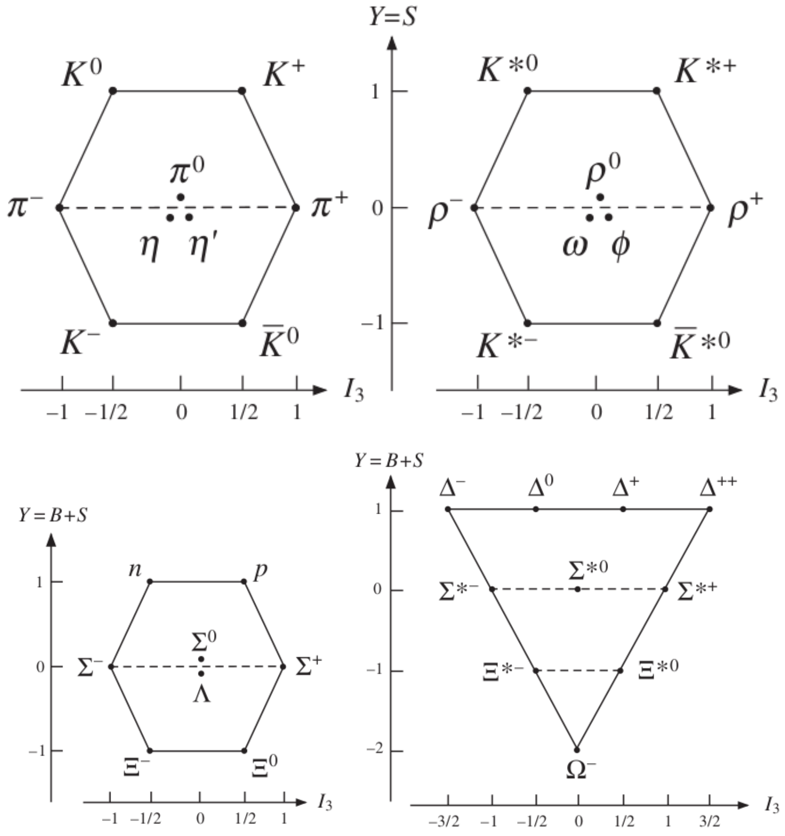

Figure 1.1: Octet for spin 0 and spin 1 mesons (upper row) and octet and decuplet for spin 1/2 and spin 3/2 baryons (lower row), according to the Eightfold Way [4].

bers, and the third component of the isosopin I_3. With this classification, regular patterns emerge, as the octet for the spin 0 mesons and for spin 1/2 baryons, and their excited states, with the octet for the spin 1 mesons and the decuplet for spin 3/2 baryons: Fig. 1.1 shows these described structures. The Eightfold Way lead the way for the development of the *Quark Model* by Gell-Mann [5] and Zweig [6]. According to this theory, the constituent particles of the matter are the *quarks*, subatomic particles of three different flavours, called *up*, *down* and *strange*. The hadrons are formed by a combination of quarks, depending on their nature: the baryons are made by three different quarks, *qqq*, while the mesons are formed by a quark-antiquark pair, $q\bar{q}$. The model was able to explain both the already observed hadrons and to correctly predict new particles not yet observed, such as Ω^-. Despite these successes, the theory was not fully accepted by the scientific community of that time, considering three crucial aspects:

- the already discovered particles have a full charge: to preserve that, the quarks should have a fractional charge;
- considering the baryons made by three equal quarks, such as Δ^{++} formed by three up quarks, the resulting wave function is symmetric if the particles do not have an angular momentum. This violates the Pauli exclusion principle;
- there was no observation of free quarks.

During the following years, both new theoretical hypotheses and experimental results confirmed the prediction of Gell-Mann and Zweig's model. The quarks fractional charge was demonstrated with Deep Inelastic Scattering (DIS) experiments performed at SLAC [7, 8], proving the composite nature of protons and neutrons. To justify the apparent violation of the Pauli's principle, Greenberg [9] introduced a new quantum number that also explains the confinement of the quarks into the hadrons. According to Greenberg's theory each quark has an additional degree of freedom expressed by a new additive quantum number called *colour*, that can assume three different values: *red*, *green* and *blue*. The correspondent anticolours are assigned for the antiquarks. The hadrons, however, are not-coloured state: for this reason, the hypothesis is that (anti)baryon are formed by three (anti)quarks of different colours, while mesons are formed by a quark-antiquark pair of the same colour. The mediators of the strong force, the gluons, have a colour charge, since they are formed by a colour and a different anticolour, and the exchange of a gluon between two quarks results in a colour change. The confinement arises since the attractive force of the quark-antiquark pair does not decrease with the distance, but remains constant up until the threshold energy for the creation of a new quark-antiquark pair is reached. Hence, only the final states, *i.e.* baryons and mesons, are observed. These assumptions were

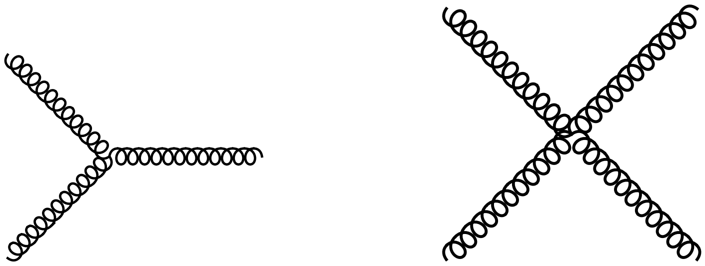

Figure 1.2: 3-gluons (left) and 4-gluons (right) vertices in QCD.

experimentally proved by the so-called *ratio R*, that is the cross section ratio between the production of hadrons and $\mu^+\mu^-$ pairs in e^+e^- collisions [10].

1.2 Quantum ChromoDynamic

Within the Standard Model (SM), the strong interaction is described by the QCD, a Gauge theory based on the SU(3) symmetry group. The QCD Lagrangian describes the interaction between the quark fields, described by the Dirac spinors $\psi_q^i(x)$, and the gluon fields $A_\mu^a(x)$ with the form:

$$\mathcal{L}_{QCD} = -\frac{1}{4}F_{\mu\nu}^a F_a^{\mu\nu} + \sum_q \bar{\psi}_q^i (i\gamma^\mu D_\mu - m_q)_{ij} \psi_q^j \tag{1.1}$$

where the field strength tensor $F_{\mu\nu}^a$ and the covariant derivative $(D_\mu)_{ij}$ can be defined as

$$F_{\mu\nu}^a = \partial_\mu A_\nu^a - \partial_\nu A_\mu^a - g_s f_{abc} A_\mu^b A_\nu^c \tag{1.2}$$

$$(D_\mu)_{ij} = \delta_{ij}\partial_\mu + i g_s \sum_a \frac{\lambda_{ij}^a}{2} A_\mu^a \tag{1.3}$$

where $g_s = \sqrt{4\pi\alpha_s}$ is the QCD coupling constant, f_{abc} are the structure constant of the Lie group and λ_{ij}^a are the Gell-Mann matrices. The SU(3) is a non-Abelian group, hence according to the QCD the gluons can self-interact: this interaction creates 3- and 4-gluonic vertices, as reported in Fig. 1.2. As a consequence of this type of vertices, in the QCD an *anti-screening* phenomenon occurs: the intensity of the strong force increases with the distance. This behaviour derives from the fact that gluons are coloured state. Hence, QCD is characterized by two properties:

- *asymptotic freedom*. In the case of processes with high transferred momentum, $Q > 100$ GeV, the interaction between quark and gluons is low. At this scale, the quarks can be treated as free particles instead of being considered bound inside the nucleons.

- *confinement*. For processes with a low transferred momentum, $Q \sim 1$ GeV, the interaction between the quarks is so strong that it is not possible to separate them. The confinement result in the fact that isolated quarks can not be observed, and the final states are the colourless hadrons.

These two properties are reflected in the behaviour of the coupling constant α_s. The dependence of α_s by the transferred momentum Q^2 is described by the following equation:

$$\alpha_s(|Q^2|) = \frac{12\pi}{(11N_c - 3N_f)\ln\left(\dfrac{|Q^2|}{\Lambda_{\mathrm{QCD}}}\right)} \tag{1.4}$$

where N_c is the number of colours, N_f the number of flavours and $\Lambda_{\mathrm{QCD}} \approx 200$ MeV is the scale parameter of the theory. Considering that $N_c = 3$ and $N_f = 6$, this lead to $11N_c - 3N_f > 0$: that means that the strength of the coupling constant decreases at high momentum transfer. Fig.1.3 shows the comparison between the expected behaviour, computed by the QCD prediction, and the value of α_s obtained by different measurements. The experimental results are in good agreement with the theoretical value [11].

In general, to describe the QCD different theoretical approaches can be used, according to the value of α_s:

- *perturbative QCD (pQCD)* [12]. In the case of high transferred momentum collisions ($Q^2 \to \infty$) the coupling constant α_s is very small ($\alpha_s \ll 1$), hence a perturbative expansion in series can be performed. In this approach, it is possible to calculate the transition elements of the scattering matrix.

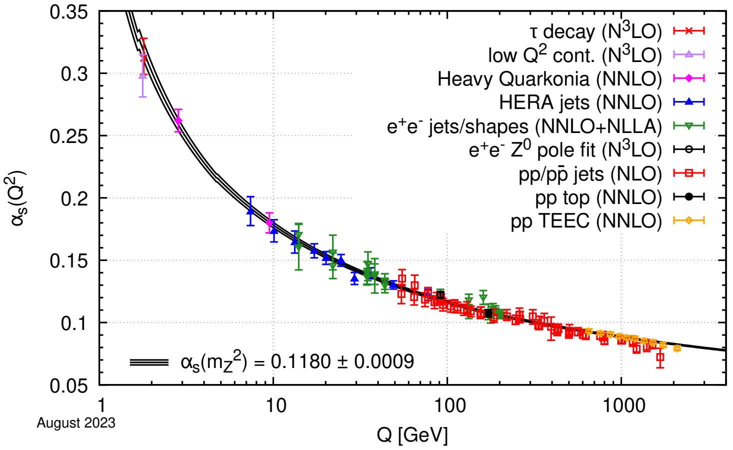

Figure 1.3: Strong coupling constant α_s as a function of the momentum transfer Q. Different colours indicate different methods used to obtain the measurement. [11].

- *lattice QCD (lQCD)* [13]. In the opposite range of energy, instead, the value of $\alpha_s \to \infty$, and this prevents the use of a perturbative approach. In this theory, the Green's function of the QCD Lagrangian are evaluated on a discrete lattice of the space-time coordinates, with a lattice pitch a. It is possible to extrapolate the results to the continuum ($a \to 0$), and compare the predictions with the experimental results. The lQCD is able to give an accurate estimate of the critical temperature [14] and the quark masses [15].

- *1/N expansion* [16]. This is a particular perturbative analysis of quantum field theory with an internal symmetry group, and consists on deriving the property of the theory as a function of 1/N, that is treated as a small parameter. In the QCD area, this is used in a modern variant in the AdS/CFT approach [17].

- *effective theories*. In this case, some specific problems can be solved using some effective theories that give qualitatively results in certain limits. Example of effective theories are chiral pertubation theory (ChPT) [18] and the heavy quark effective theory (HQET) [19].

In general, to describe the potential between a quark-antiquark pair, the Cornell potential [20] is used:

$$V(r) = -\frac{4}{3}\frac{\alpha_s}{r} + \kappa r, \tag{1.5}$$

where α_s is the coupling constant of the strong force, κ is the string tension (of about 1 GeV/c, as reported in [21]) and r is the distance between the quarks. This potential is described by two different terms: the first one, a Coulomb-like potential, is dominant for short distances, while the linear term becomes important at higher distances. The shape of the potential is verified thanks to lattice QCD calculations [22]. The Cornell's description is valid only considering the interaction in the vacuum. To describe the interaction in a coloured medium, such as the QGP, the potential is described as:

$$V(r) = -\frac{\alpha_s}{r}e^{-r/r_D} \tag{1.6}$$

where r_D is called *Debye radius*, and corresponds to the attenuation length, such as hadrons with a radius larger than r_D can not bind in the medium.

1.3 The phase diagram of the QCD

If we consider the nuclear matter, different states can be observed as a function of the temperature and the net baryonic density. A representation of the QCD phase diagram is reported in Fig. 1.4. At the temperature T = 0 MeV and baryon chemical potential μ_B = 0 the QCD vacuum is present. States with T $\approx$ 0 and $\mu_B \approx$ 1 GeV correspond to the ordinary nuclear matter. Moving along the μ_B axis, a phase transition to a Color Superconductor state is expected, and the existence of such state is predicted in the core of the neutron stars [24]. If, instead, $\mu_B \approx 0$ (as happens in high energy hadronic collisions at LHC [25]), and T $\gg \Lambda_{\mathrm{QCD}}$, the system undergoes another type of phase transition, and a deconfined state of quarks and gluons, namely the Quark Gluon Plasma or QGP, is expected. The critical temperature at which this phase transition is expected is equal to T $\approx$ 154 – 174 MeV. This new state of matter is relevant not only in nuclear physics but also in astrophysics: in fact, as reported in Ref. [26], in the first instants of the life of the Universe, such state was reached. Hence, the knowledge of this state obtained with the study at the accelerators could also help in the early Universe comprehension.

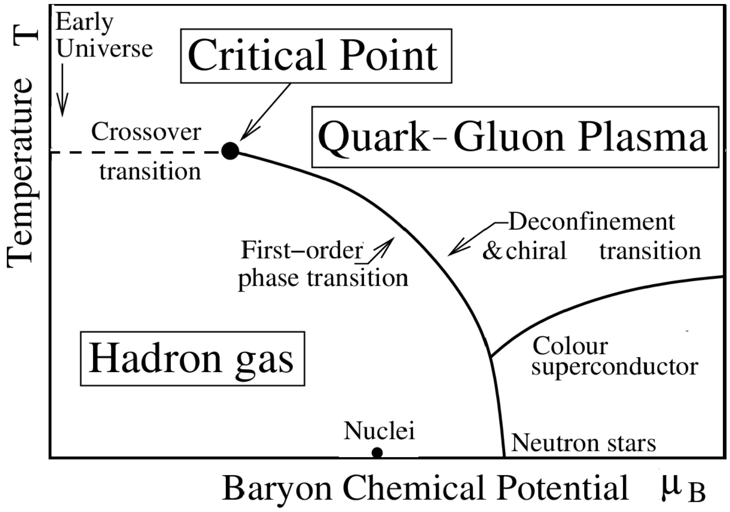

Figure 1.4: QCD phase diagram [23].

1.4 Heavy-Ion collisions

The only way to obtain the QGP state in laboratory is when ultra-relativistic heavy ions collide. The first generation of heavy ion experiments was carried out at the Super Proton Syncroton (SPS) [27] at CERN and at the Alternating Gradient Synchrotron (AGS) [28] at the Brookhaven National Laboratory (BNL). Both programmes included several fixed-target experiments at different centre-of-mass energy per nucleon pair ($\sqrt{s_{\mathrm{NN}}}$ $\approx 5 - 20$ GeV). In the following years, different experiments at increasing energies took place. Nowadays, the two main hadron colliders that include a programme on ultra-relativistic heavy ion collisions are the Relativistic Heavy Ion Collider (RHIC) at BNL and the Large Hadron Collider (LHC) at CERN, that provide respectively collisions with a maximum centre-of-mass energy of 200 GeV per nucleon and 5.36 TeV per nucleon.

1.4.1 Collision geometry

In a heavy-ion collision, a high number of particles is produced with respect to the composition of the initial nuclei and the centre-of-mass energy. Fig. 1.5 shows this expected behaviour, where the charged particle

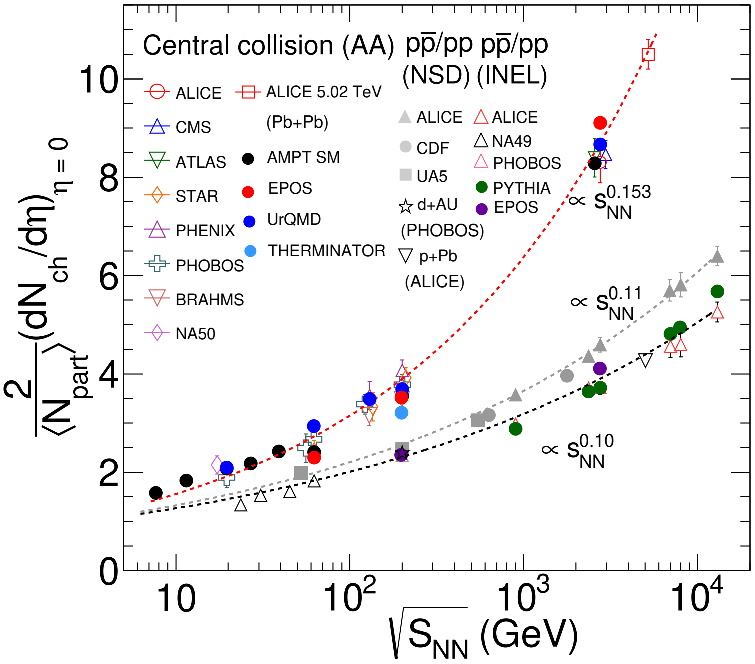

Figure 1.5: Measurements of the beam-energy dependence of charged-particle multiplicity density at mid-rapidity, scaled by the average number of participating nucleon pair ($\langle N_{\text{part}} \rangle/2$). Data from pp, p$\overline{\text{p}}$, d–Au, p–Pb, Au–Au, and Pb–Pb collisions collected from different experiments are parametrized with power-law fits (dash-lines) and compared to calculations from event generators [29].

multiplicity in different collision systems is reported. In order to estimate the relevant quantities to describe the nucleus-nucleus collisions, different models were implemented during the years. To describe the collisions some general parameters are used. In fact, during the collision of two nuclei with mass number A, only the *participant nucleons* $N_{\text{part}} \in [2, 2A]$, contribute to the collision. The other fraction, called *spectator nucleons* $N_{\text{spec}} = 2A - N_{\text{part}}$, do not participate to the collision and continue travelling along the beam direction. Another useful parameter to describe the collision is the number of elementary collisions that happens in the reaction, noted as N_{coll}. Both N_{coll} and N_{part} are correlated to the *impact parameter* b, defined as the distance between the centre of the two nuclei

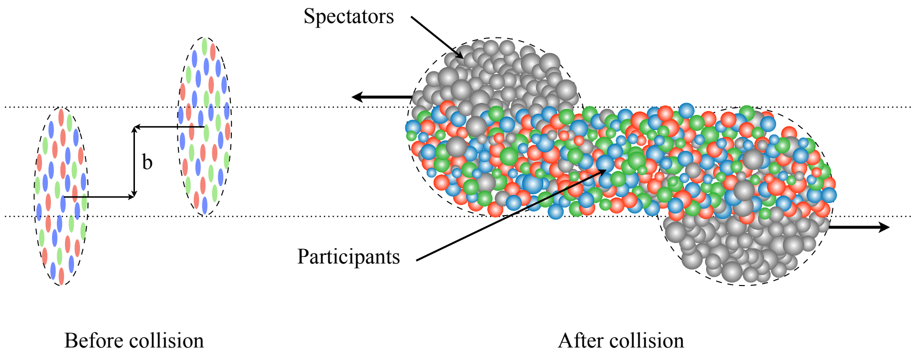

Figure 1.6: A schematic view of a heavy ion collision. Before the collision, the nuclei can be described as two discs, due to the Lorentz contraction. After the collision, two regions with the participant and spectators nucleons can be found [30].

in the direction of motion. With respect to the different values of b, the collisions can be described as *central* ($b \sim 0$) or *peripheral* ($b \sim 2A$). A schematic representation of this type of collision is reported in Fig. 1.6. Centrality and impact parameter are strictly correlated by the following relation:

$$c = \frac{1}{\sigma_{tot}} \int_0^b \frac{db}{db'} db', \tag{1.7}$$

where σ_{tot} is the total cross section of the process. Both the centrality and the impact parameter can not directly be measured during the collision. To estimate them, different quantities are used. In the case of the ALICE experiment [31], the centrality can be estimated through two different variables: the *average charged particle multiplicity* N_{ch} and the E_{ZDC}, i.e. the charge measured by the Zero Degree Calorimeters (see Sect. 3.3.4 for the description of such detector). In particular N_{ch} is expected to decrease monotonically with the increase on the impact parameter: in central collisions, in fact, the overlap region between the two nucleons is bigger, so it carries more energy and can create an elevated number of charged particles. In peripheral collisions, instead, the overlapping region is small, hence less charged particles are created. The E_{ZDC}, instead, is expected to have a different behaviour, since it is linked to the nucleons that do not participate to the collision. The remaining nucleons can create nuclear fragments with a magnetic rigidity similar to the one of the beam nuclei, hence they can remain in the beam pipe and not be detected. The fragment formation is more important in peripheral collision, hence the monotonically relation between E_{ZDC} and b is valid only in central events: for this reason, E_{ZDC} is always used coupled with a different observable. With these definitions, the centrality in ALICE can be defined as the percentile of the hadronic cross section that corresponds to a fraction of the particle multiplicity above a certain threshold, or as the energy deposited in the ZDC below a given value in the ZDC distribution:

$$c \approx \frac{1}{\sigma_{AA}} \int_{N_{ch}^{THR}}^{\infty} \frac{d\sigma}{dN'_{ch}} dN'_{ch} \approx \frac{1}{\sigma_{AA}} \int_{0}^{E_{ZDC}^{THR}} \frac{d\sigma}{dE'_{ZDC}} dE'_{ZDC}. \tag{1.8}$$

To simplify the procedure, the total cross section can be substituted with the number of the observed events corrected by the trigger efficiency.

One of the most successful and yet simple model to describe the heavy ion collisions is the *Glauber model* [32], where the collision geometry is described as an incoherent superposition of the nucleon-nucleon interactions based on the following assumptions, called *optical limit*:

- In the interaction, the nucleons move in straight lines and they are not deflected by the collision;
- The nucleons interact only via strong interactions, hence protons and neutrons are not distinguishable;
- The inelastic nucleon-nucleon cross section does not depend on the number of collisions a nucleon has already undergone, and remains constant during the different overlapping processes.

The nucleons position inside the nucleus can be described with a nuclear density function, with the functional form of a Wood-Saxon potential:

$$\rho(r) = \frac{\rho_0}{1 + \exp\left(\frac{r-R}{A}\right)}, \tag{1.9}$$

with r the distance of the nucleons from the centre, $\rho_0 = 0.16\,\mathrm{fm}^{-3}$ the nuclear density saturation, while R as the half density parameter and a as the diffuseness parameter can be derived from high energy electron scattering measurements [33].

The Glauber model is implemented in Monte Carlo simulations: the two colliding nuclei A and B are built distributing A and B nucleons in three dimensions according to the respective density distribution. The impact parameter is sampled uniformly according to the distribution $d\sigma/db = 2\pi b$. The nucleons are assumed to interact inelastically if their distance d in the transverse plane satisfies the condition:

$$d < \sqrt{\sigma_{inel}^{NN}/\pi}. \tag{1.10}$$

The value of σ_{inel}^{NN}, i.e. the total inelastic nucleus-nucleus cross section, is typically estimated by the interpolation of pp data at different values of centre-of-mass energy $\sqrt{s}$ and from cosmic ray measurements.

The Glauber model alone can not describe the totality of the collision: for this reason, it is coupled with a model that describes the particle production in order to simulate the charged particle distribution in a given detector. Usually, a two component model [34, 35] is used: in this case, the nuclear interactions are decomposed into soft and hard ones. In the soft interactions, the particles are produced with an average particle multiplicity proportional to N_{part}. The hard interactions, instead, produce particles with a probability proportional to N_{coll}. The fraction of soft and hard processes is a free parameter of the model. The total particle production can be described in terms of *ancestors*, that are independently emitting sources of particles, parametrized by:

$$N_{\mathrm{ancestors}} = f \cdot N_{\mathrm{part}} + (1-f) \cdot N_{\mathrm{coll}} \tag{1.11}$$

The particle multiplicity can be described with a negative binomial distribution (NBD):

$$P_{\mu,k}(n) = \frac{\Gamma(n+k)}{\Gamma(n+1)\Gamma(k)} \cdot \frac{(\mu/k)^n}{(\mu/k+1)^{n+k}} \tag{1.12}$$

where $P_{\mu,k}(n)$ is the probability of measuring n particles per ancestor, with μ the mean multiplicity per ancestor and k the width of the distribution.

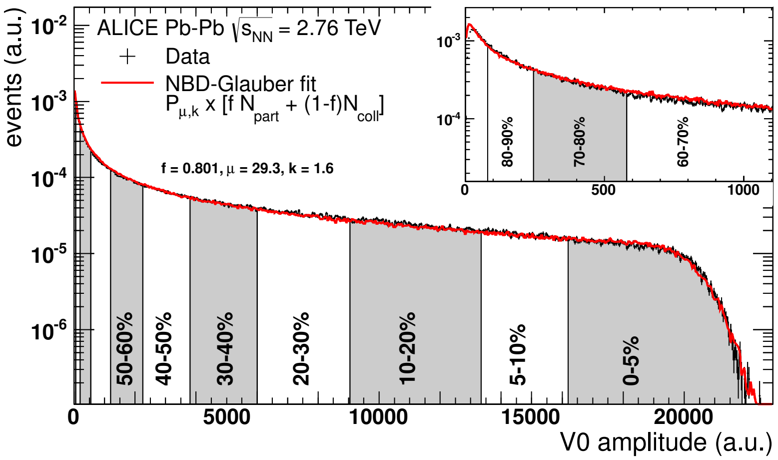

Figure 1.7: Distribution of the sum of the signal amplitudes measured in the V0 detectors in Pb–Pb collisions at $\sqrt{s_{\mathrm{NN}}} = 2.76$ TeV, compared with the NBD-Glauber calculations [36].

In each Monte Carlo Glauber event, the NBD is sampled $N_{\mathrm{ancestors}}$ times, in order to obtain the average simulated V0 amplitude for the event. The experimental distribution, reported in Fig. 1.7 in the case of Pb–Pb collisions at $\sqrt{s_{\mathrm{NN}}} = 2.76$ TeV, is then fitted with the NDB-Glauber calculation.

1.4.2 Space-time evolution of heavy ion collisions

During the heavy ion collision, the system undergoes different phases, that are schematically illustrated in Fig. 1.8 and can be summarized as follows:

- **Pre-collision stage**. For time $t < 0$ fm/c the two nuclei (that can be assimilated with discs, due to the Lorentz contraction), travel along the beam pipe.
- **Collision**. At $t = 0$ fm/c the two nuclei collide and their interaction can be described with the Glauber formalism, as described previously.
- **Pre-equilibrium stage**. In the first instants of the collision (0 fm/c <

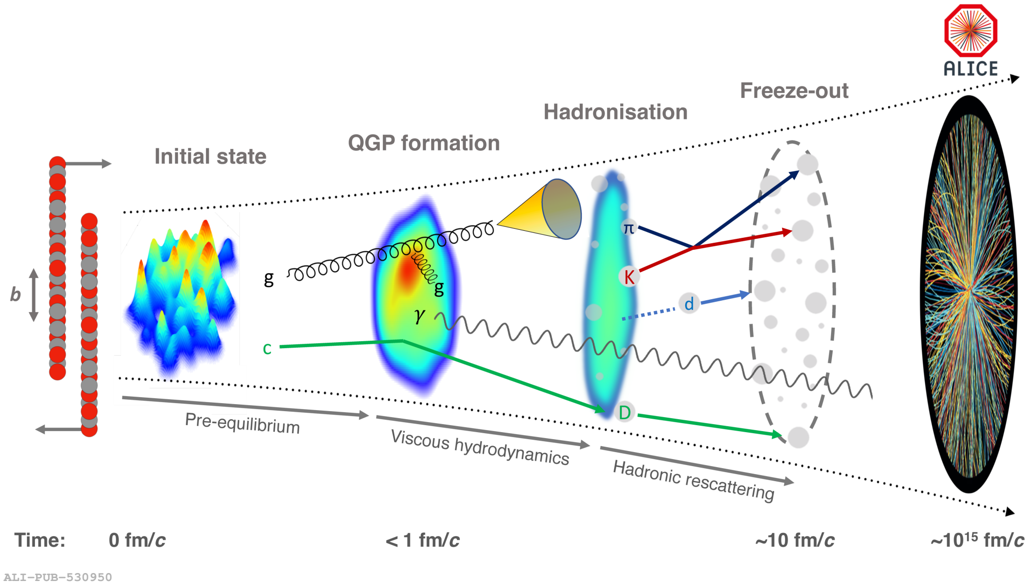

Figure 1.8: Schematic representation of the different phases that describes the evolution of a heavy ion collision [37].

t < 0.1 fm/c) the hard processes happen. Particles with high mass or high momentum are created, due to process characterized by high transferred momentum between the colliding partons. Also, direct photon are expected to be produced in this stage of the collision.

- **Thermal equilibrium**. The majority of the soft interactions happens in the time interval of 0 fm/c < t < $\tau_0 \sim 1$ fm/c. In fact, the constituent partons of nuclei undergo several interactions, losing their energy in the midrapidity region and escaping at forward rapidities. The obtained system at midrapidity is a hot and interacting medium, the QGP, that is grouped in droplets.

- **Phase transition**. In the following instants, 1 fm/c < t < 10 fm/c, the QGP droplets expand due to the effects of the thermal pressure gradient and the system boundaries. To describe this expansion, viscous hydrodinamic models are used [38]. As a consequence of the expansion, the system gradually cools down, crossing the phase boundary between the QGP and the ordinary matter. When the system reaches the critical temperature $T_c \approx 156$ MeV, the hadronisation takes place and the system gradually evolves into an interacting hadron resonance gas.

- **Chemical freeze-out**. In such system, the hadrons are still subject to inelastic and elastic collisions. When the temperature is below the T_{chem}, i.e. the temperature of chemical freeze-out, the hadrons do not have enough momentum to continue with the inelastical collisions. Hence, the abundance of the species is fixed in this moment: baryons, mesons and light nuclei are formed.
- **Kinetic freeze-out**. After the chemical freeze-out, the results of the hadronization process still undergo elastic collisions, transferring their momentum. When the temperature of the system is lower than the temperature of kinetic freeze-out, T_{kin}, also the elastic collisions are stopped, and the momentum of the particles is fixed.
- **Particle detection**. Finally, for t > 15 fm/c, the particles escape from the interaction region, and they are detected by the experimental apparatus.

1.5 QGP probes

One of the main characteristic of the QGP is its short lifetime, of about $\tau \sim 10$ fm/$c \sim 3 \times 10^{-23}$ s [39, 40]: for this reason it is impossible to directly observe the phase transition. Hence, to prove the QGP formation, indirect probes are used. These observables can be divided into three groups, reported below.

1.5.1 Direct photons

Since the photons are particles that do not carry colour charge, they are not affected by the interaction while they cross the coloured medium of the QGP. Hence, they are peculiar probes to investigate the QCD. But direct photons cannot be distinguished from the background, *i.e.* other photons produced in different phases of the collision. Hence, their study is challenging. First results on direct photons production in Pb–Pb collisions, performed by the ALICE collaboration, show that the direct photons production spectrum is in agreement with the model predictions that include the effect of the QGP formation [41].

1.5.2 Hard Probes

The hard probes are particles produced in the early stage of the collision by processes with high transferred momentum ($p_{\mathrm{T}} > 1$ GeV/c). They are rare processes, due to the small production cross section, and can be studied with pQCD. Since these probes are produced in the first instants of the collision, they are also influenced by the evolution of the medium.

High momentum particles and heavy flavour

In the initial stages of the collision, high momentum quarks and heavy flavour quarks, such as charm and bottom, can be created. Hence, the study of open-heavy flavour hadrons, such as D and B mesons, and the effect of their energy loss while crossing the medium, can give useful hint for the QGP. In fact, studying the D and B production in heavy-ion collisions, where the QGP is formed, and in pp collisions, where the QGP is not expected, could give explanation on the energy loss of high momentum particles in the QGP. To better study these differences, a variable is used, the nuclear modification factor R_{AA}, defined as:

$$R_{\mathrm{AA}} = \frac{1}{N_{\mathrm{coll}}} \frac{\mathrm{d}^2 N_{\mathrm{AA}}/(\mathrm{d}y \mathrm{d}p_{\mathrm{T}})}{\mathrm{d}^2 N_{\mathrm{pp}}/(\mathrm{d}y \mathrm{d}p_{\mathrm{T}})} \tag{1.13}$$

where N_{coll} is the number of binary collisions between two nucleons. Another useful variable that characterize the initial state of the collision, and then can be used in the study of the open heavy-flavours hadrons, is the elliptic flow v_2. This quantity describes the azimuthal anisotropy in the distribution of the produced particles, that is caused by the initial asymmetries in the geometry of the system produced in the collision. More details on the elliptic flow and, in general, on the anisotropic flow are described in Sect. 1.5.3. Fig. 1.9 shows the behaviour of R_{AA} and v_2 for the D mesons (in particular D^0, D^+ and D^{*+}) in central (0–10%) and semicentral (30–50%) Pb–Pb collisions at $\sqrt{s_{\mathrm{NN}}} = 5.02$ TeV [42]. The

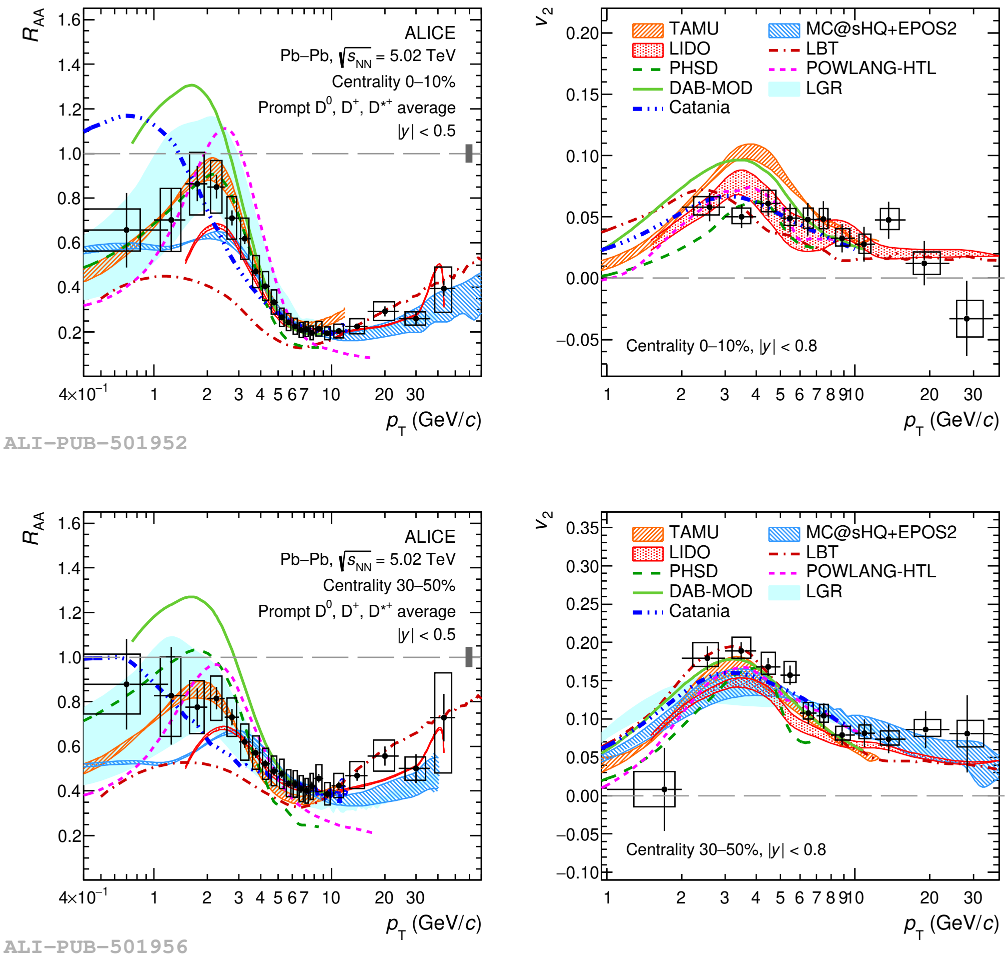

Figure 1.9: Nuclear modification factor R_{AA} (left) and elliptic flow v_2 (right) of prompt D^0, D^+ and D^{*+} mesons in central (0–10%) (top) and semicentral (30–50%) (bottom) centrality classes in Pb–Pb collisions at $\sqrt{s_{NN}}$ = 5.02 TeV, compared with different models implementing the charm-quark transport in a hydrodynamically expanding QGP [42].

experimental data are compared to different models, which implement the transport of the charm quark in a hydrodynamically expanding QCD. All the models qualitatively reproduce the experimental results, although some tensions are observed at low p_T.

Jet quenching

Another phenomenon that happens in high transferred momentum collisions is the formation of *jets*, that are a collimated spray of charged particles. In such collisions, in addition to the jets also other particles, referred as *underlying event*, are formed. While the jet originates from the hard parton-parton scattering, the underlying event is linked to all the other phenomena that happen in the collision, like initial and final state radiations and multipartons interaction. Among the events with jet production the collisions with a dijet event, where two back-to-back jets of equal transverse momentum are produced, are of a great importance in the QGP studies. In the case of pp collisions, since no medium is present, the two jets emerge from the collision with similar characteristics. In the case of heavy ion collisions, instead, where the QGP is formed, the partons that originate the dijet interact with the colour-charged constituents of the QGP. After these interactions, the parton shower is modified, with the jets that are not equivalent any more. This phenomenon is called *jet quenching*. Experimentally, the jet quenching manifests itself in different ways:

1. Energy loss, that is a medium-induced energy transport to large angles to the hard parton or jet direction. This behaviour is commonly observed through inclusive yield suppression;

2. Modification of the distribution of jet constituents due to medium effect, observed through the radial energy profile, jet substructure, and fragmentation functions;

3. The deflection of the jet centroid due to scattering effect, such as soft multiple scattering or scattering from quasi-particles in the QGP. This phenomenon is observed as medium-induced acoplanarity in coincidence measurements.

The first results of the jet quenching were already published by the STAR experiment at RHIC [43], as reported in Fig. 1.10. In fact, the plot shows

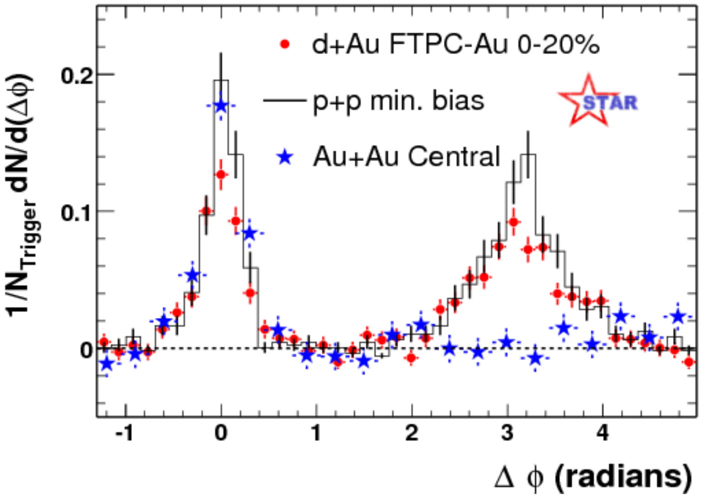

Figure 1.10: Jet measurements obtained by the STAR collaboration in pp, d–Au and central Au–Au collisions with the di-hadron correlation technique. $\Delta\phi$ is the opening angle between the trigger ($4 < p_{\mathrm{T}}^{\mathrm{trig}} < 6$ GeV/c) and associated particles ($2 < p_{\mathrm{T}}^{\mathrm{assoc}} < p_{\mathrm{T}}^{\mathrm{trig}}$ GeV/c) [43].

the particle yield normalized to the number of triggered particles as a function of the relative azimuthal angle $\Delta\phi$, defined as the azimuthal angle between the trigger particle and the associated particle. The experimental results show a suppression of particles in the direction opposite to the leading particle (called away region) in central Au–Au collisions, where a hot and dense medium (the QGP) is formed, but not in pp and d–Au collisions, where such medium is not formed. This probe has been extensively studied by the ALICE collaboration considering the energy loss measurements, the substructure modification and the acoplanarity: selected results are reported in Refs. [44–48].

Quarkonia production

The heavy quarkonia, that are the bound states of charmonium ($c\bar{c}$) and bottomonium ($b\bar{b}$), are important probes for the QGP studies, considering their formation in the deconfined medium. In fact, the free colour charges in the QGP leads to a screening of the QCD and the dissolution of the

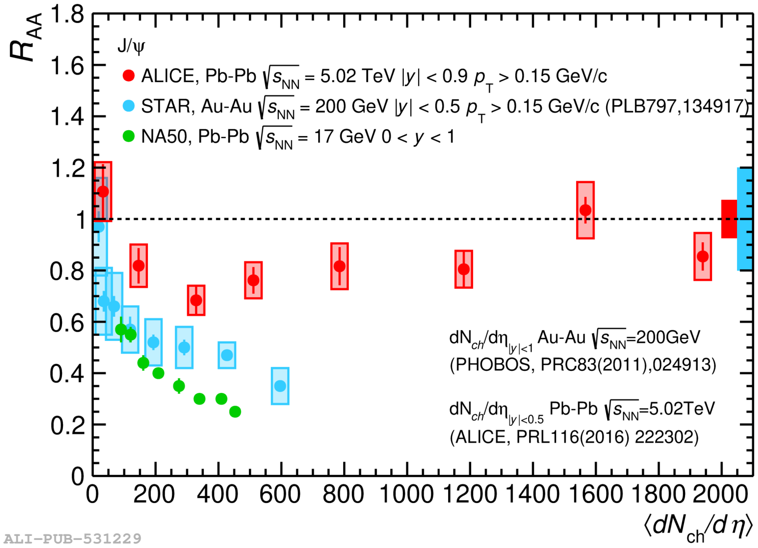

Figure 1.11: Nuclear modification factor R_{AA} for J/ψ particle measured by ALICE in Pb–Pb collisions at $\sqrt{s_{NN}} = 5.02$ TeV, compared with the results from NA50 and STAR [57].

quarkonia [49]. The quarkonia production in such medium is complex, since it is a multi stage process, with the production of the $q\bar{q}$ pair and the successive formation of the bound state, spanning over a significant time fraction of the collision history. Hence, what is expected is from one hand a suppression of the quarkonia production due to the QCD screening, but from another hand an enhancement of the quarkonia states produced due to effects of recombination in high density medium. The quarkonia production, with the focus on the J/ψ and other excited states of the charmonium, has been extensively studied at different energies at SPS [50, 51], RHIC [52–56] and LHC. Recent results from the ALICE experiment [57] are reported in Fig. 1.11. In such figure, the nuclear modification factor R_{AA} for the J/ψ measured by ALICE in Pb–Pb collisions at $\sqrt{s_{NN}} = 5.02$ TeV is compared with the same quantity measured by NA50 [51] and STAR [56] experiments. In such comparison, the prominent result is the strong decrease of the J/ψ suppression moving from low to high energy experiments, and also the disappear of the suppression moving through central collisions. These observations provide a strong indication on the (re)generation effects on the J/ψ.

At the LHC it is also possible studying the bottomonium state, in particular the Υ states. According to the theoretical predictions, these states are strongly suppressed with a hierarchy dictated by the binding energy [58]. This hypothesis has been confirmed by the CMS Collaboration at midrapidity [59] and by the ALICE Collaboration at forward rapidity [60, 61].

1.5.3 Soft Probes

The soft probes, characterized by a low transverse momentum ($p_{\mathrm{T}} < 1$ GeV/c), are the majority of the probes produced in heavy ion collisions. In fact, they are about 99% of the total particles produced, and they are formed in the final steps of the collisions, where only interactions with a low transferred momentum happen.

Particle spectra and radial flow One strong probe for the QGP can be obtained by the study of the transverse momentum distributions of low momentum hadrons. These can be modelled using a Bolztmann-Gibbs distribution at the kinetic freeze out:

$$\frac{1}{m_{\mathrm{T}}}\frac{\mathrm{d}^2N_i}{\mathrm{d}m_{\mathrm{T}}\mathrm{d}y} \propto e^{-\frac{m_{\mathrm{T}}}{T_{slope}}} \tag{1.14}$$

where T_{slope} is a fit parameter. If we consider only the thermal component of the distributions with a common emission temperature we expect to have the same slope for all the particles. This behaviour, instead, has not been observed at RHIC [62] and LHC [63, 64], where different T_{slope} values have been found. To explain the experimental results, an additional term to T_{slope} must be considered, such as:

$$T_{slope} = T_{kin} + \frac{1}{2}m\langle v_{\perp}\rangle^2 \tag{1.15}$$

where T_{kin} is the temperature of kinetic freeze-out, and the additional term keeps into account the mean kinetic energy acquired by each particle species due to the hydrodinamical collective expansion of the medium along the transverse plane. This phenomenon is called *radial flow*, and can be observed looking at the different particles production distributions. As reported in Fig. 1.12, that shows the pions, kaons, and protons distributions in Pb–Pb collisions at $\sqrt{s_{\mathrm{NN}}} = 2.76$ TeV measured by the ALICE experiment, the slope for the pions spectrum is steeper, while the protons spectrum is reduced. The effect of the radial flow, in general, is well reproduced by hydrodynamical calculations describing the QGP expansion, such as HKM [65] and Krakow [66].

Anisotropic flow

Another evidence of the QGP can be searched through the eventual azimuthal anisotropies in particle production distributions. In particular, it is possible to find a correlation between the particle emission angles and the impact parameter in the case of collisions where the nuclei only partially overlap, *i.e.* peripheral collisions. These anisotropies can be measured looking at the Fourier expansion in the azimuthal angle of the production spectra:

$$\frac{\mathrm{d}N}{\mathrm{d}\phi} \propto 1 + 2\sum_{n=1}^{\infty} v_n \cos[n(\phi - \Psi_n)] \tag{1.16}$$

where v_n is the Fourier coefficient and Ψ_n is the azimuthal angle of the reaction plane. During the reaction, due to the presence of the expanding QGP, the anisotropies are converted into a pressure gradient parallel to the plane defined by the beam direction and the impact parameter vector. It is possible to define the Fourier coefficients v_n as:

$$v_n = \langle \cos[n(\phi - \Psi_n)] \rangle \tag{1.17}$$

and, in particular, they take the name of directed, elliptic, an triangular flow for n = 1, 2, 3 respectively. The directed flow v_1 corresponds to an asymmetry in the parallel and antiparallel directions with respect to the impact parameter, hence showing a preferential direction of the particle emission in the direction of the beam. For the elliptic flow v_2, instead, there is a difference between the number of particles emitted in the directions parallel and perpendicular to the impact parameter, and this is related to the almond shaped overlap region of the two colliding nuclei. Finally, the higher order coefficients are related to the fluctuations in the initial distributions of nucleons in the overlap region. Fig. 1.13 shows the values

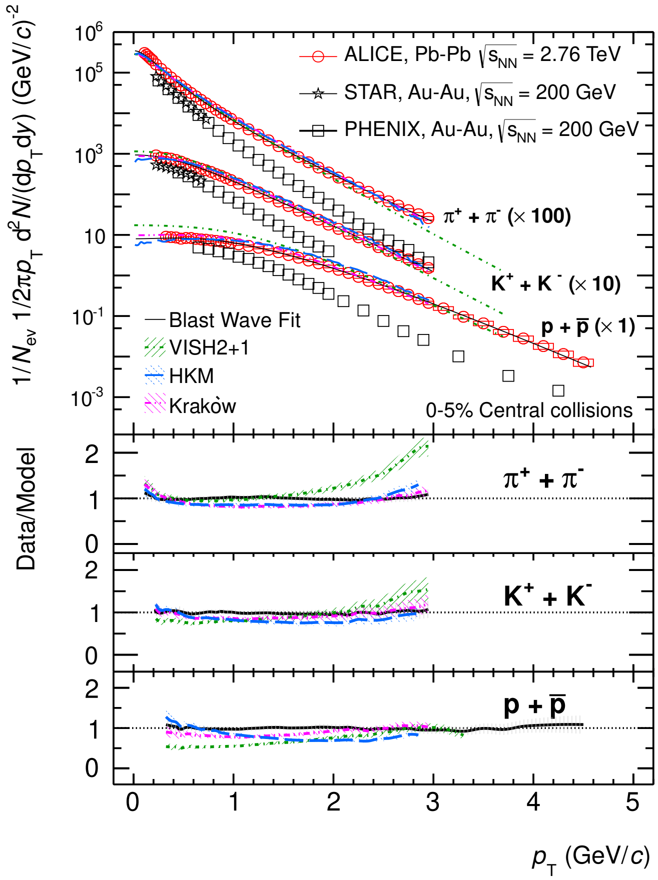

Figure 1.12: Transverse momentum distributions for pions, kaons and protons in Au–Au collisions at $\sqrt{s_{NN}}$ = 200 GeV at RHIC and in Pb–Pb collisions at $\sqrt{s_{NN}}$ = 2.76 TeV at the LHC. The data are fitted with a Blast-Wave model (lines) and compared with the prediction from different hydrodynamical models (shaded areas) [63].

of elliptic, triangular and higher order flow in Pb–Pb collisions measured by the ALICE Collaboration, compared with the values predicted by hydrodynamic calculations [67].

Strangeness enhancement

One of the first signature proposed by theoreticians [68] as a probe for the QGP formation in high-energy hadronic collisions is the strangeness enhancement, *i.e.* an enhanced production of strange hadrons in heavy ion collisions with respect to minimum bias collisions. The origin of this phenomenon lies in the fact that the $s\bar{s}$ quark pairs are easily formed in the QGP since their mass is well below the QGP temperature. Moreover, the high density of strangeness at hadronization results in an enhanced production of baryons with multi-strange content, like Ω^- (sss) and $\Xi^{0,-}$ (uss and dss, respectively), that are produced more with respect to single strange baryons like kaons and Λ. Fig. 1.14 shows the hadron-to-pion ratio for different strange hadrons as a function of the charged particle multiplicity measured at midrapidity. The measurements are obtained by the ALICE experiment in different collision systems, from pp to Pb–Pb. It is possible to observe that these ratios, for the different hadrons, evolve smoothly with the multiplicity: the larger value measured in Pb–Pb collisions is interpreted as the signature of the formation of the QGP. Moreover, particles with a higher content of strangeness are produced in major quantities with the increase of the multiplicity: this behaviour can be better observed in Fig. 1.15, where the strange hadron-to-pion yields measured in pp collisions at $\sqrt{s} = 7$ TeV and in p–Pb collisions at $\sqrt{s_{\rm NN}} = 5.02$ TeV, divided by the values measured in the inclusive pp sample, are reported as a function of the particle multiplicity [70].

1.6 Kinematic variables of interest

In high-energy hadronics collisions it is useful to define some quantities, that are Lorentz invariant, to describe the system. The observables are defined on a right-handed Cartesian system, centred in the collision point. The z axis is parallel with the beam direction, the x axis is aligned with the accelerator plane and it is pointing toward the centre of the LHC ring,

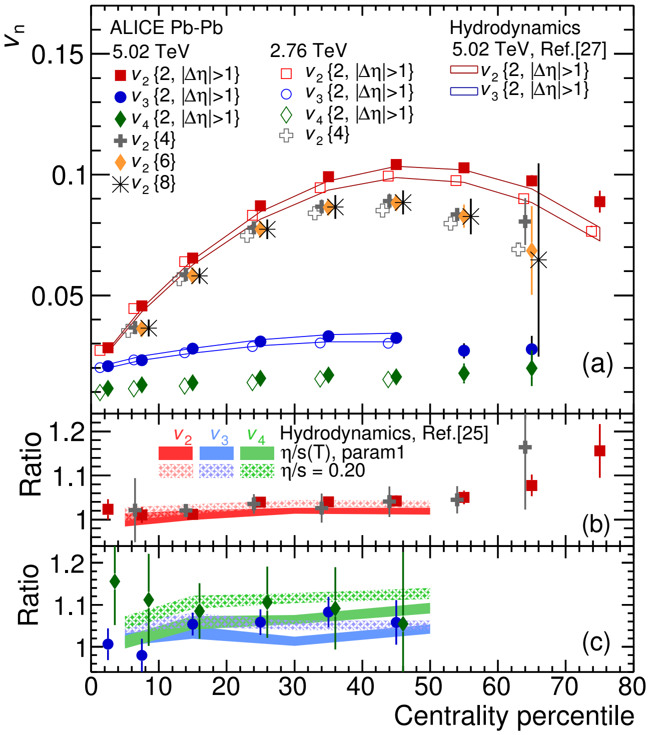

Figure 1.13: Anisotropic flow v_n integrated over the p_T range $0.2 < p_T < 5.0$ GeV/c measured in Pb–Pb collisions at $\sqrt{s_{NN}} = 5.02$ TeV (solid marker) and $\sqrt{s_{NN}} = 2.76$ TeV (open marker) as a function of event centrality. The ratios of v_n between Pb–Pb collisions at $\sqrt{s_{NN}} = 5.02$ TeV and $\sqrt{s_{NN}} = 2.76$ TeV are shown in the lower panels. Various hydrodynamic calculations are also presented, showing a good agreement with data for low values of the shear viscosity η/s [67].

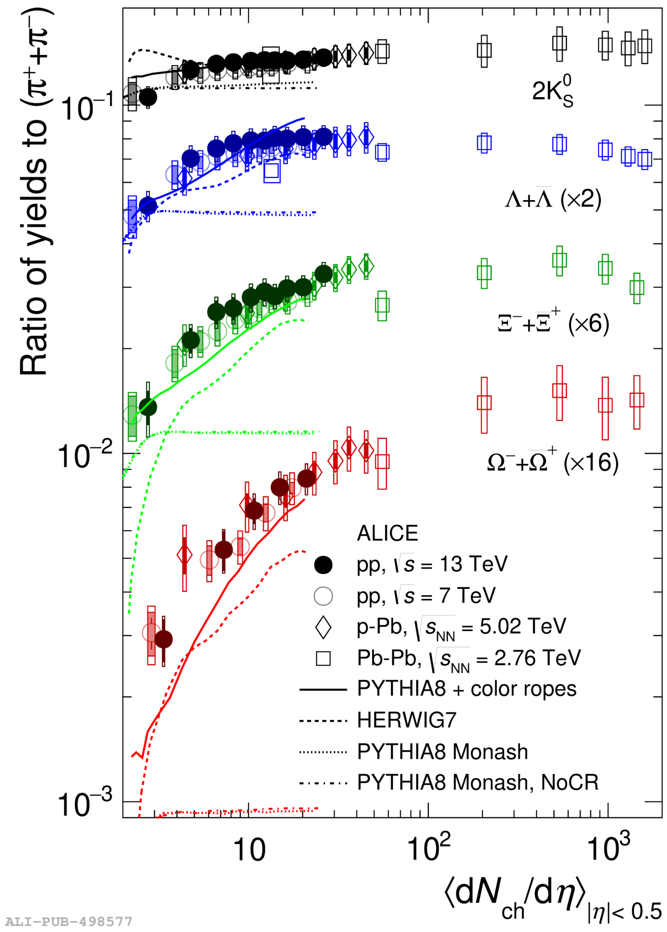

Figure 1.14: Integrated strange hadron-to-pion ratios as a function of the particle multiplicity measured in pp, p–Pb and Pb–Pb collisions by the ALICE experiment. Different lines represent predictions from different Monte Carlo generators [69].

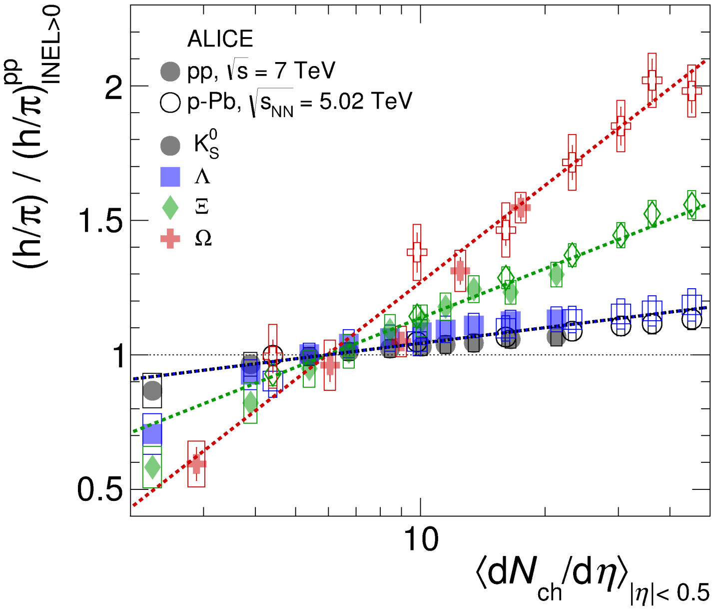

Figure 1.15: Ratios of strange hadron yield to pions measured in pp collisions at $\sqrt{s} = 7$ TeV and in p–Pb collisions at $\sqrt{s_{\mathrm{NN}}} = 5.02$ TeV, normalized by the value measured in the minimum bias pp sample. The different colors refer to different (multi)strange hadrons [70].

while the y axis is pointing upwards. The z direction is called *longitudinal*, while the xy plane is referred as the *transverse plane*. With this notation, is possible to decompose the total momentum p of the particle into two components, p_z and $p_T = \sqrt{p_x^2 + p_y^2}$. Another useful quantity linked to the coordinate system is the angle θ, that is the angle with respect to the z axis.

The rapidity y of a particle is defined as:

$$y = \frac{1}{2} \ln \left(\frac{E + p_z}{E - p_z} \right) \tag{1.18}$$

where E is the total energy of the particle. This quantity is useful to describe the space distribution of the emitted particles in the collision: if $y \approx 0$ then the p_z component is negligible and the particle's direction is prevalent in the transverse plane, while large values of y indicate that the particle moves on the beam direction. In order to obtain a precise y value, the particle must be correctly identified, that means having a precise measurement of E and p_z: unfortunately this is not always possible. For this reason, another variable with a similar meaning, the pseudorapidity η, is often used. The pseudorapidity is defined as:

$$\eta = -\frac{1}{2} \ln \left(\tan \frac{\theta}{2} \right) \tag{1.19}$$

where θ is the angle between the beam axis and the particle direction. At high energies we have $y \sim \eta$, since $E \sim |p|$.

1.7 Particle multiplicity and system size

The charged particle multiplicity dN/dy, referred as *multiplicity* from here, is the number of charged particles produced per unit of rapidity. This observable, of the uttermost importance in describing the results in high-energy hadronic collisions, is used to estimate the centrality of the collision. Since the multiplicity is defined for each collision system, this allows the direct comparison between different collision systems.

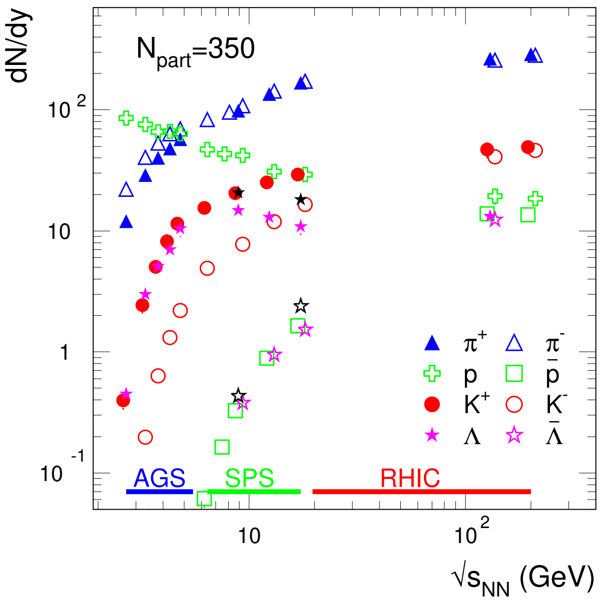

Figure 1.16: Production of different hadron yields at midrapidity in central Au–Au and Pb–Pb collisions as a function of the centre-of-mass energy $\sqrt{s_{\mathrm{NN}}}$, measured by different experiments [71].

The dependence of the multiplicity with the energy of the colliding systems is reported in Fig. 1.16 [71]. The yields of different hadrons, from pions to Λs, measured by different experiments in central Au–Au and Pb–Pb collisions at midrapidity, are reported as a function of the centre-of-mass energy $\sqrt{s_{\rm NN}}$. At low energy, $\sqrt{s_{\rm NN}} < 5$ GeV/c, the data measured by the AGS experiment show that the final state is dominated by the incoming nucleons. Moreover, due to the isospin effect, the particle and antiparticle yields are different. At higher energies, instead, the pions are the majority of the produced particles, and the production of particles and antiparticles is observed to be the same.

The multiplicity can be related to the size of the colliding system. Generally, this quantity is estimated from the study of two-particle correlations using the Hanbury Brown-Twiss (HBT) method [72]. This method, initially born to measure the star radii with the intensity interferometry measurement, is now employed in different physical cases. According to the results reported in Ref. [73], the HBT radius R can be parametrized as a function of the multiplicity with the following relation:

$$R = a\langle {\rm d}N_{ch}/{\rm d}y\rangle^{1/3} + b \tag{1.20}$$

where a and b are fit parameter, equal respectively to $a = 0.473$ fm and $b = 0$. Fig. 1.17 shows the value of different HBT parametrizations as a function of the multiplicity. The dotted gray line is the result of a linear fit to the ALICE HBT data measured in pp collisions at $\sqrt{s} = 7$ TeV [74], p–Pb collisions at $\sqrt{s_{\rm NN}} = 5.02$ TeV [75] and Pb–Pb collisions at $\sqrt{s_{\rm NN}} = 2.76$ TeV [40]. The solid black line corresponds to a different parametrisation, obtained by fixing the parameters of Eq. 1.20 in order to reproduce the coalescence parameter B_2 (see Eq. 2.13 for the definition) in the most central Pb–Pb collisions at $\sqrt{s_{\rm NN}} = 2.76$ TeV. Finally, the dashed blue line shows the relation between the system radius and the charged particle multiplicity used in Ref. [76], which does not rely on the HBT data.

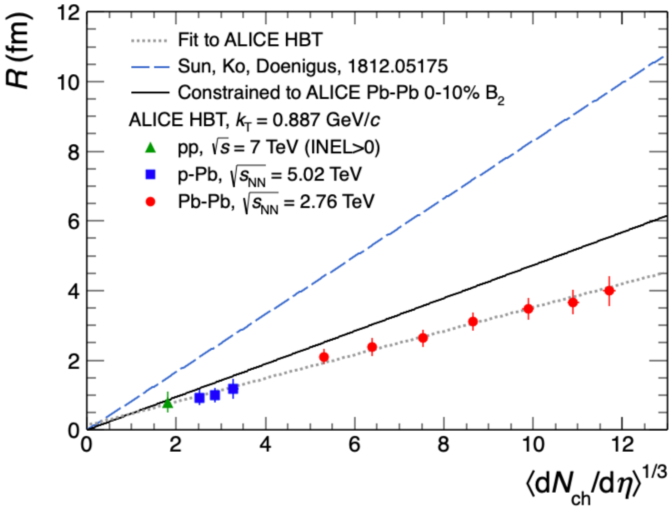

Figure 1.17: Comparison of different source volume parametrisations as a function of the multiplicity with the data measured by the ALICE experiment in pp, p–Pb and Pb–Pb collisions [73].

Chapter 2

Production of light (anti)nuclei in high-energy hadronic collisions

In high-energy hadronic collisions a large variety of particles, from pions to light (anti)nuclei, are produced. In particular, the study of how (anti)nuclei are formed is interesting from different points of view, not only for the understanding of the formation mechanism, but also for astrophysical aspects. Despite the abundance of experimental results, the production mechanism of light (anti)nuclei is not well understood: if we consider the nuclei binding energy, of the order of 1 MeV per nucleon [77], this value is very low compared to the temperature of chemical freeze-out, hence is unclear how the nuclei can survive the hot medium created in high energy hadronic collisions.

In order to understand the production mechanism of light (anti)nuclei, their production has been studied in depth from different experiments at different energies, in both fixed-target setups and in hadron colliders. Results from the Alternating Gradient Synchrotron (AGS) at the Brookhaven National Laboratory (BNL) [78–81], Super Proton Synchrotron (SPS) at CERN [82], and Relativistic Heavy Ion Collider (RHIC) at BNL [83–88] paved the way to the studies performed by the ALICE Collaboration [89–108]. The experimental data recorded by all the experiments have been compared with two classes of phenomenological models that describe the hadronization process: the Statistical Hadronization Model and the baryon coalescence. These two models are described in detail in the following

Sections.

2.1 Statistical Hadronization Model

The Statistical Hadronization Model (SHM) describes the abundances of hadrons produced in hadronic collisions. The first idea of using statistical concepts to describe the particles production can be traced back to Enrico Fermi in 1950 [109], and then the idea was further developed by Rolf Hagedorn [110]. The general idea on a statistical model is that the final state is composed by all the particles compatible with the conservation laws imposed by the theory that describes the interaction of the system: in the case of particle physics, this theory is the Standard Model. The relative particles abundance, then, is set by the maximization of the system phase space. According to the system size, two different approaches are used. In the case of large volume systems, such as Pb–Pb collisions, a gran canonical approach is used. For small volume system, instead, a canonical approach is necessary, in order to respect the constraints on the conserved charge(s). The two approaches are reported in detail below.

2.1.1 Gran Canonical SHM

In heavy ion collisions the requirements to use the gran canonical ensemble, as discussed in Ref. [111], are satisfied. In fact, the system under study, *i.e.* the midrapidity region, is only a sub-system of the interaction system, that is the rest of the medium created in the collisions. Hence, the system under study is in constant equilibrium with an energy and charge reservoir. Therefore, the system energy and charges are conserved on average and their values are determined by the temperature and the chemical potentials.

The properties of a system in thermodynamic equilibrium is described by the grand partition function Z:

$$Z(T, V, \mu) = \mathrm{Tr}\left[\exp\left(-\frac{H + \sum_i \mu_i Q_i}{T}\right)\right] \quad \text{with}\, \mu = \sum_i \mu_i Q_i \tag{2.1}$$

where H, T, and V are, respectively, the system's Hamiltonian, temperature, and volume, Q_i are the conserved charges and μ_i their respective chemical potentials. The system is described by the Hadron Resonance Gas (HRG) Hamiltonian: this form is used since it is able to describe the interaction of a strong interacting medium and can reproduce the equation of state obtained with lQCD over a wide range of temperature. In such system, the conserved charges are the electric charge Q, the strangeness content S and the baryon number B. The partition function of the system Z is the product of the single partition functions Z_i of all the particles inside the HRG:

$$Z(T,V,\mu) = \prod_i Z_i(T,V,\mu_i) \rightarrow \log Z(T,V,\mu) = \sum_i \log Z_i(T,V,\mu_i) \quad (2.2)$$

The particles partition functions Z_i are defined as:

$$\log Z_i(T,V,\mu_i) = \frac{Vg_i}{2\pi} \int_0^\infty \pm p^2 \mathrm{d}p \log\left(1 \pm \lambda_i\left(T,\mu_i\right) e^{-\epsilon_i/T}\right) \quad (2.3)$$

with the ± signs that denote the considered particle, + for fermions and − for bosons. The factor g_i is linked to the spin-isospin degeneracy, while $\epsilon_i = \sqrt{m_i^2 + p^2}$ is the particle energy. The *fugacity* λ_i contains the dependence on the chemical potentials, according to the following formula:

$$\lambda_i(T,\mu_i) = e^{(B_i\mu_B + S_i\mu_S + Q_i\mu_Q)/T} = e^{\mu/T} \quad (2.4)$$

where B_i, S_i and Q_i are, respectively, the baryon number, the strangeness number and the electric charge. Considering the expansion of the logarithm with a Taylor series and performing the integration over the momentum range (as reported in Ref. [112]), the partition function for the specie i takes the form:

$$\log Z_i(T,V,\mu_i) = \frac{VTg_i}{2\pi^2} \sum_{k=1}^{\infty} \frac{(\pm 1)^{k+1}}{k^2} \lambda_i^k m_i^2 K_2\left(\frac{km_i}{T}\right) \quad (2.5)$$

with K_2 the modified Bessel function. The average number of particles for each species i can be expressed as:

$$\langle N_i \rangle^{th}(T,V,\mu_i) = T\frac{\partial}{\partial \mu_i} \log Z_i(T,V,\mu_i) = \frac{VTg_i}{2\pi^2} \sum_{k=1}^{\infty} \frac{(\pm 1)^{k+1}}{k} \lambda_i^k m_i^2 K_2\left(\frac{km_i}{T}\right) \quad (2.6)$$

It is important to notice that this formula describes only the primary particles produced in the collision. To compare this quantity with the measured yields, the contribution due to the feed-down of other species j that decade into particles i must be taken into account. With this knowledge, the total number of particles of species i produced in the collision can be described with:

$$\langle N_i \rangle (T, V, \mu_i) = \langle N_i \rangle^{th} (T, V, \mu_i) + \sum_j \Gamma_{j \to i} \langle N_j \rangle^{th} (T, V, \mu_j) \qquad (2.7)$$

where $\Gamma_{j \to i}$ is the branching ratio of species j toward the species i.

The model that we have described above is valid only in a low density system. In fact, the HRG is described as a gas of not interacting hadrons and resonances, and in systems with low density the repulsive and attractive interactions between the particles can be neglected. More advanced implementations of the SHM model the repulsive correction as van der Waals force type, as shown in Ref. [113].

The particle yield, as reported in Eq. 2.7, depends on five different parameters: the system temperature T, the system volume V, and the three chemical potentials μ_B, μ_S, and μ_Q. In general, in the initial system, two of the three potentials are already fixed. In fact, $\mu_S = 0$ since the colliding nuclei do not carry a strangeness content, while μ_Q is fixed by the isospin asymmetry of the initial stage. For the baryochemical potential, instead, this is not *a priori* fixed, since it depends on the energy of the collisions. Finally, the dependence of the volume can be removed if we consider not the yields of the single particle species but considering the ratio between them. Hence, the only free parameter of the model (in the case of ratio of particle yields) is the temperature of the system.

The SHM is used to predict the particle yields in the collision, from the lightest particles as charged pions to the heaviest ones, light (anti)nuclei and (anti)hypernuclei, that are nuclei in which one neutron is replaced with a hyperon. Considering the binding energy of the light (anti)nuclei and (anti)hypernuclei, that is very low with respect to the temperature of chemical freeze out of the system, it seems unnatural that these particles can survive in the hot medium created in heavy-ion collisions. However, the model does not take into account the internal structure of the hadrons: hence, the hadron yields are a consequence of their phase space distribu-

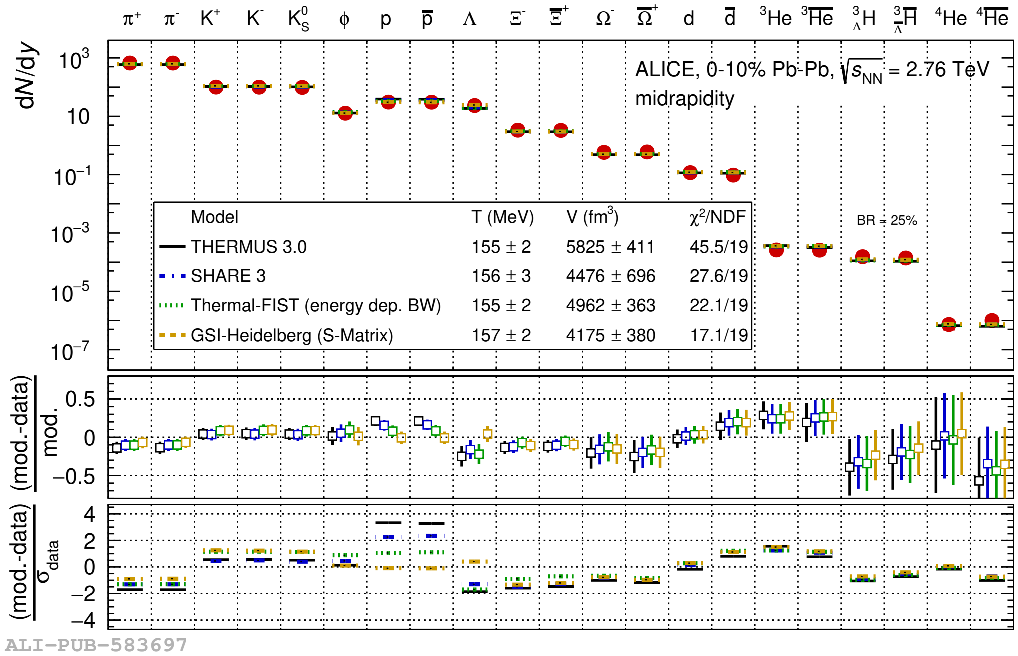

Figure 2.1: Hadron yields for different particles, from pions to ^{4}He, measured in central Pb–Pb collisions at $\sqrt{s_{\mathrm{NN}}} = 2.76$ TeV by the ALICE Collaboration. The experimental yields are compared with four different SHM implementations: THERMUS (black line), SHARE 3 (blue line), Thermal-FIST (green line) and GSI-Heideberg (yellow line) [37].

tion, and the particles emerge naturally when the system temperature and the baryochemical potential are fixed.

Figure 2.1 shows the hadron yields measured by the ALICE Collaboration compared with theoretical predictions of different SHM implementations. In particular, the considered particles vary from pions to ^{4}He, with the note that the hypertriton yield is obtained using a theoretical estimation with a branching ratio BR = 25% considering the $^3_\Lambda\mathrm{He} \rightarrow {}^3\mathrm{He} + \pi^-$ decay channel. The experimental data are compared with four different implementations for the SHM: THERMUS [114, 115], SHARE [116–119], Thermal-FIST [120, 121] and GSI-Heideberg [112, 122, 123]. The models differ in the list of resonance included in the Hamiltonian and in the hypothesis on the hadron volume. For all the models, the fit to the hadrons provides a temperature of chemical freeze-out of T_{chem} = 156 MeV [94]. Moreover, the models reproduce the experimental yields with a good accuracy over a large number of order of magnitude.

2.1.2 Canonical SHM

In smaller system, such as pp and p–Pb, the gran canonical approach can not be used: the minimal requirement for the application are not satisfied due to the smaller reaction volume. In this case, the exact conservation of the quantum number across the correlation volume V_c must be taken into account: for this reason, the canonical approach of the SHM is used. One of the consequence of the exact charge conservation is a suppression of the hadron yield with respect to a gran canonical description: this phenomenon is called *canonical suppression*, and it is stronger for multi-charged particles, such as multi-strange hyperons and light (anti)nuclei. The Canonical Standard Model (CSM) has been successfully used to describe the hadron yield in e^+e^- [124], pp and $\mathrm{p\overline{p}}$ [125] collisions.

In the following section, the CSM approach reported in Ref. [126] is described, implemented within the Thermal-FIST package [120, 121]. In this model, a full canonical treatment for the electrical charge, baryon number and strangeness content is consider, and also the production of light (anti)nuclei is taken into account. The system is described as a HRG in full thermal and chemical equilibrium, and the Boltzmann approximation is used. The charges (B, Q, S) are fixed to the exact values that are conserved across the correlation volume V_c. In such system, the partition function has the following form:

$$\begin{aligned} Z(B,Q,S) = \int_{-\pi}^{\pi} \frac{\mathrm{d}\phi_B}{2\pi} \int_{-\pi}^{\pi} \frac{\mathrm{d}\phi_Q}{2\pi} \int_{-\pi}^{\pi} \frac{\mathrm{d}\phi_S}{2\pi} e^{-i(B\phi_B + Q\phi_q + S\phi_s)} \\ \times \exp\left[\sum_j z_j^1 e^{i(B\phi_B + Q\phi_q + S\phi_s)}\right] \end{aligned} \tag{2.8}$$

The single particle partition function z_j^1 is defined as:

$$z_j^1 = V_c \int \mathrm{d}m \rho_j(m) g_j \frac{m^2 T}{2\pi^2} K_2\left(\frac{m}{T}\right) \tag{2.9}$$

with g_j the degeneracy factor for the species j, $\rho_j(m)$ is the mass distribution of the species j (that also takes into account the resonances width), and K_2 is the second modified Bessel function. In the CSM implementation, the mean particle multiplicity can be written as:

$$\langle N_j^{th} \rangle^{CE} = \frac{Z(B - B_j, Q - Q_j, S - S_j)}{Z(B, Q, S)} \langle N_j^{ch} \rangle^{GCE} \tag{2.10}$$

where $\langle N_j^{ch} \rangle^{GCE}$ is the mean multiplicity for the specie j calculated in a gran canonical ensemble, supposing the same temperature T and volume V. The proportional factor between the two mean particle multiplicity is called *chemical factor*, and reflects the exact conservation of the charges. Also in the case of the canonical ensemble, the feed-down contribution must be taken into account. Hence, the total particle yield is described by:

$$\langle N_j \rangle^{CE} = \langle N_j^{th} \rangle^{CE} + \sum_i \Gamma_{i \to j} \langle N_i^{th} \rangle^{CE} \tag{2.11}$$

As already reported above, the described CSM is implemented inside the Thermal-FIST package. In this version, the conserved charges are fixed to the initial values of Q = S = B = 0. Moreover, all the particles are considered as point-like, a temperature of T_{chem} = 155 MeV is assumed and different values of correlation volumes V_c, ranging from one to three midrapidity units, are considered. Fig. 2.2 shows the predicted ratio between the p_{T} integrated yields of different nuclei and the protons as a function of the pion multiplicity $\mathrm{d}N_{\pi}/\mathrm{d}y$. The pion multiplicity is used since this variable is both measured by the experiments and predicted by the model. The experimental data from the ALICE Collaboration, obtained in Pb–Pb collisions at $\sqrt{s_{\text{NN}}} = 2.76$ TeV [90, 94, 127] and in pp collisions at different energies [93] are compared with three different implementations of the model, that vary for both T_{chem} and V_c. In particular, the predictions for T_{chem} = 155 MeV and $V_c = \mathrm{d}V/\mathrm{d}y$ (black solid lines), T_{chem} = 155 MeV and $V_c = 3\mathrm{d}V/\mathrm{d}y$ (black dashed lines) and T_{chem} = 170 MeV and $V_c = \mathrm{d}V/\mathrm{d}y$ (blue dash-dotted lines) are reported. The predictions grow monotonically with increasing pion multiplicity, and they saturate at the corresponding gran-canonical values at high multiplicity.

In the context of the SHM, the microscopic description of the hadron formation is still an open point. According to Ref. [128], one possible explanation is that the light (anti)nuclei are produced at the QGP hadronization

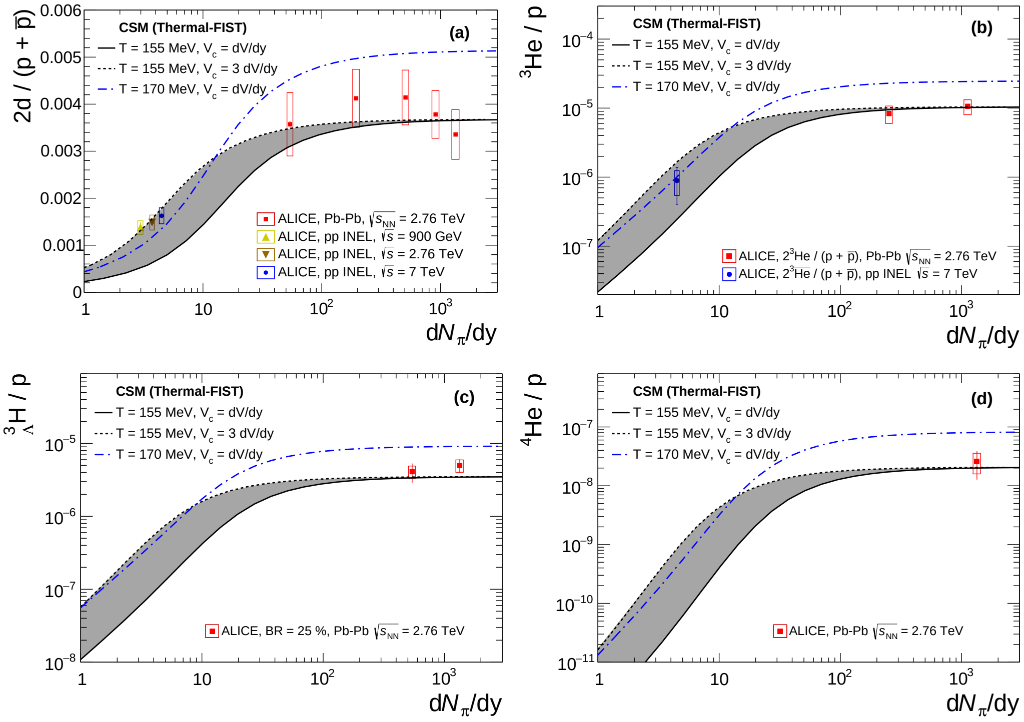

Figure 2.2: Prediction for d/p (top left), ^{3}He/p (top right), $^3_\Lambda$He/p (bottom left) and ^{4}He/p (bottom right) as a function of the pion multiplicity dN_π/dy, obtained by the Thermal-FIST package. The experimental data from the ALICE Collaboration (available at the moment of the publication of Ref. [126], from where the figure is taken) are compared with different predictions of the model.

as compact, colorless droplets of quark matter, that have the same quantum numbers of the final states. These droplets are characterized by a lifetime of 5 fm or longer, and exitaction energies of 40 MeV or less, in order to survive in the hot and dense hadronic medium. Moreover, due to their initially compact nature, these states would exhibit a negligible final-state interaction cross section with other hadrons in the hadron gas phase.

2.2 Coalescence Model

Another model that describes the production of light (anti)nuclei is the baryon coalescence. This model relies on the fundamental idea that the nuclei formation is due to the proximity of the constituent nucleons in the phase space. The first coalescence model was developed by Butler and Pearson, related to proton-nucleus collisions [129]. In fact, they suggested that, in such reactions, the deuteron production is due to the biding of cascade nucleons in the presence of the target nuclear optical potential. During the following years works from Kapusta [130], Scheibl and Heinz [131] and many others shaped the model with the current characteristics.

The key parameter of this model is the *coalescence parameter* B_A, defined as:

$$\begin{aligned} B_\mathrm{A} = E_\mathrm{A}\frac{\mathrm{d}^3N_\mathrm{A}}{\mathrm{d}p^3_\mathrm{A}} \bigg/ \left(E_\mathrm{p}\frac{\mathrm{d}^3N_\mathrm{p}}{\mathrm{d}p^3_\mathrm{p}}\right)^\mathrm{A} = \\ = \frac{1}{2\pi p^\mathrm{A}_\mathrm{T}}\frac{\mathrm{d}^2N_\mathrm{A}}{\mathrm{d}y\mathrm{d}p^\mathrm{A}_\mathrm{T}} \bigg/ \left(\frac{1}{2\pi p^\mathrm{p}_\mathrm{T}}\frac{\mathrm{d}^2N_\mathrm{p}}{\mathrm{d}y\mathrm{d}p^\mathrm{p}_\mathrm{T}}\right)^\mathrm{A} \end{aligned} \tag{2.12}$$

where the numerators are the invariant yield of the nuclei, while on the denominators there are the invariant yield of primary protons, raised to the power of A, where A is the mass number of the considered nucleus. In principle, in the denominator the proton and neutron yield should be considered separately: but, at the LHC energies, the isospin chemical potential is expected to be vanishing [132]. Hence, since protons and neutrons belong to the same isospin doublet, only the proton yield is used, considering also the experimental difficulties to measure neutral charged particles in experiments like ALICE. The coalescence parameter is reported as a function of the reduced transverse momentum $p_{\mathrm{T}}^{\mathrm{p}} = p_{\mathrm{T}}^{\mathrm{A}}/\mathrm{A}$, since the momentum of the nucleus is the sum of the momenta of A nucleons.

In the following sections, the coalescence model will be treated in detail. A simple implementation, where only the momentum-space correlations are taken into account, and the more advanced ones, based on the Wigner formalisms, will be presented.

2.2.1 Simple Coalescence Model

One of the first implementation of the coalescence model, the so-called *simple coalescence*, is based on the work from Kapusta [130]. In such implementation, only the momentum-space correlation, and not the space-time ones, are considered. Two nucleons can coalesce and form a nucleus if the difference between their momenta is smaller than a given threshold called *coalescence momentum*, $\Delta p < p_0$. No further assumption on the proximity of the nucleons in the space is done. In small system, such as pp collisions, this hypothesis is plausible, since the system size is compatible with the nucleus size, hence the nucleons can be produced close to each other. In larger system, such as Pb–Pb collisions, this assumption is not valid any more: the system size is larger with respect to the nucleus one, the nucleons can be produced far away from each other, and then they can not form the nucleus even if they are close in the momentum space.

In this implementation, neglecting the nucleon isospin, the coalescence parameter can be expressed as:

$$B_{\mathrm{A}} = \left(\frac{4\pi}{3} p_0^3\right)^{\mathrm{A}-1} \frac{m_{\mathrm{A}}}{m_{\mathrm{p}}^{\mathrm{A}}} \tag{2.13}$$

where A is the nucleus mass number, m_{A} the nucleus mass, m_{p} the proton mass and p_0 the coalescence momentum. With this definition, B_{A} should not depend neither on transverse momentum nor on the charged multiplicity, that is directly linked to the system size. Instead, as reported in Fig 2.3, in pp collisions the deuteron coalescence parameter is constant as a function of the transverse momentum, while in Pb–Pb collisions it shows an increasing trend. Moreover, also in pp collisions it is observed

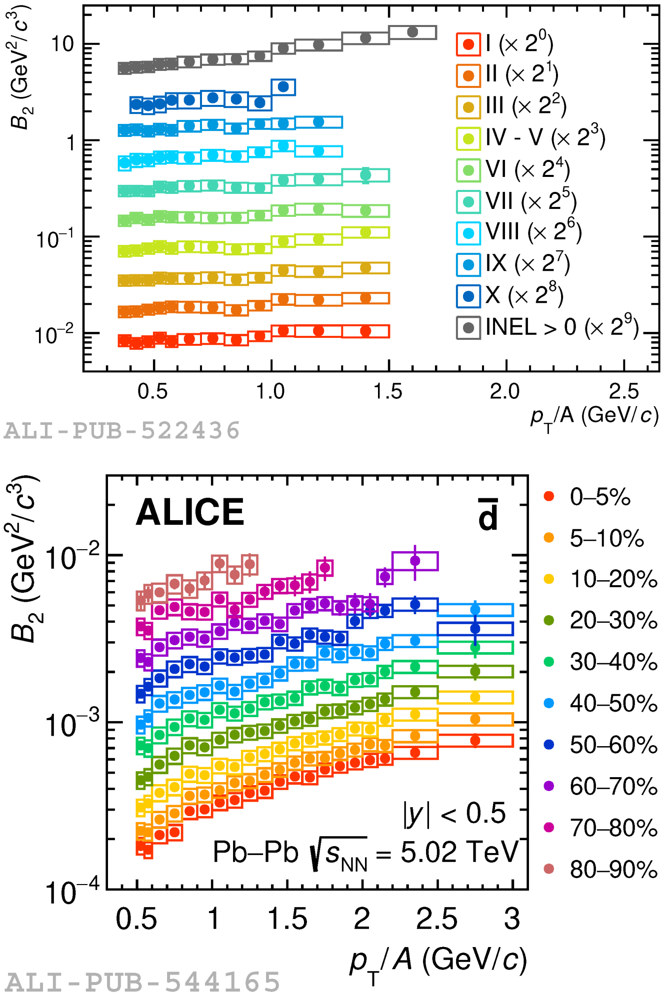

ALI-PUB-522436

ALI-PUB-544165

Figure 2.3: Deuteron coalescence parameter B_2 in different multiplicity classes, measured in pp collisions at $\sqrt{s}$ = 5.02 TeV (top) [100] and in Pb–Pb collisions at $\sqrt{s_{NN}}$ = 5.02 TeV (bottom) [107].

a dependence of the coalescence parameter from the transverse momentum, in the case of minimum bias (MB) collisions. This behaviour can be explained as a consequence of the hardening of the proton spectra with increasing multiplicity [93]. These observations, with also the fact that B_{A} decreases with the charged particle multiplicity (see Sect. 2.3), underlines that more advanced implementation of the coalescence model are needed.

2.2.2 Advanced Coalescence Model

In order to take into account the system size, an advanced implementation of the coalescence model based on the Wigner formalism, as reported in Refs [73, 76, 133], is used. The key concept is the overlap between the phase-space distributions of the nucleons and the phase-space of the nucleus. In general, the number of produced nuclei N_{A} is defined as:

$$\begin{aligned} N_{\mathrm{A}} = g_{\mathrm{A}} \int \mathrm{d}^3x_1 \ldots \mathrm{d}^3x_{\mathrm{A}} \int \mathrm{d}^3k_1 \ldots \mathrm{d}^3k_{\mathrm{A}} \times \\ \times f_1(x_1, k_1) \ldots f_{\mathrm{A}}(x_{\mathrm{A}}, k_{\mathrm{A}}) W_{\mathrm{A}}(x_1, \ldots, x_{\mathrm{A}}, k_1, \ldots, k_{\mathrm{A}}) \end{aligned} \tag{2.14}$$

where g_{A} is a factor that takes into account the spin-isospin degeneracy of the nucleus, f_{A} is the phase-space distribution of the nucleons and W_{A} is the Wigner density of the final state. This last term depends on the wave function assumed for the nucleus, that can vary. With this formulation, the size of the the source enters into the calculation of the coalescence parameter.

One of the simplest wave function assumed is the ground state of a isotropic harmonic oscillator. This choice, even if it not the most realistic, has the advantage to obtain a Wigner density function that had the form of a Gaussian, hence can be resolved analytically. This approach is employed in Ref. [73], with the focus on the deuteron. The wave function has the form:

$$\varphi_{\mathrm{d}}(r) = \left(2\pi r_{\mathrm{d}}^2\right)^{-3/4} \exp\left(-\frac{r^2}{-2r_{\mathrm{d}}^2}\right) \tag{2.15}$$

where the characteristic size parameter $r_{\mathrm{d}} = \sqrt{8/3}\lambda_{\mathrm{d}}$, with λ_{d} the root mean square of the charge wave function of the deuteron. As shown in Ref. [76], the dependence of the deuteron coalescence parameter on the source value can be expressed as:

$$B_2 = \frac{3\pi^{3/2}\langle C_\mathrm{d}\rangle}{2m_\mathrm{T}R_\perp^2(m_\mathrm{T})R_\parallel^2(m_\mathrm{T})} \tag{2.16}$$

with $R_\perp$ and $R_\parallel$ the homogeneity radii of the source, measured by HBT interferometry [72], while m_T is the transverse mass of the coalescing nucleons. The term $\langle C_\mathrm{d}\rangle$ is the quantum-canonical correction factor, that describes the quantum nature of the coalescence process. This factor has the following form:

$$\langle C_\mathrm{d}\rangle = \frac{1}{\left[1+\left(\frac{r_\mathrm{d}}{2R_\perp(m_\mathrm{T})}\right)^2\right]\sqrt{1+\left(\frac{r_\mathrm{d}}{2R_\parallel(m_\mathrm{T})}\right)^2}} \tag{2.17}$$

Assuming $R_\perp = R_\parallel = R$, with R the source radius, the previous equations for B_2 and $\langle C_\mathrm{d}\rangle$ can be simplified with:

$$B_2 = \frac{3\pi^{3/2}\langle C_\mathrm{d}\rangle}{2m_\mathrm{T}R^3(m_\mathrm{T})} \tag{2.18}$$

and

$$\langle C_\mathrm{d}\rangle = \left[1+\left(\frac{r_\mathrm{d}}{2R(m_\mathrm{T})}\right)^2\right]^{-3/2} \tag{2.19}$$

Fig. 2.4 shows the evolution of B_2 and $\langle C_\mathrm{d}\rangle$ as a function of the source volume. These predictions are computed with different values of the characteristic size parameter r_d. For r_d = 0, *i.e.* a point-like deuteron, the quantum correction factor is equal to unity, as expected. For finite values of r_d, instead, the $\langle C_\mathrm{d}\rangle$ has a growing trend, starting from zero for a point-like source, increasing with the increase of the source size R and saturates to unity: for larger r_d a slower raise is present. With these parametrizations, it is also possible to observe the behaviour of the deuteron coalescence parameter B_2. At lower values of R, B_2 is dominated by the correction factor, with a finite values for $R = 0$. For $R \gg r_\mathrm{d}$, instead, the coalescence parameter is dominated by the classical phase-space separation, hence it shows a decreasing trend.

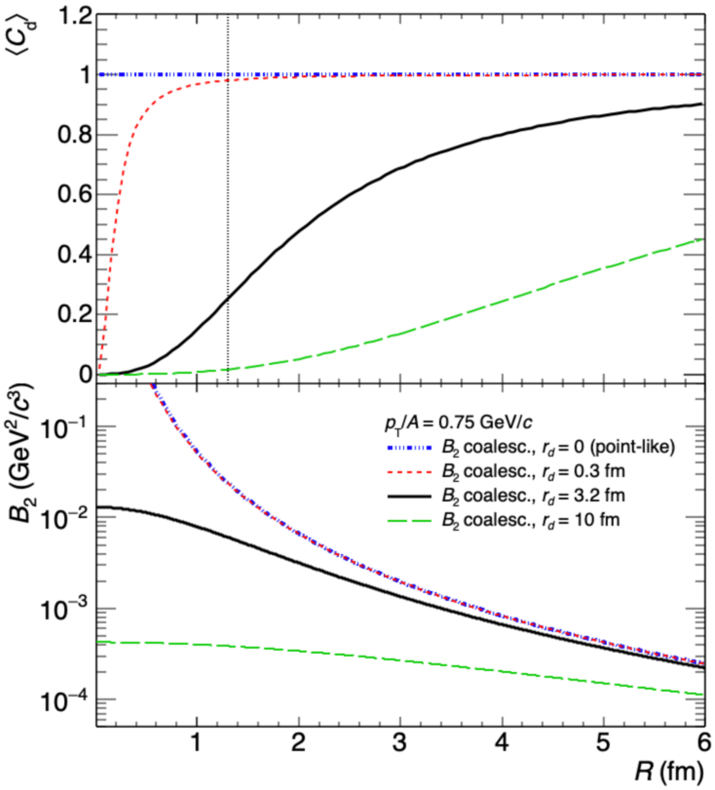

Figure 2.4: Quantum-mechanical correction factor $\langle C_d \rangle$ (top) and deuteron coalescence parameter B_2 (bottom) as a function of the source radius, calculated assuming different values for the deuteron size parameter [73].

With the same deuteron wave function, as reported in Ref. [76], it is also possible to obtain predictions on the yield ratio between the light nuclei and the proton. In such work, the phase-space distributions of the nucleons are taken by a thermalised expanding spherical fireball, with a temperature of kinetic freeze-out T_{kin} and a radius R:

$$f_{\mathrm{p,n}}(\vec{x},\vec{p}) = \frac{N_{\mathrm{p,n}}}{(2\pi)^3(mT_{kin}R^2)^{3/2}}\, e^{-\frac{p^2}{2mT_{kin}}}\, e^{-\frac{x^2}{2R^2}} \tag{2.20}$$

with m the nucleon mass and $N_{\mathrm{p,n}}$ the number of protons or neutrons. From the calculations it is possible to obtain the number of deuterons N_{d}

$$N_{\mathrm{d}} = \frac{3N_{\mathrm{p}}N_{\mathrm{n}}}{4(mT_{kin}R^2)^{3/2}} \frac{1}{\left(1+\dfrac{1}{mT_{kin}\sigma^2}\right)^{3/2}} \frac{1}{\left(1+\dfrac{\sigma^2}{4R^2}\right)^{3/2}} \tag{2.21}$$

where the parameter σ is linked to the root-mean-square matter radius of the deuteron, $\sigma = \sqrt{8/3}r_{\mathrm{d}} \approx 3.2$ fm. Since the nuclei temperature of kinetic freeze-out is of the order of 100 MeV, $mT_{kin} \gg 1/\sigma^2$. With this assumption, it is possible to compute the yield ratio d/p, that is equal to:

$$\frac{N_{\mathrm{d}}}{N_{\mathrm{p}}} \approx \frac{3N_{\mathrm{n}}}{4(mT_{kin}R^2)^{3/2}} \left[1+\left(\frac{1.6\,\mathrm{fm}}{R}\right)^2\right]^{-3/2} \tag{2.22}$$

The last factor of this equation expresses the suppression of the deuteron production, that derives from the finite size of the nuclei with respect to the nucleon emission source. The first factor, instead, describes the d/p limit for a finite source of radius R much larger than the deuteron size. This coefficient, at the LHC energies, is expected to be similar in pp, p–Pb and Pb–Pb collisions. From the d/p measured in Pb–Pb collisions at $\sqrt{s_{\mathrm{NN}}} = 2.76$ TeV, this first factor can be approximated with the value 4.0×10^{-3}. Hence, Eq. 2.22 can be rewritten as:

$$\frac{N_{\mathrm{d}}}{N_{\mathrm{p}}} \approx \frac{4.0 \times 10^{-3}}{\left[1+\left(\dfrac{1.6\,\mathrm{fm}}{R}\right)^2\right]^{3/2}} \tag{2.23}$$

With a similar approach, it is also possible to calculate the ratio ^{3}He/p, extending the formalism used for the deuteron and assuming that the ^{3}He production derives from the coalescence of two protons and one neutron. Thus, the ^{3}He/p can be expressed as:

$$\frac{N_{^3\mathrm{He}}}{N_\mathrm{p}} \approx \frac{N_\mathrm{n} N_\mathrm{p}}{4(mT_{kin}R^2)^3} \frac{1}{\left(1+\dfrac{r^2_{^3\mathrm{He}}}{2R^2}\right)^3} \tag{2.24}$$

where $r_{^3\mathrm{He}}$ = 1.76 fm is the matter radius for the ^{3}He [134]. In the equation reported above, the statistical factor 1/4 for forming a spin 1/2 ^{3}He from three spin 1/2 nucleons is considered, and also the condition $mT_{kin} \gg 1/r_{^3\mathrm{He}}$ is satisfied. Also in this case it is possible to calculate the first term, and the equation can be approximated with:

$$\frac{N_{^3\mathrm{He}}}{N_\mathrm{p}} \approx \frac{7.1 \times 10^{-6}}{\left[1+\left(\dfrac{1.24\,\mathrm{fm}}{R}\right)^2\right]} \tag{2.25}$$

But, the coalescence mechanism described above is not the only one that can give ^{3}He: in fact, this nucleus can be formed by the coalescence of a deuteron and a neutron. In this case, the root-mean-square radius of ^{3}He can be estimated as:

$$r_{^3\mathrm{He}} \approx \sqrt{\frac{3}{8}\langle r_{pd}\rangle^2} = 1.15\,\mathrm{fm} \tag{2.26}$$

where $\sqrt{\langle r_{pd}\rangle^2} \sim$ 2.6 fm is the distance between the proton and the centre of mass of the deuteron inside the ^{3}He. With this assumption, the ^{3}He/p ratio is given by:

$$\frac{N_{^3\mathrm{He}}}{N_\mathrm{p}} \approx \frac{7.1 \times 10^{-6}}{\left[1+\left(\dfrac{1.15\,\mathrm{fm}}{R}\right)^2\right]^{3/2}\left[1+\left(\dfrac{1.16\,\mathrm{fm}}{R}\right)^2\right]^{3/2}} \tag{2.27}$$

where the statistical factor 1/3 for the coalescence of a spin 1 deuteron and a spin 1/2 proton is considered, and the suppression factor for the deuteron is included.

Finally, the calculation exploited for the ^{3}He can be extended to ^{3}H production. Since $r_{^3\mathrm{H}}$ = 1.59 fm [134], at low multiplicity the ^{3}H production is predicted to be less suppressed with respect to the ^{3}He. The ^{3}H/^{3}He ratio in the hypothesis of two-body and three-body coalescence is equal to, respectively:

$$\frac{N_{^3\mathrm{H}}}{N_{^3\mathrm{He}}} \approx \frac{\left[1+\left(\frac{1.24\,\mathrm{fm}}{R}\right)^2\right]^3}{\left[1+\left(\frac{1.12\,\mathrm{fm}}{R}\right)^2\right]^3} \tag{2.28}$$

and

$$\frac{N_{^3\mathrm{H}}}{N_{^3\mathrm{He}}} \approx \frac{\left[1+\left(\frac{1.15\,\mathrm{fm}}{R}\right)^2\right]^{3/2}}{\left[1+\left(\frac{1.039\,\mathrm{fm}}{R}\right)^2\right]^{3/2}} \tag{2.29}$$

Fig 2.5 shows the prediction for d/p, ^{3}He/p and ^{3}H/^{3}He ratios as a function of the charged particle multiplicity. The theoretical predictions uncertainties (shaded bands) consider the uncertainties on the emission source size. These predictions are compared with experimental results from ALICE [90, 93, 135, 136]. The theoretical prediction reproduces the experimental data with a good agreement for both the d/p and the ^{3}He/p ratios. For the ^{3}H/^{3}He, instead, theoretical prediction shows that, to fully discriminate between the two-body and the three-body coalescence, measurements in very low multiplicity systems are needed.

The theoretical predictions reported above, based on Refs. [73, 76], use a deuteron wave function form that is not fully physically accurate. Recent studies reported in Ref. [133] explore different realistic wave functions for the deuteron. In detail, the different wave function employed, reported in Fig. 2.6, are Gaussian, Hultén [137], and Argonne v_{18} [138]. In particular, both the Hultén and the Argonne v_{18} are realistic potential, since the first one is based on the Yukawa theory of interaction, while the latter is a phenomenological potential constrained to proton-neutron scattering measurements. The Gaussian parametrization is used in order to have a direct comparison with previous results. Moreover, the χEFT [139] wave

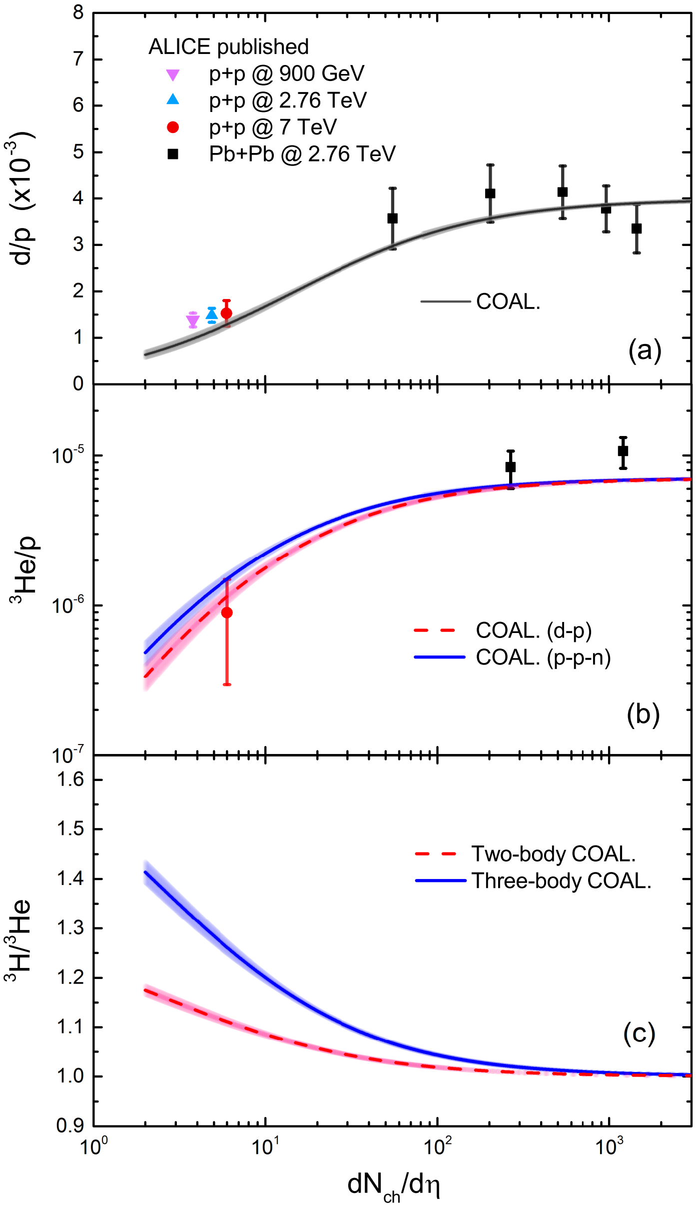

Figure 2.5: Yield ratios d/p (top), ^{3}He/p (middle) and ^{3}H/^{3}He (bottom) as a function of the charged particle multiplicity. The theoretical predictions are compared with ALICE experimental data [76].

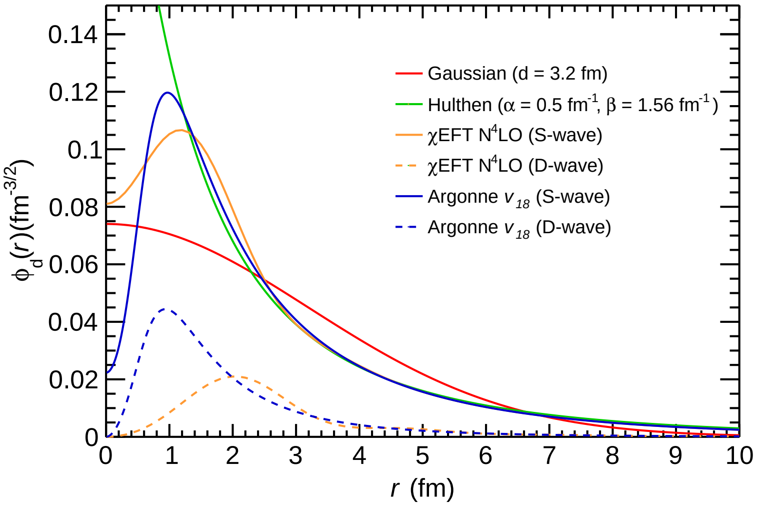

Figure 2.6: Different deuteron wave function employed: Gaussian (red), Hulthén (green), χEFT N^{4}LO S-wave and D-wave (solid and dashed orange), Argonne v_{18} S-wave and D-wave (solid and dashed blue) [133].

function is used to test the core part of the strong-interaction potentials and the deuteron yield. In fact, this function is obtained from *ab initio* calculations in QCD, and this function and the Argonne v_{18} are fully compatible, with the except of very short ranges. The approach followed in Ref. [133] to obtain the model expectations can be summarized with the following steps:

- The collisions are generated with two different Monte Carlo generators: EPOS 3 [140] and PYTHIA 8.3 [141] with the Monash tune [142]. The obtained distributions for protons and neutrons are reweighted to match the experimental distributions measured by ALICE [98]. The selected data sample is the one of pp collisions at $\sqrt{s} = 13$ TeV, with a high multiplicity trigger: this selection is important because, for this dataset, both the measurements of deuteron production and baryon source size are available.

- An event-by-event deuteron production is simulated with a coalescence afterburner that takes into account realistic particle emission and correlations. To achieve this, the nucleon emitting source must

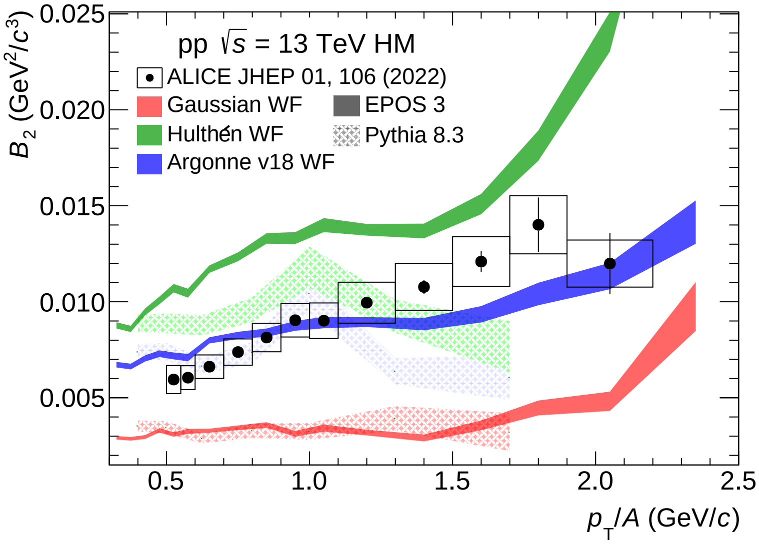

Figure 2.7: Coalescence parameter B_2 obtained with EPOS 3 (solid shade) and PYTHIA 8.3 (dotted shade) in the case of Gaussian (red), Hulthén (green) and Argonne v_{18} (blue) wave functions, compared with the ALICE measurements [133].

take into account the overall final state particle multiplicity, the possible contribution of feed-down from strongly decaying resonances and the phase-space correlations among the particles of interest.

- The obtained deuteron distributions are compared with the experimental data, and the coalescence probability is calculated taking into account the different wave functions available.

The obtained results on the deuteron coalescence parameter B_2 with the different deuteron wave functions are reported in Fig. 2.7 and compared with the ALICE experimental data. The predictions using the Gaussian wave function underestimate the coalescence parameter by about 50% to 70%, while the predictions using the Hulthén wave function overestimate the experimental results, by a factor between 20% to 50%. The Argonne v_{18} wave function, instead, provides the best agreement with the experimental data.

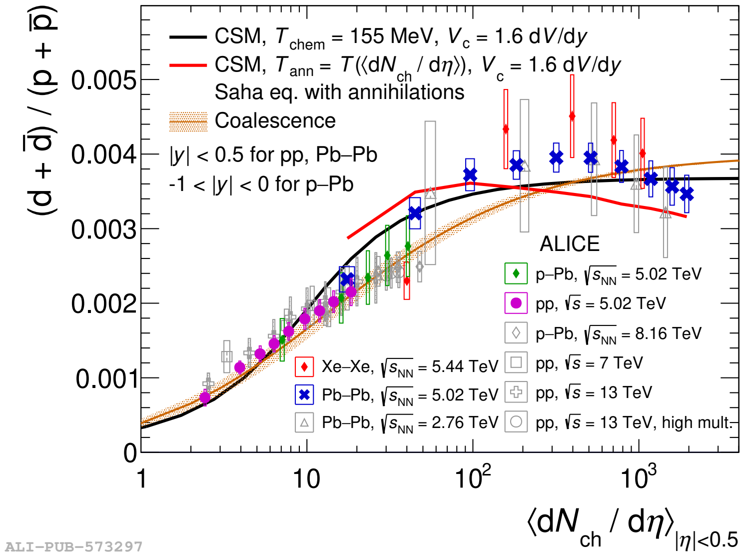

Figure 2.8: Deuteron over proton ratio as a function of particle multiplicity measured in different collision systems. The lines represent the predictions from the SHM and the coalescence models [108].

2.3 How to constrain the models?

The two classes of models described in the previous sections, the SHMs and the baryon coalescence, give some insights on the production of light (anti)nuclei in high energy hadronic collisions. Despite their difference, the models do not exclude each other, since they describe different properties: as an example, SHM can predict the particle yields but no microscopic description on nucleus production is provided. A comparison between the two models is given looking at the yield ratio of nuclei with the proton as a function of the particle multiplicity. This quantity is reported in Figs. 2.8-2.10 for the deuteron, ^{3}He and ^{4}He respectively. In the case of the d/p yield ratio the measurements are taken in pp, p–Pb, Xe–Xe and Pb–Pb collisions at different energies, and are compared with both the coalescence predictions and two different implementation of the CSM, with the same correlation volume V_c but different values of the T_{chem}. In fact, in the first implementation the medium is considered in a full chemical

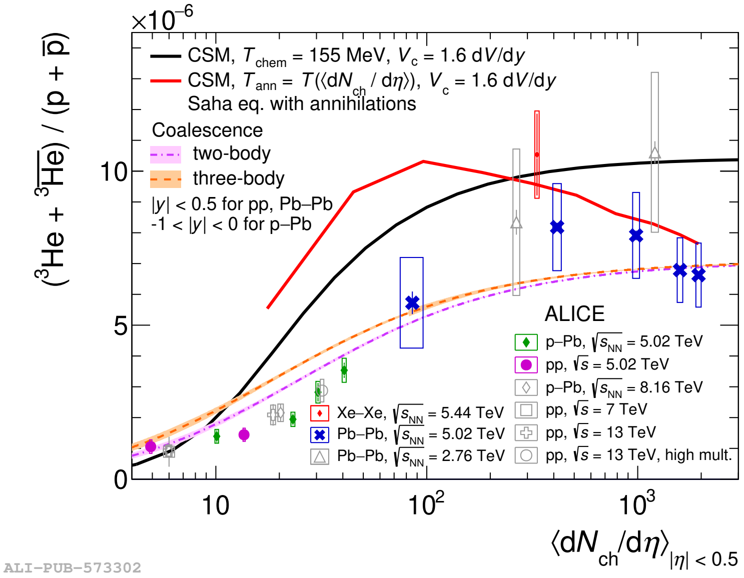

Figure 2.9: Helium-3 over proton ratio as a function of particle multiplicity measured in different collision systems. The lines represent the predictions from the SHM and the coalescence models [108].

equilibrium and T_{chem} is considered independent of multiplicity, with a value of 155 MeV. In the second approach, instead, the Saha equation [143] is used to estimate the light nuclei abundances in the hadronic phase, and also a T_{chem} that depends on the multiplicity, raising from 160 MeV for multiplicities of about 20 to values of 132 MeV for multiplicity of about 2000, is employed [144]. Both the models qualitatively reproduce the data, although some tensions at intermediate values of multiplicity are present. Moreover, the models do not have enough discrimination power: new types of studies are needed in order to disentangle the problem. For the ^{3}He/p ratio, instead, the models have a larger discrimination power, since at high multiplicity the obtained predictions differ. Although, the experimental data are not precise enough to discriminate between the models. Finally, the ^{4}He/p ratio evaluated in Pb–Pb collisions at $\sqrt{s_{\text{NN}}} = 2.76$ TeV and $\sqrt{s_{\text{NN}}} = 5.02$ TeV is compared with the CSM implementation with a fixed T_{chem} of 155 MeV and different correlation volumes V_c, and with analytical coalescence prediction considering the ^{4}He particle structureless

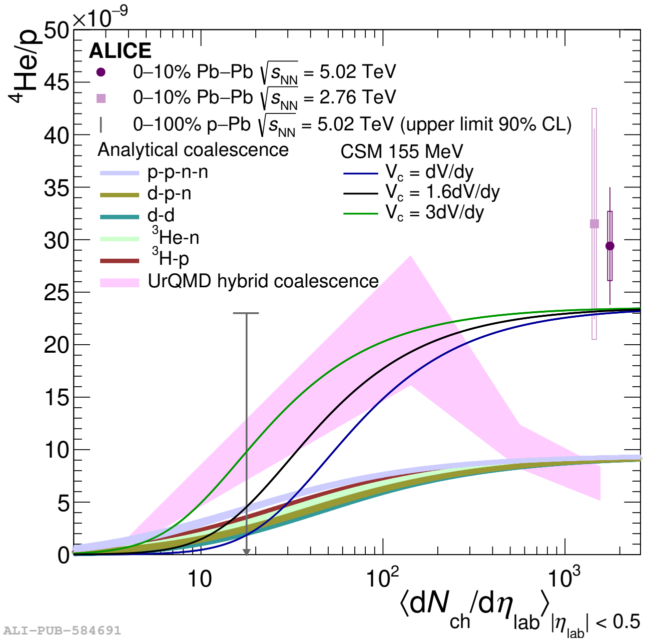

Figure 2.10: Helium-4 over proton ratio as a function of particle multiplicity measured in Pb–Pb collisions at different energies. The lines represent the predictions from the SHM and the coalescence models [146].

(p-p-n-n) or with some substructures (like d-p-n, d-d, ^{3}He-n and ^{3}H-p). Moreover a comparison with the UrQMD model [145], where the coalescence is treated like a "box coalescence", where the maximal difference in coordinate space and momentum for the coalescing partners is considered, is performed. The experimental results are consistent within the uncertainties with the CSM implementation, while both the analytical coalescence and the one implemented in the UrQMD model, underestimate the data of a factor about 3. One explanation of such large difference could arise from the fact that the analytical models do not take into account the binding energy of the nucleus: while for deuteron, ^{3}H and ^{3}He the binding energy is low and the approximation can work well, the elevated binding energy of the ^{4}He, $E_B = 28.3$ MeV, must be taken into account in the coalescence predictions.

It is also possible to compare the experimental data on the coalescence parameter $B_{\rm A}$ with the predictions obtained by the model, studying the

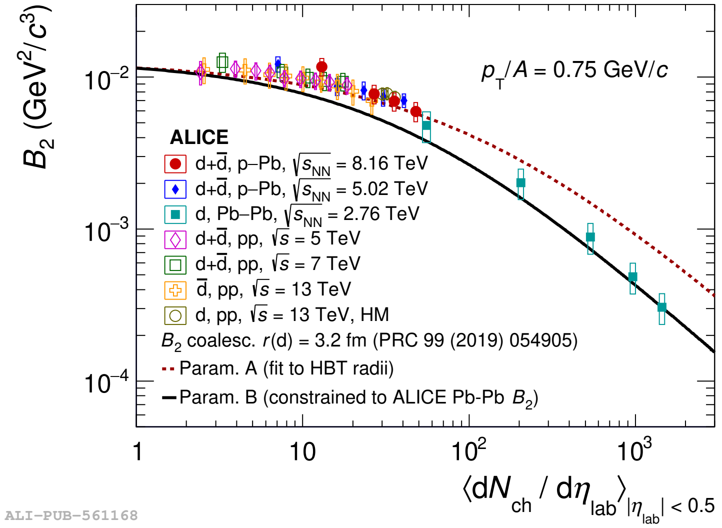

Figure 2.11: Deuteron coalescence parameter B_2 as a function of the charged particle multiplicity measured in different collision systems. The lines represent two different parametrization of the source radius, fitted to HBT radii or constrained to Pb–Pb results [105].

evolution of such quantity with the charged particle multiplicity. This observable is reported in Fig. 2.11 and Fig. 2.12 for the deuteron and ^{3}He, respectively. The experimental results are compared with two different theoretical predictions, with different source radii. In the first case, a fit of the HBT radii is performed, while in the second case the source size is constrained with the experimental results for the B_2 in Pb–Pb collisions. For both nuclei, as expected, the coalescence parameter decreases with the source radius, but at higher multiplicity the two parametrizations diverge.

With these observables is it clear that, at the moment, there is not a unique answer on which model between the SHM and the baryon coalescence better describes the experimental data. For these reasons, new types of measurements are needed in order to constraint the hadronization process.

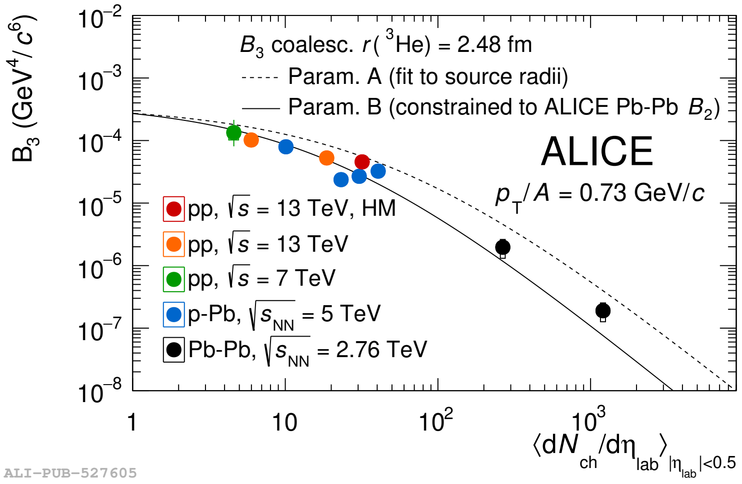

Figure 2.12: Helium-3 coalescence parameter B_3 as a function of the charged particle multiplicity measured in different collision systems. The lines represent two different parametrizations of the source radius, fitted to HBT radii or constrained to Pb–Pb results [98].

2.3.1 Production of nuclei in jets

An innovative approach that can help to clarify the mechanism of nucleus formation is the study of the production of nuclei inside and outside of jets. In fact, since the jet is a collimated emission of particles, it is expected that the nucleons inside it are closer in the phase space, hence an enhancement of the coalescence probability in jets is expected. In particular, this study has been performed in pp collisions at $\sqrt{s} = 13$ TeV [104] and in p–Pb collisions at $\sqrt{s_{\mathrm{NN}}} = 5.02$ TeV, subject of this thesis. In these studies, due to the limited data sample available, the jet is not fully reconstructed using jet finder algorithms, but the technique used by the CDF collaboration is employed [147]. In particular, the particle with the highest p_{T}, and also higher with respect to a given threshold, is used as a proxy of the jet axis. To this particle, an azimuthal angle $\phi_l = 0$ is assigned. All the other particles produced in the collision are classified in three different azimuthal regions, according to the $\Delta\phi = |\phi - \phi_l|$ value, precisely:

- **Toward**, $|\Delta\phi| < 60^{\mathrm{o}}$. This region contains both the jet contribution

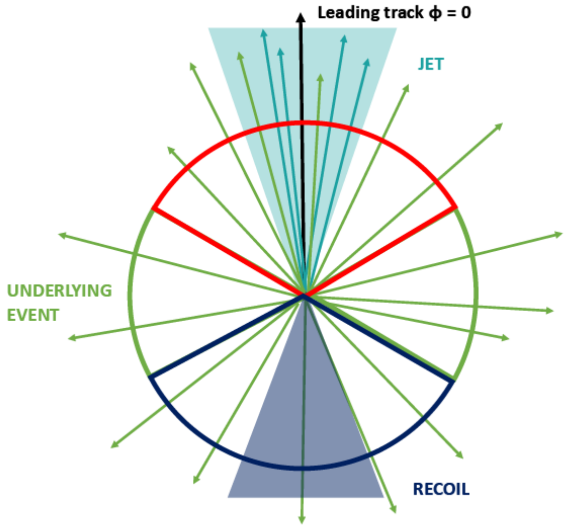

Figure 2.13: Schematic view of the azimuthal regions.

and the underlying event;

- **Away**, $|\Delta\phi| > 120^{\text{o}}$. This region, back to back to the Toward one, contains the recoil jet and the underlying event;
- **Transverse**, $60^{\text{o}} < |\Delta\phi| < 120^{\text{o}}$. This region is characterized from the underlying event.

A schematic representation of such regions is reported in Fig. 2.13. The threshold value on the transverse momentum of the leading particle is chosen accordingly to the studies reported in Refs. [148, 149], where it is observed that the density of particle in the Transverse region, after $p_{\mathrm{T,lead}} > 5$ GeV/c, shows a plateaux, hence it is not more influenced by the primary hard parton-parton scattering. In order to quantify the jet contribution, a subtraction between the Toward and the Transverse region is performed. Studying the nucleus production in and out of jets could help to constrain the coalescence expectations, evaluating the behaviour of the coalescence parameter in different regions and collision systems.

2.3.2 ^{3}H/^{3}He ratio

Another useful physical observable that can give a discrimination between the two hadronization models, as already pointed out in the previous sections, is the yield ratio between the triton and the helium-3. Both particles are nuclei with a mass number A = 3, and they differ for three aspects:

- *composition*. The ^{3}H is a hydrogen isotope, hence it is formed by one proton and two neutrons. The ^{3}He, instead, is an isotope of the helium, and it is composed by two protons and one neutron.
- *mass*. Since their different composition, ^{3}H and ^{3}He have a slight different mass. In particular, the triton mass is 2.80892 GeV, while the ^{3}He one is 2.80839 GeV, hence their difference is of only the 0.019% [150].
- *matter radius*. Due to the Coulombian repulsion between the protons in the ^{3}He structure, this particle has a higher radius with respect to the ^{3}H one, 1.76 fm and 1.59 fm respectively [134].

In the context of the hadronization models description, the two important characteristics are the mass and the matter radius. In fact, according to the SHM, since the mass difference between the two nuclei is negligible, the yield of the two particles is expected to be the same. In the coalescence approach, instead, due to the different nucleus size, a larger yield of ^{3}H is expected with respect to ^{3}He, with the maximum difference predicted by the models at low multiplicity. This study has been performed by the ALICE collaboration in pp collisions at $\sqrt{s} = 13$ TeV with a high multiplicity trigger and p–Pb collisions at $\sqrt{s_{\mathrm{NN}}} = 5.02$ TeV. The obtained results are reported in Fig. 2.14 and Fig. 2.15 for the two collision systems.

In both cases, the ^{3}H/^{3}He ratio hints to values larger than unity, as predicted by the coalescence model. However, due to the large statistical and systematic uncertainties that affect the measurements, no decisive answers can be drawn at the moment. However, thanks to the extended data sample that will be collected at the end of Run3, new estimation of this quantity can be performed.

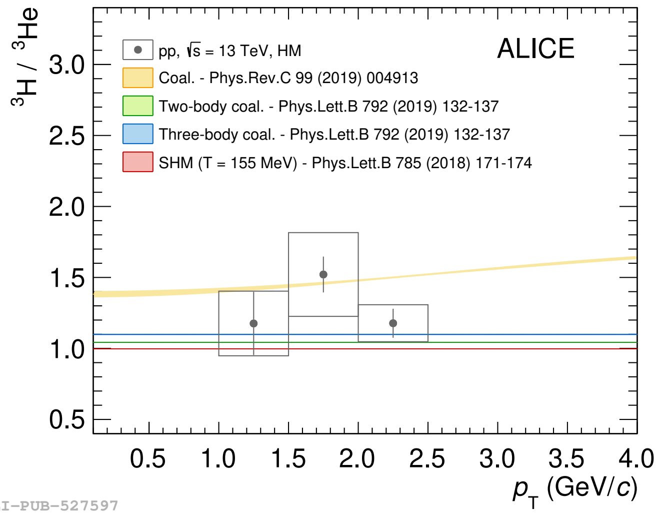

Figure 2.14: ^{3}H/^{3}He ratio in pp collisions at $\sqrt{s} = 13$ TeV, compared with the expectation from the SHM and the coalescence models [98].

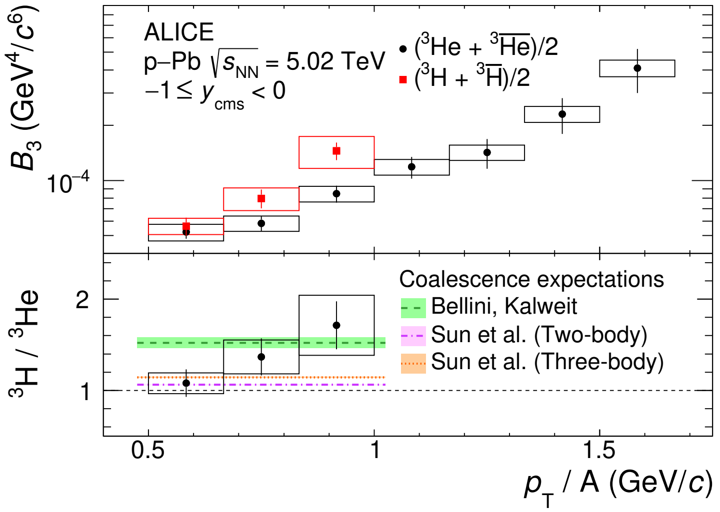

Figure 2.15: Triton and helium-3 coalescence parameter (top) and ^{3}H/^{3}He ratio (bottom) measured in p–Pb collisions at $\sqrt{s_{\mathrm{NN}}} = 5.02$ TeV, compared with the coalescence expectations [96].

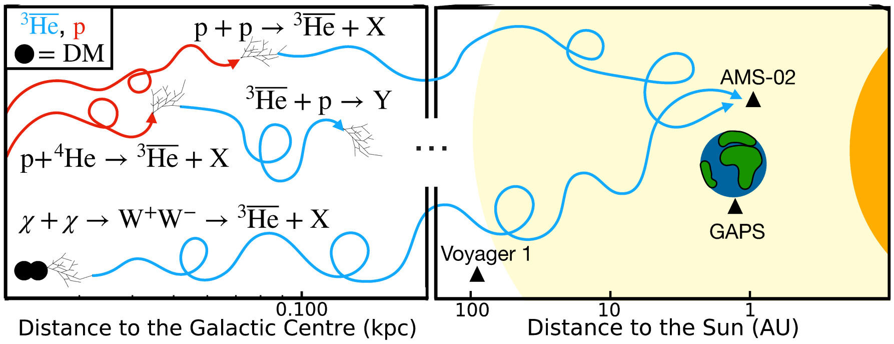

ALI-PUB-532052

Figure 2.16: Schematic representation of the antinuclei source in space: collision of high energy cosmic rays with the interstellar medium or annihilation of dark matter candidates [153].

2.4 Light (anti)nuclei and Dark Matter searches

The detailed study of light (anti)nuclei formation, and their interaction with the matter, are not only important in the nuclear physics field, but also in astrophysics. In fact, according to recent results, production of light (anti)nuclei in space, detected by experiments such as AMS-02 [151] and the next to be operative GAPS [152], can derive not only from the interaction of very high energetic cosmic rays with the interstellar medium, but also from Dark Matter (DM) annihilation. A schematic representation of the possible sources of antinuclei in space is reported in Fig. 2.16. In particular, the observation of $^3\overline{\mathrm{He}}$ nuclei is one of the most prominent signature of DM annihilation, in the hypothesis of weakly interactive massive particles (WIMPs) as DM candidate [154–157]. The advantage of these antinuclei, compared to the lighter antideuterons, is that at low energy (1-2 GeV/c per nucleon), the contribution from cosmic rays interactions should be small, order of magnitude lower with respect to the signal expected from DM candidates.

In order to calculate the expected flux of antinuclei near the Earth, the antinucleus formation and annihilation processes must be precisely known. While the formation probability is widely studied, as we have seen in the previous sections, for the annihilation the study of the nuclei propagation in the Galaxy is needed. One of the key parameter in the

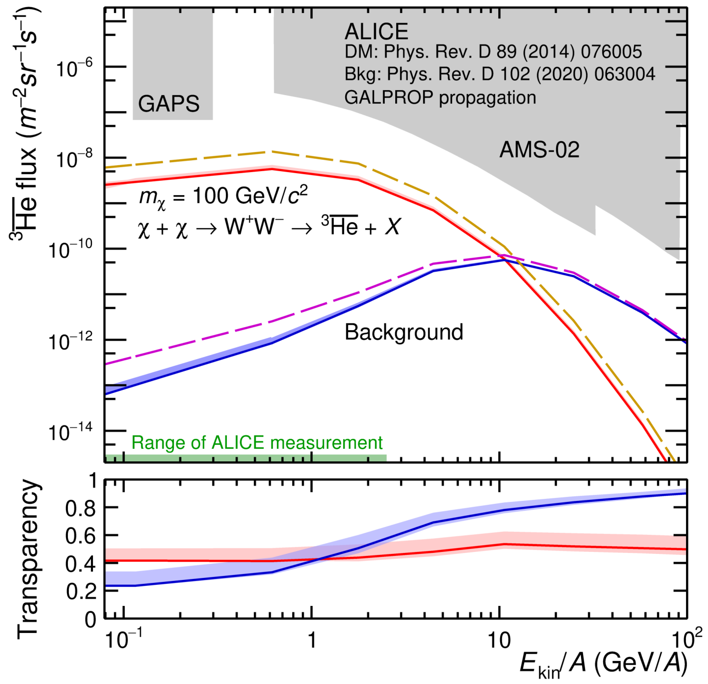

ALI-PUB-532060

Figure 2.17: Top: Expected $^3\overline{\mathrm{He}}$ flux as a function of kinetic energy per nucleon for the DM signal (red) and cosmic-ray background (blue) hypotheses, compared with the sensitivity of the AMS-02 and GAPS experiments. Bottom: Transparency of our Galaxy to the propagation of $^3\overline{\mathrm{He}}$ inside the Solar System [153].

propagation codes is the inelastic cross section of the antinuclei with the matter: this subject was recently studied by the ALICE Collaboration, that performed for the first time the measurement of the inelastic cross section for antideuteron [158], $^3\overline{\mathrm{He}}$ [153] and $^3\overline{\mathrm{H}}$ [159]. Moreover, in the case of $^3\overline{\mathrm{He}}$, the expected flux of antimatter in the case of antinuclei from interaction with the interstellar medium and from DM searches were calculated, and compared with the sensitivity of the AMS-02 and GAPS experiments: the results are reported in Fig. 2.17. It is possible to observe that at low kinetic energy per nucleon the DM signal is order of magnitude higher with respect to the background, even if, in the whole analysed range, the flux is below the sensitivity of the AMS-02 and GAPS experiments. It is also possible to define the *transparency*, equal to the ratio of the $^{3}\overline{\mathrm{He}}$ flux obtained in the propagation code with and without inelastic cross section. This quantity can be interpreted as the survival probability of the antinuclei in their propagation from their source through the Galaxy. In the case of DM hypothesis, the transparency is about of 50%, hence these nuclei have a high survival probability, and a good probability to be detected by the experimental apparatus. The use of this type of measurements, combined with the latest results on antinuclei formation and improvement on the transport models codes, can help to understand the results from the AMS-02 Collaboration, that announced in different CERN colloquia [160, 161] the observation of different candidates of $^{3}\overline{\mathrm{He}}$ and $^{4}\overline{\mathrm{He}}$ nuclei, that could be an important result for the indirect Dark Matter searches.

Chapter 3

The ALICE experiment at the LHC

The largest and more powerful particle collider in the word is the Large Hadron Collider (LHC), located near Geneva at CERN (European Center for the Nuclear Research). The accelerator is able to deliver both proton-proton and nucleus-nucleus collisions in order to study different aspects of particle physics. Exploiting the data from pp collisions, that is the beam provided for the majority of the year, different fundamental results in particle physics have been achieved, such as the discovery of the Higgs boson [162, 163], heavy tetraquark [164] and pentaquark [165] states and the odderon [166]. Nevertheless, a significant part of the LHC physics programme exploits nucleus-nucleus collisions, such as Pb–Pb, to characterize the QGP. The ALICE experiment is particularly focused on this type of study but, thanks to its peculiar characteristics on particle identification, it is also able to study the production of light (anti)nuclei.

In this Chapter the LHC complex and the ALICE detector will be described. In particular, since the work in this thesis is based on the p–Pb data at $\sqrt{s_{\mathrm{NN}}} = 5.02$ TeV recorded in 2016, the condition of the experimental apparatus in such period is reported. Particular emphasis is given to the central barrel detectors, used to identify the light (anti)nuclei. In 2021 ALICE has completed a major upgrade, that enhanced its capabilities: this upgrade will be reported in Sect. 3.4. Moreover, Sect. 3.5 describes the data acquisition process and the event reconstruction used during the Run2 data-taking, that is the LHC Run during which the data used in this analysis were collected. Finally, Sect. 3.6 reports the particle identification

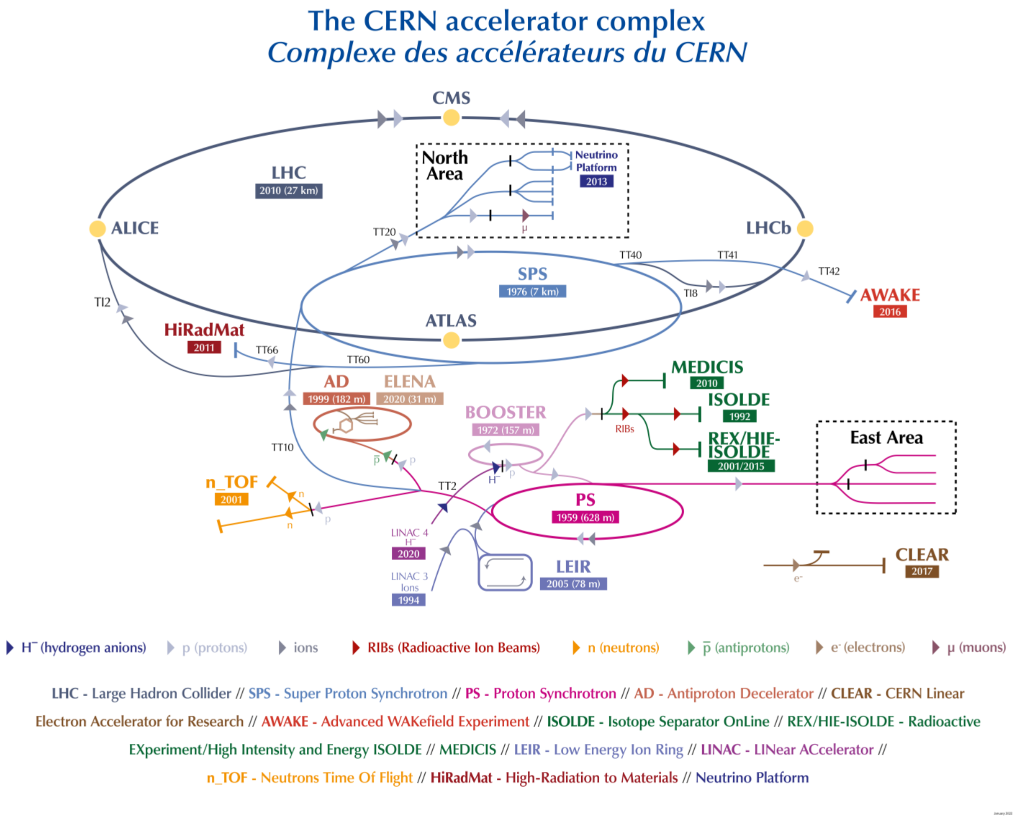

Figure 3.1: The CERN accelerator complex [167].

capabilities of the ALICE apparatus.

3.1 The Large Hadron Collider

The LHC ring, where the protons or lead ions are accelerated to the top energies and where the collisions happen, is only the last part of a complex acceleration facility, as reported in Fig 3.1. All the accelerators are used in order to accelerate protons and ions at increasing energies. Moreover, the first stages of the accelerator chain provide the beams for different experiments, such as n_TOF, ISOLDE and many others.

The LHC is a two-ring superconducting hadron collider with a circumference of 26.7 km and it is located underground between 50 m and 175 m deep in the Swiss and French territory. It consist of $\sim$ 1200 dipole magnets, used to bend the beams, and $\sim$ 400 quadrupole magnets, for beam focusing. It is designed in order to accelerate both protons and ions beams, such as lead and xenon. The sources for these beams are different among them, in particular:

- For the proton, the starting point is a bottle of hydrogen gas. The electrons are stripped by an electric field in order to create the protons. The particles are then moved in the Linac 2, where they are accelerated to the energy of 50 MeV.

- In the case of lead ions, instead, the starting point is a source of vaporized lead, that enters in the Linac 3 and in the Low Energy Ion Ring (LEIR).

- Finally, for xenon ions, a procedure similar to that used for lead is employed, with a particular setup in the Super Proton Synchrotron (SPS) to optimize the beam quality.

All the beams then follow the same pattern of acceleration, even if the different sources reach different energies at each step: they are firstly injected in the Proton Synchrotron Booster (PSB) and then in the Proton Synchrotron (PS). From there, the particles are transferred in the Super Proton Synchrotron, where they are further accelerated before being injected in the LHC ring, where the particles are accelerated to the desired energy.

The LHC data-taking is organized in *Runs* separated by *Long Shutdown (LS)*. Each Run lasts for a couple of years, and for each year the beams circulate in the March-November period, while the other part of the year is dedicated to a Technical Stop, where the maintenance of the accelerator and detectors is performed. The Long Shutdown, instead, is the period at the end of each Run: also in this case, it lasts a couple of years, that are characterized by upgrades on both the accelerator complex and the detectors. In particular, from the beginning of the LHC data-taking up to now, it is possible to identify the following periods:

- **Run1** (2010 - 2013). The first run of data-taking, it was characterized by an increasing energy in pp collisions, from 0.9 to 8 TeV. The accelerator was able to deliver p–Pb and Pb–Pb collisions at, respectively, 5.02 TeV and 2.76 TeV. The ALICE detector was able to collect data for each collision system and energy.

- **Long Shutdown 1** (2013 - 2015). During the LS1 the LHC performed a series of operation to ensure the magnet-circuit consolidation. The ALICE detector finished its installation, adding some missing modules for selected detectors, and generally improving the readout of the whole experimental apparatus.

- **Run2** (2015 - 2018). In this period, the LHC accelerator was able to deliver pp collisions up to $\sqrt{s} = 13$ TeV, p–Pb collisions at $\sqrt{s_{\mathrm{NN}}} = 5.02$ TeV and 8.16 TeV, Pb–Pb at $\sqrt{s_{\mathrm{NN}}} = 5.02$ TeV, and a special Xe–Xe run at $\sqrt{s_{\mathrm{NN}}} = 5.44$ TeV. Thanks to the complete apparatus, the ALICE detector successfully collected data in all the collision systems.

- **Long Shutdown 2** (2018 - 2022). During the LS2 the LHC replaced 22 magnets (in particular, 19 dipoles and 3 quadrupoles), improved the cryogenic power and the electrical insulations, and installed new collimators and beam absorbers. The ALICE detector completed a large upgrade, described in detail in Sect. 3.4, where both the experimental apparatus, the readout and the analysis software have been improved.

- **Run3** (2022 - ongoing). The ALICE detector have been able to successfully collect the data from pp collisions up to $\sqrt{s} = 13.6$ TeV and Pb–Pb at $\sqrt{s_{\mathrm{NN}}} = 5.36$ TeV provided by the LHC accelerator. In July 2025, special p–O and O–O runs are planned.

A summary of the different energies reached in the different Runs is reported in Tab. 3.1.

In a collider not only the maximum reached energy is important, but also the delivered *luminosity* [168]. This parameter, in scattering theory, is defined as the ratio between the number of detected events in a certain

Collision system	Run1 energies (TeV)	Run2 energies (TeV)	Run3 energies (TeV)
pp	0.9, 2.76, 7, 8	5.02, 13	0.9, 5.36, 13.6
p–Pb	5.02	5.02, 8.16	-
Xe–Xe	-	5.44	-
Pb–Pb	2.76	5.02	5.36

Table 3.1: Different energies achieved by the LHC accelerator for different collision systems across the data-taking periods.

time and the interaction cross section:

$$L = \frac{1}{\sigma}\frac{\mathrm{d}N}{\mathrm{d}t}. \tag{3.1}$$

The case of collider is peculiar, since both beams act like target and incoming beam. Moreover, the beam is not a continuos flux of particles, but it is divided into bunches. In this case, it is possible to define the luminosity as:

$$L \propto K \iiiint_{-\infty}^{+\infty} \rho_1(x,y,s,-s_0)\,\rho_2(x,y,s,s_0)\mathrm{d}x\,\mathrm{d}y\,\mathrm{d}s\,\mathrm{d}s_0 \tag{3.2}$$

where K is a kinematic factor, $\rho_1(x,y,s,-s_0)$ and $\rho_2(x,y,s,s_0)$ are the time dependent beam density distributions, where s denotes the beam direction and $s_0 = c \cdot t$ is the distance of the two beams to the central collision point, that acts like a time coordinate. Assuming a Gaussian distribution for the beams density distributions and considering head-on collisions, the luminosity assumes the notation:

$$L = \frac{N_1 N_2 f N_b}{4\pi\sigma_x\sigma_y} \tag{3.3}$$

that depends only on the number of particles per bunch for the two beams N_i, the revolution frequency f, the number of bunches per beam N_b and the transverse section σ of the two beams in the x and y direction, assuming they are equal. In a more general case, where $\sigma_{1x} \neq \sigma_{2x}$ and $\sigma_{1y} \neq \sigma_{2y}$ the equation has the modified form:

$$L = \frac{N_1 N_2 f n_b}{2\pi \sqrt{\sigma_{1x}^2 + \sigma_{2x}^2} \sqrt{\sigma_{1y}^2 + \sigma_{2y}^2}} \tag{3.4}$$

In order to measure the luminosity, a special procedure called *van der Meer scan* is performed each year of data-taking, for the different collision systems and energies. This method, developed by S. van der Meer at the ISR [169], provides the lowest calibration systematic uncertainty with respect to other methods, and it still employed nowadays.

3.2 The LHC experiments

The LHC is a complex particle accelerator, and it is able to provide hadronic collisions simultaneously to more than one experiment. In fact, nine different experiments, 4 big and 5 smaller, are located along the LHC ring. These experiments are:

- **ATLAS** (A Toroidal LHC ApparatuS) [170]. One of the two general purpose detectors at the LHC, it investigates a wide range of particle physics, from the Higgs boson to extra dimensions and dark matter.

- **CMS** (Compact Muon Solenoid) [171]. The second general-purpose apparatus at the LHC, it has the same scientific goals of the ATLAS experiment, with a different magnet setup. The presence of two general purpose apparatus with a different setup is important to cross validate breakthrough experimental results, such as the Higgs boson discovery.

- **ALICE** (A Large Ion Collider Experiment) [172]. Experimental apparatus designed for the study of heavy ion collisions and the QGP physics. The detector layout is described in detail in the next sections.

- **LHCb** (Large Hadron Collider beauty) [173]. Unlike the other big LHC experiments, that are enclosed detectors, the LHCb apparatus is mainly developed in the beam axis direction, with a total length of about 20 m from the interaction point. The scientific goals of this experiment are the investigation of the difference between matter and antimatter thanks to the study of the beauty quark, and the CP symmetry violation.

- **TOTEM** (Total Elastic and diffractive cross section Measurement) [174]. Made of different detectors located on both sides of the CMS interaction point, it uses protons that emerge from the collisions at small angles in order to provide cross section measurements.
- **LHCf** (Large Hadron Collider forward) [175]. The scientific goal of LHCf is to use the proton collisions provided by the LHC to simulate the cosmic rays interactions with the atmosphere, and to interpret and calibrate large scale cosmic rays experiments. It is located in the LHC beamline, at about 140 m in both directions of the ATLAS interaction point.
- **MoEDAL-MAPP** (Monopole and Exotics Detector at the LHC - MoEDAL Apparatus for Penetrating Particles) [176]. Located nearby the LHCb interaction point, it investigates the existence of the magnetic monopole and other exotic particles that would indicate new physics beyond the Standard Model, such as dyons, Q-balls, black-hole remnants, multiply charged particles and massive singly charged particles. The MAPP upgrade provides the sensitivity for milli-charged particles and long-lived exotic particles.
- **FASER** (ForwArd Search ExpeRiment) [177]. Located along the beam trajectory, 480 metres downstream the ATLAS detector, FASER is designed to search for light and extremely weakly interacting particles, that could be dark matter candidates. Moreover, FASER has a dedicated neutrino detector, FASERν in order to investigate high energy neutrino interactions.
- **SND@LHC** (Scattering and Neutrino Detector at the LHC) [178]. The scientific goal of this experiment is similar to FASER, hence to detect and study high energies neutrinos produced in the LHC high energy hadronic collisions. Also in this case the detector is located near the ATLAS interaction point, in a unused SPS tunnel, but differs from FASERν since it covers larger angles.

3.3 The ALICE detector

As already mentioned before, the ALICE detector is specifically designed to study heavy-ion collisions at ultra-relativistic energies. The principal scientific goal is to study and characterize the QGP but, thanks to the excellent particle identification capabilities, it is also possible to study the production of light (anti)nuclei. The overall dimension of the experimental apparatus is 16x16x26 m^3 with a total weight of about 10000 tons. The detector is located in a cavern 56 m below the ground level in the Interaction Point 2 (IP2) of the LHC ring, close to the French village of Saint-Genis-Pouilly. The setup of the experiment during the Run2 is reported in Fig. 3.2, while Tab. 3.2 shows the position and some details on the different subsystems. Since the data analysed in this work were taken during the Run2, the detector setup before the LS2 and the upgrade that happened during that period is described in this section. More details on the actual status of the detector are reported in Sect. 3.4.

The ALICE apparatus can be divided in two different parts: the *central barrel*, which measures hadrons, electrons, and photons, and the *forward muon spectrometer*, that is able to identify muons in the forward direction. In particular, the central barrel is embedded in a large solenoidal magnet that provides a magnetic field of 0.5 T, and covers the polar angle from 45^o to 135^o. From inside out, the central barrel contains the Inner Tracking System (ITS), a cylindrical Time Projection Chamber (TPC), the Transition Radiation Detector (TRD), the Time-of-Flight detector (TOF), Ring Imaging Cherenkov (HMPID) and two electromagnetic calorimeters (PHOS and EMCal). The forward muon spectrometer, instead, covers the small forward angles (2^o - 9^o), and consists of a complex arrangement of absorbers, a dipole magnet, tracking planes and triggering chambers. Moreover, at small angles, several small detectors for the characterization of the event are located, such as ZDC, PMD, FMD, T0 and V0. Finally, on top of the solenoidal magnet, an array of scintillators (ACORDE) is used as trigger for the cosmic rays.

In the next sections, the detectors used in this work, namely the ITS, TPC and TOF, are described in details. The other detectors are described briefly in Sect. 3.3.4.

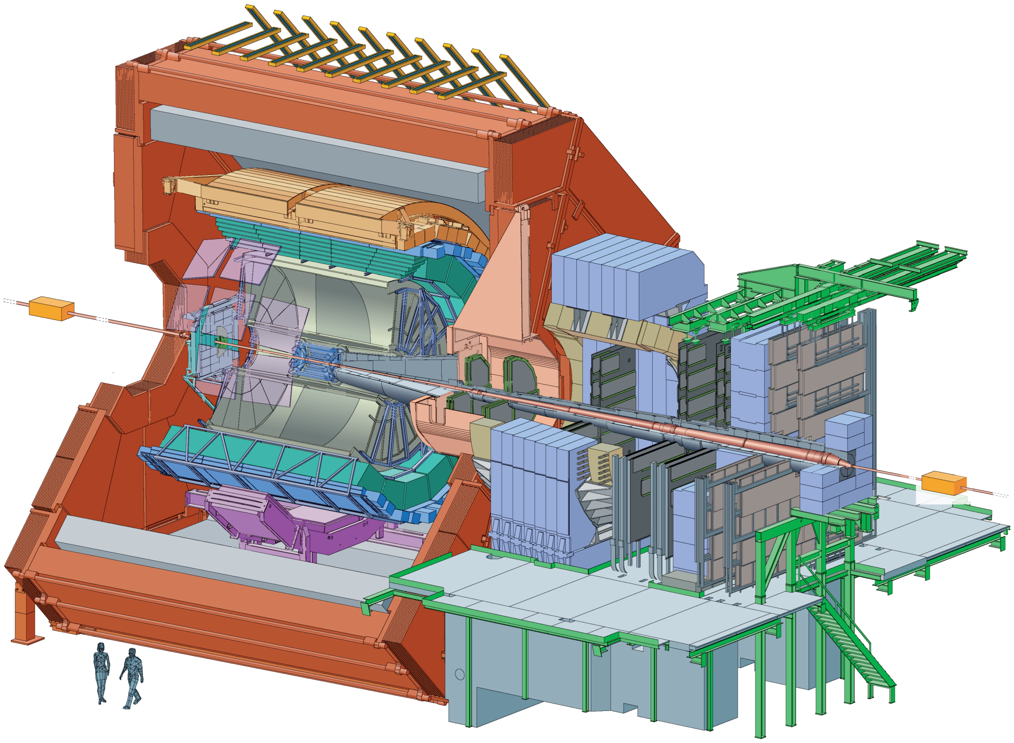

Figure 3.2: The ALICE detector layout during the Run2 [179].

Detector	Acceptance (η, ϕ)	Position (m)	Dimension (m^2)
ITS layer 1, 2 (SPD)	±2, ±1.4	0.039, 0.076	0.21
ITS layer 3, 4 (SDD)	±0.9, ±0.9	0.150, 0.239	1.31
ITS layer 5, 6 (SSD)	±0.97, ±0.97	0.380, 0.430	5.0
TPC	±0.9 at r = 2.8 m ±1.5 at r = 1.4 m	0.848, 2.466	readout 32.5 m^2 Vol. 90 m^3
TRD	±0.84	2.90, 3.86	716
TOF	±0.9	3.78	141
HMPID	±0.6 $1.2° < \phi < 58.8°$	5.0	11
PHOS	±0.12 $220° < \phi < 320°$	4.6	8.6
EMCal	±0.7 $80° < \phi < 187°$	4.36	44
ACORDE	±1.3 $-60° < \phi < 60°$	8.5	43
Muon Tracking 1, 2 3, 4, 5	$-2.5 < \eta < -4.0$	-5.36, -6.86 -12.92, -14.22, -16.12	4.7, 7.9 14.4, 26.5, 41.8
Muon Trigger 1, 2	$-2.5 < \eta < -4.0$	-16.12, -17.12	73.1
ZDC:ZN	$\|\eta\| < 8.8$	±116	2×0.0049
ZDC:ZP	$6.5 < \|\eta\| < 7.5$ $-9.7° < \phi < 9.7°$	±116	2×0.027
ZDC:ZEM	$4.8 < \eta < 5.7$ $-16° < \phi < 16°$ and $164° < \phi < 169°$	7.25	2×0.0049
PMD	$2.3 < \eta < 3.7$	3.64	2.59
FMD disc 1	$3.62 < \eta < 5.03$	inner: 3.2	0.266
FMD disc 2	$1.7 < \eta < 3.68$	inner:0.834 outer:0.752	
FMD disc 3	$-3.4 < \eta < -1.7$	inner:-0.628 outer:-0.752	
V0A	$2.8 < \eta < 5.1$	3.4	0.548
V0C	$-1.7 < \eta < -3.7$	-0.897	0.315
T0A	$4.61 < \eta < 4.92$	3.75	0.0038
T0C	$-3.28 < \eta < -2.97$	-0.727	0.0038

Table 3.2: Principal geometric characteristics of the ALICE subdetectors. When it is not specified, the azimuthal coverage for the detector is 2π [179].

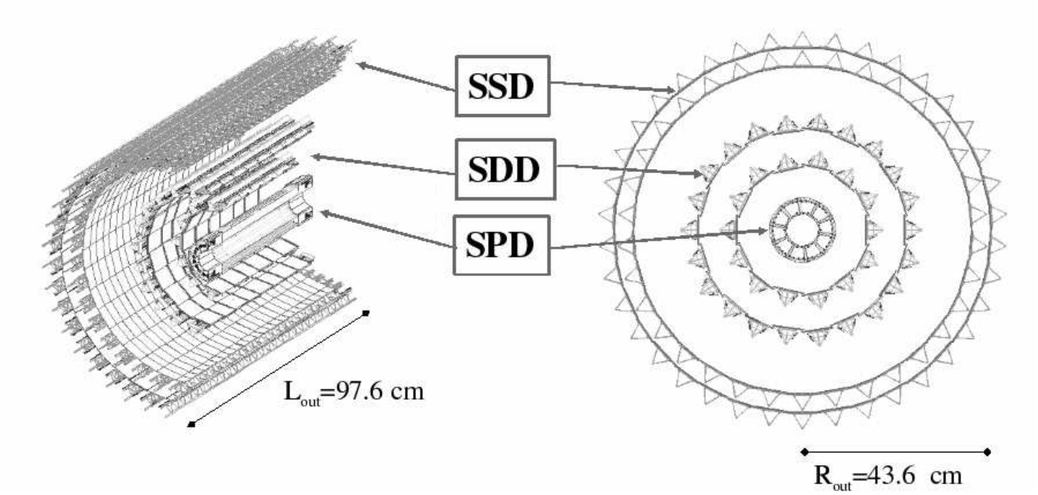

Figure 3.3: ITS layout during Run1 and Run2 [179].

3.3.1 Inner Tracking System (ITS)

The Inner Tracking System (ITS) [179] is the innermost subdetector of the ALICE apparatus. Its principal tasks are to locate the primary vertex of the collision with an accuracy of 100 μm, to reconstruct the secondary vertices from unstable particles decay, to track low momentum ($\approx$ 200 MeV/c) particles, to improve the momentum and angle resolution for the particles reconstructed by the TPC, and to reconstruct particles tracks that traverse the dead regions of the TPC. The detector, that surrounds the beam pipe, is located at radii between 4 and 43 cm, covering a pseudorapidity region $|\eta| < 0.9$. The number, position and segmentation of the layers were optimized for efficient track finding and high impact-parameter resolution.

The ITS consist of six cylindrical layers of silicon detectors of different technologies, as reported in Fig. 3.3. In particular, the innermost layers are Silicon Pixel Detector (SPD), followed by Silicon Drift Detector (SDD) and finally double-sided Silicon micro-Strip Detector (SSD). The three technologies are chosen according to different parameters. In fact, the SPD layers are chosen since, thanks to their segmentation, provide a 2D readout with high geometrical precision, important parameters for a correct vertexing procedure. The intermediate SDD layers are chosen since they are able to couple a good multi-track capability with the dE/dx

Parameter	Silicon Pixel	Silicon Drift	Silicon Strip
Spacial precision rϕ (μm)	12	35	20
Spacial precision z (μm)	100	25	830
Two track resolution rϕ (μm)	100	200	300
Two track resolution z (μm)	850	600	2400
Cell size (μm^2)	50×425	202×294	95×40000
Active area per module (mm^2)	12.8×69.6	72.5×75.3	73×40
Readout channels per module	40960	2×256	2×768
Total number of modules	240	260	1698
Total number of readout channels (k)	9835	133	2608
Total number of cells (M)	9.84	23	2.6
Max. occupancy for central Pb-Pb (inner layer) (%)	2.1	2.5	4
Max. occupancy for central Pb-Pb (outer layer) (%)	0.6	1.0	3.3
Power dissipation in barrel (W)	1350	1060	850
Power dissipation in endcap (W)	30	1750	1150

Table 3.3: Parameters of the different detectors of the ITS during Run1 and Run2. A module represents a single sensor element [179].

information. Finally, the SSD information are crucial in order to connect the tracks between the ITS and the TPC, hence the dE/dx information is crucial to correctly identify very low momentum particles. Tab. 3.3 summarizes the principal characteristics of the ITS.

3.3.2 Time Projection Chamber (TPC)

The Time Projection Chamber (TPC) [180] is the main tracking detector of the ALICE experiment, and it is used to identify the charged particles and measure their momentum. Moreover, the information provided by the track reconstruction helps to locate the primary vertex. The detector covers the full azimuth angle (with the exceptions of the dead zones) and the pseudorapidity range $|\eta| < 0.9$ if the tracks match in ITS, TRD and TOF, while if the tracks have a reduced length the pseudorapidity interval covered is $|\eta| < 1.5$. The detector is able to measure particles in a large interval of p_{T}, from about 0.1 GeV/c up to about 100 GeV/c. A schematic layout of the TPC is shown in Fig. 3.4, while in Tab. 3.4 the principal

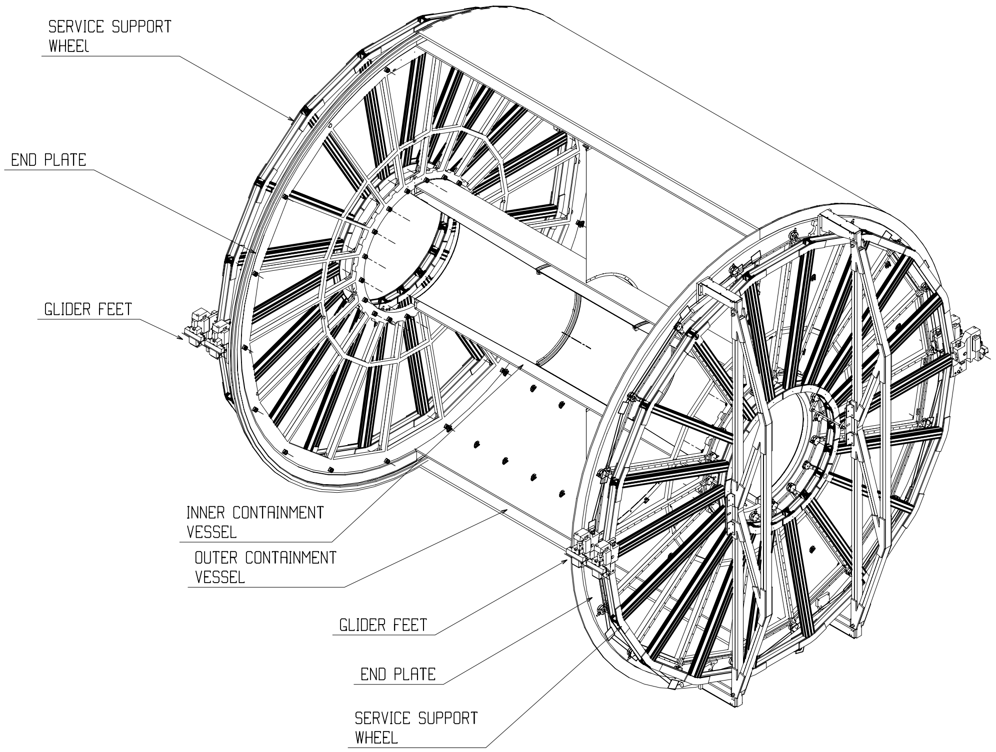

Figure 3.4: Layout of the TPC detector during the Run1 and Run2 [179].

characteristics of the detector are reported.

The TPC is made of a cylindrical field cage of about 90 m^3, with an inner radius of 85 cm and an outer radius of 250 cm, and an overall length along the beam direction of 5 m. The field cage is filled with a mixture of $Ne/CO_2/N_2$ (90/10/5), chosen to optimize the drift velocity and minimize the multiple scattering. The cage is closed with two endcaps of Multi-Wire Proportional Chambers (MWPC) segmented into 18 trapezoidal shapes, with cathode pad readout. Because of the radial dependence of the track density, the readout is segmented radially into two readout chambers with slightly different wire geometry adapted to the varying pad sizes. In order to create a highly uniform electrostatic field, a central high-voltage electrode of stretched aluminized Mylar foil and two opposite axial potential dividers are used, providing a high voltage gradient of

Length (active volume)	2×2500 mm
Segmentation in ϕ	18 sections
Segmentation in r	2 chambers per sector
Total number of readout chambers	2×2×18 = 72
Detector gas	$Ne/CO_2/N_2$ 90/10/5
Gas volume	90 m^3
Drift length	2×2500 mm
Drift field	400 V/cm
Drift Velocity	2.7 cm/μs
Maximum drift time	92 μs
Total HV	100 kV
Diffusion	$D_L = D_T = 220\mu\text{m}/\sqrt{\text{cm}}$
Material budget	X/X_0 = 3.5% near η = 0
Position resolution (σ) in rϕ	1100 to 800 μm inner/outer radii
Position resolution (σ) in z	1250 to 1100 μm
dE/dx resolution, isolated tracks	5.0%
dE/dx resolution, dN/dy = 8000	6.8%

Table 3.4: TPC principal parameters in Run1 and Run2 [179].

about 400 V/cm. The insulation of the TPC vessel is made by a gas envelope of CO_2.

3.3.3 Time-Of-Flight (TOF)

The Time-of-Flight (TOF) [181] detector complements the particle identification provided by the TPC. It measures the time spent by the particle to travel from the collision point to the TOF radius. The detector covers the full azimuthal angle and the pseudorapidity interval $|\eta| < 0.9$, except for the region $|\eta| < 0.12$, where the photon spectrometer is located, in order to avoid to cover it with more material. The whole detector is inscribed in a cylindrical shell with internal and external radii of, respectively, 370 cm and 399 cm. Fig. 3.5 shows a schematic layout of the TOF detector, while Tab. 3.5 reports a summary of the detector characteristics.

The TOF is formed by 18 sectors in azimuthal angle and 5 segment in the beam direction. The basic unit of the TOF system is a 10 gap double-stack Multigap Resistive Plate Chamber (MPRC), where the gaps are of

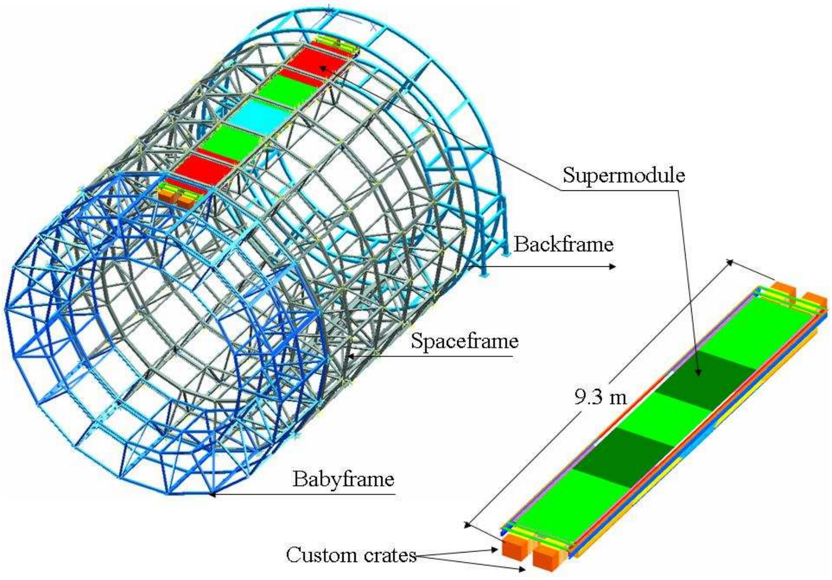

Figure 3.5: Schematic layout of the TOF detector during Run1 and Run2 [179].

Length active region	741 cm
Segmentation in ϕ	18-fold
Segmentation in z	5-fold
Total number of modules	90
Central module (A)	117×128 cm^2
Intermediate module (B)	137×128 cm^2
External module (C)	177×128 cm^2
Detector active area (total area)	141 m^2 (171 m^2)
Detector radial thickness	X/X_0 = 29.5%
Number of MRPC strips per module	15 (A), 19 (B), 19 (C)
Number of readout pads per MRPC strip	96
Module segmentation in ϕ	48 pads
Module segmentation in z	30 (A), 38 (B), 38 (C) pads
Readout pad geometry	3.5×2.5 cm^2
Total number of MRPC strips	1638
Total number of readout pads	157 248
Detector gas	$C_2H_2F_4$ (90%), i-C_4H_10 (5%), SF_6 (5%)
Gas volume	17.5 m^3
Total flow rate	1 m^3/h
Working overpressure	< 3 mbar
Fresh gas flow rate	0.02 m^3/h

Table 3.5: Summary of the TOF main parameters in Run1 and Run2 [179].

250 μm. This detector is chosen for its high and uniform electric field over the full sensitive gaseous volume, the possibility to operate at atmospheric pressure, an high-gain operation possible due to the absence of sparks, and a construction technique that is rather simple and uses commercially available materials. Every module of the TOF detector consists of a group of MRPC strips (15 in the central, 19 in the intermediate and in the external modules) closed inside a box that defines and seals the gas volume and supports the front-end electronics and services. The strips are enclosed between two panels of aluminium (0.1 cm thick) and honeycomb (1.5 cm thick), that provide the necessary mechanical stiffness to the system. Finally, a cover made of 0.3 cm fibreglass closes the total gas volume.

3.3.4 Other detectors

Besides the already described detectors, the ALICE apparatus is formed by different other subdetectors. In particular, the other detectors present in the central barrel, as described in Ref. [179], are:

- *Transition Radiation Detector (TRD)*. Located in the space between the TPC and TOF, its main purpose is to provide the electron identification in the central barrel for particles with momenta above 1 GeV/c, where the TPC is not able to correctly identify the electrons. It is formed by 540 modules arranged in 18 supermodules, containing each 30 modules arranged in five stacks along the beam direction and six layers in radius. Each module is formed by a radiator material (propylene fibres), a drift section and MWPC with pad readout.

- *High-Momentum Particle Identification (HMPID)*. The HMPID is dedicated to inclusive measurement of high momenta hadrons, enhancing the particle identification capabilities of ITS, TPC and TOF. The detector is based on a proximity-focus Ring Imaging Cherenkov (RICH) counter, mounted on a independent support cradle fixed in the spaceframe at the two o'clock position. The RICH radiator is a 15 mm thick layer of low chromaticity C_6F_{14} liquid, and the emitted photons are collected by a photon counter made of a layer of CsI deposited onto the pad cathode of a Multi-Wire Pad Chamber (MWPC).

- *PHOton Spectrometer (PHOS) and Charged Particle Veto detector (CPV)*. The PHOS detector is a high resolution electromagnetic spectrometer that covers a limited high central rapidity region ($|\eta| < 0.12$). As the name suggests, it detects photons, in order to test the thermal and dynamical properties of the initial phase of the collision. The detector is a single-arm high-resolution and high-granularity electromagnetic calorimeter made of lead-tungstate crystals ($PbWO_4$) coupled with Avalanche Photo-Diodes (APD). On top of PHOS, at a distance of about 5 mm, is placed the CPV, that acts like a veto detector for the calorimeter. The CPV is a MWPC with a cathode-pad readout, and has a high charged particle detection efficiency better than 99%.

- *ElectroMagnetic CALorimeter (EMCal)*. To identify photons and electrons at high transverse momenta, the EMCal detector is used. It is a cylindrical sampling calorimeter, located adjacent to the ALICE magnet coil at a radius of approximately 4.5 m from the beam line, positioned approximately opposite in azimuth to the PHOS detector. Each of the 12288 towers of the EMCal is made by layers of 1.44 mm Pb and 1.76 mm scintillator, crossed by longitudinal wavelenght-shifting fibres for the light collection coupled with APD.

- *ALICE COsmic Ray DEtector (ACORDE)*. On top of the solenoidal magnet is placed the ACORDE detector, suited for cosmic rays measurements. It has two main tasks: to provide a fast trigger signal for the commissioning, calibration and alignment procedure of some ALICE subdetectors and, in combination with the TPC, TRD and TOF, to detect single and multi-muons atmospheric events. It is made of two scintillator counters placed on top of each other and read out in coincidence.

Moreover, in the forward direction, different detectors are placed, in order to characterize the event, provide the trigger signal and the multiplicity of the collision, and to measure penetrating particles as muons. These detectors, also described in Ref. [179], are:

- *Muon spectrometer*. Formed by a complex arrangement of absorbers and tracking devices, its main purpose is to detect muons in the pseudorapidity region $-4.0 < \eta < -2.5$. In particular, the spectrometer is composed of: a passive front absorber made of carbon and concrete in order to absorb hadrons and photons from the interaction vertex; an inner beam shield made by tungsten, lead and stainless steel; a high-granularity tracking system of 10 detector planes of tracking chambers arranged in five stations; a large dipole magnet; a passive muon-filter wall, followed by four planes of trigger chambers; an inner beam shield to protect the chambers from primary and secondary particles produced at large rapidities.

- *Zero Degree Calorimeter (ZDC)*. Composed by three different setups, for neutrons (ZN), protons (ZP) and electrons (ZEM), their main task is to measure the number of spectator nucleons, in order to estimate the multiplicity of the collision. The ZEM are placed at about 7 m from the IP, opposite to the muon arm. The ZN and ZP, instead, are located on both side of the IP at around 116 m: the first one placed between the beam pipe at 0^o relative to the LCH axis, while the second one is placed externally to the outgoing beam pipe on the side where positive particles are deflected. Moreover, the ZN and ZP are installed on lifting platforms, in order to lower them out of the horizontal beam when they are not in use. The hadronic calorimeters are quartz fiber sampling ones, with a very dense W-alloy used as passive material for the ZN due to space limitations, while for the ZP brass is used. The light developed by the towers are collected by different Photo Multipliers (PMT). Also for the ZEM the active material is made of quarz fibers, while the passive one is lead. An air light guide positioned on the top of the detector directs the developed light up to a PMT.

- *Photon Multiplicity Detector (PMD)*. The PMD detector provides both the multiplicity and spacial distribution of photons in the forward direction ($2.3 \leq \eta \leq 3.7$) and the estimation on the transverse electromagnetic energy and the reaction plane. Considering the large particle density present in the forward direction, it is not possible to use the common calorimetric technique. For this reason, the PMD use a preshower method where a tree radiation length thick converter made of lead and stainless steel is sandwiched between two planes of high granular gas proportional counters.

- *Forward Multiplicity Detector (FMD)*. The main purpose of this detector is to provide the charged particle multiplicity information in the pseudorapidity range $-3.4 < \eta < -1.7$ and $1.7 < \eta < 5.0$. The experimental apparatus is formed by three rings of silicon strip sensors. While both FMD2 and FMD3 consist of both an inner and outer ring, located on both side of ITS, the FMD1 is composed only by the inner ring and it is placed further along the IP opposite to the muon spectrometer in order to extend the charged particle multiplicity coverage.

- *V0 detector*. A small angle detector, it is formed by two array of scintillator counters, namely V0A and V0C, installed on both side on the IP. In detail, the V0A is located 340 cm from the vertex on the side opposite to the muon spectrometer, while V0C is fixed to the front face of the hadronic absorber, 90 cm from the vertex. They are composed of BC404 scintillation material, connected with wavelength shifter fibers and PMT. The scope of these detectors is to provide a minimum bias trigger in pp and A−A collisions, to estimate the centrality of the collisions via the multiplicity recorded in it, and to participate in the luminosity measurements in pp collisions.

- *T0 detector*. The detector was designed for several purposes: to generate a start time (T0) for the TOF detector, to measure the vertex position, to provide a trigger when the vertex position is within the preset values, in order to discriminate against beam-gas interactions, to generate a "wake-up" signal for the TRD, and to provide redundancy to the V0 counters, generating minimum bias trigger. The T0 experimental apparatus consists of two arrays of Cherenkov counters, 12 counters per array. The counter is made of a PMT coupled to quartz as radiator material. Also the T0 is formed by two different subdetectors: T0-C, placed 72.7 cm from the nominal vertex (distance chosen accordingly to the constraints imposed by the front cone of the muon absorber) and T0-A, placed on the opposite side at around 375 cm, grouped with other forward detectors (FMD, V0 and PMD). In the radial direction, both the T0 arrays are placed close to the beam pipe to maximize the trigger efficiency.

3.4 ALICE Upgrade during the LS2

During the Long Shutdown 2, in the years 2019-2022, both the LHC complex and the different experiments updated their setup in order to be able to reach higher energies with respect to the one achieved in Run1 and Run2, collect more luminosity and improve the data acquisition techniques. In particular, the ALICE experiment performed different upgrades, not only from the detector point of view, but also on the online/offline system for data acquisition and processing, developing a new analysis framework. All the details on the upgrades are reported in Ref. [182]. In the following sections some of the key points are reported.

3.4.1 Physics goals

The scientific goals for the upgraded ALICE detector are aimed to improve the measurements in different open physics points, such as: the understanding of heavy quark production at low momenta; quarkonia production and interaction in the QGP; thermal emissions of dielectron pairs; initial temperature and partonic equation of state; possible effects of chiral symmetry restoration; parton energy loss, medium modification and its dependence on properties of the partons and the QGP; exotic hadronic states. Moreover, the upgrades significantly improve the precision of measurements in several other areas, such as jet quenching phenomena, the production of light nuclei, momentum correlations of hadrons, and the study of collective effects in collisions of protons with high multiplicity.

In order to access these physics areas two main characteristics are considered: improve the pointing resolution and increase the readout rate of the whole apparatus, in order to collect more data. Using a thinner and lighter inner tracker, with the first layer closer to the interaction point, improves the pointing resolution of a factor 3 in the transverse direction and a factor 6 in the longitudinal direction. Moreover, it also provides a background suppression in the reconstruction of decays of heavy-flavoured particles and in the dielectron emission measurements. For the readout

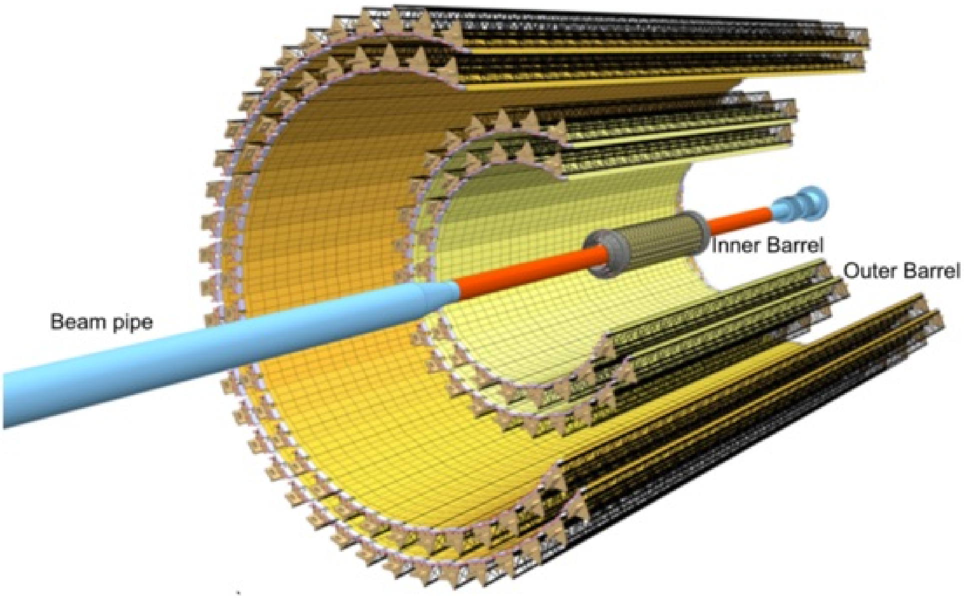

Figure 3.6: Layout of the ITS2 detector [183].

rate, instead, a untriggered readout mode, combined with online data compression for the upgraded readout and data acquisition system, was adopted.

3.4.2 The ITS2

As already said before, the use of a thinner and lighter inner tracker detector can improve the pointing resolution. For this reason, the ITS as described in Sect. 3.3.1 was removed during the LS2 and was replaced by the so-called ITS2 [183]. A schematic view of such detector is reported in Fig. 3.6. It is formed by 7 layers of all-pixel silicon detectors made of Monolithic Active Pixel Sensors (MAPS) based on the ALPIDE sensor technology [184]. The main feature of such technology is that both the sensor for the charge collection and the readout circuit for the digitalization are hosted on the same piece of silicon, and not bump-bonded together. The detector is grouped into Inner Barrel (IB), consisting in the three innermost layers, and Outer Barrel (OB) arranged in two double layers.

With respect to the ITS, the layers positions of the ITS2 are different, with the first layer at a radius of 22 mm from the beam pipe, that is newly redesign with a smaller radius (18.6 mm) and a central beryllium section. Moreover, the radial position of each layer is optimized to achieve the best performance in terms of pointing resolution, p_{T} resolution, and tracking efficiency. The detector covers a pseudorapidity region $|\eta| < 1.22$, having a total sensor surface area of about 10 m^2 and about 12.5 billion pixels. The material budget of the IB is of only 0.36% X_0, while for the OB it is limited to 1.1% X_0.

3.4.3 The TPC upgrade

An important upgrade was also done in the TPC detector. In fact, with the goal of 50 kHz readout in Pb–Pb collisions during the Run3 data-taking, tracks from five collisions pile up in the TPC drift time window of 100 μs. For this reason, a continuos readout must be implemented, with the additional requirement to keep the ion-induced space-charge distortions at a tolerable level. To do so, during the LS2 the MWPCs were replaced with Gas Electron Multipliers (GEM) detectors [185]. These detectors, recently developed at CERN, can be arranged in stacks, creating layers of amplification that can be opportunely tuned. Hence, optimizing the gain share among the GEMs and blocking the path of back-drifting ions using subsequent layers, it is possible to achieve the detector requirements for the Run3 data-taking. In particular, the readout chamber is based on a stack formed by four GEM foils with different hole pitches, standard (S, 140 μm) and large (LP, 280μm), in the S-LP-LP-S configuration, as shown in Fig. 3.7. Most of the ions are produced in the last amplification step, *i.e.* GEM 4. Their drift path is efficiently blocked by the upper GEM layers by optimizing the GEM voltages and transfer fields, and by choosing GEM hole patterns avoiding the accidental alignment of holes in subsequent layers. Finally, for the gas part, no changes on the mixture or hardware were necessary.

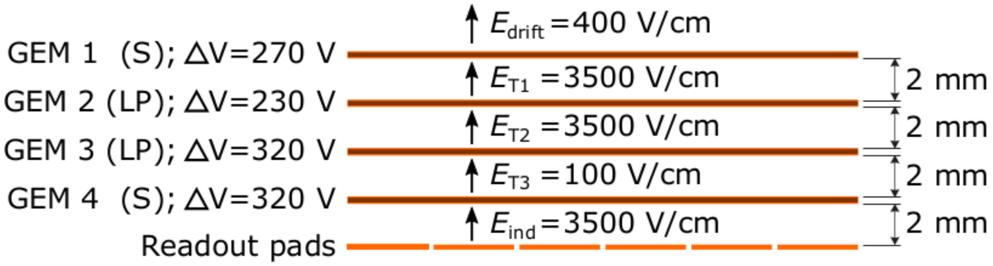

Figure 3.7: Schematic view of a TPC stack with 4 GEM foils [182].

3.4.4 Other upgrades

One another important upgrade on the ALICE apparatus during the LS2 was the installation of the Fast Interaction Trigger (FIT) that substitutes the V0 and T0 detectors. The FIT system serves as interaction trigger, online and offline luminometer, initial indicator of the vertex position and forward multiplicity counter. It consists of five different detector stations, positioned at different locations along the beam line. It employs three different technologies: quartz Cherenkov radiators optically coupled to microchannel plate-based (MCP) photomultipliers for the FTO; plastic, segmented scintillator coupled with PMTs for the FV0; plastic scintillator, wavelenght fibers and PMTs for the FDD.

To extend the physics program of the muon spectrometer the Muon Forward Tracker (MFT) was designed and installed. It is a high position resolution detector made of ALPIDE silicon sensors, and it is located between the interaction point and the front absorber. Its primary goal is to improve the pointing resolution of muons by matching the tracks reconstructed downstream of the hadron absorber to those reconstructed inside the MFT upstream of the absorber. This approach allows the removal of multiple scattering effects in the hadron absorber and improves the pointing resolution of muon tracks down to about 100 μm.

All the others detectors have been undergone to maintenance and improvements in the readout electronics, in order to handle the increased readout. In order to be able to process the data from a higher and continuos readout, also the readout infrastructure is renewed. The raw data from the detectors are mostly transmitted through optical links and received by First Level Processors (FLPs). Here the data are assembled to time frames for further processing, where a time frame is a temporal unit defined as 128 LHC orbits ($\sim$ 11 ms). A dedicated farm of Event Processing Nodes (EPN) was installed for the online reconstruction of all collisions. The output of this synchronous reconstruction is stored on mass storage systems and is used in the asynchronous reconstruction stage with improved calibration. The output of the latter is then used for physics analysis. In order to handle the online and offline reconstruction and the physics analyses a new software framework, O^2 [186, 187], was developed.

3.5 Data acquisition and event reconstruction

Considering the high number of collisions and charged particle produced, it is not possible to store all the data, due to their large dimension on disk. For this reason, it is of the uttermost importance to have a high efficiency trigger, in order to maximize the collection of good data. Moreover, the nature of the collected data from the detectors is not a physical observable but simply an electrical signal. Hence, a reconstruction from the detector output to physical observables is needed. In the following sections, the trigger strategy and the event reconstruction algorithm employed during the Run2, on which the analysis reported on this work is based, is reported.

3.5.1 Data Acquisition

The ALICE trigger system is composed by a low-level hardware trigger, the Central Trigger Processor (CTP), and a High-Level software Trigger (HLT). The CTP generates the trigger decision by combining the informations from the different subdetectors. Considering the different detectors readout times, the decision is divided into three levels, called L0, L1 and L2. The L0 decision is taken $\sim$0.9 μs after every collision: only the events that pass this selection are sent to the next level, L1. In this case, the decision is taken $\sim$ 6.5 μs after the collision, in order to take into account the computation time and the signal propagation from the farther detector. If a signal passes both the L0 and L1 trigger, a L2 decision is taken after $\sim$

100 μs, that is the time gap necessary to allow the complete ion drift in the TPC volume. Only the collisions that successfully pass all the hardware level triggers are sent to the HLT. This software trigger receives a copy of the data, does a full event reconstruction and the result are sent to the final stage for the trigger decision. Moreover, the size of the selected data is compressed using advanced encoding techniques, without losing the relevant physical informations.

In order to store, process and analyse the data collected a huge infrastructure is needed. The data processing is distributed among different worldwide computing centres and coordinated by the Worldwide LHC Computing Grid (WLCG) project [188]. The project is formed by a hierarchical three-levels structure: the largest computing centre, Tier-0, is located at CERN, and together with other large computing centres, the so-called Tier-1, logically clustered around the Tier-0, shares the responsibility of storing the raw data. The smallest centres, the Tier-2, are logically clustered around the Tier-1. The grid infrastructure is used to store and process the data, from calibration to reconstruction, simulation and analysis. The data can be easily accessed through the AliEn (ALICE Environment) service [189]. The data are analysed using the ALICE software environment called AliRoot, based on the ROOT framework. Finally, the analysis code is collected in a repository called AliPhysics [190]. Two different types of data are available: the Event Summary Data (ESD), that contains all the information about the event at the track and collision level; the Analysis Object Data (AOD), where only a summary of the most relevant information of the ESDs are stored.

3.5.2 Event and track reconstruction

In order to convert the signals received by the detector to a physical observables, available in the ESD and AOD formats, a multi-step event reconstruction process must be performed. Considering the large geometrical coverage, the number of subdetectors employed, the elevated number of particles, thus of signals, produced, the event reconstruction process is complex, and involves a multi-step procedure, described below.

The first step is to perform a local reconstruction: for each detector the collected signal must be converted into the space-time informations of the particle that generated it. The first obtained information is a *hit*, and adjacent hits are grouped forming a so-called *cluster*. To each cluster additional informations can be attached, such as the particle identification ones. Once the clusters are available, it is possible to reconstruct the primary vertex and all the tracks.

A preliminary determination of the primary vertex can be done, already with a quite good precision, using the *SPD tracklets*. They are defined as straight lines that connect pairs of clusters in the SPD layers of the ITS. The primary vertex is then defined as the space point where the maximum number of tracklets converge. Such approximation is valid since the SPD are the two ITS innermost layers, hence the deviation between the curved and straight trajectory is negligible.

The track finding and fitting are performed using the information from the ITS and TPC clusters and applying the Kalman filter technique [191]. This is performed in three stages, following an inward-outward-inward scheme. In particular:

- The first inward stage is the so-called TPC seed finding. Track seeds are sets of a few neighbouring clusters, located in the outer layers of the TPC, that are roughly compatible with a track: this means that they lay on the helix that roughly points to the primary vertex. The seed finding is performed with a combinatorial seeding algorithm [192]. The seeds are built first with two TPC clusters and the vertex point, and then with three clusters and no vertex constraint. The seeds are propagated inward in the TPC volume with the information on the nearest cluster updated in each iteration. In order to ensure a good quality of the reconstructed tracks, only the ones with at least 20 clusters are accepted. Moreover, the same physical track can be reconstructed more than once, since the clusters can be shared by different seeds. In order to address this problem, an algorithm searches for pairs of tracks with a fraction of common clusters exceeding a specific limit, between 25% and 50% depending on the momentum. Then, the worst track in terms of some defined quality parameters is discarded. The surviving tracks are then propagated to the outermost ITS layer, with a rather delicate procedure, due to the large distance between the TPC inner radius and the last layer of

ITS ($\sim$ 0.5 m) and the high particle density of the ITS, that implies the presence of more than one cluster in the prolongation window. For these reasons, since there is a non-negligible probability of a wrong cluster-track matching, different prolongation hypotheses are built, and the best one at the end of the ITS reconstruction is chosen. The method applied in the ITS reconstruction is similar to the one already described for the TPC.

- The second step of the reconstruction, the outward one, starts once the ITS reconstruction is completed. The tracks are refitted with the Kalman filter through the outward direction using the points already associated in the previous stage. In the propagation, the track length integral and the time of flight in five different particle hypotheses (electrons, muons, pions, kaons, protons) are updated. At the end of the TPC, the track is extended to match a tracklet in the TRD and a cluster in the TOF. Here, the track length integration and the computation of the time of flight calculation are finalised. Then, the tracks are propagated for matching the signal in the EMCAL, PHOS and HMPID.
- The final stage of the track reconstruction, the inward one, refits the data points already found starting from the outer layers of the TPC to the point of closest approach to the primary vertex. The track's position, direction, inverse curvature, and its associated covariance matrix are determined.

Then, the final vertex determination is made. Using the global tracks reconstructed with the ITS and TPC, it is possible to find the interaction vertex with an higher precision with respect to the SPD tracklets method. The global tracks are extrapolated to the point of closest approach to the nominal position of the beam line. Then, the primary vertex coordinates are obtained though a weighted fit of the coordinates distributions.

3.6 Particle Identification

The aim of the Particle IDentification (PID) is to determine the mass of each reconstructed track that, together with its charge, provide the identity of the particle itself. According to the particle nature, the identification can be performed in different ways. A summary of the particle identification and reconstruction techniques used by the ALICE experiment is reported in Fig. 3.8. In the case of light (anti)nuclei, subject of this thesis, the approach used to perform the particle identification is the so-called nσ method. This technique can be applied to detectors with a Gaussian response function. The nσ quantity is defined as:

$$n\sigma = \frac{S - S(H_i)}{\sigma} \tag{3.5}$$

where S is the measured signal, $S(H_i)$ is the expected theoretical signal for the hypothesis of a particle of specie i, and σ is the detector resolution. A particle is then identify if its nσ value is lower with respect to a given value. This threshold is chosen accordingly to the desired statistic and purity sample. In fact, a stricter cut like $|\mathrm{n}\sigma| < 3$ reduces the number of particles that are selected, but the purity is increased, while a larger cut like $|\mathrm{n}\sigma| < 5$ allows to enlarge the selected data at the expense of a lower purity. In this thesis, (anti)deuterons and antiprotons are identified using the specific energy loss in the TPC and the time of flight measurement obtained with the TOF detector. Some details on the particle identification in such detectors are reported in the sections below.

3.6.1 TPC particle identification

In the TPC the extracted signal is the specific energy loss $\mathrm{d}E/\mathrm{d}x$ of the charged particle that passes though the medium, *i.e.* the gas mixture in the TPC. The particles ionize the molecules in the gas mixture, and this ionization causes the continuos energy loss of the charged particles. The value of $\mathrm{d}E/\mathrm{d}x$ is described by the Bethe-Bloch formula:

$$\frac{\mathrm{d}E}{\mathrm{d}x} = -\frac{4\pi}{m_e c^2}\frac{nZ^2}{\beta^2}\left(\frac{e^2}{4\pi\epsilon_0}\right)^2\left[\ln\left(\frac{2m_e c^2\beta^2}{I\,(1-\beta^2)}\right) - \beta^2\right] \tag{3.6}$$

where E is the energy of the particle, x is the travelled distance in the medium, β is particle's speed in units of speed of light in the vacuum c, ϵ_0 the vacuum permittivity, e and m_e are the electron charge and mass, Z is the incident particle charge, n the electron density in the medium, and

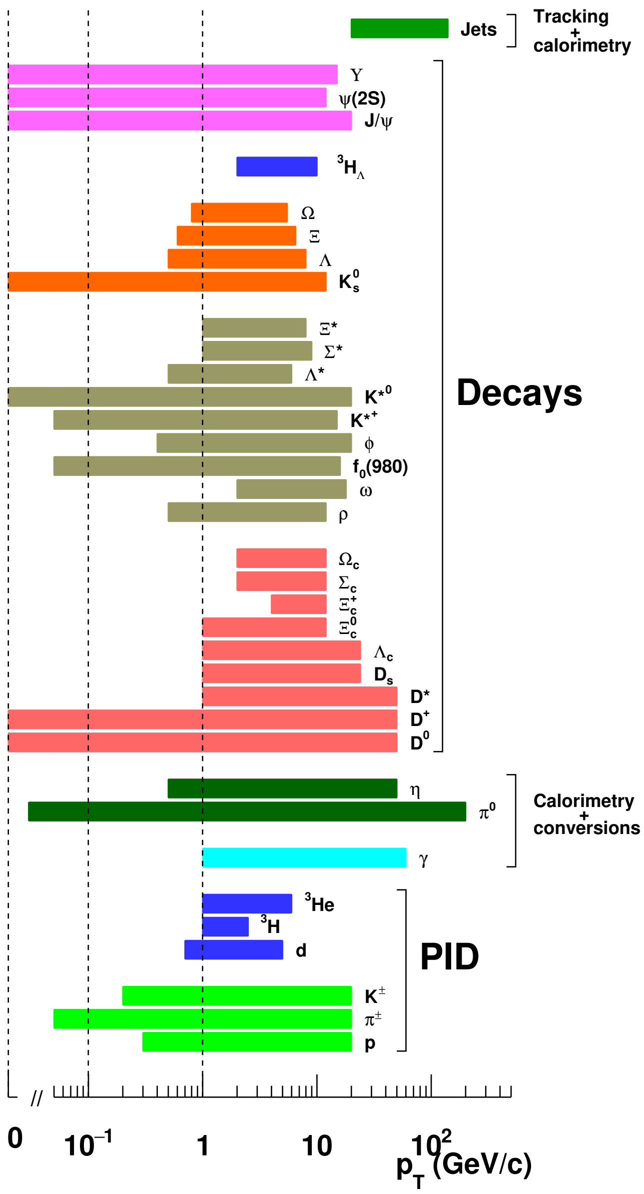

ALI−PUB−583552

Figure 3.8: ALICE particle identification and reconstruction capabilities. The p_{T} coverage corresponds to the published measurements based on pp and Pb–Pb data samples [37].

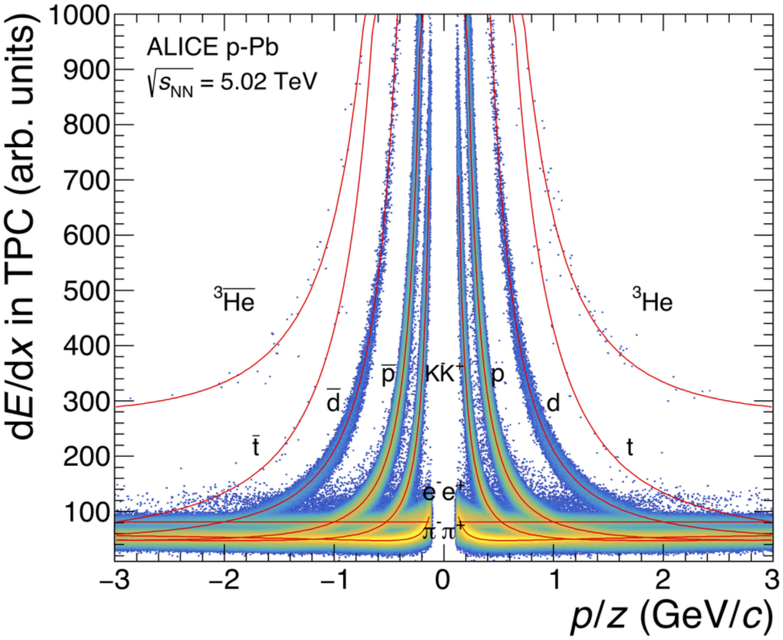

Figure 3.9: Specific energy loss for the TPC tracks as a function of the particle rigidity in p–Pb collisions at $\sqrt{s_{\mathrm{NN}}} = 5.02$ TeV. The solid lines represent the theoretical predictions [95].

I is the mean excitation potential of the medium. The measured value is then compared with the theoretical predictions and, since the energy loss depends on the particle charge and momentum, it is possible to correctly identify the particle. In the ALICE measurement the momentum of the particle is calculated through the track curvature due to the magnetic field, assuming a particle with unitary charge ($|Z| = 1$). Hence, the expected energy loss is given by the *Bischel function*, a simplified Bethe-Bloch parametrization with $|Z| = 1$. However, in the case of (anti)nuclei, not all of them have unitary charge: hence, before computing their $\mathrm{d}E/\mathrm{d}x$ information, they are converted in particles with unitary charge. Fig. 3.9 shows the specific energy loss as a function of the rigidity (defined as the ratio between the particle momentum and its charge) for the TPC tracks in p–Pb collisions at $\sqrt{s_{\mathrm{NN}}} = 5.02$ TeV. The red, solid lines represent the theoretical prediction according to the Bethe-Bloch formula for the different particle species. Thanks to its performance, the TPC is able to

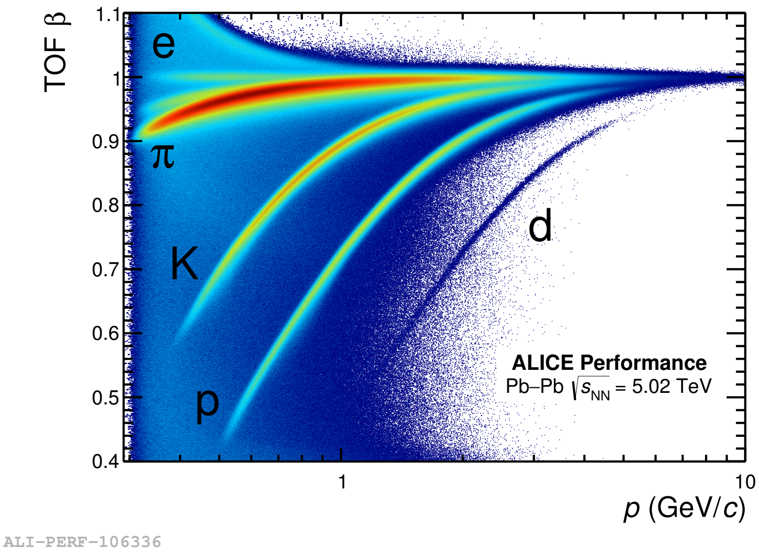

Figure 3.10: Particle speed β measured with the TOF detector as a function of the particle momentum in Pb–Pb collisions at $\sqrt{s_{\rm NN}} = 5.02$ TeV.

identify light (anti)nuclei in a wide momentum range, in particular up to about 1.5 GeV/c for the (anti)deuteron, while for (anti)^{3}He this limit is higher, due to its double charge.

3.6.2 TOF particle identification

At higher momenta, the particle identification is performed with the TOF detector, measuring the time of flight of the particle $t_{\rm TOF}$, its track length L and momentum p. Through these quantities, it is possible to calculate the particle mass:

$$m = p \cdot \frac{t_{\rm TOF}}{L}\sqrt{1 - \frac{L^2}{c^2 t_{\rm TOF}^2}} \tag{3.7}$$

The measured value is then compared with the expected ones obtained using different masses, thus different particle hypotheses. Fig. 3.10 shows the particle speed β as a function of the track momentum in Pb–Pb collisions at $\sqrt{s_{\rm NN}} = 5.02$ TeV. With respect to the TPC, the TOF performance shows a uniform background due to incorrect assignment of the TOF clusters to a track, that depends on the track density of the event. Nevertheless, the TOF is able to correctly identify light (anti)nuclei at higher larger transverse momentum, complementing the information from the TPC, from about 1 GeV/c up to about 6 GeV/c.

Chapter 4

(Anti)deuteron and antiproton production in and out of jets

The aim of the analysis reported in this work is to investigate the deuteron coalescence probability in and out of jets in p–Pb collisions at $\sqrt{s_{\mathrm{NN}}} = 5.02$ TeV, evaluating the coalescence parameter B_2. As reported in Sect. 2.3.1, the measurements of nucleus production in and out of jets could help to constraint the coalescence model. To perform such analysis, the (anti)deuteron and antiproton production is studied in the three azimuthal regions reported in Fig. 2.13: Toward, Away and Transverse. The in jet contribution is evaluated subtracting the Transverse region from the Toward one. This choice relies on the assumption that the Transverse region is dominated by the underlying event, while the Toward one contains both the in jet contribution and the underlying event. Hence, in order to isolate the jet contribution, the underlying event part must be removed. It is worth to notice that, in this analysis, while for the deuteron both the antimatter and the matter signals are considered, for the proton distributions only the antimatter signal is taken into account. As discussed in Sect. 4.3.2, in a collision both primary and secondary particles are produced, with the latter that can be produced by different mechanisms. For the antimatter case, the production of secondary nuclei due to the interaction of the primary particles with the detector material is negligible. Hence, the antiproton sample is predominantly composed by primary particles, with only a small fraction of secondaries due to weak decays. For these reasons, for the measurement of protons, that are produced with a rate of about 1 particle per event, the analysis is focused on antimatter only. On the contrary, the (anti)deuteron production is suppressed by a factor about 10^3 with respect to the (anti)proton, hence it is important to maximize the collected signal. For this reason, both the deuterons and antideuterons are measured and the corresponding corrections are made to account for secondary nuclei. With the obtained distributions, the coalescence parameter in and out of jets is evaluated, comparing the results with the ones obtained in pp collisions at $\sqrt{s} = 13$ TeV, already published in Ref. [104]. In such study, in fact, an enhanced deuteron coalescence probability in jets with respect to the underlying event is observed. It is then important to evaluate the evolution of such quantity in other collision systems, such as p–Pb, in order to test the coalescence predictions.

4.1 Event and track selection

The analysis reported in this work uses the p–Pb data sample at $\sqrt{s_{\mathrm{NN}}} =$ 5.02 TeV collected by ALICE during the Run2 campaign, in particular in the year 2016. Before applying any event selection, the available dataset corresponds to about 370 million events, with a minimum bias trigger.

In order to ensure a symmetrical acceptance, only events with the z-coordinate of the reconstructed primary vertex within the acceptance window of ± 10 cm are considered. Moreover, events that have more than one vertex identified with the SPD are tagged as pile-up and removed. After these selection criteria are applied, the number of selected events is about 310 million. For each event, the track with the highest transverse momentum is then searched, in order to assign to it the role of *leading track*. To ensure a track with good quality, the leading track is searched among the tracks that satisfy the cuts reported in the last column of Tab. 4.1. Once the leading track is found, an azimuthal angle $\phi = 0$ is assigned to it. Only events with a leading track with a transverse momentum higher than 5 GeV/c ($p_{\mathrm{T,lead}} > 5$ GeV/c), as already reported in Sect. 2.3.1, are selected: the available dataset after this selection is then reduced to about 7 millions of events, about the 2% of the whole data sample available at the beginning. In these events, in order to select tracks with good quality,

Variable		**Selection Cut**	
	(anti)deuteron	**antiproton**	**leading track**
$\lvert\eta\rvert$	< 0.8	< 0.8	< 0.8
y_{CMS}	(-1, 0)	(-1, 0)	(-1, 0)
Kink topologies	rejected	rejected	rejected
TPC and ITS refit	required	required	required
$\mathrm{n_{ITScluster}}$	≥ 2	≥ 4	
$\mathrm{n_{TPCdE/dxClusters}}$	≥ 50	≥ 60	
$\mathrm{n_{TPCCrossedRows}}$	≥ 70	≥ 80	≥ 70
$\mathrm{n_{TPCCrosRows}/n_{TPCFindClust}}$	≥ 0.8	≥ 0.8	≥ 0.8
ITS χ^2/NDF	< 36	< 36	< 36
TPC χ^2/NDF	< 4	< 4	< 4
$\lvert\mathrm{DCA_{xy}}\rvert$	< 0.1 cm	< 0.1 cm	$< 0.0105 + 0.0350/p_{\mathrm{T}}^{1.1}$ cm
$\lvert\mathrm{DCA_{z}}\rvert$	< 1.0 cm	< 1.0 cm	< 2.0 cm
$\mathrm{N_{SPDhits}}$		kAny	kAny
p_{T}			(0.15, 200) GeV/c

Table 4.1: Track selection criteria applied in this analysis, for (anti)deuterons, antiprotons and the leading track.

the cuts reported in Tab. 4.1 are applied. Only tracks in the pseudorapidity interval $|\eta| < 0.8$ are selected, to ensure that the tracks fall within the acceptance of the central barrel detectors. Moreover, also a cut on the rapidity in the centre of mass system (CMS) is applied. Since the p–Pb system is asymmetric, the rapidity values in the CMS and in the laboratory systems do not coincide. Hence, each track in the laboratory system is transformed into the CMS by applying the following relation:

$$y_{\mathrm{CMS}} = y_{\mathrm{lab}} - 0.465. \tag{4.1}$$

Then, only the tracks with $-1 < y_{\mathrm{CMS}} < 0$ are selected. To ensure a good quality of the reconstructed tracks, a series of cuts on the number of clusters in both the ITS and TPC are applied. In particular, $\mathrm{n_{ITScluster}}$ indicates the number of ITS layers in which the particle has given a signal, $\mathrm{n_{TPCdE/dxClusters}}$ is equal to the number of TPC clusters that gives an information on the specific energy loss, $\mathrm{n_{TPCCrossedRows}}$ is the number of pad rows that the track passes along its path (usually higher with respect to the previous quantity, since not all the pads hit give the specific energy loss information), and $\mathrm{n_{TPCFindClust}}$ is equal to the number of findable cluster, defined as a pad row in which, based on the geometry of the track, a cluster can be found. Additional cuts on the reduced χ^2 obtained in the track reconstruction process in both the ITS and TPC detectors, as illustrated in Sect. 3.5, are applied. To select the primary tracks a cut on both the longitudinal and transverse coordinate of the Distance of Closest Approach (DCA)[1] is applied. In each event, all the tracks are then classified into the three azimuthal regions reported in Fig. 2.13, in order to be further analysed.

4.2 Particle identification and signal extraction

4.2.1 ITS recalibration maps

For the antiproton signal extraction in the TPC described in Sect. 4.2.2, a preselection on the $n\sigma_{\mathrm{ITS}}$ is applied, in order to ensure a purer signal. However, in both the data and Monte Carlo simulations, these distributions are not centered around zero and their width deviates from the unity in all the p_{T} intervals. In order to correct such distributions, and hence perform a correct preselection, an offline (p, η) two dimensional calibration of the ITS is performed. To do so, a high-purity data sample of antiprotons is selected with the following requirements:

- $0.3~\mathrm{GeV}/c < p < 1.0~\mathrm{GeV}/c$
- $|\eta| < 0.8$
- if $p_{\mathrm{T}} < 0.7~\mathrm{GeV}/c$: $|n\sigma_{\mathrm{ITS}}| < 3$
- if $p_{\mathrm{T}} > 0.7~\mathrm{GeV}/c$: $|n\sigma_{\mathrm{TPC}}| < 2$ and $|n\sigma_{\mathrm{TOF}}| < 2$

For each momentum and pseudorapidity interval, the $n\sigma_{\mathrm{ITS}}$ distribution is fitted with a Gaussian with an exponential tail function, that has the

---

[1] The DCA is defined as the minimum distance between the track and the primary vertex, and can be considered in the transverse plane ($\mathrm{DCA_{xy}}$) and in the longitudinal direction ($\mathrm{DCA_z}$)

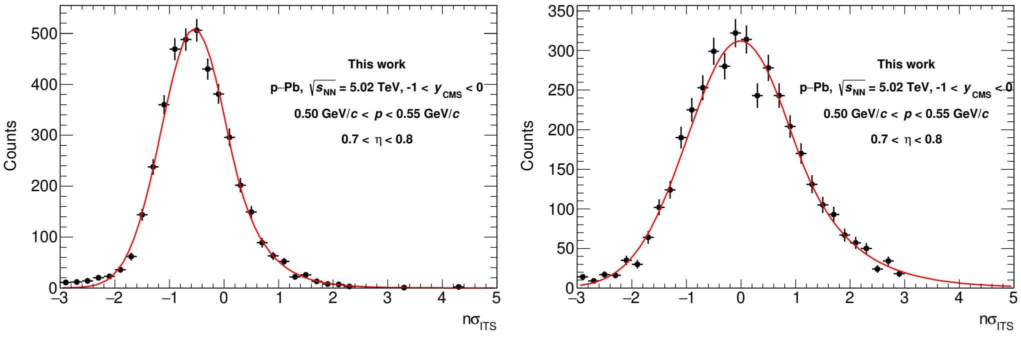

Figure 4.1: $n\sigma_{\mathrm{ITS}}$ distributions of antiprotons candidates before (left) and after (right) the ITS recalibration procedure for the experimental data. The red line represents the fit.

functional form:

$$f_{\mathrm{signal}}(n\sigma_{\mathrm{ITS}}) = \begin{cases} \mathrm{A}\exp\left(-\frac{1}{2}\left(\frac{n\sigma_{\mathrm{ITS}}-\mu}{\sigma}\right)^2\right) & \text{for } n\sigma_{\mathrm{ITS}} < \mu+\tau\sigma \\ \mathrm{A}\exp\left(-\left(\frac{n\sigma_{\mathrm{ITS}}-\mu}{\sigma}-\frac{\tau}{2}\right)\tau\right) & \text{for } n\sigma_{\mathrm{ITS}} \geq \mu+\tau\sigma \end{cases} \tag{4.2}$$

where A is a normalization factor, μ is the mean value of the distribution, σ its width and τ indicates after how many multiples of $n\sigma$ the exponential tail is considered. The values extracted from the fit are then used to correct the default values of $n\sigma$ by applying the following shift:

$$n\sigma_{\mathrm{corrected}} = \frac{n\sigma_{\mathrm{default}}-\mu}{\sigma}. \tag{4.3}$$

Fig. 4.1 shows the $n\sigma_{\mathrm{ITS}}$ distributions before (left) and after (right) the recalibration procedure for the data in one of the interested (p, η) interval, while Fig. 4.2 shows the same quantity for the MC production used in the analysis. Figs. 4.3- 4.4 show the recalibration maps for mean and width in the case of the experimental data, and in Figs. 4.5- 4.6 the same quantities for the MC production are reported.

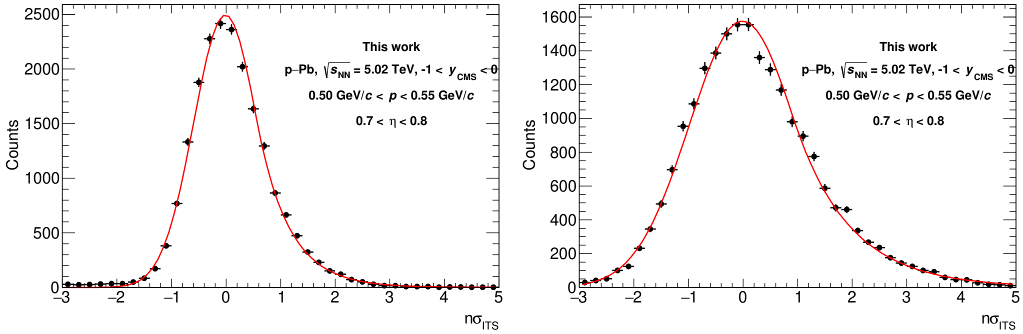

Figure 4.2: $n\sigma_{\text{ITS}}$ distributions of antiprotons candidates before (left) and after (right) the ITS recalibration procedure for the Monte Carlo production. The red line represents the fit.

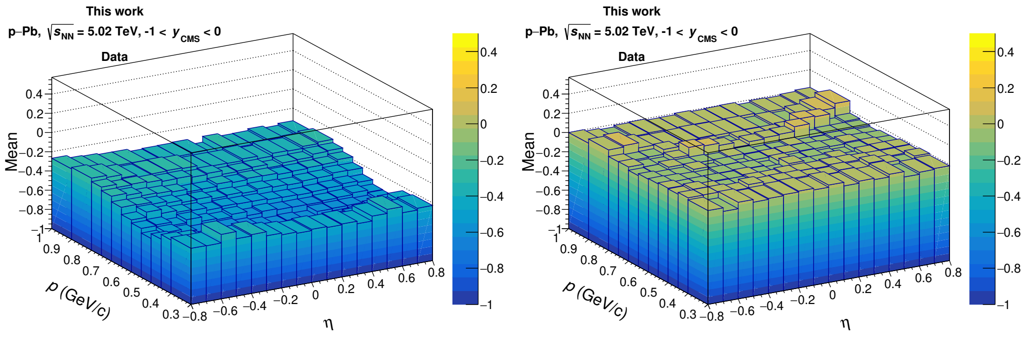

Figure 4.3: Two dimensional recalibration map of the mean extracted in the fit procedure of antiprotons candidates before (left) and after (right) the ITS recalibration procedure for the experimental data.

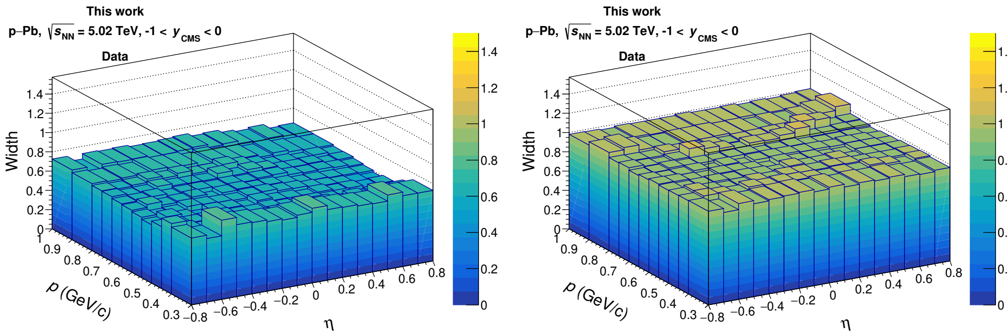

Figure 4.4: Two dimensional recalibration map of the width extracted in the fit procedure of antiprotons candidates before (left) and after (right) the ITS recalibration procedure for the experimental data.

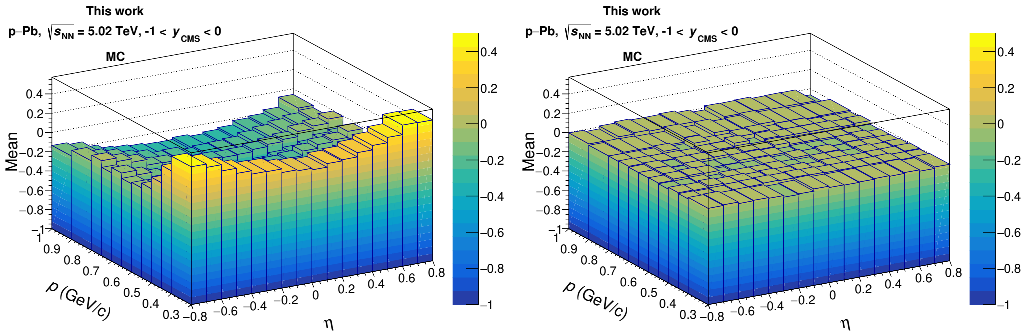

Figure 4.5: Two dimensional recalibration map of the mean extracted in the fit procedure of antiprotons candidates before (left) and after (right) the ITS recalibration procedure for the Monte Carlo production.

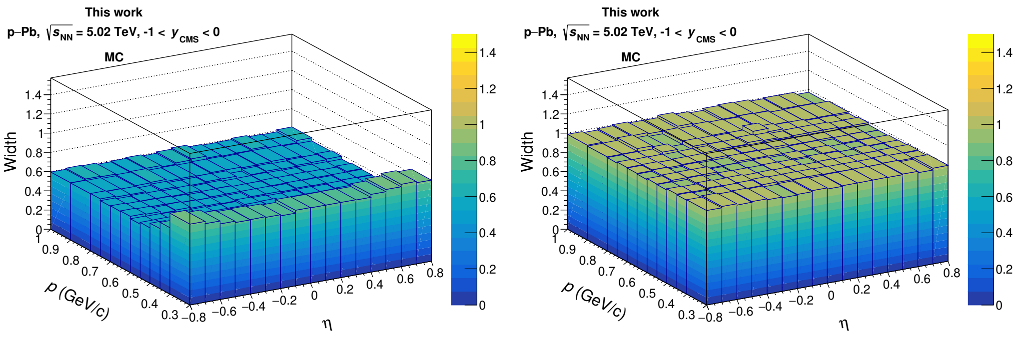

Figure 4.6: Two dimensional recalibration map of the width extracted in the fit procedure of antiprotons candidates before (left) and after (right) the ITS recalibration procedure for the Monte Carlo production.

4.2.2 Signal extraction with the TPC

(Anti)deuteron signal extraction

For the (anti)deuteron, up to $p_{\mathrm{T}} = 1.2$ GeV/c the identification is possible using only the TPC information. Fig. 4.7 shows the $n\sigma_{\mathrm{TPC}}$ distributions for deuterons (left) and antideuterons (right) in the three p_{T} intervals used in the analysis for the Toward region, while the results in the Away and Transverse regions are reported in Appendix A. In the last p_{T} interval the distributions show a contamination on the left due to wrongly identified (anti)protons: their contribution is fitted with a Gaussian function and subtracted. The $n\sigma_{\mathrm{TPC}}$ distributions are very clean, hence it is possible to perform the signal extraction integrating the distributions in the interval $|n\sigma_{\mathrm{TPC}}| < 3$.

Antiproton signal extraction

Also for antiprotons the signal extraction in the low momentum range, in particular in the interval (0.3, 0.7) GeV/c, is performed with the TPC signal. In order to obtain a distribution without background, the antiprotons candidates in the TPC are searched among the particles that satisfy the condition $|n\sigma_{\mathrm{ITS,recalib}}| < 3$. The signal extraction is performed in the same way of the one already described for the (anti)deuteron, integrating the

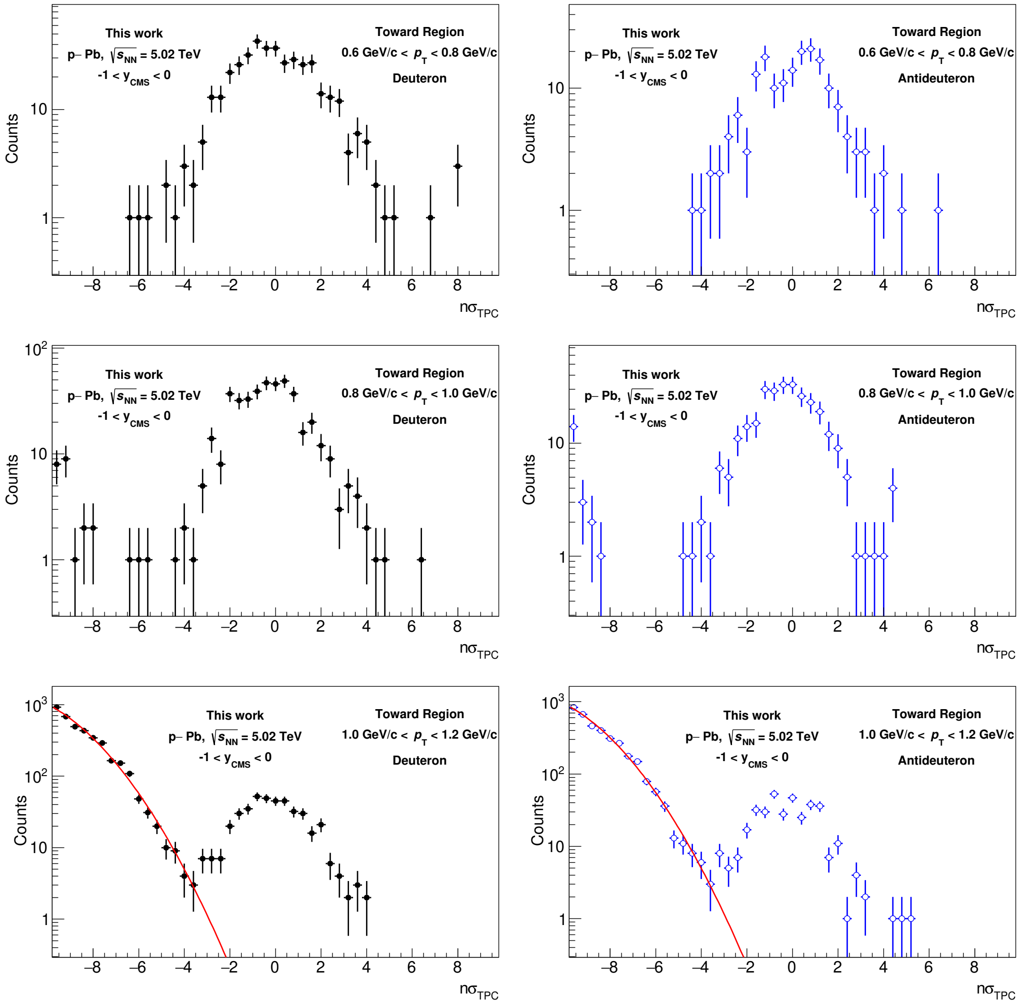

Figure 4.7: $n\sigma_{\mathrm{TPC}}$ distributions for the deuteron (left) and antideuteron (right) candidates in different p_{T} intervals in the Toward region. The red line in the last row represents the Gaussian fit for the contamination of (anti)protons.

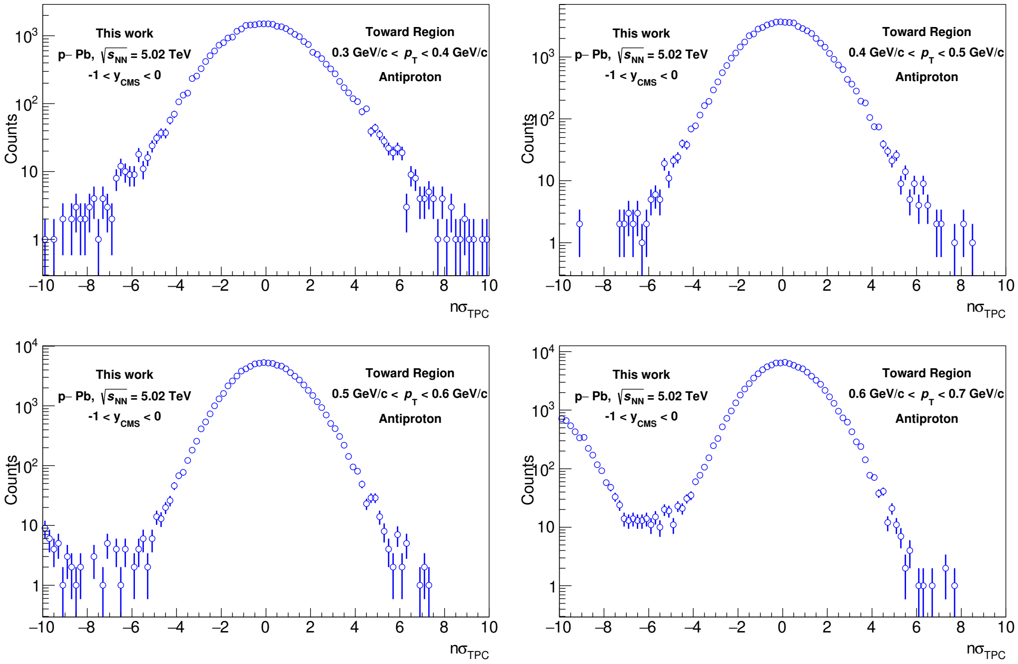

Figure 4.8: $n\sigma_{\mathrm{TPC}}$ distribution for antiprotons candidate in different p_{T} intervals in the Toward region.

distribution in the $|n\sigma_{\mathrm{TPC}}| < 3$. Fig. 4.8 shows the $n\sigma_{\mathrm{TPC}}$ distributions in the interested p_{T} interval in the Toward region, while the same distributions in the Away and Transverse regions are reported in Appendix A.

4.2.3 Signal extraction with the TOF

(Anti)deuteron signal extraction

For the signal extraction at higher transverse momentum, the information from the TOF detector is employed. In order to reduce the background due to wrongly identified particles, a preselection of $|n\sigma_{\mathrm{TPC}}| < 3$ is applied. The $n\sigma_{\mathrm{TOF}}$ distributions in the Toward region for deuteron (left) and antideuteron (right) candidates are reported in Fig. 4.9, while the same quantities in the Away and Transverse regions are reported in Appendix A. In these distributions a significant background due to mismatched tracks

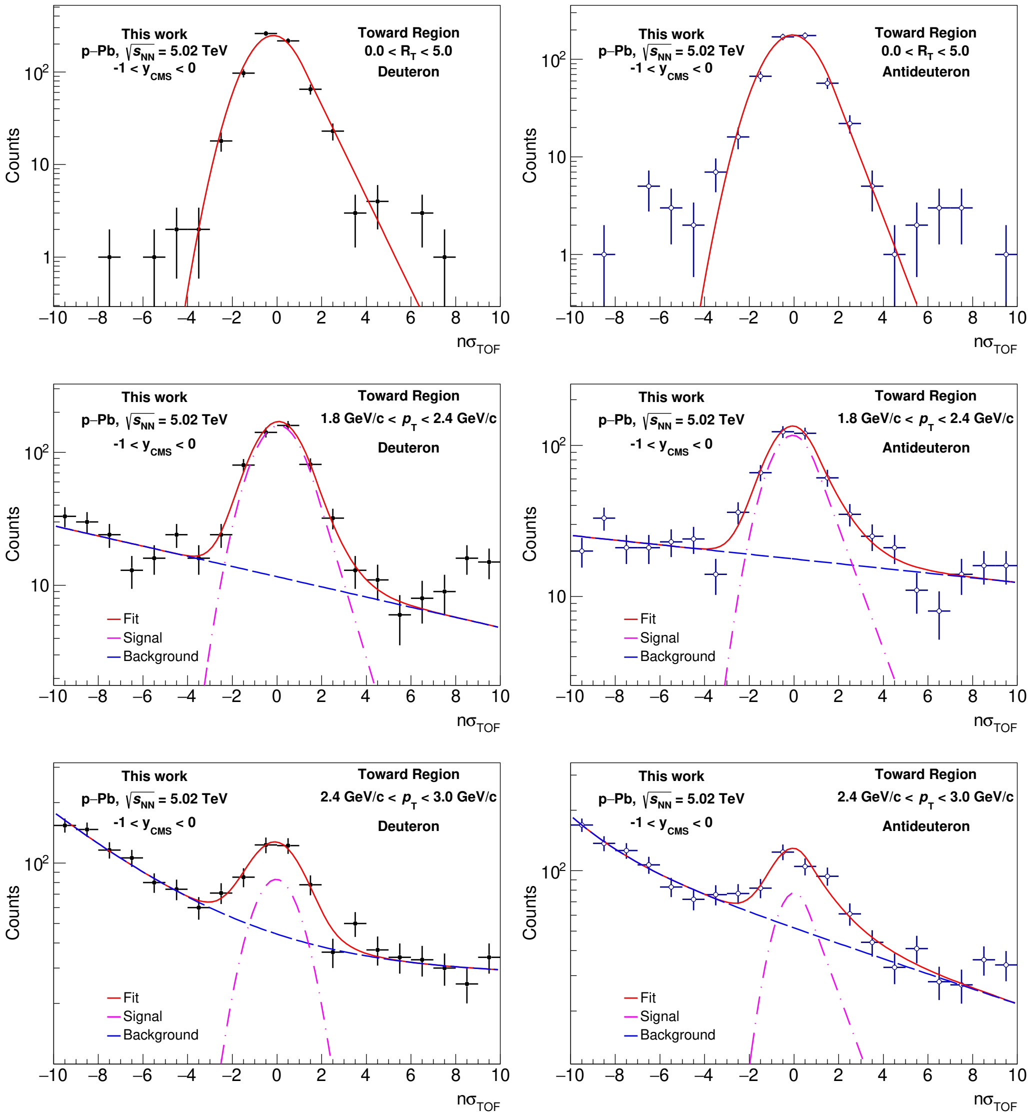

Figure 4.9: $n\sigma_{\mathrm{TOF}}$ distributions for deuterons (left) and antideuterons (right) in the whole p_{T} interval analysed in the Toward region. The red line represents the total fit, the magenta line the signal and the blue line the background parametrization.

is present. For this reason, the signal is fitted with a Gaussian function with an exponential tail:

$$f_{\mathrm{signal}}(n\sigma_{\mathrm{TOF}}) = \begin{cases} \mathrm{A}\exp\left(-\frac{1}{2}\left(\frac{n\sigma_{\mathrm{TOF}}-\mu}{\sigma}\right)^2\right) & \text{for } n\sigma_{\mathrm{TOF}} < \mu+\tau\sigma \\ \mathrm{A}\exp\left(-\left(\frac{n\sigma_{\mathrm{TOF}}-\mu}{\sigma}-\frac{\tau}{2}\right)\tau\right) & \text{for } n\sigma_{\mathrm{TOF}} \geq \mu+\tau\sigma \end{cases} \tag{4.4}$$

with A, μ, σ and τ having the same meaning as the ones already described in Eq. 4.2. The background is parametrized as a single or double exponential function for, respectively, the second and third analysed intervals of transverse momentum. The functional forms for the backgrounds are:

$$f_{\mathrm{bkg}}(n\sigma_{\mathrm{TOF}}) = B\exp(C\cdot n\sigma_{\mathrm{TOF}}) \tag{4.5}$$

$$f_{\mathrm{bkg}}(n\sigma_{\mathrm{TOF}}) = B\exp(C\cdot n\sigma_{\mathrm{TOF}}) + D\exp(E\cdot n\sigma_{\mathrm{TOF}}) \tag{4.6}$$

where B, C, D, and E are the fit parameters. This background is then subtracted before the raw yield extraction. In particular, the distribution is integrated in the region (-3σ_{TOF} + x_0, 3.5σ_{TOF} + x_0), where x_0 and σ_{TOF} are, respectively, the mean and width of the Gaussian function resulting from the fit procedure for each p_{T} interval. The asymmetric integration region is chosen in order to take into account the exponential tail of the fit function, while the shift of the mean value takes into account small miscalibration effects of the detector.

Antiproton signal extraction

Also in the case of the antiproton, at higher transverse momenta the signal extraction is performed using the TOF detector. To ensure a background minimization, only tracks that satisfy the condition $|n\sigma_{\mathrm{TPC}}| < 3$ are selected. The $n\sigma_{\mathrm{TOF}}$ distributions in the Toward region are reported in Fig. 4.10, while the ones in the Away and Transverse regions are shown in Appendix A. As described for the (anti)deuteron case, the signal is fitted with a Gaussian function with an exponential tail, but the background parametrization due to mismatched tracks assumes a different functional form. In this case, in fact, the background is described by a quadratic

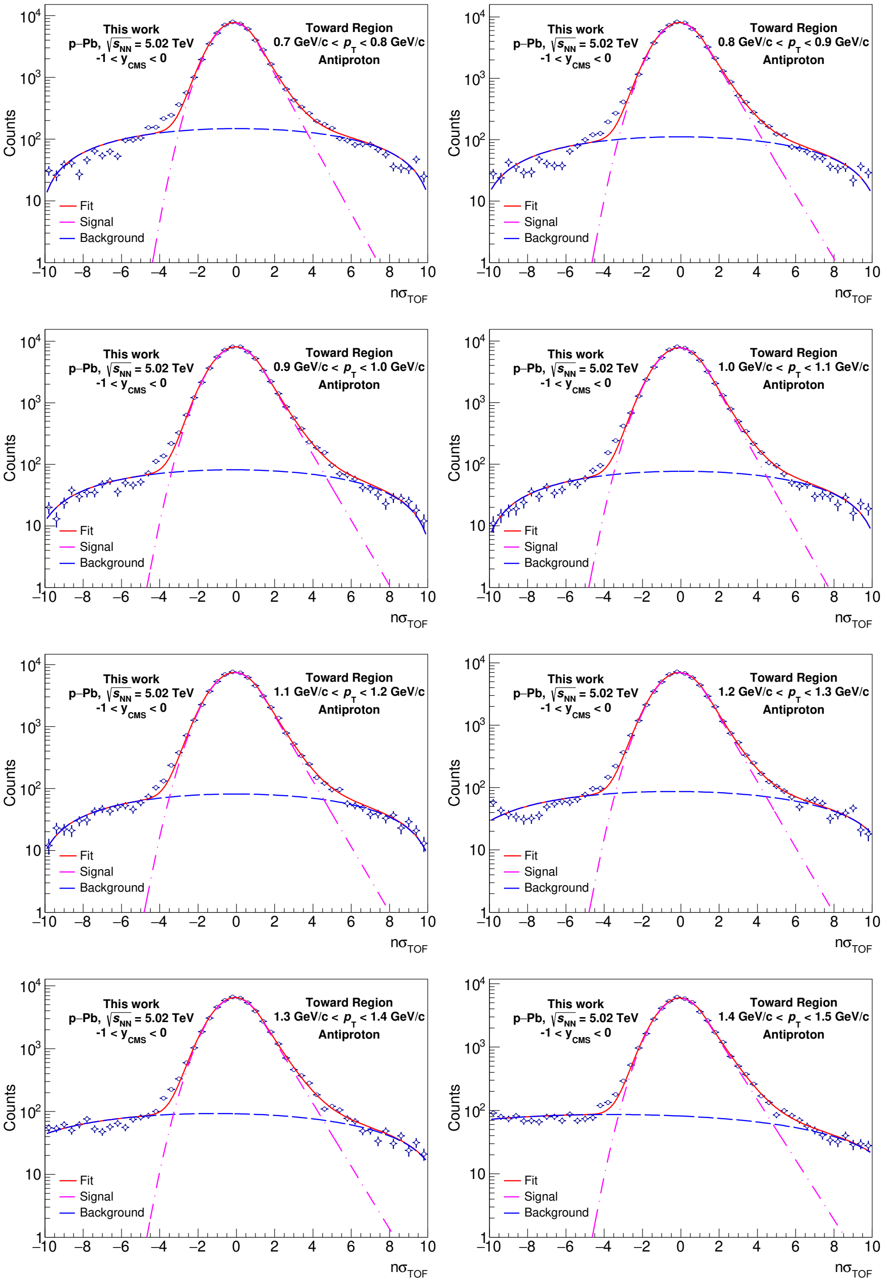

Figure 4.10: $n\sigma_{TOF}$ distributions for antiprotons in the whole p_T interval analysed in the Toward region. The red line represents the total fit, the magenta line the signal and the blue line the background parametrization.

function with the concavity downward:

$$f_{\text{bkg}}(n\sigma_{\text{TOF}}) = B + C \cdot n\sigma_{\text{TOF}} + D(n\sigma_{\text{TOF}})^2 \tag{4.7}$$

The downward concavity is guaranteed imposing the $D < 0$ condition. As already reported in the (anti)deuteron case, the raw yield is obtained integrating the distributions, after the background subtraction, in the interval (-3σ_{TOF} + x_0, 3.5σ_{TOF} + x_0).

4.2.4 Raw yield

Combining the results of the signal extraction performed using the information of the two detectors, as described in Sects. 4.2.2- 4.2.3, it is possible to obtain the raw yield for (anti)deuteron and antiproton. Such quantities are reported for the Toward region in Fig 4.11, while for the Away and Transverse regions the results can be found in Appendix A.

4.3 Corrections to raw spectra

The spectra reported in Fig. 4.11 do not reflect the primary particles produced in the collisions. In fact, two different phenomena modify these distributions: not all the particles produced in the collision are detected, and not all the particles detected are primary ones. In order to address the effect of these phenomena, the Acceptance×Efficiency ($A \times \epsilon$) and the secondary contamination must be evaluated. The methods used for the computation of these corrections are reported in the following sections.

4.3.1 Acceptance and efficiency correction

In general, in every experiment, not all the particles that are produced are detected, due to different causes: detector design and capabilities, trigger and reconstruction inefficiency, etc. In particular, in the case of this analysis, the two major contributions of not detected particles are the not-fully efficient tracking algorithms, and the not hermetic design of the ALICE subdetectors employed in the PID procedure. Hence, the correction for acceptance and efficiency must be evaluated.

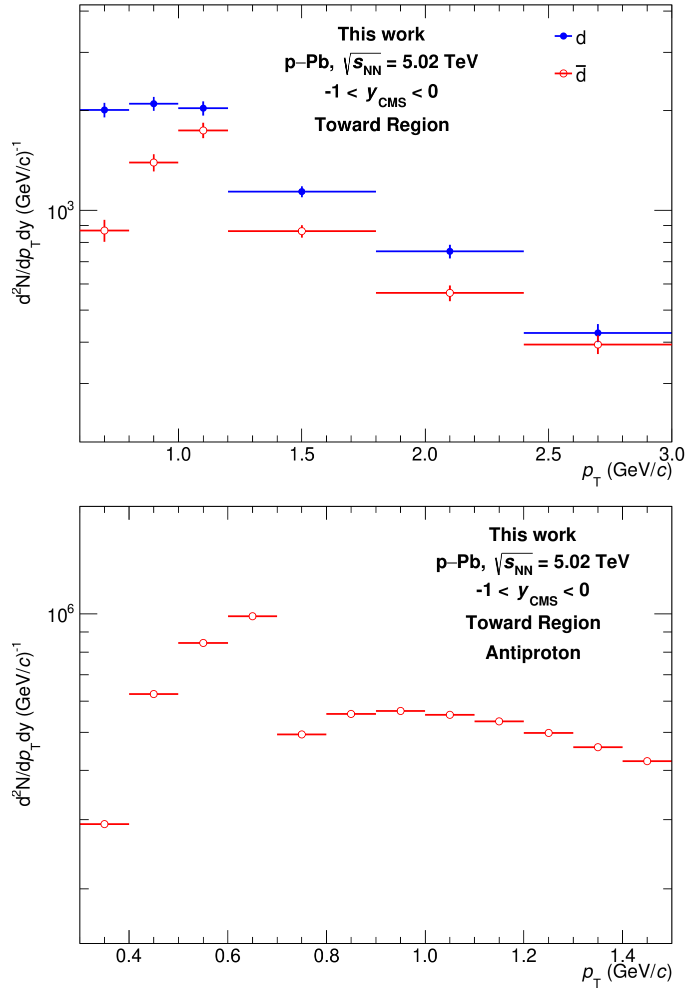

Figure 4.11: Raw spectra for (anti)deuterons (top) and antiprotons (bottom) in the Toward region.

From the experimental point of view, it is impossible to know *a priori* the number of produced particles, and then quantify how many are lost: for this reason, the Acceptance×Efficiency correction is evaluated using Monte Carlo simulations. In this case, in fact, exploiting the so-called *Monte Carlo truth*, it is possible to know the fraction of generated particles that are correctly identified. In particular, in order to evaluate the $A \times \epsilon$ correction, two different MC simulations are used:

- for the (anti)deuteron, a simulation with the HIJING [193] generator and injected (anti)nuclei is considered. This choice is taken since, if a simulation without injected (anti)nuclei is used, a large number of events are needed in order to have a good precision on the (anti)nuclei measurements, due to their rare production. The simulation consists of 250 thousands events, and for each event 10 (anti)deuteron are injected with flat distribution in p_{T}, in the interval (0.0, 8.0) GeV/c, in rapidity (y), in the interval (-1.0, 1.0), and in ϕ angle, in the interval (0, 2π).
- for the antiproton, a simulation based on the DPMJET [194] generator is used. In this case, the simulation counts about 40 million of events.

The generated particles are propagated in the volume of detector employing the GEANT4 package, and are then detected and identified in the TPC and TOF detectors. In the simulation, the same quality cuts reported in Tab. 4.1 are applied to the reconstructed tracks. Then, the reconstructred (anti)deuterons and antiprotons are identified both in the TPC and TOF detectors, and the signal is extracted in the same intervals reported in Sect. 4.2. The Acceptance×Efficiency correction is then defined as the ratio between the reconstructed and generated particles in the rapidity and pseudorapidity regions of interest:

$$A \times \epsilon = \frac{N_{\mathrm{rec},|y|<0.5,|\eta|<0.8}}{N_{\mathrm{gen},|y|<0.5}}. \tag{4.8}$$

The generated and reconstructed transverse momentum distributions are built using narrow p_{T} intervals, different to the ones used in this analysis. In order to obtain the correction to be applied to the experimental distributions, a weighted mean with a Lévy-Tsallis function is performed.

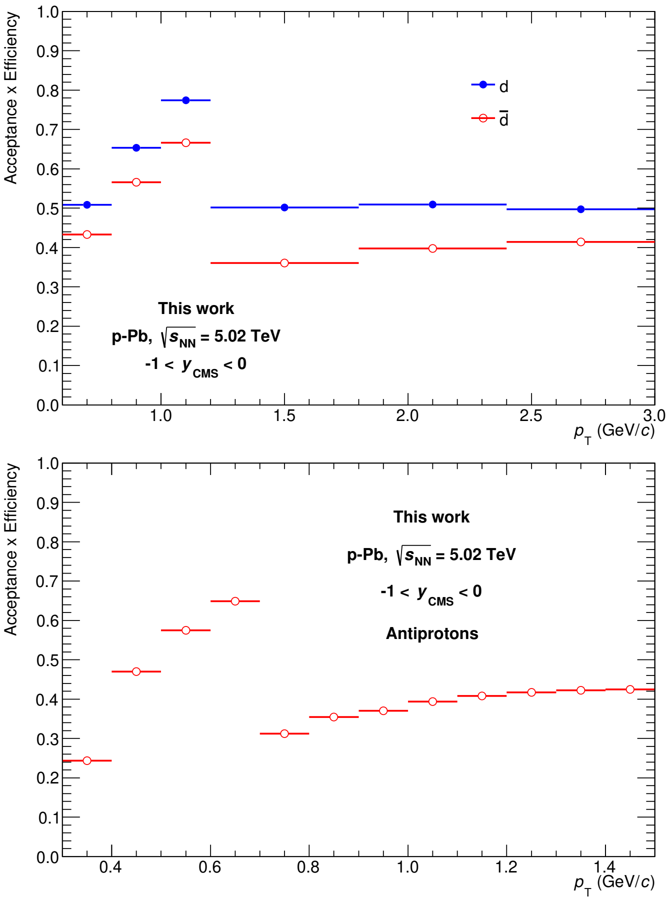

Figure 4.12: Acceptance×Efficiency correction for (anti)deuterons (top) and antiprotons (bottom) as a function of the transverse momentum p_T.

This function is chosen since it describe the transverse momentum distributions for both the (anti)deuteron and the antiproton, as described later in Sect. 5.1. For each of the experimental p_T interval, the weighted mean of the corresponding narrow intervals are considered, with the weight equal to the value of the Lévy-Tsallis function in the interval centre. Fig. 4.12 shows the Acceptance×Efficiency correction for both the (anti)deuterons and antiprotons. The efficiency for the antideuterons is lower compared to the one for the deuterons: this is due to different annihilation processes with the detector material, that differ for the matter and antimatter counterpart. Moreover, the abrupt change at p_{T} = 1.2 GeV/c for the (anti)deuterons and p_{T} = 0.7 GeV/c for the antiprotons is due to the different strategy used for the signal extraction. In fact, at lower p_{T} only the TPC information is used, while at higher p_{T} the additional information from the TOF is required. This means that at higher p_{T} the particles encounter more material up until they are detected, that leads to a reduced efficiency, since the interaction processes with the material have a higher probability.

4.3.2 Secondary particles

High energy nuclear collisions are complex events. In general, in addition to the primary particles produced in the collisions, other phenomena occur, that lead to the formation of *secondary particles*. In this analysis, it is possible to find two different sources of secondary particles: nuclei from spallation processes for the deuteron and feed-down contribution for the antiproton.

In general, to discriminate the primary from the secondary particles, the distributions of the DCA is employed. Primary particles are characterized by a small DCA, with a distribution peaked at zero, since the tracks of such particles point to the primary vertex. Secondary particles, instead show a wider DCA distribution, since they do not originate from the primary vertex. In order to identify correctly the secondary fraction, Monte Carlo simulations are used, since from an experimental point of view it is impossible to know for sure if the detected particle is a primary or a secondary one. In this case, for both the deuteron and antiproton case, the same simulation used to compute the antiproton efficiency is employed.

Deuterons from spallation processes

If a primary particle interacts with the detector material some nuclear fragments, called *spallation products*, can be formed. These secondary particles are then identified, but they should be excluded. It is important to notice that, due to the fact that the antimatter hardly interact with the detector material, and no antimatter is produced in the matter - detector material interactions, the secondary correction for spallation processes is only applied to matter particles. Hence, in this case, only the contribution for deuterons is studied.

In order to evaluate the secondary fraction the so-called *template method* is used, studying the $\mathrm{DCA_{xy}}$ distributions. This method employs MC simulations in order to reproduce the DCA distributions of both primary and secondary particles. These distributions are then used as template to fit the experimental distributions, in order to normalize and extract the primary fraction. To be able to fit the primary and secondary fractions from the experimental $\mathrm{DCA_{xy}}$ distribution, the preselection reported in Tab.4.1 for such quantity is revoked. In order to obtain the best results on the fit procedure, a clean sample of deuterons is selected, with the requisites:

- if $p_{\mathrm{T}} < 1.0$ GeV/c: $|n\sigma_{\mathrm{TPC}}| < 3$
- if $p_{\mathrm{T}} > 1.0$ GeV/c: $|n\sigma_{\mathrm{TPC}}| < 3$ and $|n\sigma_{\mathrm{TOF}}| < 3$

Then, the experimental data is fitted with two distributions that describe the primary and the secondary particles from material, in order to obtain the percentage of each contribution. In particular, for the primary particles the antideuteron data are used, since this distribution is not affected by the secondary contamination, while for the secondary fraction the distribution from the MC simulation is used. Then, these fractions are fitted to the data in the interval $|\mathrm{DCA_{xy}}| < 1.0$ cm: in this way the contribution from the spallation products is constrained by the plateaux of the $\mathrm{DCA_{xy}}$ at a larger distance, where the secondary contribution is dominant. These templates are evaluated in the whole p_{T} interval of the analysis: an example considering one of the transverse momentum interval is reported in Fig. 4.13. After the fit, the secondary fraction is calculated as:

$$s = \frac{\mathrm{integral\,DCA_{xy}}\,(-0.1, 0.1)\ \mathrm{secondary\ template}}{\mathrm{integral\,DCA_{xy}}\,(-0.1, 0.1)\ \mathrm{data}} \tag{4.9}$$

In this type of analysis, instead of talking in terms of secondary fraction, the primary fraction is commonly used, since only the primary particles produced in the collision are the interest of our study. Hence, the primary

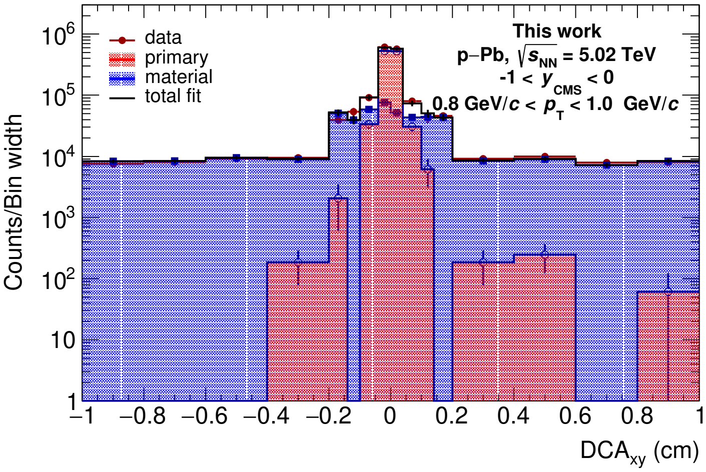

Figure 4.13: DCA$_{xy}$ distribution for deuterons extracted using the template method.

fraction f can be calculated as:

$$f = 1 - s = 1 - \frac{\text{integral}\,\text{DCA}_{\text{xy}}\,(-0.1, 0.1)\,\text{secondary template}}{\text{integral}\,\text{DCA}_{\text{xy}}\,(-0.1, 0.1)\,\text{data}} \tag{4.10}$$

The primary fraction of deuteron as a function of the transverse momentum p_T is reported in Fig. 4.14. The primary fraction is small at low p_T, meaning that the secondary contribution is relevant in such region. At high transverse momentum, instead, the primary fraction is set to unity since the secondary contribution is negligible.

Feed-down antiprotons

In the case of antiprotons the secondary contamination does not arise from spallation processes, since we are considering antimatter, but from feed-down contributions linked to weak decays. In fact, heavier particles like Λ and Σ can decay in the volume of the detector, and one of the daughters of this decay is the antiproton, with a branching ratio of, respectively, 64% and 51%. The approach carried out for the estimation of the primary fraction is similar to the one already described for the deuteron. For the

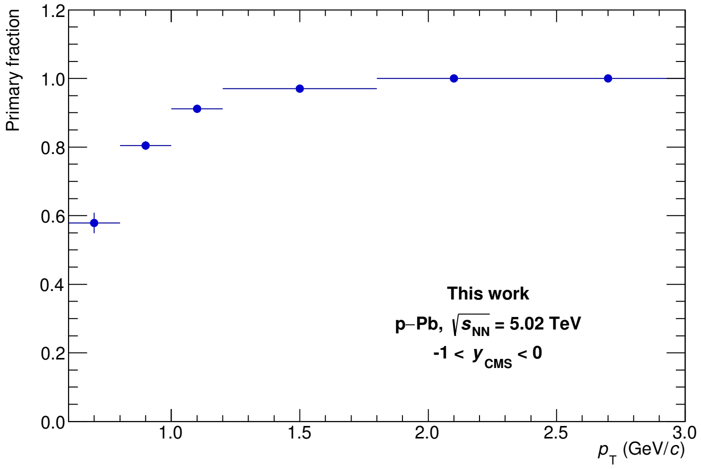

Figure 4.14: Deuteron primary fraction as a function of the transverse momentum.

data to be fitted, a high-purity data sample of antiprotons is obtained by applying the following requirements:

- if $p_T < 0.7$ GeV/c: $|n\sigma_{\mathrm{ITS,recalib}}| < 3$ and $|n\sigma_{\mathrm{TPC}}| < 3$
- if $p_T > 0.7$ GeV/c: $|n\sigma_{\mathrm{TPC}}| < 2$ and $|n\sigma_{\mathrm{TOF}}| < 2$

The templates for both the primary and the secondary particles are taken from Monte Carlo simulations. An example of such distributions obtained for a specific p_T interval is reported in Fig. 4.15. The primary fraction for antiprotons, reported in Fig. 4.16, is obtained through the Eq. 4.10.

4.4 Systematic uncertainties

To complete the analysis, a study of the systematic uncertainties that affect the results is performed. The sources of systematic uncertainties, for both (anti)deuterons and antiprotons, can be divided into six different categories, in particular:

- Tracking cuts
- ITS-TPC matching efficiency

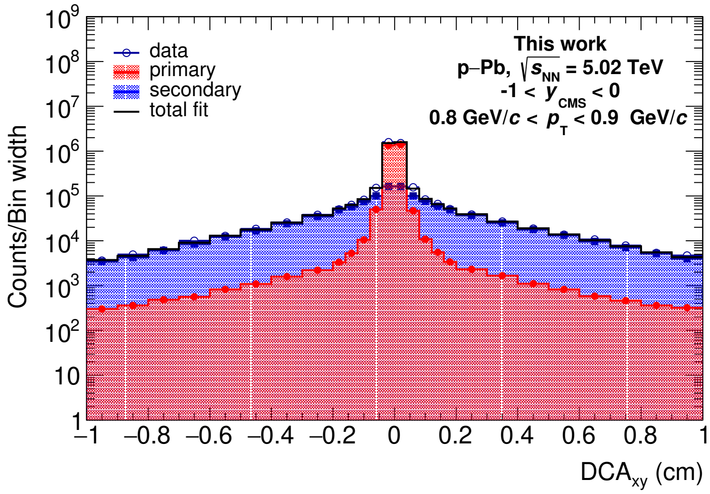

Figure 4.15: DCA_{xy} distribution for antiprotons extracted using the template method.

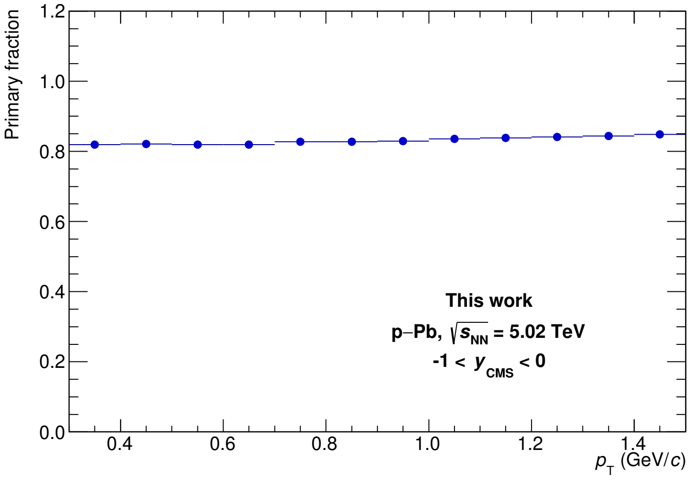

Figure 4.16: Antiproton primary fraction as a function of the transverse momentum.

Particle		**d ($\overline{\mathbf{d}}$)**		**$\overline{\mathbf{p}}$**	
p_T range (GeV/c)		**0.6 - 0.8**	**2.4 - 3.0**	**0.3 - 0.4**	**1.4 - 1.5**
Source of uncertainty					
Tracking		0.3 (1.5)	0.5 (0.9)	0.7	2.4
ITS-TPC matching		1.0 (1.0)	1.0 (1.0)	1.0	1.0
Material budget		1.0 (1.0)	1.0 (1.0)	1.0	1.0
Hadronic interaction		0.4 (3.0)	0.7 (4.0)	0.3	1.4
Primary fraction		5.0 (-)	negl. (-)	1.0	1.1
Signal extraction	Toward	1.4 (1.0)	1.8 (2.6)	0.7	0.5
	Transverse	1.4 (1.9)	3.7 (2.8)	0.6	0.5
	Away	2.1 (1.5)	2.8 (2.1)	0.7	0.6

Table 4.2: Summary of the different contributions of the systematic uncertainties, both for (anti)deuterons and antiprotons, in the lowest and highest p_T intervals. All values are given in percent.

- Material budget
- Hadronic interaction
- Primary fraction
- Signal extraction

The details on the estimation of each single source, with the difference for the two particle species, are discussed in the next sections. The total systematic uncertainty is calculated as the sum in quadrature of each contribution. Tab. 4.2 shows a summary of the systematic uncertainty in the first and last transverse momentum interval, while Figs. 4.17-4.18 visually represent such uncertainties for, respectively, (anti)deuterons and antiprotons in the Toward region. The same results for the Away and Transverse regions are reported in Appendix A.

4.4.1 Tracking cuts

To estimate the tracking related systematic uncertainty, a multi variational approach is used. In fact, each selection cut reported in Tab. 4.1 has been

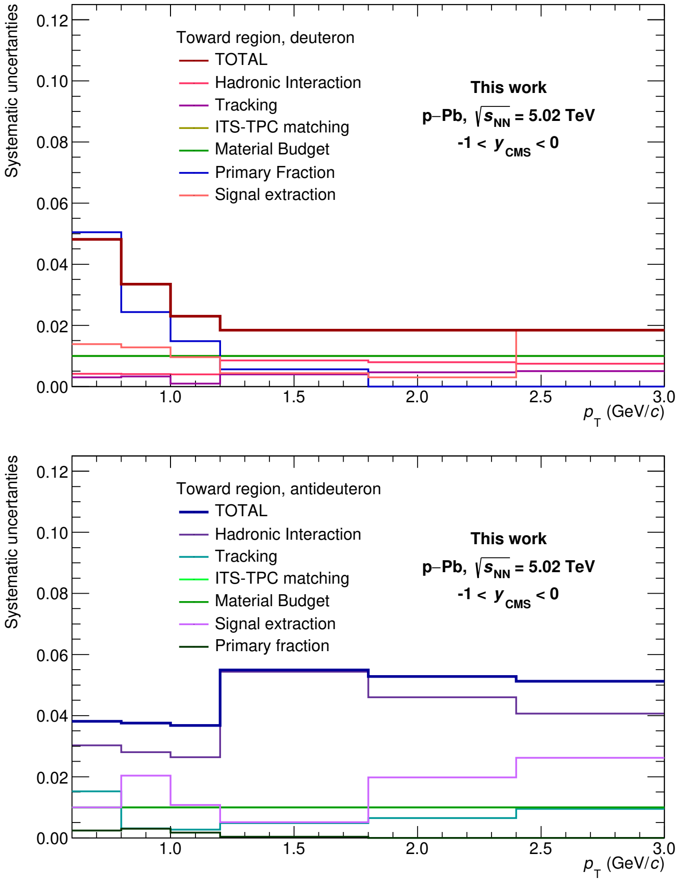

Figure 4.17: Summary of the different sources of systematic uncertainties for the deuteron (top) and antideuteron (bottom) case in the Toward region.

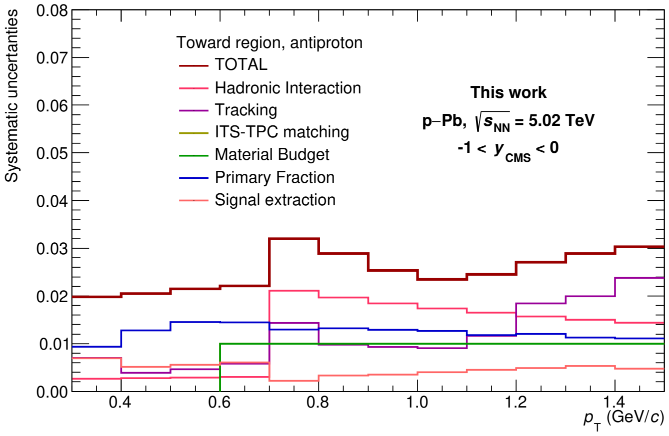

Figure 4.18: Summary of the different sources of systematic uncertainties for the antiprotons in the Toward region.

varied using a random uniform distribution around the nominal value. In particular, such variations are reported in Tab. 4.3, for the (anti)deuterons and in Tab. 4.4 for the antiprotons. The main difference between the (anti)deuterons and antiprotons case is that, for the (anti)deuterons, the contribution on the cuts on the DCA is taken into account in a separate part, in particular in Sect. 4.4.5. This choice is made because, at low transverse momentum, the contribution due to the DCA cuts for the deuteron is dominant with respect to the other cuts. Hence, to proper understand how the other tracking cuts affect the analysis, the DCA cuts are studied

Variable	Default value	Interval of uniform variation
$n_{\text{ITSClusters}}$	2	(2, 4)
$n_{\text{TPCdE/dxClusters}}$	50	(40, 60)
$n_{\text{TPCCrossedRows}}$	70	(60, 80)
$n_{\text{TPCCrossedRows}}/n_{\text{TPCFind.Clusters}}$	0.8	(0.6, 0.8)
TPC χ^2/NDF	4	(3, 5)
ITS χ^2/NDF	36	(30, 40)

Table 4.3: Summary of track selection variations applied for the evaluation of systematic uncertainty for the (anti)deuteron. Each variable is randomly extracted with a uniform distribution in the interval specified.

Variable	**Default value**	**Interval of uniform variation**
$n_{\mathrm{ITSClusters}}$	4	(3, 6)
$n_{\mathrm{TPCdE/dxClusters}}$	60	(50, 70)
$n_{\mathrm{TPCCrossedRows}}$	80	(70, 100)
$n_{\mathrm{TPCCrossedRows}}/n_{\mathrm{TPCFind.Clusters}}$	0.8	(0.7, 0.9)
TPC χ^2/NDF	4	(2, 5)
ITS χ^2/NDF	36	(36, 50)
$\mathrm{DCA_z}$	1.0 cm	(0.5, 1.4) cm
$\mathrm{DCA_{xy}}$	0.1 cm	(0.08, 0.1, 0.12, 0.14, 0.16) cm
$n\sigma_{\mathrm{ITS}}$ preselection cut for TPC PID	3	(2, 4)
$n\sigma_{\mathrm{TPC}}$ preselection cut for TOF PID	3	(2, 4)

Table 4.4: Summary of track selection variations applied for the evaluation of systematic uncertainty for the antiproton. Each variable is randomly extracted with a uniform distribution in the interval specified.

separately. The cuts are applied simultaneously, and the procedure is performed for 50 times. The same cuts are also applied to the reconstructed Monte Carlo particles, in order to obtain the correlated efficiency for each set of variation. Then, the analysis strategy is repeated: (anti)deuterons and antiprotons signal is extracted with the information from the TPC and TOF detectors, the raw yield is corrected for the corresponding efficiency and primary fraction. For each transverse momentum interval, a histogram with the corrected yield is filled. Then, the systematic uncertainty is estimated as the ratio between the width and the mean of such distributions. The obtained values as a function of the transverse momentum are reported in Fig. 4.19.

4.4.2 ITS-TPC matching efficiency

For the ITS-TPC matching efficiency contribution, several studies have been performed by the ALICE Data Preparation Group [195]. This contribution arises from the track quality cuts and the track propagation between the two detectors. For the p–Pb dataset, it has been estimated as a 1% contribution, with no dependence on the analysed p_{T} interval.

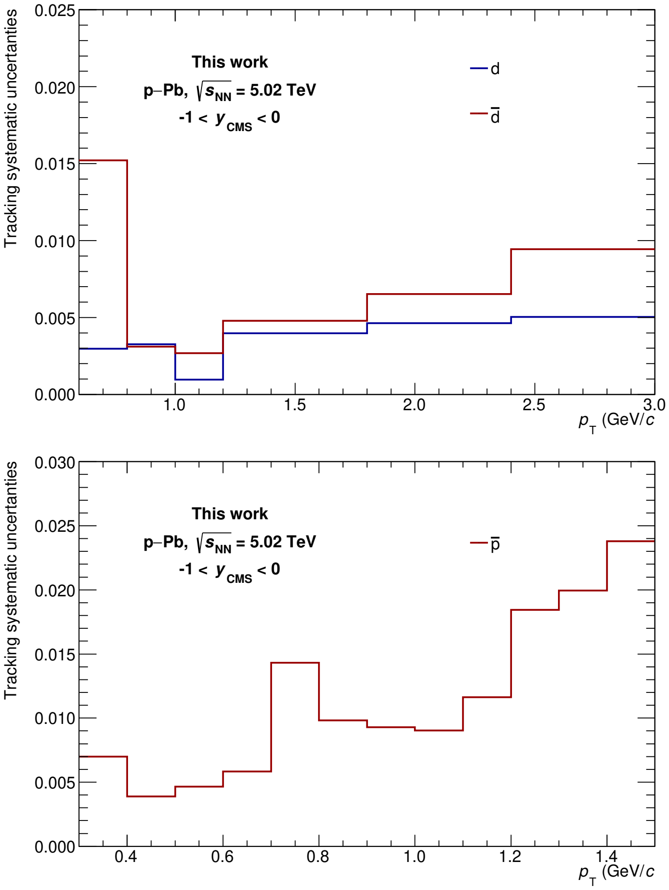

Figure 4.19: Systematic uncertainty due to tracking cuts for (anti)deuterons (top) and antiprotons (bottom) as a function of the transverse momentum.

Species	TPC	TOF
Deuterons	$0.00397 \cdot p_{\mathrm{T}}^{-0.09846}$	$0.00939 \cdot p_{\mathrm{T}}^{-0.23572}$
Antideuterons	$0.02717 \cdot p_{\mathrm{T}}^{-0.30436}$	$0.06654 \cdot p_{\mathrm{T}}^{-0.49699}$
Antiprotons	$0.00327 \cdot p_{\mathrm{T}}^{0.19716}$	$0.01788 \cdot p_{\mathrm{T}}^{-0.58252}$

Table 4.5: Functional form for the parametrization of the hadronic interaction systematic uncertainty.

4.4.3 Material budget

Another source of systematic uncertainty can be related to the incomplete knowledge of the material budget of the detector. Thanks to photon conversion measurements, the material budget is known with a uncertainty of 4.5% [36]. As described in Ref. [95], from where this source of uncertainty is inherited, the effect of the material budget is evaluated comparing different Monte Carlo simulations with a material budget variated by ± 4.5%. For both (anti)deuterons and antiprotons this contribution is found to be equal to 1% in the whole p_{T} interval considered in the analysis.

4.4.4 Hadronic interaction

It is also possible to estimate the contribution to the systematic uncertainty due to the non perfect knowledge of the hadronic interaction cross section of (anti)deuterons and antiprotons. The procedure to estimate this value is based on the variation of the default value of the inelastic cross section found in the GEANT4 package within its uncertainty. To obtain a more accurate estimation, all the values of the hadronic cross section, measured using different targets, are considered and a cumulative fit is performed. The value of this correction is p_{T} dependent, due to the fact that the particles are identified with different experimental apparatus, hence they traverse different materials and different hadronic processes may happen. In general, this result can be summarized in a parametric function for each species and detector. The functional forms of such parametrization are reported in Tab. 4.5. The obtained values are reported in Fig. 4.20 as a function of the transverse momentum.

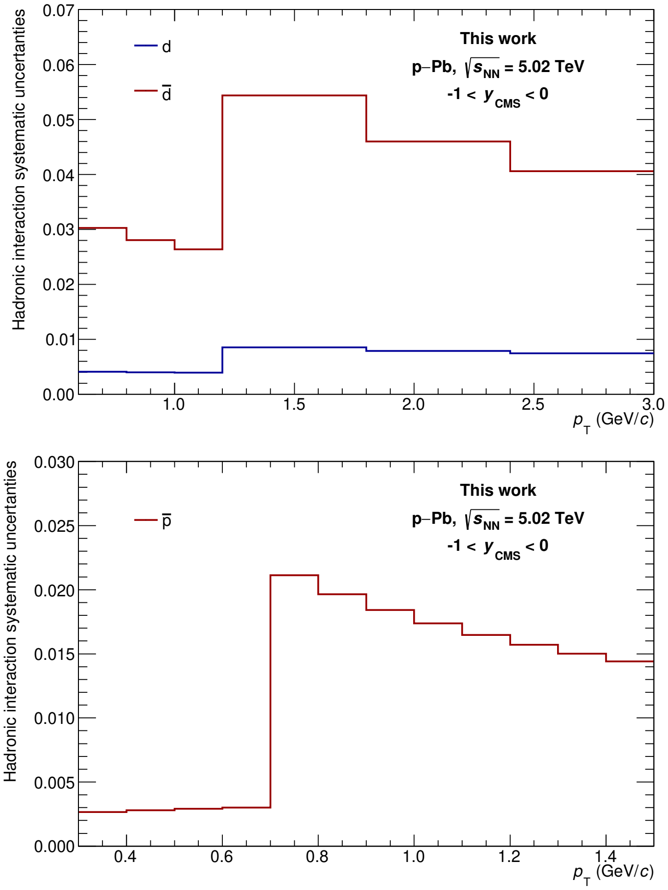

Figure 4.20: Systematic uncertainty due to the hadronic interaction for (anti)deuterons (top) and antiprotons (bottom) as a function on the transverse momentum p_{T}.

4.4.5 Primary fraction

The systematic uncertainty due to the primary fraction can be evaluated studying how this quantity varies as a function of different approaches used for its evaluation. In particular two different sources are explored for the antiprotons while, as already anticipated in Sect. 4.4.1, for the (anti)deuterons an additional source in considered. In particular, it is possible to group these contributions as:

- variation of interval width of $\mathrm{DCA_{xy}}$ distributions
- variation of fitting interval
- variation of DCA cuts (only for (anti)deuteron)

Moreover, it is worth to notice that, since the primary fraction evaluation for the (anti)deuteron study has been performed only for the deuteron, as already explained in Sect. 4.3.2, the first two contributions are related only to the deuteron case. The study of the DCA cuts, instead, are evaluated both for deuterons and antideuterons. The details of each contribution are reported below. The total value of the systematic uncertainty due to the primary fraction is equal to the sum in quadrature of each of these contributions. Fig. 4.21 shows the total contribution as a function of the transverse momentum for both (anti)deuterons and antiprotons.

Interval width variation

The fraction of primary particles can be influenced by the choice of the interval width of the $\mathrm{DCA_{xy}}$ distribution to be fitted. In general, wider intervals are used in the tails of the distribution, $|\mathrm{DCA_{xy}}| > 0.2$ cm, while for the central region of the distribution narrow intervals are used. This choice reflects the fact that, in the tails, only the secondary contribution is present, while in the central region both the primary and secondary particles are present, hence their distribution must be known with more accuracy. In order to take into account the influence of the choice of the interval's width used in Sect. 4.4.5, nine different variations of $\mathrm{DCA_{xy}}$ distributions with different intervals width are generated, using both wider and smaller intervals. Then, the primary fraction is evaluated as

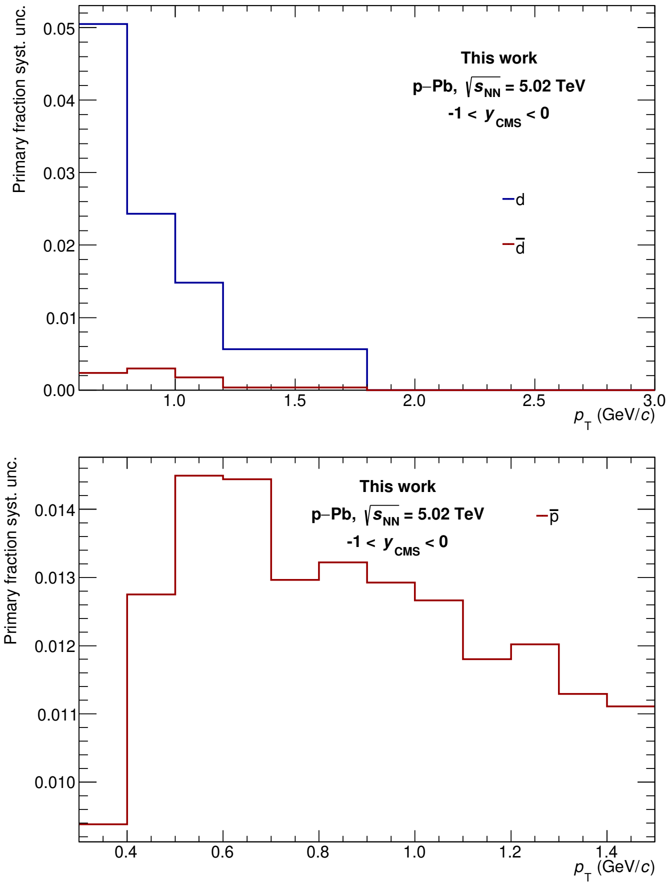

Figure 4.21: Total systematic uncertainty due to the primary fraction for (anti)deuterons (top) and antiprotons (bottom) as a function of the transverse momentum.

reported in Eq. 4.10 using the same fit interval of (-1.0, 1.0) cm. For each p_{T} interval, the half-difference between the lower and higher value is considered as systematic uncertainty. Fig. 4.22 shows the spread of the 9 different variations with respect to the default value for deuterons and antiprotons, while Fig. 4.23 shows the value of the obtained systematic uncertainty as a function of the transverse momentum.

Fitting interval variation

Another source that can vary the value of the primary fraction is the interval chosen to perform the fit procedure, hence considering wider or narrow tails to parametrize the secondary contribution. In the analysis, the $|\mathrm{DCA}_{\mathrm{xy}}| < 1.0$ cm interval is considered. In order to evaluate the influence of this choice to the obtained primary fraction value, 10 different variations have been carried out, varying the integration interval from $|\mathrm{DCA}_{\mathrm{xy}}| < 1.0$ cm to $|\mathrm{DCA}_{\mathrm{xy}}| < 0.5$ cm with a step of 0.05 cm. In this case, the interval width of the distribution is fixed to the default values. The systematic uncertainty is then calculated as the half-difference between the lower and higher value obtained. Fig. 4.24 shows the value of this source of systematic uncertainty as a function of the transverse momentum.

DCA cuts variation

The last contribution for the primary systematic uncertainty, evaluated for both deuteron and antideuteron, is due to the variation of the $\mathrm{DCA}_{\mathrm{xy}}$ and $\mathrm{DCA}_{\mathrm{z}}$ cuts in the particle selection. This source of uncertainty, strictly linked to the tracking cuts, has been already considered for antiprotons, as reported in Sect. 4.4.1. In order to estimate this contribution, a total of 25 variations of the cuts, arising from all the possible combinations of the values reported in Tab. 4.6, have been considered. All the other cuts are set to the standard values. For each of the 25 variations, the $n\sigma_{\mathrm{TPC}}$ and $n\sigma_{\mathrm{TOF}}$ distributions are studied, extracting the signal. Then, the raw yield is corrected for the corresponding efficiency and primary fraction, evaluated with Monte Carlo distributions with the same $\mathrm{DCA}_{\mathrm{xy}}$ and $\mathrm{DCA}_{\mathrm{z}}$ cuts reported in Tab. 4.6. For each p_{T} interval a histogram with the corrected yield is filled, and the systematic uncertainty is evaluated as the ratio of the width and the mean of the distribution. The obtained

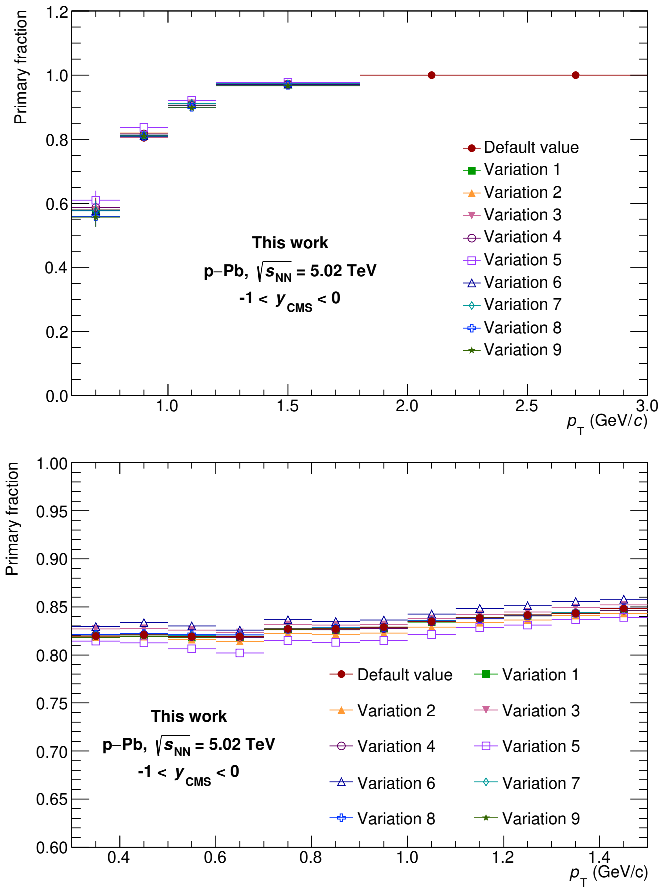

Figure 4.22: Spread of the primary fraction obtained with different interval's width of the DCA_{xy} distributions for deuterons (top) and antiprotons (bottom) compared with the default value, as a function of the transverse momentum.

DCA component	Standard value (cm)	Variations (cm)
DCA_{xy}	0.1	0.08, 0.1, 0.12, 0.14, 0.16
DCA_z	1.0	0.8, 1.0, 1.2, 1.4, 1.6

Table 4.6: List of DCA_{xy} and DCA_z cut variations used to study the systematic uncertainty.

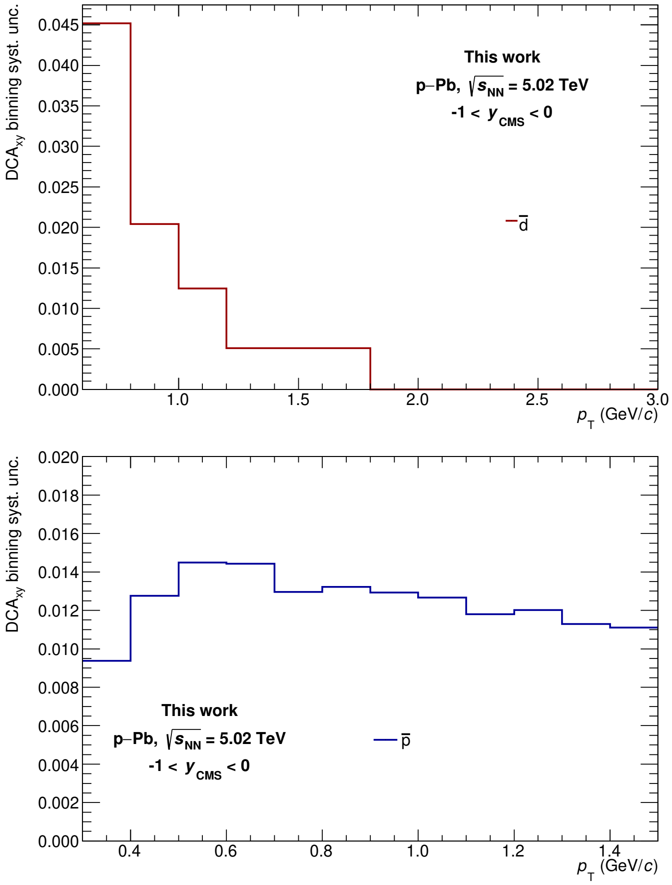

Figure 4.23: Systematic uncertainty due to the variation of the interval's width of the DCA$_{xy}$ distributions in the evaluation of the primary fraction for deuterons (top) and antiprotons (bottom) as a function of the transverse momentum.

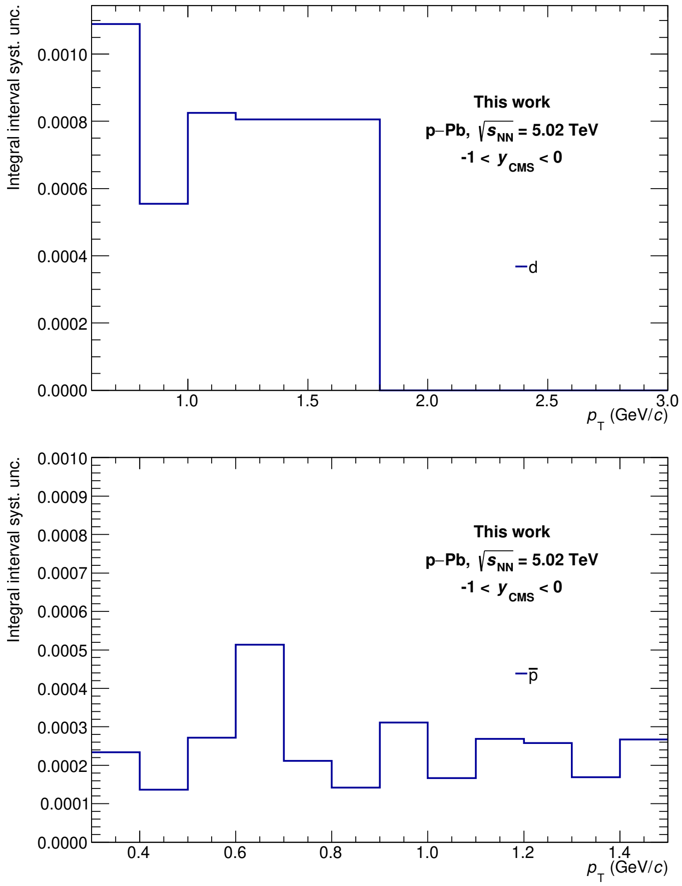

Figure 4.24: Systematic uncertainty due to the different intervals chosen in the fit procedure for the deuterons (top) and antiprotons (bottom) as a function of the transverse momentum.

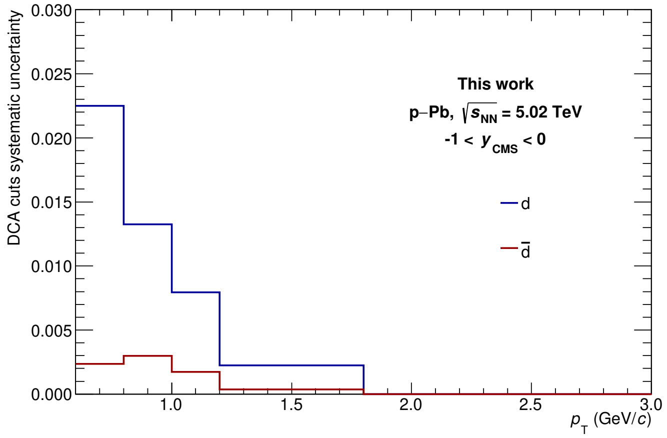

Figure 4.25: Systematic uncertainty for (anti)deuteron due to the $\mathrm{DCA}_{\mathrm{xy}}$ and $\mathrm{DCA}_{\mathrm{z}}$ cuts as a function of the transverse momentum.

values are reported in Fig. 4.25 as a function of the transverse momentum p_{T}. It is worth to notice that, for antideuterons, this source of uncertainty is much smaller with respect to the deuterons one: this because, as already reported in the previous sections, it is assumed that the antideuterons produced in the collision are all primary particles, hence the variation of the DCA cuts does not affect drastically the studied distributions.

4.4.6 Signal extraction

Another important source of systematic uncertainty is linked to the signal extraction. Considering the peculiarity of the signal extraction procedure in the analysis, performed in the three azimuthal regions, this source of systematic uncertainty is evaluated for each region separately. Moreover, different contributions are taken into account. In particular, the explored contributions are:

- Different integration interval
- Different fit functions for the background
- Different integration methods for the raw yield estimation

The total value of the systematic uncertainty is equal to the sum in quadrature of all the sources. Fig. 4.26 shows the value of this source for (anti)deuterons and antiprotons in the Toward region, while the same results for the Away and Transverse regions are reported in Appendix A. The details on the evaluation on the different contributions are reported in the next sections.

Integration interval

The first source that contributes to the signal extraction systematic uncertainty is the integration interval. In order to take into account this effect, the signal extraction procedure is repeated for 50 times, for both particle species and detectors. In all cases, the performed fits are equal to the one described in Sect. 4.2, while the integration extremes are randomly extracted in the intervals:

- (-3.5σ_{TPC}, -2.0σ_{TPC}) and (2.0σ_{TPC}, 3.5σ_{TPC}) for the TPC analysis
- (-3.5σ_{TOF}, -2.0σ_{TOF}) and (3.0σ_{TOF}, 4.5σ_{TOF}) for the TOF analysis.

The asymmetric values chosen for the TOF case reflect the asymmetric interval in the signal extraction. The raw yield is then extracted within the new integration interval generated. Each raw yield is then corrected for the corresponding efficiency, where the same integration interval is used for the reconstructed particles, in order to obtain the correlated efficiency for each case. Once the distributions are corrected, for each p_{T} bin a histogram is filled, and the systematic uncertainty is equal to the ratio between the width and the mean of the distribution. Fig. 4.27 shows this contribution for (anti)deuterons and antiprotons in the Toward region, while the results in the Away and Transverse regions are reported in Appendix A.

Fit function

Another source of uncertainty in the signal extraction procedure can be linked to the choice of the functional form of the background function. In particular, this source of uncertainty has been investigated only in the case of (anti)deuterons in the last transverse momentum interval of the TPC signal extraction. This because, for both the (anti)deuterons and

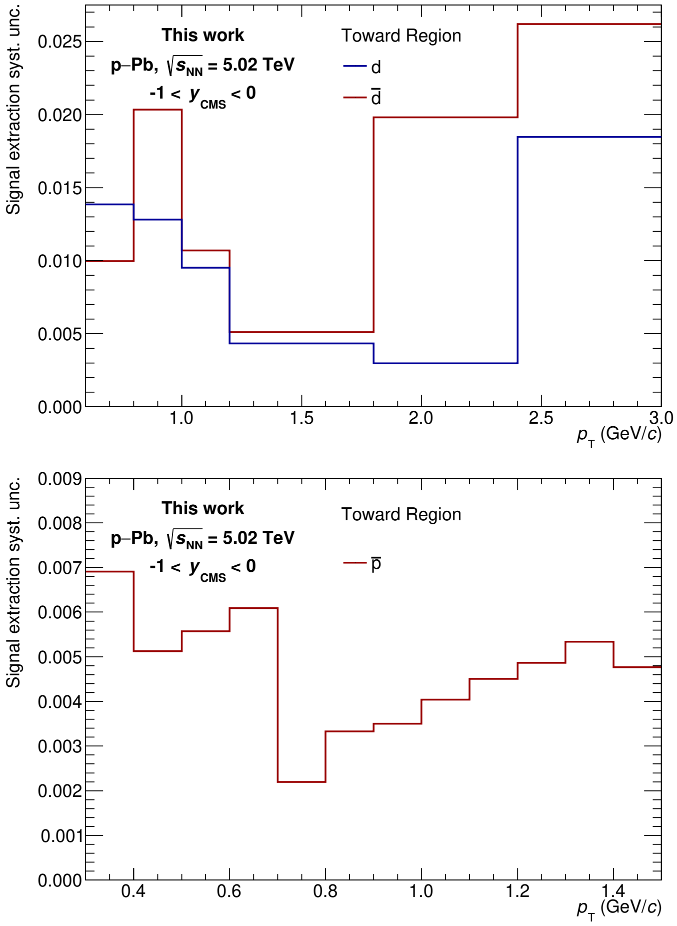

Figure 4.26: Systematic uncertainty due to the signal extraction for (anti)deuterons (top) and antiprotons (bottom) in the Toward region as a function of the transverse momentum.

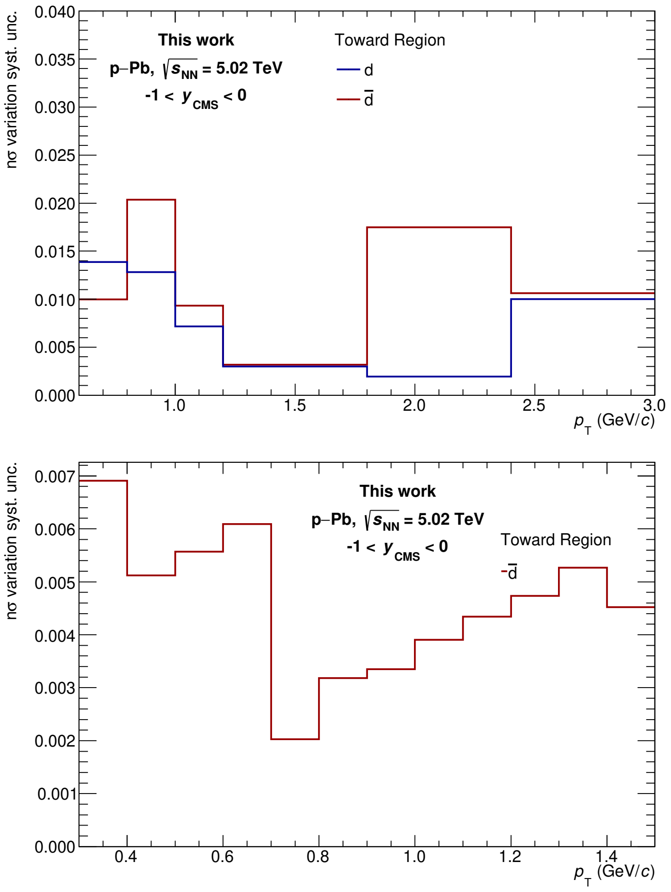

Figure 4.27: Systematic uncertainty due to the different signal integration intervals for (anti)deuterons (top) and antiprotons (bottom) in the Toward region as a function of the transverse momentum.

antiprotons signal extraction in the TOF, the use of a different functional form of the background prevent the convergence of the total fit procedure, hence this approach is discarded. In the considered case, then, two different functions have been used to fit the contamination observed on the left of the distributions (see Fig. 4.7): an exponential function and a skewed Gaussian function. The systematic uncertainty is then evaluated as half of the difference between the raw yield obtained with the new background parametrization and the standard case. In the case of the skewed Gaussian function the systematic uncertainty is negligible, with a maximum value of 0.07%, while the case of the exponential function leads to a maximum value of about 1%.

Integration method

The last source of the systematic uncertainty related to the signal extraction, evaluated only in the case of the TOF analysis for both (anti)deuterons and antiprotons, is related to the method of the signal extraction. In the analysis, in fact, the histogram (after the background subtraction) is integrated in the interval ($-3.0\sigma_{\mathrm{TOF}} + x_0$, $3.5\sigma_{\mathrm{TOF}} + x_0$), with the values of σ and x_0 extracted from the fit. However, the raw yield can also be obtained integrating the signal fit function in the same interval. Hence, also this value is obtained, and the systematic uncertainty is evaluated as the half of the difference of the two values of the raw yield obtained from the histogram or from the function integration. The obtained results for the Toward region are reported in Fig 4.28, while the same quantities for the Away and Transverse regions are reported in Appendix A.

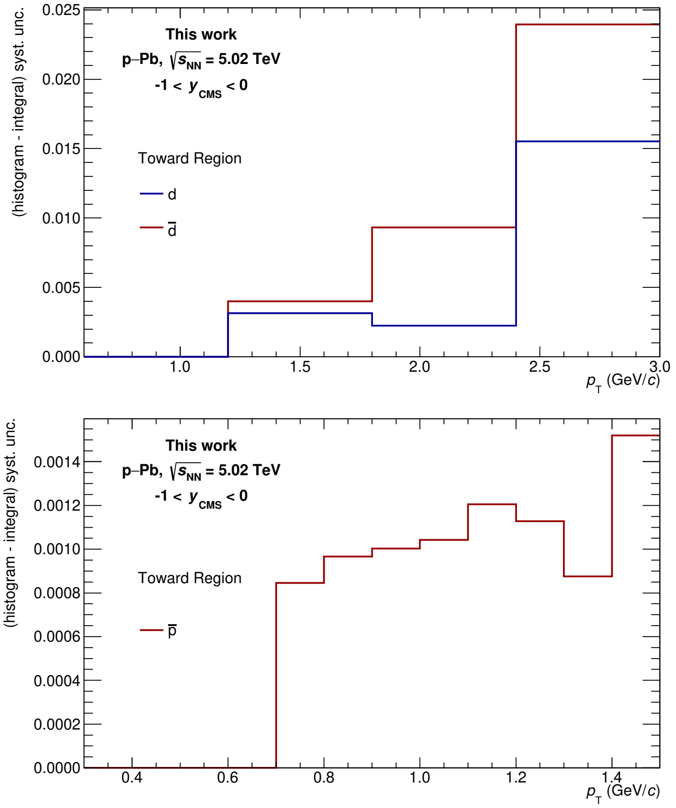

Figure 4.28: Systematic uncertainty due to the different integration methods for (anti)deuterons (top) and antiprotons (bottom) in the Toward region as a function of the transverse momentum.

Chapter 5

Particle spectra and coalescence parameter in and out of jets

5.1 (Anti)deuteron and antiproton spectra in and out of jets

With the procedure described in Chapter 4, the transverse momentum distributions of (anti)deuterons and antiprotons are evaluated. The experimental results for the (anti)deuteron are reported in Fig. 5.1. The distributions in the Toward and Transverse regions are scaled by a factor of 4 and 2, respectively, in order to better visualize the results. At the LHC energies, as already discussed in Ref. [25], the baryochemical potential is equal to zero, hence the same quantity of matter and antimatter is produced. In this analysis, the ratio between the antideuteron and the deuteron is studied in the three azimuthal regions, as reported in Fig. 5.2. In all regions, the ratio is consistent with the unity within the uncertainties. Then, in order to maximize the statistical sample available for the analysis, hence reducing the statistical uncertainty, and to reduce the systematic uncertainty at low transverse momentum, dominated for the deuteron signal from the secondary contribution, the mean of deuteron and antideuteron signals is considered from now on.

The final distributions that consider the $(\mathrm{d}+\overline{\mathrm{d}})/2$ value are reported in Fig. 5.3, while the transverse momentum distributions for antiproton

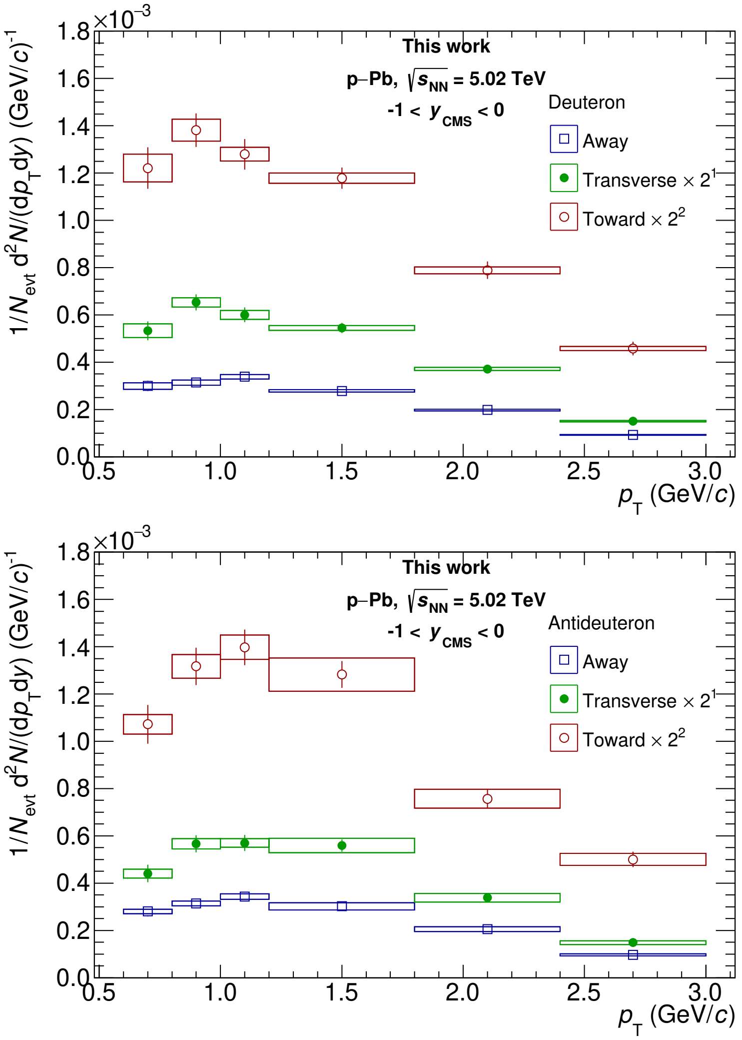

Figure 5.1: Transverse momentum distributions for deuterons (top) and antideuterons (bottom) in the Toward (red), Transverse (green), and Away (blue) regions. Vertical bars represent the statistical uncertainty, while boxes represent the systematic one.

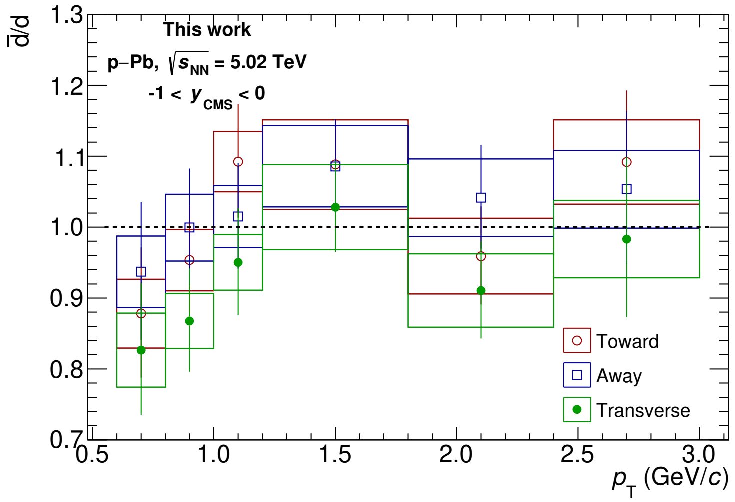

Figure 5.2: Antideuteron over deuteron ratio in the Toward (red), Transverse (green) and Away (blue) regions as a function of the transverse momentum. Vertical bars represent the statistical uncertainty, while boxes represent the systematic one. The dotted black line represents the unity.

are reported in Fig. 5.4. In both figures, the Toward and Transverse distributions are scaled by a factor of, respectively, 4 and 2 to better visualize the results. The dotted line represents a Lévy-Tsallis fit, that has the functional form:

$$\frac{d^2N}{dp_T dy} = \frac{dN}{dy}\frac{p_T}{nC}\frac{(n-1)(n-2)}{(nC+m(n-2))}\left(1+\frac{m_T-m}{nC}\right)^{-n} \qquad (5.1)$$

where m_T is the transverse mass, defined as $m_T = \sqrt{m^2 + p_T^2}$, m is the mass of the nucleus, fixed at 1.87 GeV/c^2 for the (anti)deuteron and 0.938 GeV/c^2 for the antiproton, n and C are fit parameters. These distributions are the ones that are used in the next sections in order to evaluate the in-jet spectra, the coalescence parameter and the deuteron over proton ratio.

The in-jet distributions for both the mean of deuteron and antideuteron, and the antiproton are obtained subtracting the Transverse region from the Toward one. The obtained results are reported in Fig. 5.5 for the two particle species. Also in this case, the dotted line represents a Lévy-

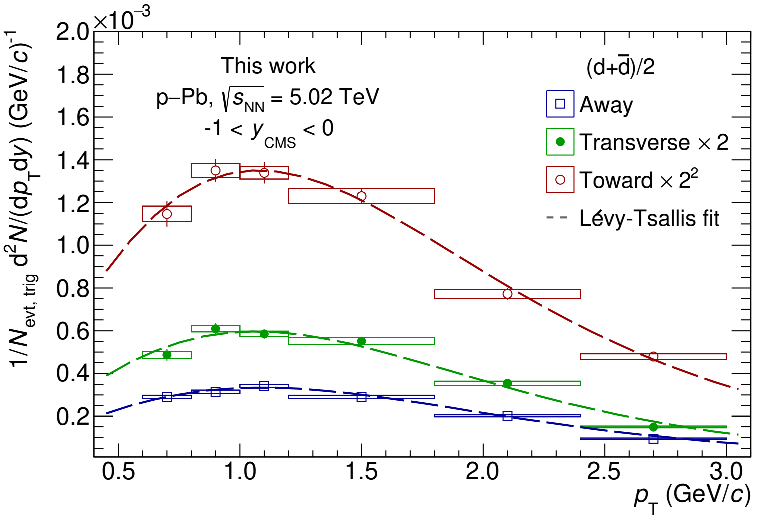

Figure 5.3: Transverse momentum distributions of the mean of deuteron and antideuteron in the Toward (red), Transverse (green) and Away (blue) regions. Vertical bars represent the statistical uncertainty, while boxes represent the systematic one.

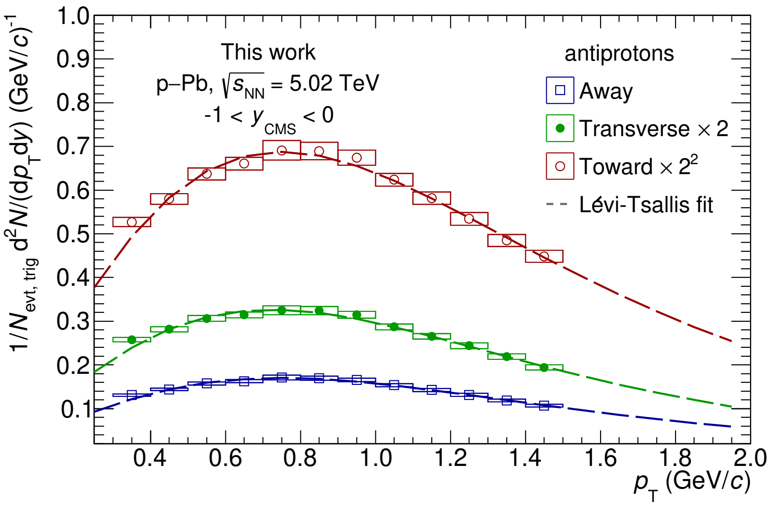

Figure 5.4: Antiproton transverse momentum distributions in the Toward (red), Transverse (green) and Away (blue) regions. Vertical bars represent the statistical uncertainty, while boxes represent the systematic one.

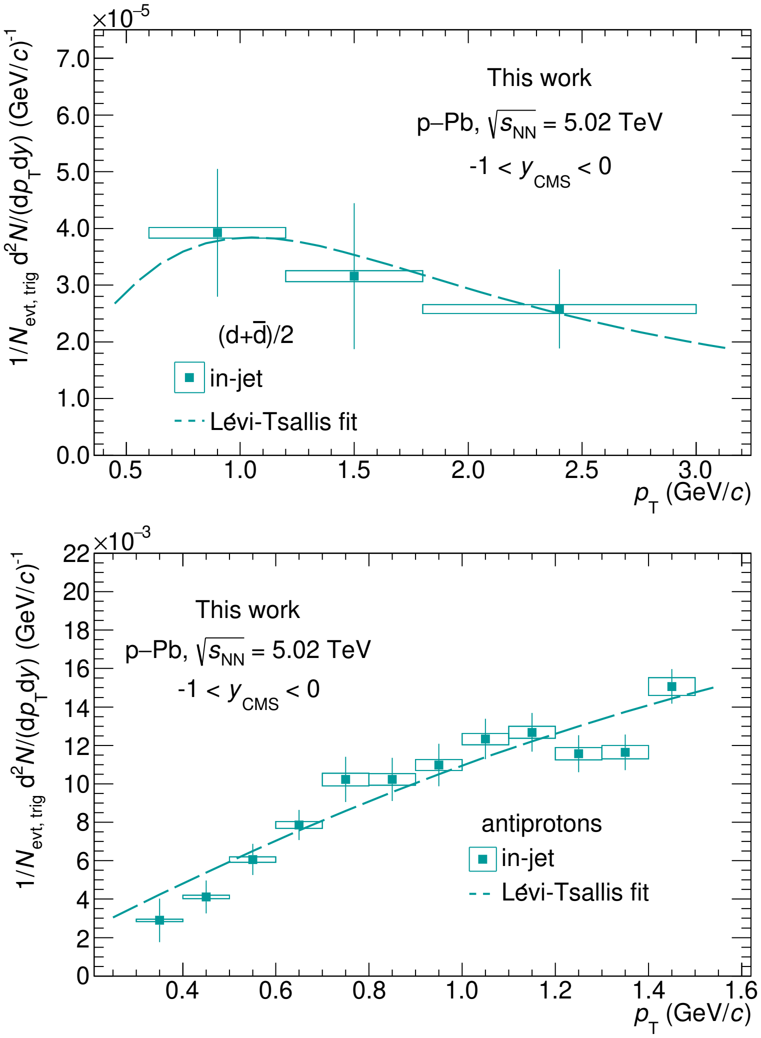

Figure 5.5: In-jet transverse momentum distributions for the deuteron and antideuteron mean (top) and antiproton (bottom). Vertical bars represent the statistical uncertainty, while boxes represent the systematic one.

Tsallis distribution. In the case of the deuteron, due to the reduced data sample available, the TPC transverse momentum intervals and the two last TOF p_{T} intervals have been merged. Compared with the Toward distributions, for both the (anti)deuteron and the antiproton, the in-jet contribution only accounts for about 10% of the total signal. Hence, with the jets reconstruction adopted in this analysis, also the Toward region is dominated by the underlying event. Similar results have been observed in pp collisions at $\sqrt{s} = 13$ TeV [104].

5.2 Coalescence parameter in and out of jets

The obtained distributions for deuteron and antideuteron mean and antiproton in jets and in the Transverse region, that describes the out of jets contribution, are then used to calculate the coalescence parameter. From now on, the out of jets contribution will be referred also as underlying event. The antiproton distributions are rebinned, using a Lévy-Tsallis distribution, in order to match the transverse momentum intervals used in the deuteron case. With respect to the formula reported in Eq. 2.12, the equation is modified to take into account the reduced azimuthal space in which the distributions are studied. Hence, the coalescence parameter is calculated as:

$$B_2 = \left(\frac{1}{(2\pi/3)p_{\mathrm{T}}^{\mathrm{d}}} \frac{1}{N_{\mathrm{evt,trig}}} \frac{\mathrm{d}^2 N_{\mathrm{d}}}{\mathrm{d}y\mathrm{d}p_{\mathrm{T}}^{\mathrm{d}}} \right) \Big/ \left(\frac{1}{(2\pi/3)p_{\mathrm{T}}^{\mathrm{p}}} \frac{1}{N_{\mathrm{evt,trig}}} \frac{\mathrm{d}^2 N_{\mathrm{p}}}{\mathrm{d}y\mathrm{d}p_{\mathrm{T}}^{\mathrm{p}}} \right)^2 . \tag{5.2}$$

In this formula, $N_{\mathrm{evt,trig}}$ corresponds to the number of events that satisfies the $p_{\mathrm{T}} > 5$ GeV/c condition that, in this analysis, correspond to the triggered events.

The coalescence parameter in and out of jets, from now on referred also as B_2^{jet} and B_2^{UE}, obtained in this work are reported in Fig. 5.6, and they are compared with the values already measured in pp collisions at $\sqrt{s} = 13$ TeV [104]. The results are reported as a function of the reduced transverse momentum $p_{\mathrm{T}}/\mathrm{A}$, with A = 2 the deuteron mass number. As already observed in pp collisions, also in the p–Pb system an enhanced coalescence parameter in jets is observed with respect to the same quantity

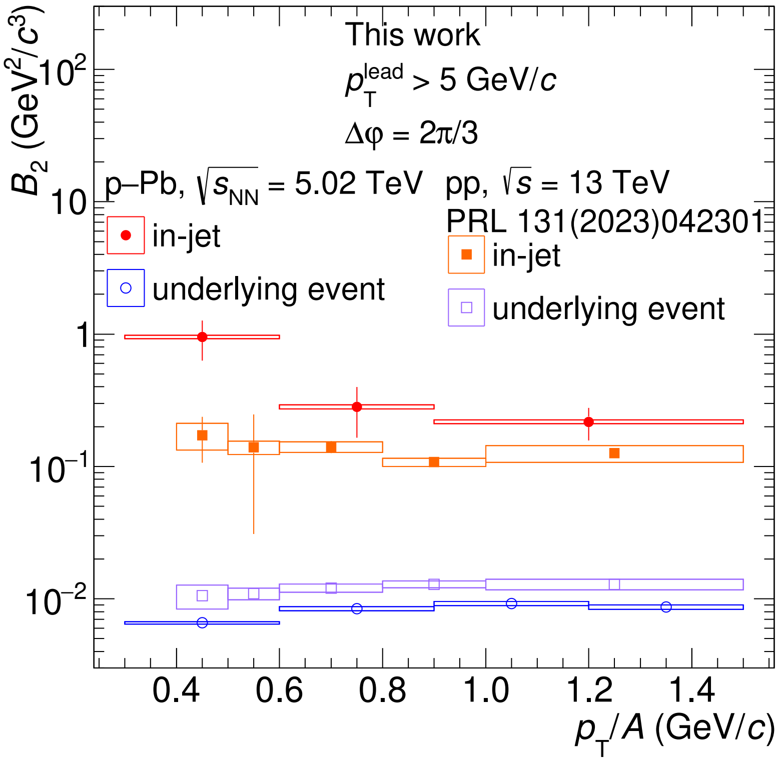

Figure 5.6: Coalescence parameter in-jet (full marker) and in the underlying event (open marker) as a function of the reduced transverse momentum p_T/A in p–Pb collisions at $\sqrt{s_{NN}} = 5.02$ TeV (circle marker) and pp collisions at $\sqrt{s} = 13$ TeV (square marker). Vertical bars represent the statistical uncertainty, while boxes represent the systematic one.

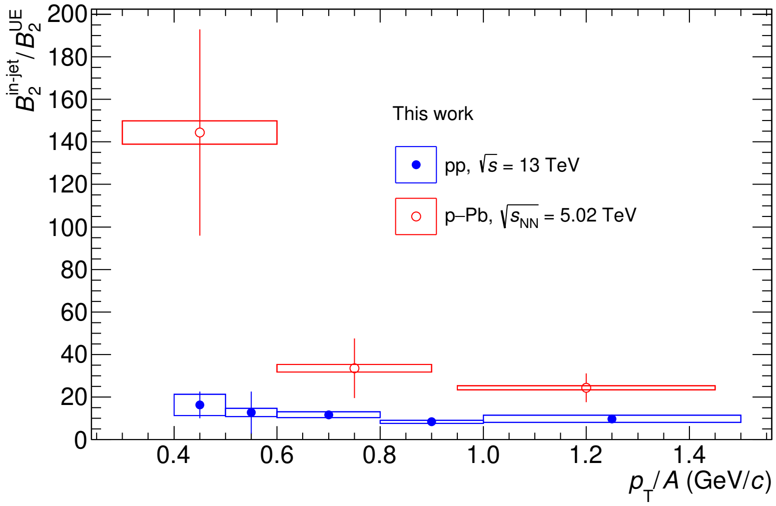

Figure 5.7: $B_2^{\text{jet}}/B_2^{\text{UE}}$ in p–Pb collisions at $\sqrt{s_{\text{NN}}} = 5.02$ TeV (red) and pp collisions at $\sqrt{s} = 13$ TeV. Vertical bars represent the statistical uncertainty, while boxes represent the systematic one.

in the underlying event. This result is coherent with the coalescence picture: since the jets are collimated spray of particles, the nucleons inside them are more closer in the phase space with respect to other azimuthal regions, hence a larger coalescence parameter is expected. While the gap between the two regions is equal to a factor about 14 in pp collisions, such gap is larger in p–Pb collisions, with a value of about 24 in the high p_{T}/A region, and even higher at low p_{T}/A. Fig. 5.7 shows the gap between the B_2^{jet} and B_2^{UE} in both pp and p–Pb collision systems. In order to better understand the results, it is worth to focus the discussion only in one region of the azimuthal space at the time.

Looking at the underlying event region, that describes the out of jets contribution, it is possible to notice that B_2^{UE} (p–Pb) $<$ B_2^{UE} (pp). The comparison of the two results is better reproduced in Fig. 5.8. This experimental result is in agreement with the coalescence picture. In fact, as described in Sect. 2.2.2 and observed experimentally in Fig. 2.11, the coalescence parameter depends on the system source size. The source size of both the pp and p–Pb systems have been measured by the ALICE experiment through the femtoscopy technique [196, 197]. The experimental

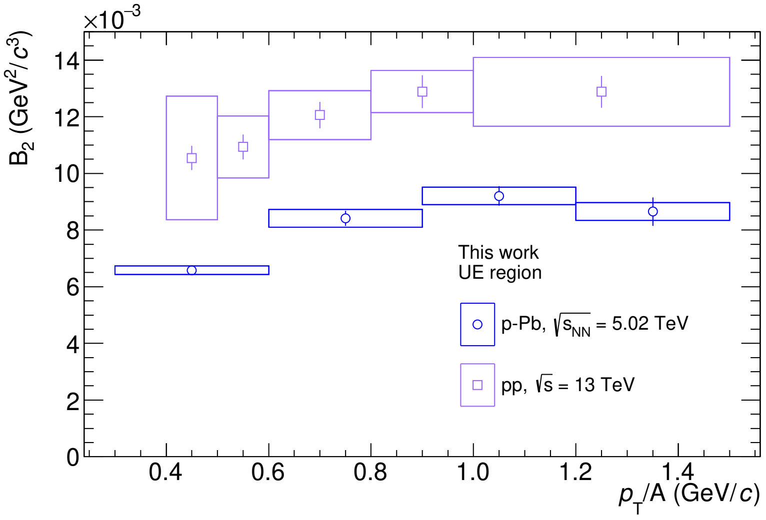

Figure 5.8: B_2^{UE} in p–Pb collisions at $\sqrt{s_{\mathrm{NN}}} = 5.02$ TeV (blue, circle marker) and in pp collisions at $\sqrt{s} = 13$ TeV (violet, square marker). Vertical bars represent the statistical uncertainty, while boxes represent the systematic one.

results show a source size of about 1 fm in pp collisions and of about 1.5 fm in p–Pb collisions. Hence, since the p–Pb system has a source size larger with respect to the pp case, the coalescence model predicts a smaller coalescence parameter, as observed in this analysis.

The results in the in-jet region are more challenging to interpret. Fig. 5.9 shows the comparison on the obtained values of B_2^{jet} in p–Pb collisions at $\sqrt{s_{\mathrm{NN}}} = 5.02$ TeV and pp collisions at $\sqrt{s} = 13$ TeV. The experimental results show that B_2^{jet} (p–Pb) > B_2^{jet} (pp). This result, at the moment, could be explained with different hypotheses. In fact, it could arise from different particle composition in jets in the pp and p–Pb systems, contrary to the current knowledge. In fact, jets are considered fundamental objects in QCD, formed by the fragmentation of energetic quarks and gluons generated in high-Q^2 interactions, and their hadrochemistry is independent of the collision system from which the jets originate. Other possible interpretations of the results could derive from stronger momentum correlations among the nucleons in p–Pb system, that reflect in a larger B_2^{jet}, or

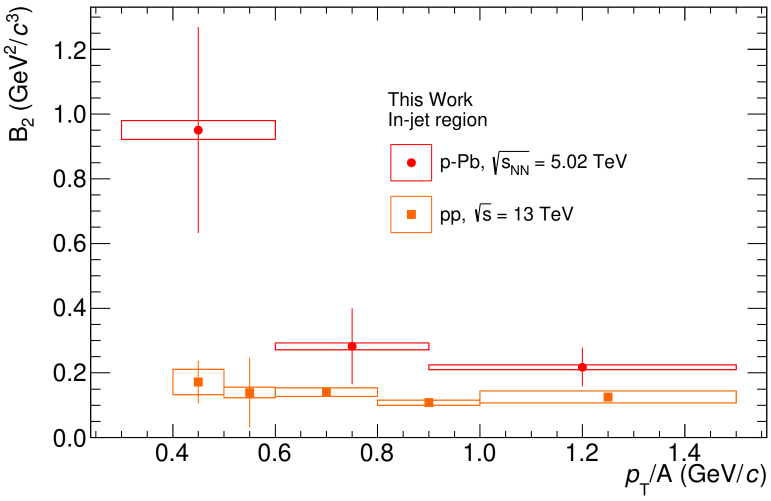

Figure 5.9: B_2^{jet} in p–Pb collisions at $\sqrt{s_{\text{NN}}} = 5.02$ TeV (red, circle marker) and in pp collisions at $\sqrt{s} = 13$ TeV (orange, square marker). Vertical bars represent the statistical uncertainty, while boxes represent the systematic one.

also a higher average p_{T} value. At the moment, neither of the hypotheses could be ruled out: this is because, both in pp and p–Pb case, the B_2^{jet} measurement is affected by a large statistical uncertainty, hence more advanced types of analysis with a larger data sample are needed.

The experimental results are compared with the predictions obtained by the PYTHIA 8.3 [198] model, chosen to have a comparison with the published results [104], coupled with Angantyr [199], in order to simulate the heavy ion collision. The deuteron production in the PYTHIA package is included as a reaction production model. The deuteron can be formed through the following reactions:

- $p + n \to \gamma + d$
- $p + n \to \pi^0 + d$
- $p + n \to \pi^- + \pi^+ + d$
- $p + n \to \pi^0 + \pi^0 + d$
- $p + p \to \pi^+ + d$
- $p + p \to \pi^+ + \pi^0 + d$
- $n + n \to \pi^- + d$
- $n + n \to \pi^- + \pi^0 + d$

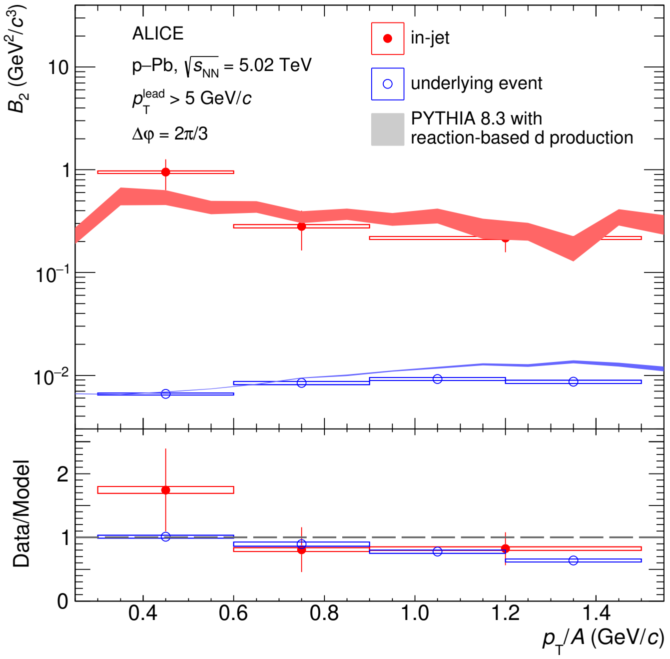

Figure 5.10: Top: B_2^{jet} and B_2^{UE} in p–Pb collisions at $\sqrt{s_{\text{NN}}} = 5.02$ TeV compared with the expectations from the PYTHIA 8.3 Angantyr model. Vertical bars represent the statistical uncertainty, while boxes represent the systematic one. For the model, only the statistical uncertainty is computed. Bottom: Ratio between the experimental data and the model prediction.

The different reactions have an energy dependent cross section tuned on experimental data. The proton and deuteron distributions from the model are normalized to the ones measured experimentally. With the normalized distributions, the B_2^{UE} and B_2^{jet} are calculated. The comparison with the experimental data is reported in Fig. 5.10. The model, as already observed in pp collisions at $\sqrt{s} = 13$ TeV [104], qualitatively reproduces the data, in particular it is able to reproduce the large gap between the B_2^{jet} and B_2^{UE}. The values of the coalescence parameter in the two regions are overestimated by the model at high p_{T}/A, while the B_2^{jet} is underestimated by the model at low transverse momentum.

5.3 d/p ratio in and out of jets

In order to complement the results obtained with the coalescence parameter reported in Fig. 5.6, the deuteron-over-proton ratio, both in pp at $\sqrt{s} = 13$ TeV and p–Pb at $\sqrt{s_{\mathrm{NN}}} = 5.02$ TeV, is evaluated. This quantity is defined as the ratio of the transverse momentum distributions of the two particles, reported as a function of the reduced transverse momentum. For the pp case, the deuteron and proton transverse momentum distributions are taken, respectively, by Refs. [104, 148]. This ratio, in fact, can give insights on the particle production in and out of jets. With respect to previous results, such as the one reported in Fig. 2.8, the d/p ratio is not studied as a function of the charged particle multiplicity but as a function of the reduced transverse momentum. The motivation of this choice relies on the fact that, with the technique that we have used in order to obtain the in-jet distributions, the multiplicity of such system can not be obtained in the same way of the minimum bias case, hence the comparison of these results is not consistent. The top panel of Fig. 5.11 shows in detail the d/p ratio in pp collisions at $\sqrt{s} = 13$ TeV and p–Pb collisions at $\sqrt{s_{\mathrm{NN}}} = 5.02$ TeV. It is observed that, in both systems, the deuteron-over-proton ratio is higher in-jet with respect to the underlying event. In order to estimate better such gap, the double ratio $(\mathrm{d/p})_{\mathrm{in-jet}}/(\mathrm{d/p})_{\mathrm{UE}}$ is considered, as reported in the bottom row of Fig. 5.11. In the evaluation of such double ratio, the systematic uncertainties are considered uncorrelated. The experimental results show that, in pp collisions, the in-jet d/p ratio is higher of a factor between 1 and 2.5 with respect to the underlying event, while the same quantity in p–Pb collisions shows a value between 2 and 4. The results show that the deuteron production is favoured in-jet with respect to the underlying event, and this could be explained by the coalescence model, as already observed in the study of the coalescence parameter.

In order to further study the deuteron-over-proton ratio, another comparison can be done. In fact, it is possible to compare the in-jet and underlying event values in the two collision systems. This comparison is reported in Fig. 5.12. As shown in the top row, for both the in jets and underlying event regions, the d/p ratio is higher in p–Pb collisions with respect to the pp ones. In particular, it is possible to estimate this gap, as reported in the bottom row of Fig. 5.12, evaluating the double ratio

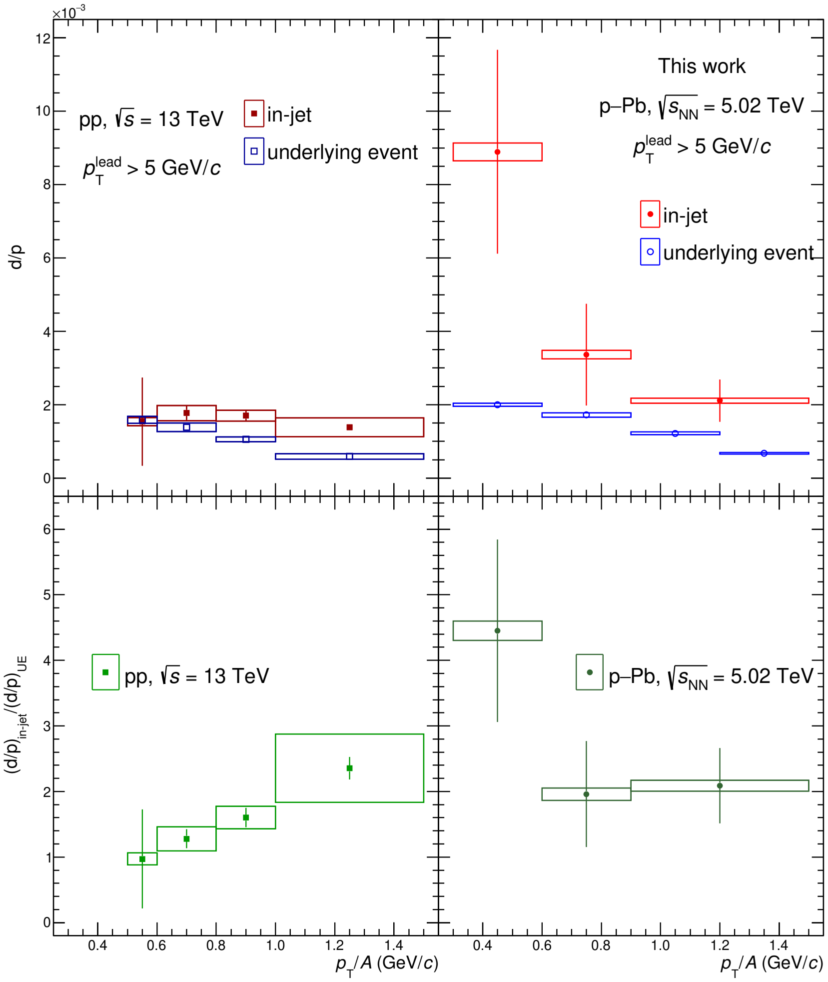

Figure 5.11: Top: Deuteron-over-proton ratio in-jet (red, full marker) and in underlying event (blue, open marker) as a function of the reduced transverse momentum in pp collisions at $\sqrt{s} = 13$ TeV (left) and p–Pb collisions at $\sqrt{s_{NN}} = 5.02$ TeV (right). Bottom: Double ratio $(d/p)_{in-jet}/(d/p)_{UE}$ in pp (left) and p–Pb (right) collisions. Vertical bars represent the statistical uncertainty, while boxes represent the systematic one.

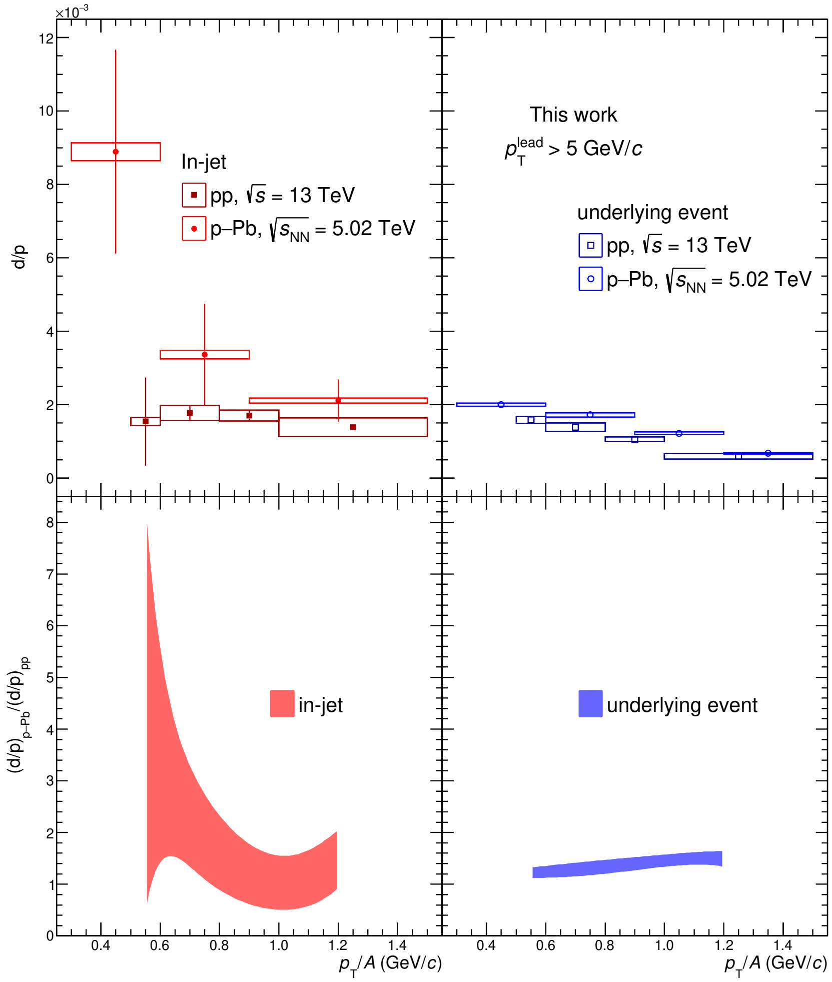

Figure 5.12: Top: deuteron-over-proton ratio in-jet (left) and in underlying event (right) measured in pp collisions at $\sqrt{s} = 13$ TeV and in p–Pb collisions at $\sqrt{s_{\mathrm{NN}}} = 5.02$ TeV. Bottom: Double ratio $(\mathrm{d/p})_{\mathrm{p-Pb}}/(\mathrm{d/p})_{\mathrm{pp}}$ in-jet (left) and underlying event (right). Vertical bars represent the statistical uncertainty, while boxes represent the systematic one.

$(\mathrm{d}/\mathrm{p})_{\mathrm{p-pPb}}/(\mathrm{d}/\mathrm{p})_{\mathrm{pp}}$. To do so, since the reduced transverse momentum intervals of the two analyses do not coincide, an interpolation of the experimental points is used. Moreover, to the double ratio is assigned a total error equal to the sum in quadrature of the statistical and systematic uncertainties. For the in jets region, the statistical contribution is prevalent, about 90% in the whole $p_{\mathrm{T}}/\mathrm{A}$ interval, while for the underlying event the statistical and systematic uncertainties have similar weights. The results show a ratio between 1.2 and 1.4 in the underlying event, while for the in jets region this ratio is higher, with a value between 1.5 and 4. These results could hint at a different particle composition in jets in the two collision systems, in contrary to the current knowledge. Nevertheless, the errors associated to the measured data, especially the statistical ones, are not negligible. For these reasons, a more detailed study on the jets hadrochemistry, exploiting a larger data sample, is needed.

5.3.1 Pion production in and out of jets

In order to understand if a different hadrochemistry of jets in pp and p–Pb collisions could explain the observed values of the d/p ratio, an attempt to study the pion production in and out of jets is made. This choice is based on the knowledge that pions are the most abundant produced particles in high energy hadronic collisions, hence they are a proxy to investigate the particle composition of jets. If, in fact, a different production of pions in jets in the two collision systems is observed, this result could corroborate the hypothesis of different jet hadrochemistry.

However, to perform this analysis some caveats have been used, which do not allow the analysis to be fully reliable and hence conclusive. In fact, the TOF distributions of the pion candidates are affected from a significative background, due to track mismatch. This combinatorial background is present in high-occupancy environments, and it is due to a track correctly reconstructed in the TPC, to which is assigned a time signal generated by a different particle. Different attempts have been performed in order to parametrize such contribution, both using a data-driven approach and MC simulations. However, in both cases, the obtained mismatch parametrizations do not follow the same trend of the experimental data. In the latter case, the MC simulations show a peak structure that is not expected, while in the former case, even if the shape of the mismatch is the expected one, the data-driven method shows a different slope on the rising edge of the distribution and a shift toward low values of $n\sigma_{\mathrm{TOF}}$. Since both attempts were not successful, the signal extraction procedure in the TOF detector is performed assuming a parametrization for the total background given by the sum of an exponential function, that describes the mismatch, and Gaussian functions with exponential tails that describe the kaon and proton contributions at higher values of $n\sigma_{\mathrm{TOF}}$. Under these assumptions, the background contribution is underestimated. However, it is worth noticing that the obtained result is still a good approximation, since all the azimuthal distributions are affected by the same problem, and the background should be two order of magnitude lower with respect to the signal.

The transverse momentum distributions for the sum of positive and negative pions in the Toward, Transverse and in-jet regions are reported in Fig. 5.13. The distributions are compared with the data obtained in pp collisions, taken from Ref. [148]. It is observed that, both in the Toward and Transverse regions, the distributions in the two collision systems are different, with higher values in p–Pb. Instead, when the in-jet contribution is evaluated, the two systems are compatible within errors, contrary to what is expected. Moreover, the in-jet distribution in the p–Pb system shows a discontinuity at $p_{\mathrm{T}} = 0.8$ GeV/c, that is the limit value between the signal extraction performed with the TPC ($p_{\mathrm{T}} < 0.8$ GeV/c) and TOF ($p_{\mathrm{T}} > 0.8$ GeV/c) detectors, hence could be influenced by the non perfect mismatch parametrization. However, considering also the caveats of this comparison, no conclusions can be made and more detailed studies on the jet hadrochemistry are needed, exploiting a larger data sample, as the one of the ongoing LHC Run3.

5.4 Theoretical predictions on the production of nuclei in jets

The experimental results on the enhancement of the B_2^{jet} have recently gained interest in the theoretical community. In fact different works,

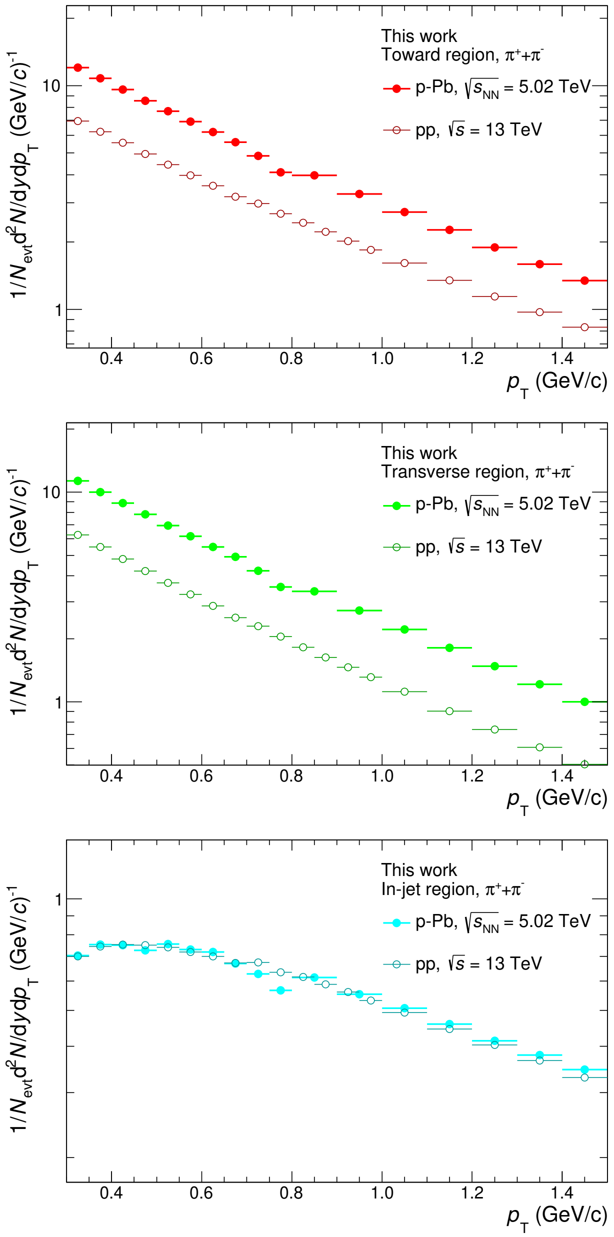

Figure 5.13: Transverse momentum distribution for the sum of positive and negative pions in the Toward (top), Transverse (middle) and in-jet regions in p–Pb collisions at $\sqrt{s_{\rm NN}}$ = 5.02 TeV (full markers) and pp collisions at $\sqrt{s}$ = 13 TeV (empty markers).

reported in Refs. [200–202], have been published, and each work explores different causes on the enhancement of the nuclei coalescence parameter in jets.

According to the study reported in Ref. [200], the observed enhancement could derive from a combination of two independent effects: the collimation of jets nucleons and the smallness of the nucleon source. According to the coalescence model, the yield of deuterons with a momentum $\boldsymbol{p}$ can be written as:

$$\frac{\mathrm{d}N_d}{\mathrm{d}^3\boldsymbol{p}} = \mathcal{A}\left(\frac{\mathrm{d}N_p}{\mathrm{d}^3\left(\frac{1}{2}\boldsymbol{p}\right)}\right)^2 \tag{5.3}$$

where $\mathcal{A}$ denotes the deuteron formation rate, defined as:

$$\mathcal{A} = \frac{3}{4}(2\pi)^3 \int \mathrm{d}^3 r D(r)|\phi_d(\boldsymbol{r})|^2. \tag{5.4}$$

In this quantity, the factor 3/4 takes into account the fact that the deuteron is formed by a neutron-proton pair in the spin triplet state, while $D(\boldsymbol{r})$ and $\phi_d(\boldsymbol{r})$ are, respectively, the source function of the proton and neutron and the deuteron wave function. In order to show the influence of the jet collimation on the deuteron production, a simplified momentum distribution of jets nucleons is assumed. In such approximation, the proton yield can be written as:

$$\frac{\mathrm{d}N_p}{\mathrm{d}^3\boldsymbol{p}} = N_p \frac{e^{-\alpha p}}{\pi\alpha^3} \frac{\Theta(\cos\theta - \cos\theta_c)}{1-\cos\theta_c} \tag{5.5}$$

with α a real positive parameter, $\Theta(x)$ a step function, and θ_c the critical zenith angle such that jet nucleons are produced within the cone of angle θ_c. This angle is typically expressed in radians and, in first approximation, gives the jet radius R. Substituting this value in Eq. 5.3 and integrating such equation, the total yield of jet deuterons can be expressed as:

$$N_d^{\mathrm{jet}} = \frac{2\mathcal{A}N_p^2}{\pi\alpha^3(1-\cos\theta_c)} \tag{5.6}$$

According to this relation, the deuteron yield increases when θ_c decreases, that is when the jet is more collimated. The effect of the nucleus source can

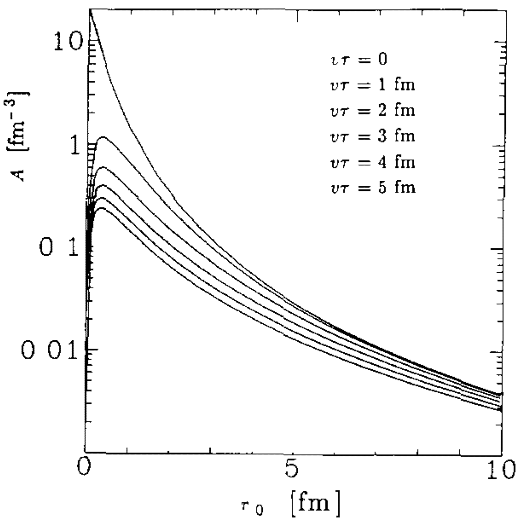

Figure 5.14: Deuteron formation rate as a function of r_0. The value of $v\tau$ increases from the highest line ($v\tau = 0$) to the lowest line ($v\tau = 5$ fm) [203].

be investigated assuming a Gaussian parametrization for the $D(r)$ function and a Hulthén wave function for the $\phi_d(r)$ wave function, evaluating the formation rate $\mathcal{A}$ as a function of r_0, defined as the root-mean-square of the nucleon source. The value of $\mathcal{A}$, obtained resolving numerically the integral reported in Eq. 5.4, is shown in Fig. 5.14 as a function of r_0. The integration has been made for different values of $v\tau$, with v the velocity of the deuteron and τ the source lifetime, with the product that assumes the meaning of the distance that the proton-neutron pair traverses during the source life time. It is observed that the formation rate $\mathcal{A}$ is a monotonously decreasing function of r_0 with the maximum at $r_0 = 0$, which is reached when the radius of the nucleon source is much smaller than the deuteron radius. It is possible to compare these predictions with the experimental value in the case of pp collisions, considering that the coalescence parameter B_2 and the deuteron formation rate $\mathcal{A}$ are related through the formula $B = 2\mathcal{A}/m$, with m the nucleon mass. In this case, it is observed that the source size of the jets deuteron is equal to $r_0 = 0.3 \pm 0.2$ fm, which is smaller with respect to the deuteron radius, of about 2 fm.

The value of the source size in jets is about a factor 10 smaller with respect to the same quantity in the underlying event, $r_0 = 1.3 \pm 0.2$ fm.

Another interpretation, published in Ref. [201], predicts an enhanced deuteron production due to the interaction of Medium-Medium or Medium-Jet nucleons, with the pure Jet-Jet contribution that arises at higher transverse momentum. In this study, the collision is simulated with the AMPT model [204, 205], and the deuteron production study is performed in the same way as the experimental results, exploiting the CDF technique and selecting events with $p_{\mathrm{T,lead}} > 5$ GeV/c. Fig. 5.15 shows the transverse momentum distributions for protons (top row) and deuterons (bottom row) in pp collisions at $\sqrt{s} = 13$ TeV (left) and p–Pb collisions at $\sqrt{s_{\mathrm{NN}}} = 5.02$ TeV (right) predicted by the AMPT model in the Toward (red), Transverse (blue) and In-Jet region (orange). In the pp case, the predictions from the model are compared with the experimental results: the model reproduces the data in the Toward region and slightly underestimates the data in the Transverse region. With these distributions, both the coalescence parameter and the d/p ratio are computed. The results are reported in Fig. 5.16 and compared with the experimental results in the pp case. For the d/p ratio, the model predicts a decreasing trend with increasing p_{T} both in the Toward and Transverse regions, with a larger absolute value in the latter, and their difference increases with p_{T}. For the coalescence parameter, instead, the model is able to reproduce a similar gap between B_2^{jet} and B_2^{UE} as the one observed in the experimental data. Such a study is able to reproduce the data measured by ALICE in pp collisions, but provides a different interpretation for the cause of such enhancement. In fact, the nucleons in the Toward region ($N_{p,n}^{\mathrm{Toward}}$) consist of both nucleons from the underlying event, also called medium ($N_{p,n}^{\mathrm{Medium}}$), and nucleons from the jet ($N_{p,n}^{\mathrm{In-jet}}$). Hence, the deuteron in the Toward region can be produced from three different contributions: Jet-Jet nucleon coalescence, Medium-Medium nucleon coalescence, and Jet-Medium nucleon coalescence. In particular, assuming $N_n \approx N_p$, the fraction of these three contributions to the deuteron production in the Toward region are:

$$\mathrm{Fraction}_{\mathrm{jet}} \approx \frac{(N_p^{\mathrm{In-Jet}})^2}{(N_p^{\mathrm{Toward}})^2} \tag{5.7}$$

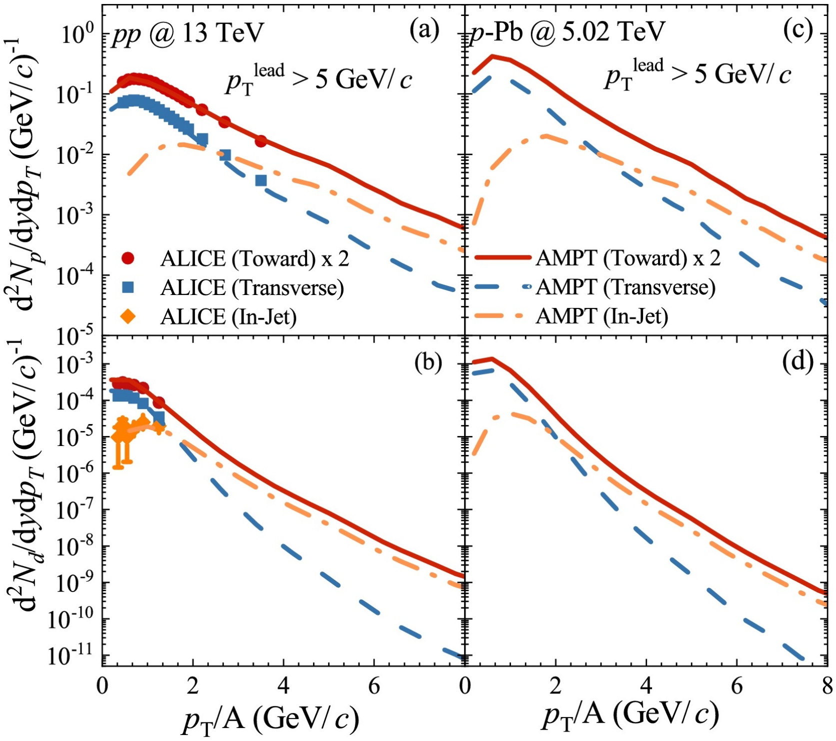

Figure 5.15: Transverse momentum distributions from the AMPT model in the Toward (red), Transverse (blue) and In-Jet (orange) regions for proton (top row) and deuteron (bottom row) in pp collisions at $\sqrt{s} = 13$ TeV (left) and p–Pb collisions at $\sqrt{s_{NN}} = 5.02$ TeV (right). The markers in pp collisions represent the ALICE data [201].

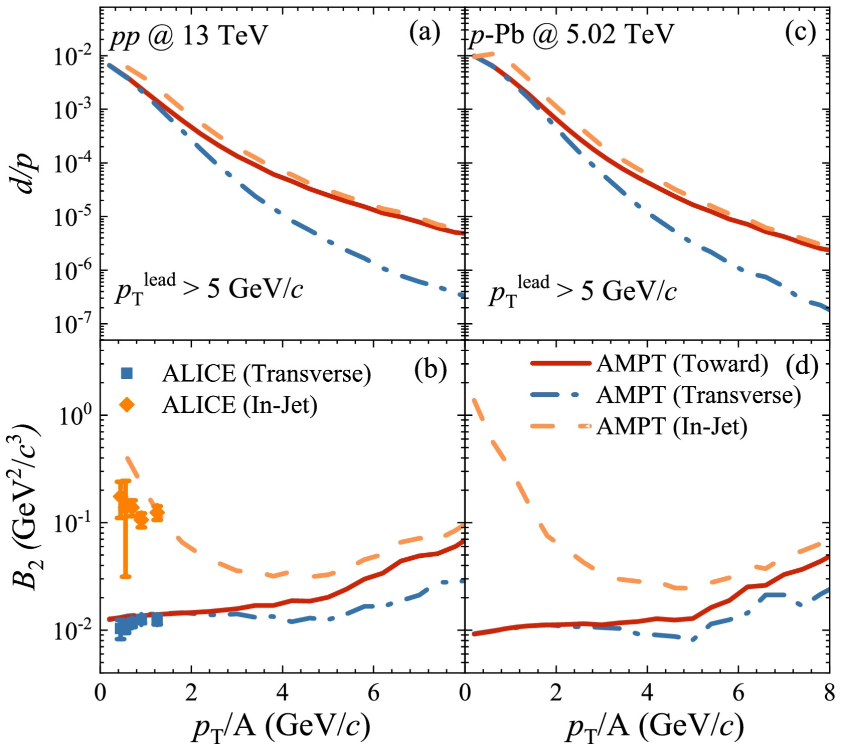

Figure 5.16: d/p (top row) and B_2 (bottom row) in pp collisions at $\sqrt{s} = 13$ TeV and p–Pb collisions at $\sqrt{s_{NN}} = 5.02$ TeV in the Toward (red), Transverse (blue) and In-Jet (orange) regions predicted by the AMPT model. The markers in pp collisions represent the ALICE data [201].

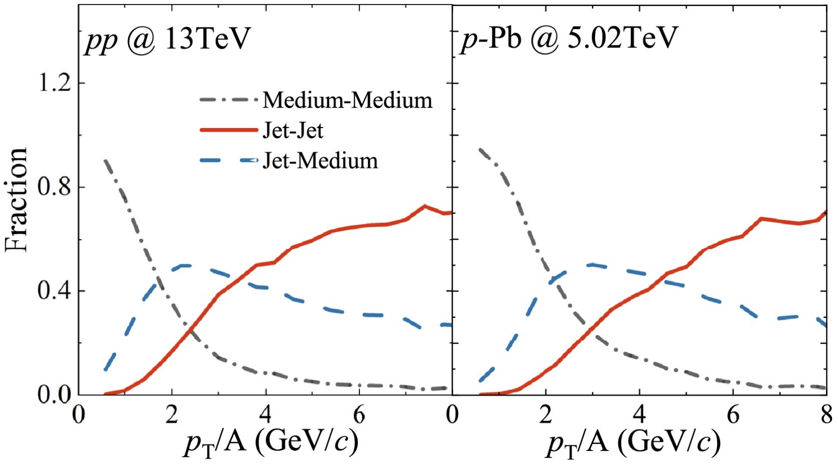

Figure 5.17: Fractions of deuterons produced in the Toward region by Jet-Jet nucleon coalescence (red, solid line), Medium-Medium nucleon coalescence (grey, dash-dotted line), and Jet-Medium nucleon coalescence (blue, dashed line) as a function of the reduced transverse momentum [201].

$$\text{Fraction}_{\text{Medium}} \approx \frac{(N_p^{\text{Medium}})^2}{(N_p^{\text{Toward}})^2} \tag{5.8}$$

$$\text{Fraction}_{\text{Jet-Medium}} \approx 2\frac{N_p^{\text{In-Jet}} \times N_p^{\text{Medium}}}{(N_p^{\text{Toward}})^2} \tag{5.9}$$

The weight of these fractions to the total deuteron yield in the Toward region is reported in Fig. 5.17. In the region of reduced transverse momentum explored in our analysis, $p_{\mathrm{T}}/\mathrm{A} < 1.5$ GeV/c, the dominant fraction is the Medium-Medium and Jet-Medium coalescence, with the pure Jet-Jet nucleon coalescence that arises at higher reduced transverse momentum. Hence, new measurements at higher $p_{\mathrm{T}}/\mathrm{A}$ are needed in order to fully address this hypothesis.

Finally, according to the work described in Ref. [202], the enhanced deuteron coalescence probability in jets could arise from the restoration of the strong spatiomomenta correlations of the nucleon pairs produced from the jet fragmentation. In this work, with respect to the ones already described, the deuteron production in pp collisions is explored using the transverse spherocity in order to distinguish "jetty" and "isotropic" events.

The transverse spherocity S_0 is defined for a unit transverse vector $\hat{\mathbf{n}}$ that minimizes the ratio:

$$S_0 = \frac{\pi^2}{4}\left(\frac{\sum_i \overrightarrow{p_{\mathrm{T}i}} \times \hat{\mathbf{n}}}{\sum_i \overrightarrow{p_{\mathrm{T}i}}}\right)^2 \tag{5.10}$$

Defining the percentiles of S_0, "jetty" events correspond to the 0-20% percentile, while "isotropic" events correspond to the 80-100%. Although S_0 does not offer a direct in-jet and out of jet classification, this quantity is close enough to investigate deuterons in events with jets and perform a multidifferential study. In this work, pp collisions at $\sqrt{s} = 13$ TeV are simulated with the PYTHIA8 model with the Monash tune, considering both MB I (0-1%) and HM I (0-0.17%) multiplicity events. The coalescence is performed using the Wigner function formalism, implemented as an afterburner in PYTHIA. In such implementation, two different wave functions are used for the deuteron: a Gaussian and a Double Gaussian function, despite the limits already described in Sect. 2.2.2. The obtained results on the coalescence parameter are reported in Fig. 5.18. In both multiplicity intervals, the “jetty” deuterons show a slightly higher coalescence parameter, which increases with increasing p_{T}. Even if this difference is noticeable, the results of "jetty" and "isotropic" deuterons are compatible. It is worth noticing that, in the case of the "jetty" production, the contribution of the underlying event is still considered, hence we do not have a pure in-jet contribution. To obtain it, the difference between the "jetty" and the "isotropic" distribution is performed, assuming that the "isotropic" one describes the underlying event. The coalescence parameter of this new case is reported in purple in Fig. 5.18. This quantity shows an enhancement with respect to the "isotropic" case, of a factor of about 10 in the MB I multiplicity class and up to 25 in the HM I class, even if the statistical uncertainties for the latter case are too large to obtain a conclusive estimate. These results could be explained by the favourable coalescence conditions put forward by the restoration of the strong spatiomomenta correlations of the nucleon pairs produced from the jet fragmentation. Even if these predictions can not be directly compared with the value of B_2^{jet} published in Ref. [104], due to the different selections applied in the analysis to estimate the jet, the results corroborate the claim for the enhanced deuteron coalescence probability in jets.

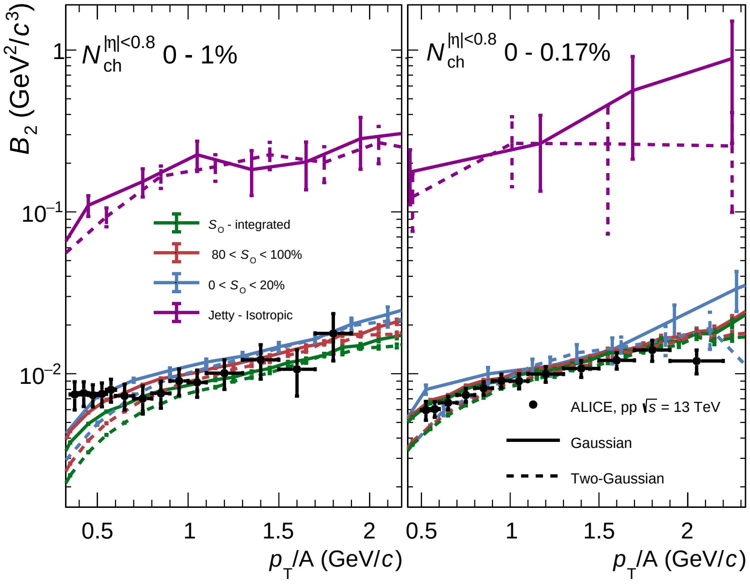

Figure 5.18: Deuteron coalescence parameter as a function of the reduced transverse momentum in pp collisions at $\sqrt{s} = 13$ TeV in MB I (left) and HM I (right) multiplicity classes. Solid and dashed lines represent the predictions from single and double Gaussian wave functions, respectively. The results are compared to experimental measurements from ALICE [202].

Conclusions

In this work the first measurement of the (anti)deuteron and antiproton production in and out of jets in p–Pb collisions at $\sqrt{s_{\mathrm{NN}}} = 5.02$ TeV measured by the ALICE detector have been presented and discussed. These results, in particular with the estimation of the coalescence parameter in and out of jets, contribute to understand the production mechanism of light (anti)nuclei.

In order to evaluate the coalescence parameter in and out of jets, the (anti)deuteron and antiproton transverse momentum distributions are needed. In the analysis the jets are reconstructed using the CDF technique: for each event, the particle with the highest transverse momentum is selected and assimilated to the jet axis. Then, all the other particles are divided in three azimuthal regions, according to the azimuthal angular distance between the particle and the jet axis: Toward ($|\Delta\phi| < 60^{\mathrm{o}}$), Away ($|\Delta\phi| > 120^{\mathrm{o}}$), and Transverse ($60^{\mathrm{o}} < |\Delta\phi| < 120^{\mathrm{o}}$). The (anti)deuteron and antiproton distributions are then evaluated in these regions. In order to obtain the in-jet distributions, a subtraction between the Toward and Transverse region is performed.

The (anti)deuteron and antiproton distributions in the three azimuthal regions and in the in-jet region are presented in this work. The particle identification has been performed employing the information from the TPC and TOF detectors. After evaluating the correction for the acceptance and efficiency of the detector and the secondary contribution, a full study on the systematic uncertainties is performed. For both particle species, as already observed in pp collisions at $\sqrt{s} = 13$ TeV, the in-jet contribution is only about the 10% of the Toward region, showing how, with the CDF technique, also the Toward region is characterized by the underlying event. Nevertheless, it is possible to extract the in-jet contribution and use it for further studies.

The coalescence parameter in and out of jets, B_2^{jet} and B_2^{UE}, has been evaluated from the obtained transverse momentum distributions. As already observed in pp collisions at $\sqrt{s} = 13$ TeV, the coalescence parameter in-jet is enhanced with respect to the same quantity in the underlying event, as predicted by the coalescence model. The observed enhancement factor, of about 24, is larger with respect to the one already observed in pp collisions, of about 15. It is also possible to further investigate the difference between the two collision systems. For the underlying event, it is observed that B_2^{UE} (p–Pb) < B_2^{UE} (pp). This experimental result is in agreement with the coalescence model, since the source size of the p–Pb system, ~ 1.5 fm, is slightly larger with respect to the pp system, ~ 1 fm, hence a smaller coalescence parameter is expected. For the in-jet region, instead, the experimental data show that B_2^{jet} (p–Pb) > B_2^{jet} (pp). This result can be explained by different hypotheses, such as a different particle composition in jets in the two collision systems, stronger momentum correlations among the hadrons, or an higher average value of transverse momentum. With the current experimental results, that are dominated by the statistic uncertainty, it is not possible to discriminate between these hypotheses. The experimental results are also compared with the prediction obtained by the PYTHIA 8.3 Angantyr model with a reaction-based deuteron production, that is able to reproduce the gap observed between B_2^{jet} and B_2^{UE}.

To complement the results, the deuteron-over-proton ratio is studied both in pp and p–Pb collisions. It is observed that, in both cases, the ratio in-jet is higher with respect to the same quantity in the underlying event, with a factor between 1 and 2.5 in the pp case and between 2 and 4 in p–Pb case. It is also possible to study how the d/p ratio differs in the two collision systems for a common azimuthal region. It is observed that, for both the in-jet and underlying event case, the d/p ratio in the p–Pb system is higher with respect to the pp one, with a factor that varies between 1.2 and 1.4 in underlying event and 1.5 and 4 in jets. These experimental results suggest that the deuteron production is favoured in-jet with respect to the underlying event, as predicted by the coalescence model. Moreover, the different values in pp and p–Pb systems could be explained as a hint of a different particle composition in jets. However, since the experimental data are dominated by the statistical uncertainty, more studies with a larger data sample are needed, exploring also a full measurements of the jet hadrochemistry in different collision systems.

The presented results, coupled with the ones already published in pp collisions at $\sqrt{s} = 13$ TeV, help to constrain the coalescence model, using a novel approach and new observables. In order to further investigate the nucleus production in jets, and also to address the recent theoretical publications on this argument, a larger data sample is needed. To do so, it is possible to exploit the full data sample that will be collected at the end of the Run3, currently ongoing. In fact, thanks to the upgraded detector, the novel continuos readout and the new analysis framework, it is expected to collect an enlarged data sample with respect to the one already obtained in the Run2, in particular a factor 1000 in pp and 50 in Pb–Pb events more. With the full data sample, then, a new approach on the production of nuclei in jets can be adopted: it will be possible, in fact, to fully reconstruct the jets with jet finders algorithms, like the anti-k_T, and perform multi differential studies as a function of the jet cone radius, the jet total transverse momentum, the event multiplicity, etc.. Moreover, the use of the anti-k_T jet finder will allow to explore different jet/underlying event ratio with respect to the one presented in Run2, equal to 0.1 in both pp and p–Pb systems, hence testing the coalescence predictions reported in [201]. Finally, it will be possible to extend the study to other light (anti)nuclei, such as (anti)^{3}He, and to improve the current measurements, reducing the statistical uncertainties and exploring higher values of reduced transverse momentum.

Appendices

Appendix A

Additional experimental results

As presented in Chapter 4, the analysis reported in this work is performed in three azimuthal regions for both (anti)deuteron and antiproton. The procedure followed in the three azimuthal regions for the signal extraction and the correlated systematic uncertainty are the same, and the obtained results are similar. Only a selection of plots in the Toward region are reported in Chapter 4. Since the final spectra for all the azimuthal regions are presented, for completeness the additional experimental plots are reported in this appendix.

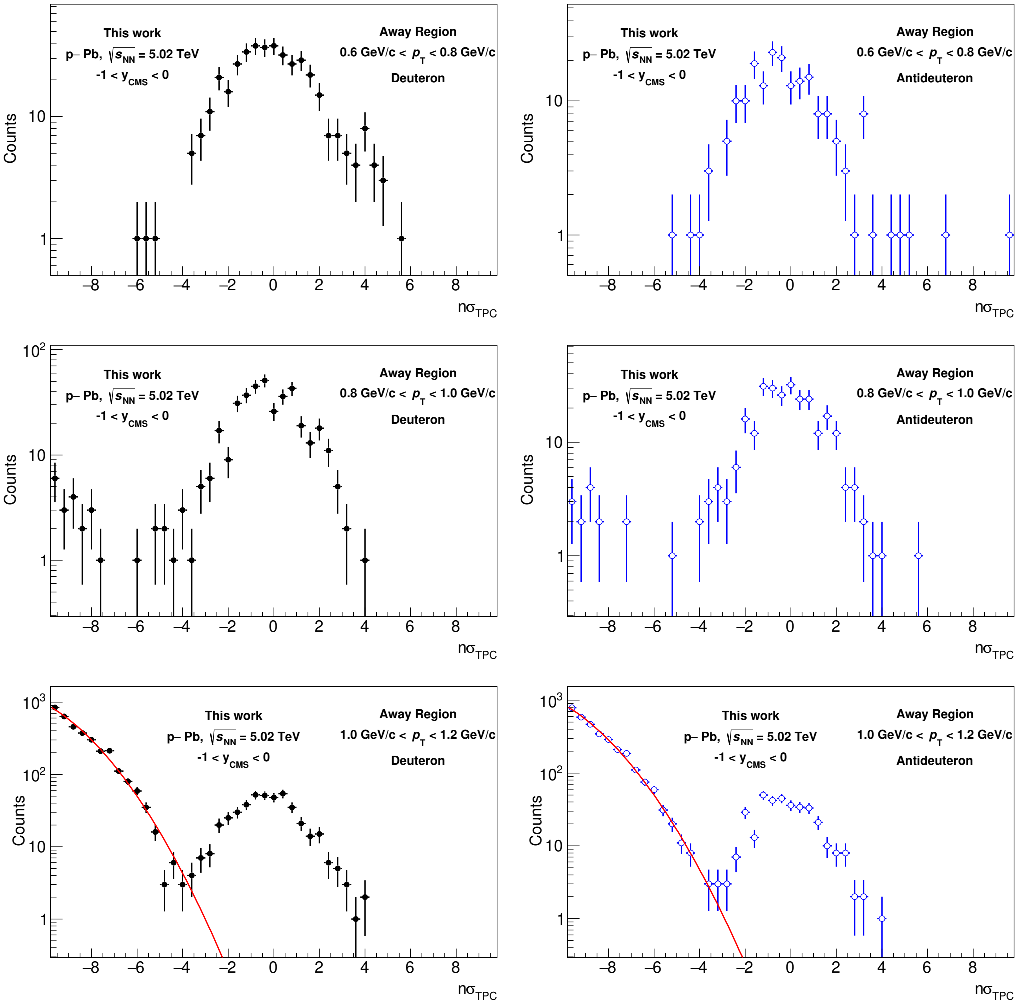

Figure A.1: $n\sigma_{\text{TPC}}$ distributions for the deuteron (left) and antideuteron (right) candidates in different p_{T} intervals in the Away region. The red line in the last row represents the Gaussian fit for the contamination of (anti)protons.

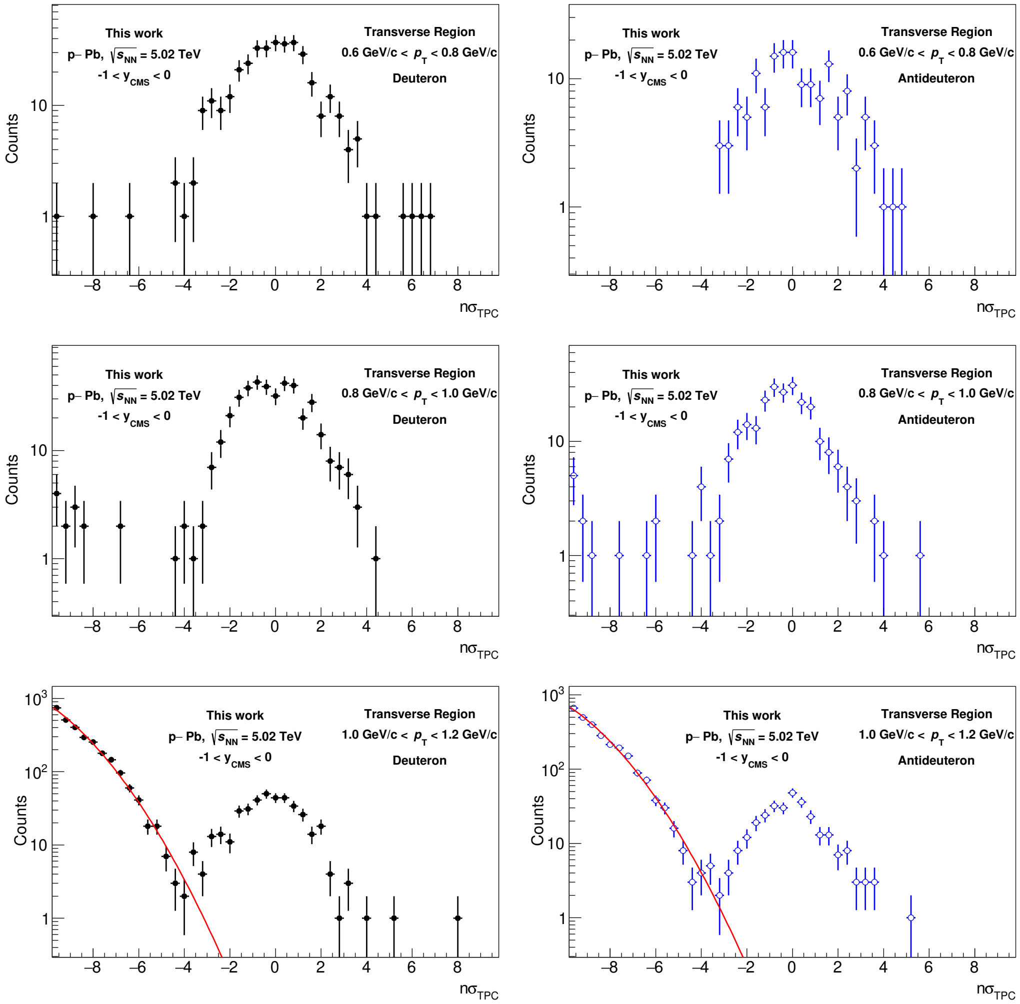

Figure A.2: $n\sigma_{\mathrm{TPC}}$ distributions for the deuteron (left) and antideuteron (right) candidates in different p_{T} intervals in the Transverse region. The red line in the last row represents the Gaussian fit for the contamination of (anti)protons.

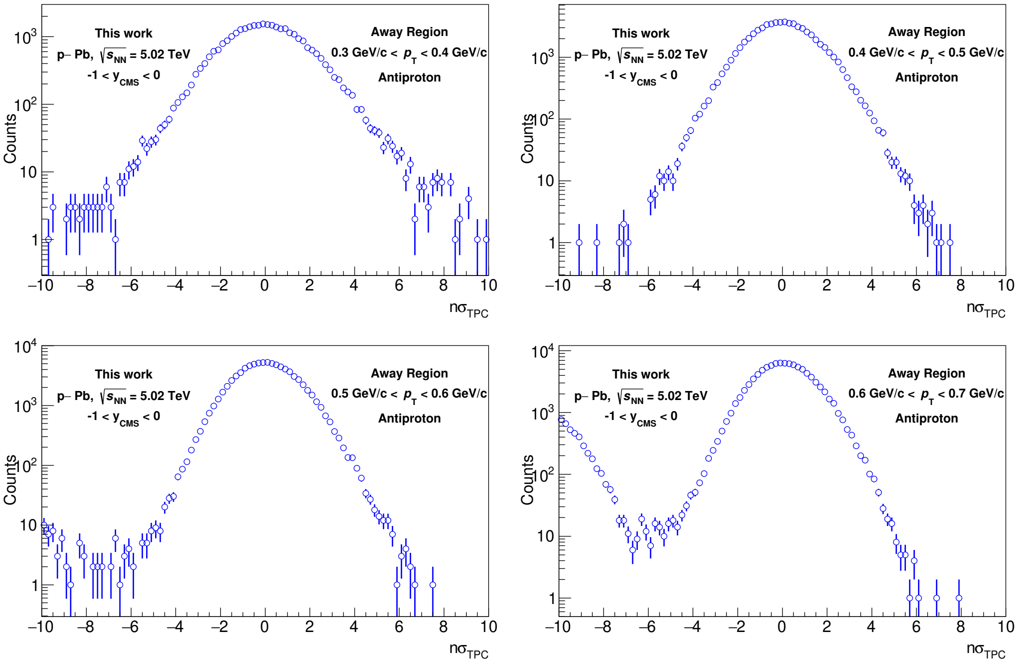

Figure A.3: $n\sigma_{\mathrm{TPC}}$ distribution for antiproton candidates in different p_{T} intervals in the Away region.

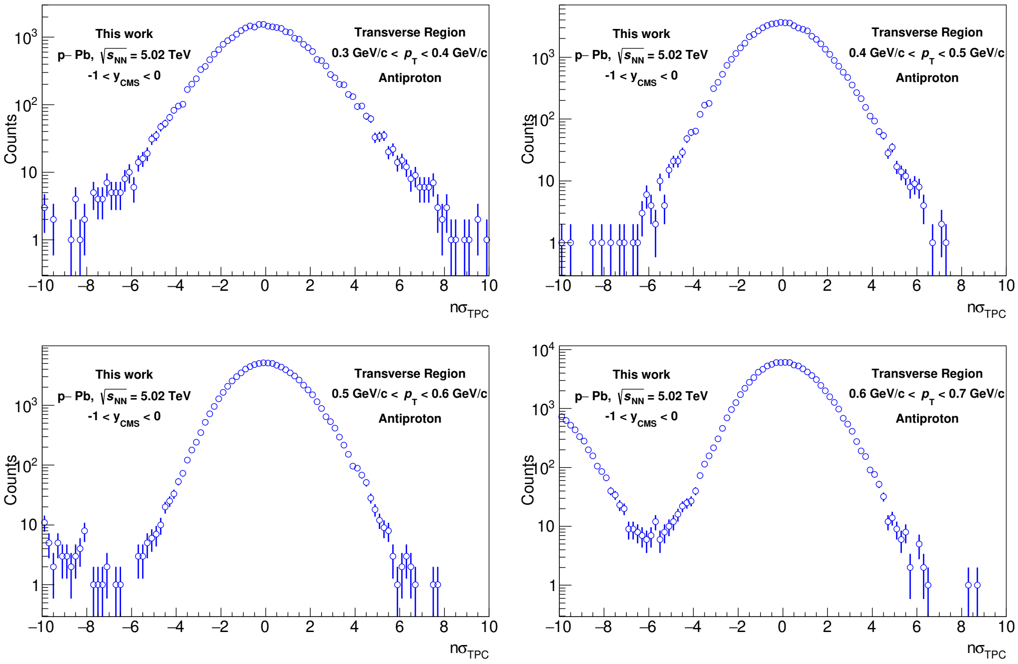

Figure A.4: $n\sigma_{\mathrm{TPC}}$ distribution for antiproton candidates in different p_{T} intervals in the Transverse region.

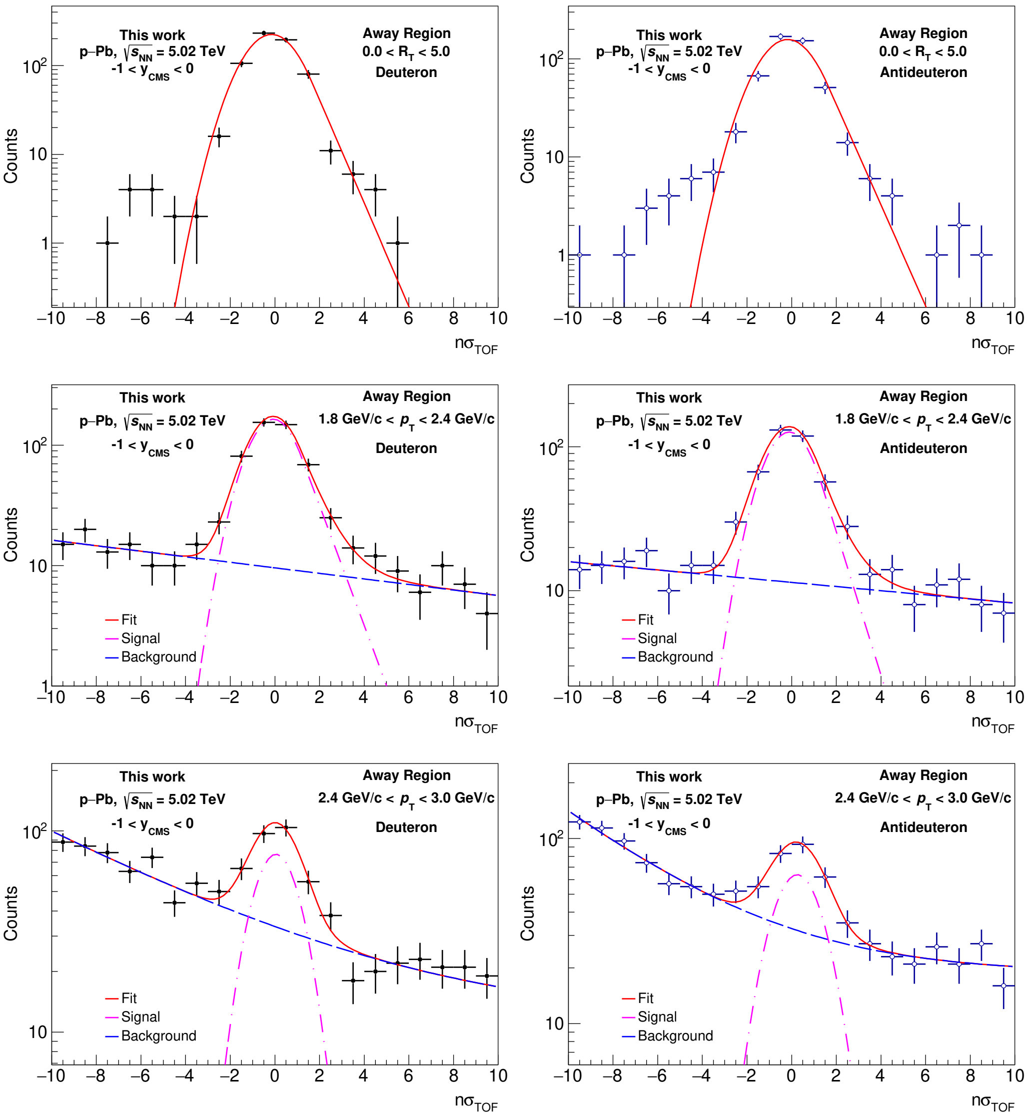

Figure A.5: $n\sigma_{\mathrm{TOF}}$ distributions for deuterons in the whole p_{T} interval analysed in the Away region. The red line represents the total fit, the magenta line the signal and the blue line the background parametrization.

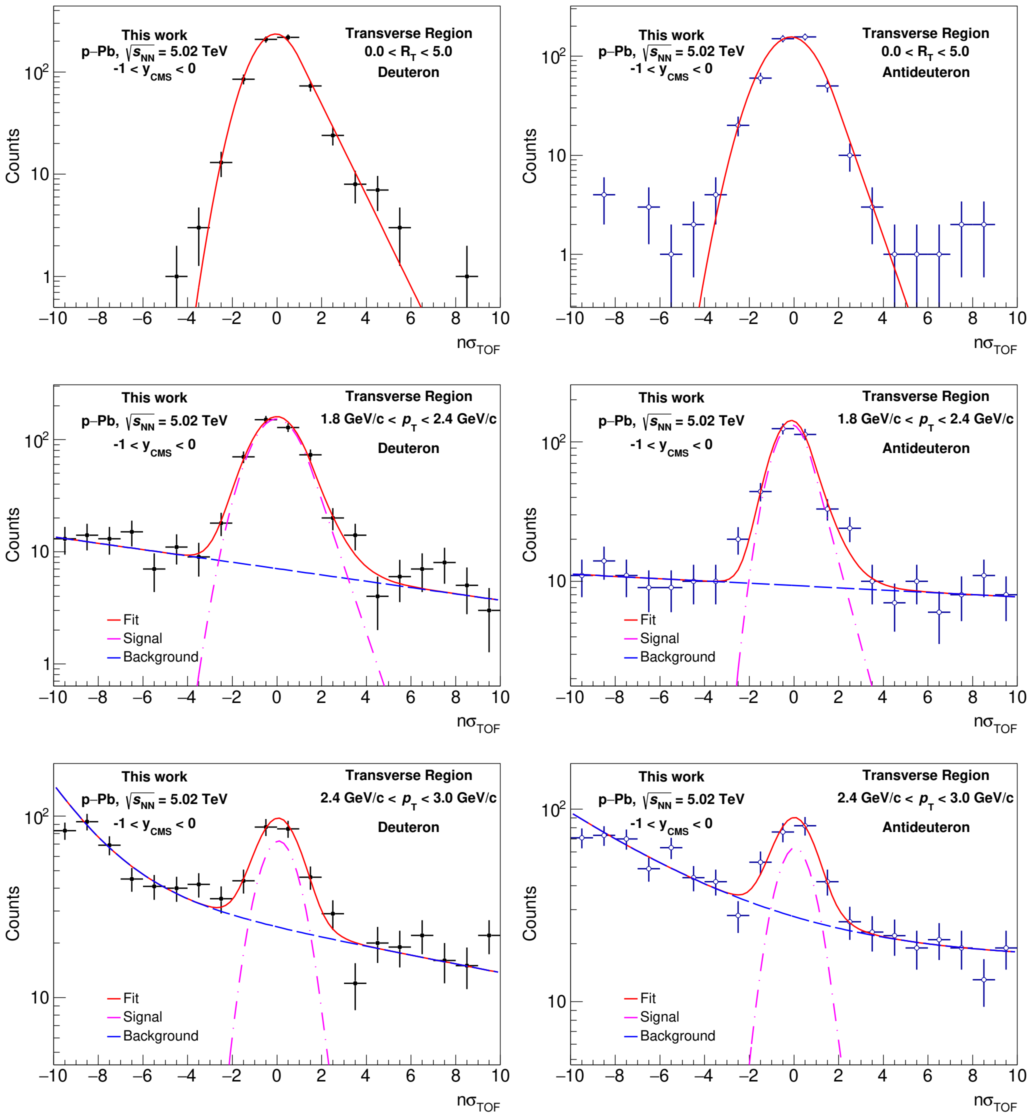

Figure A.6: $n\sigma_{\mathrm{TOF}}$ distributions for deuterons in the whole p_{T} interval analysed in the Transverse region. The red line represents the total fit, the magenta line the signal and the blue line the background parametrization.

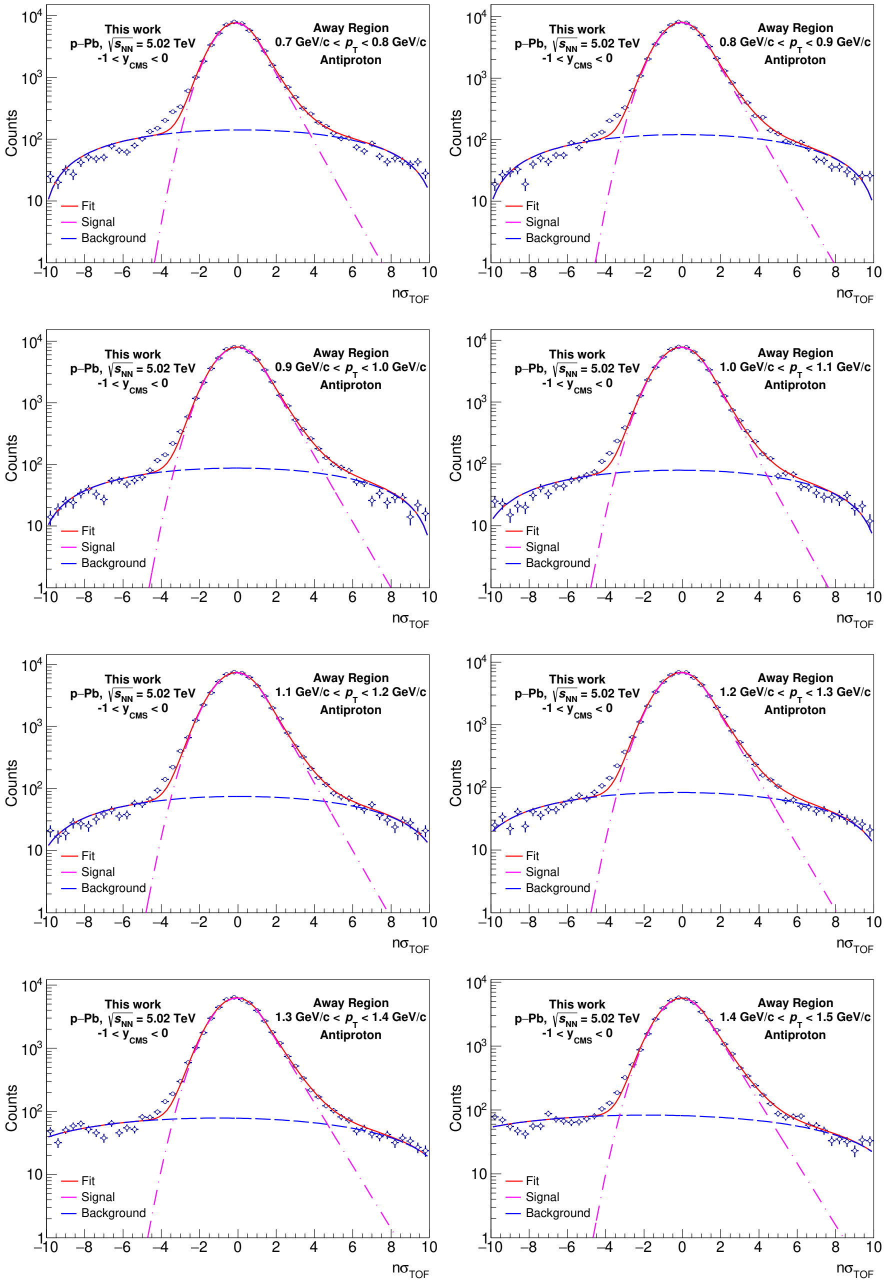

Figure A.7: $n\sigma_{\mathrm{TOF}}$ distributions for antiprotons in the whole p_{T} interval analysed in the Away region. The red line represents the total fit, the magenta line the signal and the blue line the background parametrization.

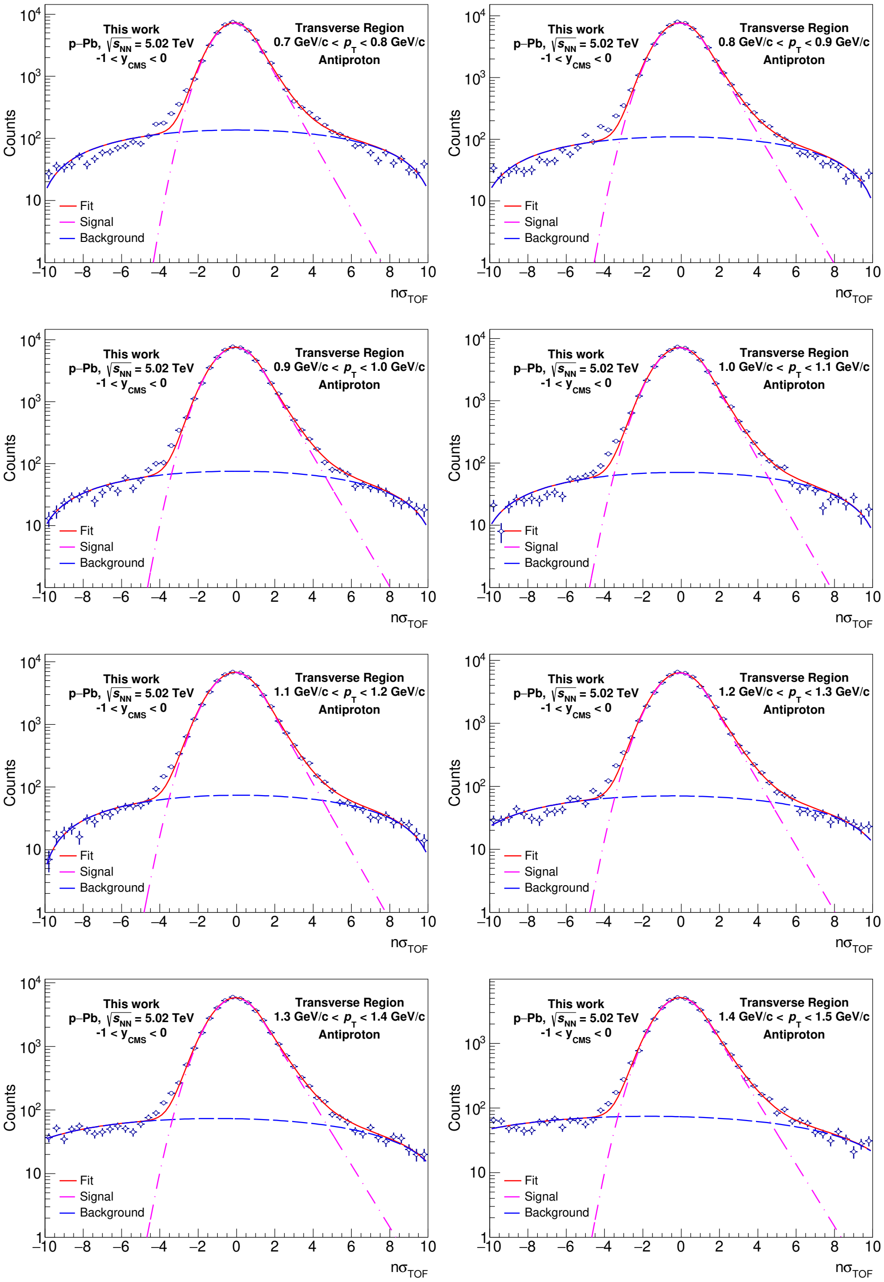

Figure A.8: $n\sigma_{\mathrm{TOF}}$ distributions for antiprotons in the whole p_{T} interval analysed in the Transverse region. The red line represents the total fit, the magenta line the signal and the blue line the background parametrization.

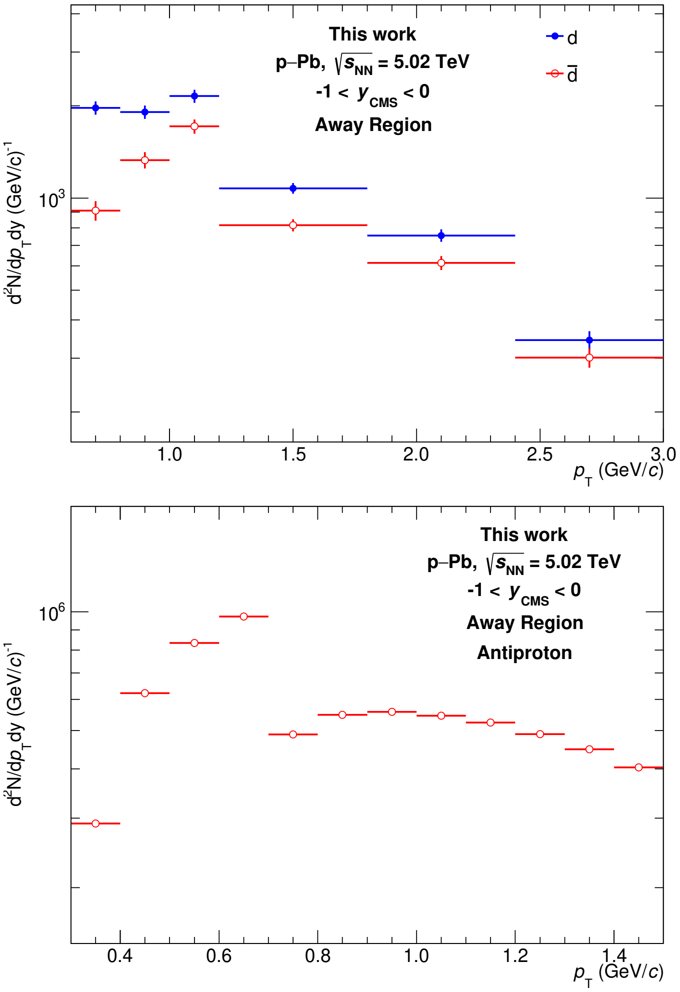

Figure A.9: Raw spectra for (anti)deuterons (top) and antiprotons (bottom) in the Away region as a function of the transverse momentum.

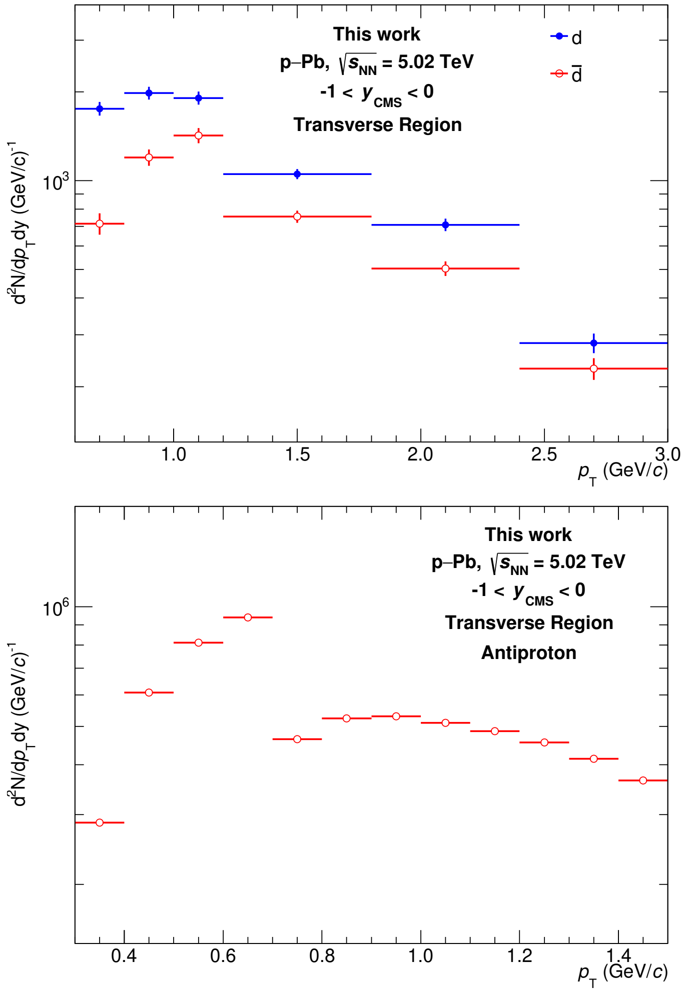

Figure A.10: Raw spectra for (anti)deuterons (top) and antiprotons (bottom) in the Transverse region as a function of the transverse momentum.

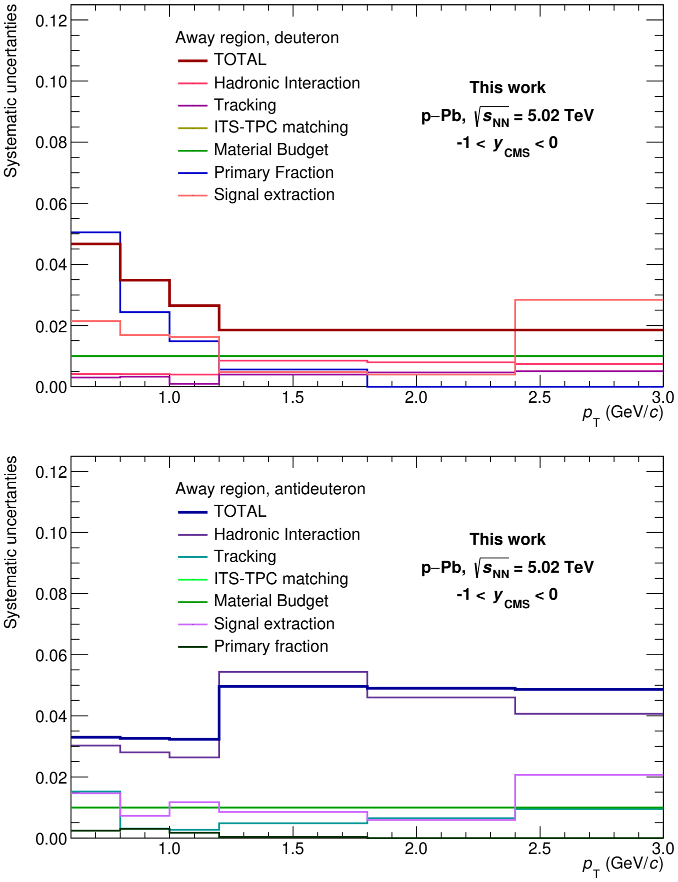

Figure A.11: Summary of the different sources of systematic uncertainties for the deuteron (top) and antideuteron (bottom) case in the Away region as a function of the transverse momentum.

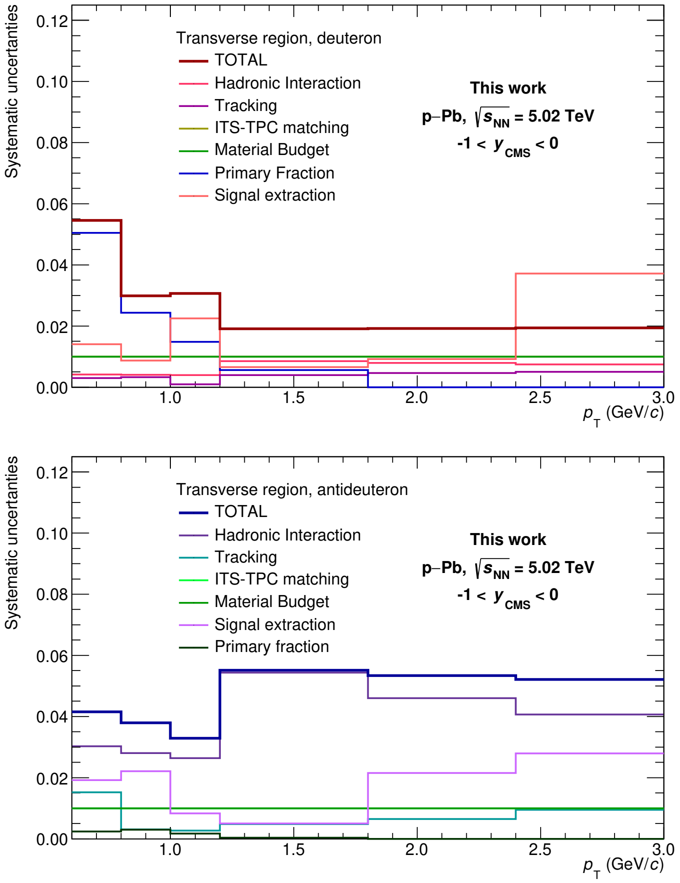

Figure A.12: Summary of the different sources of systematic uncertainties for the deuteron (top) and antideuteron (bottom) case in the Transverse region as a function of the transverse momentum.

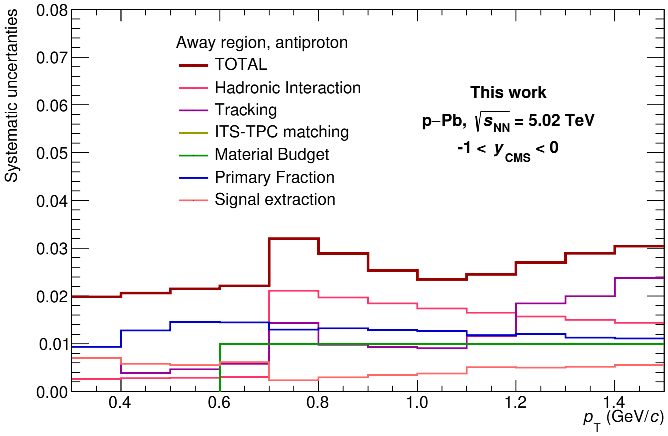

Figure A.13: Summary of the different sources of systematic uncertainties for the antiproton in the Away region.

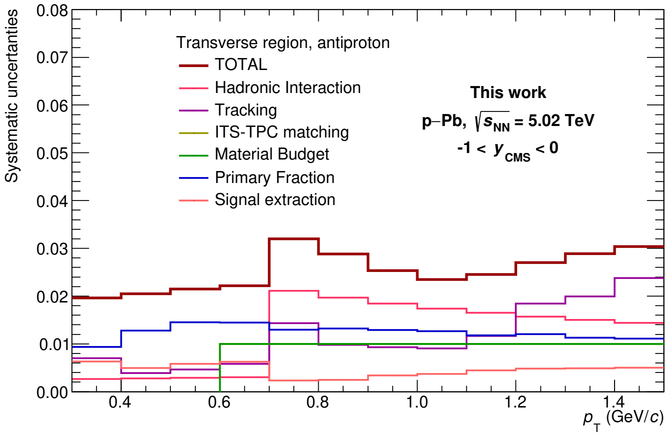

Figure A.14: Summary of the different sources of systematic uncertainties for the antiproton in the Transverse region.

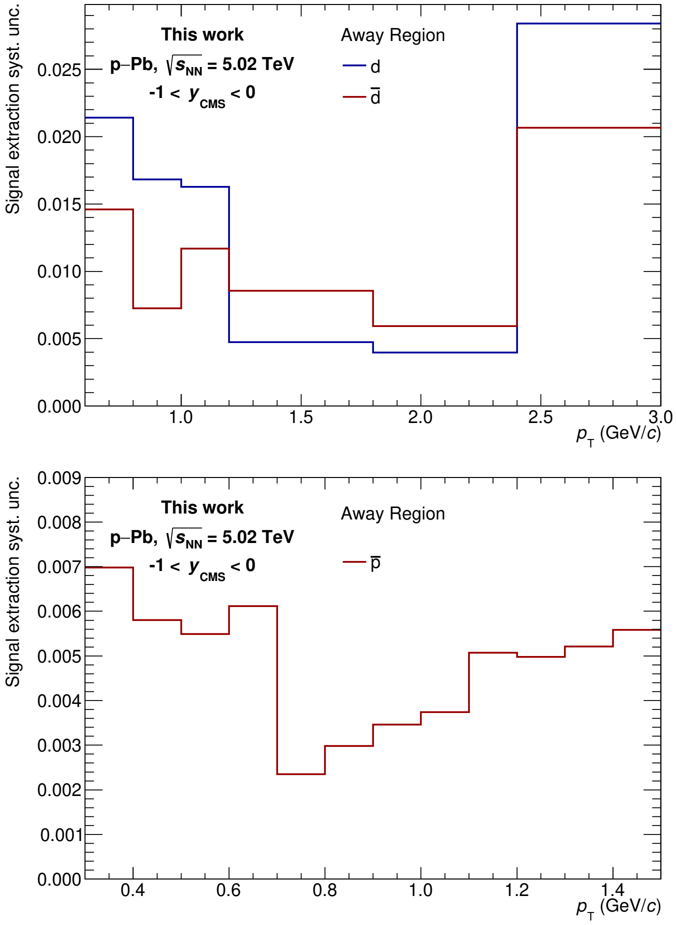

Figure A.15: Systematic uncertainty due to the signal extraction for (anti)deuterons (top) and antiprotons (bottom) in the Away region as a function of the transverse momentum.

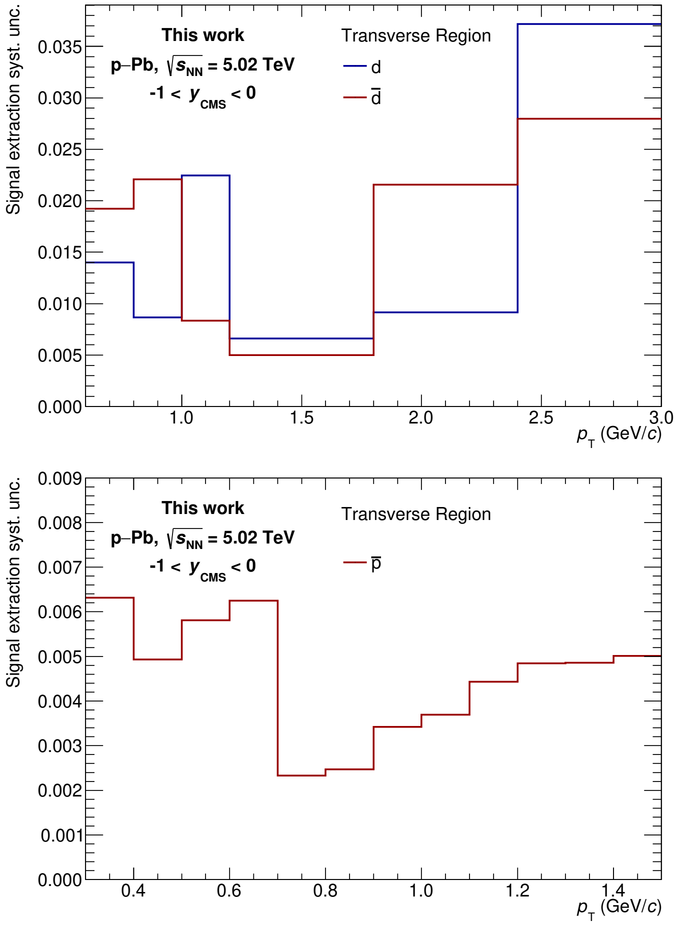

Figure A.16: Systematic uncertainty due to the signal extraction for (anti)deuterons (top) and antiprotons (bottom) in the Transverse region as a function of the transverse momentum.

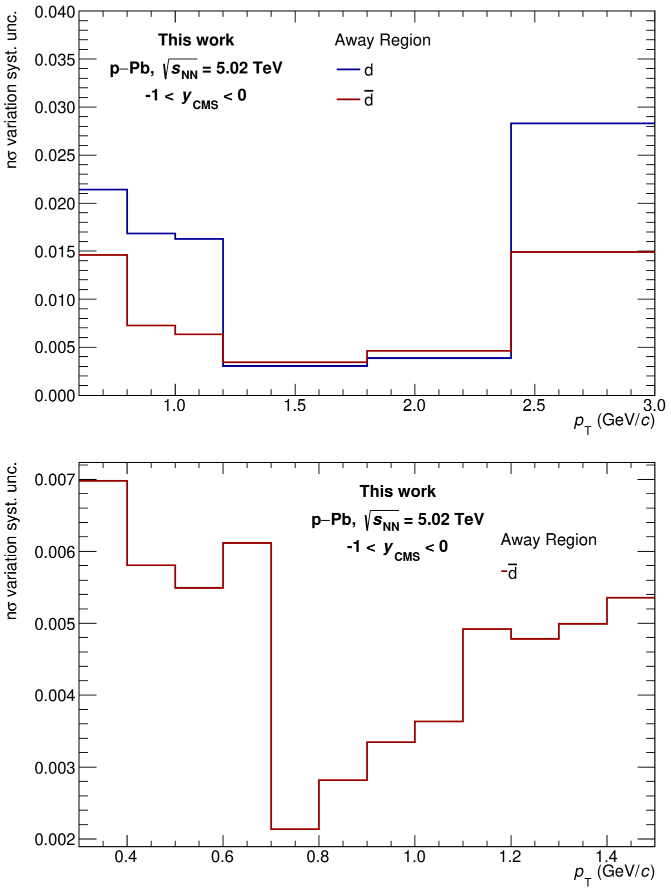

Figure A.17: Systematic uncertainty due to the different signal integration intervals for (anti)deuterons (top) and antiprotons (bottom) in the Away region as a function of the transverse momentum.

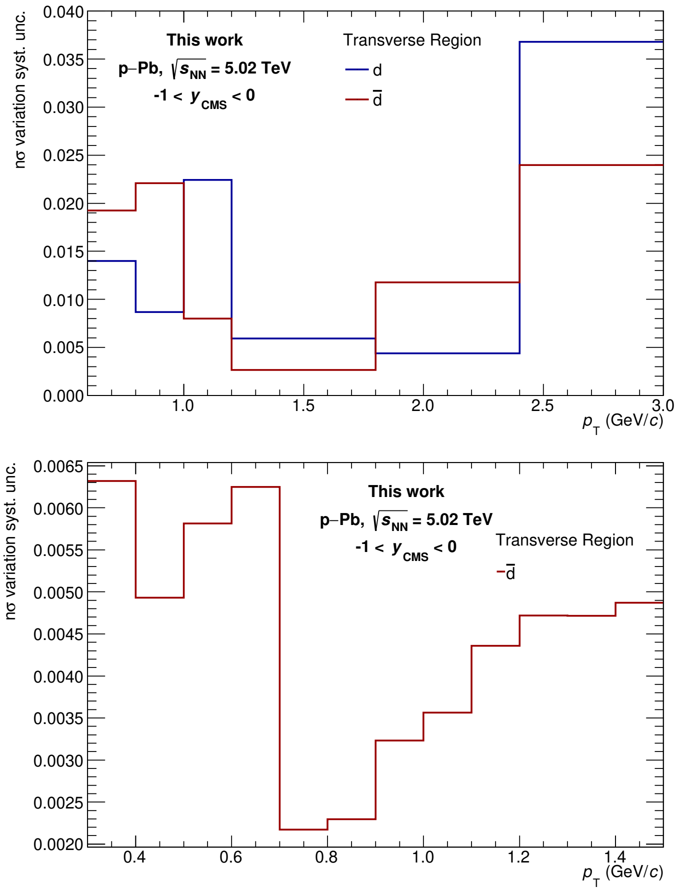

Figure A.18: Systematic uncertainty due to the different signal integration intervals for (anti)deuterons (top) and antiprotons (bottom) in the Transverse region as a function of the transverse momentum.

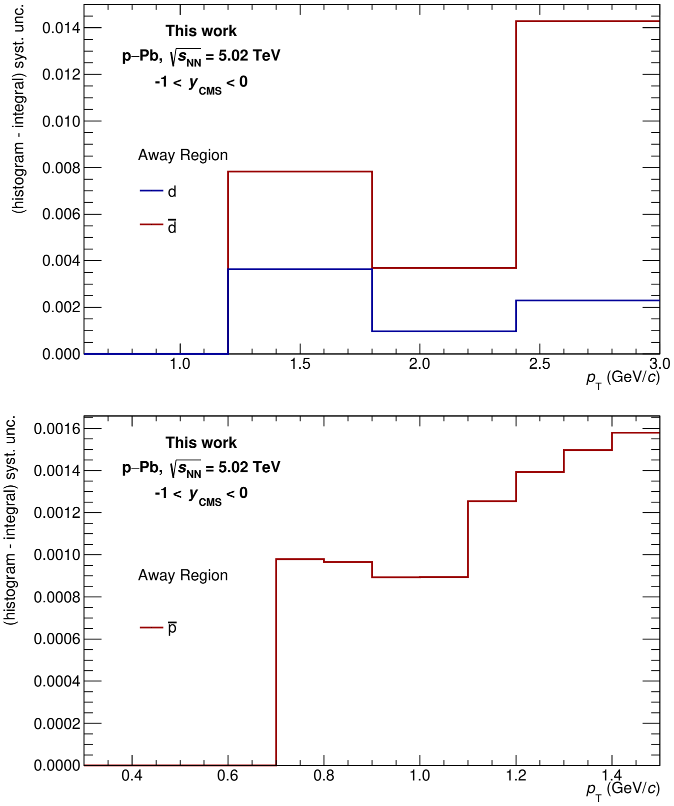

Figure A.19: Systematic uncertainty due to the different integration methods for (anti)deuterons (top) and antiprotons (bottom) in the Away region as a function of the transverse momentum.

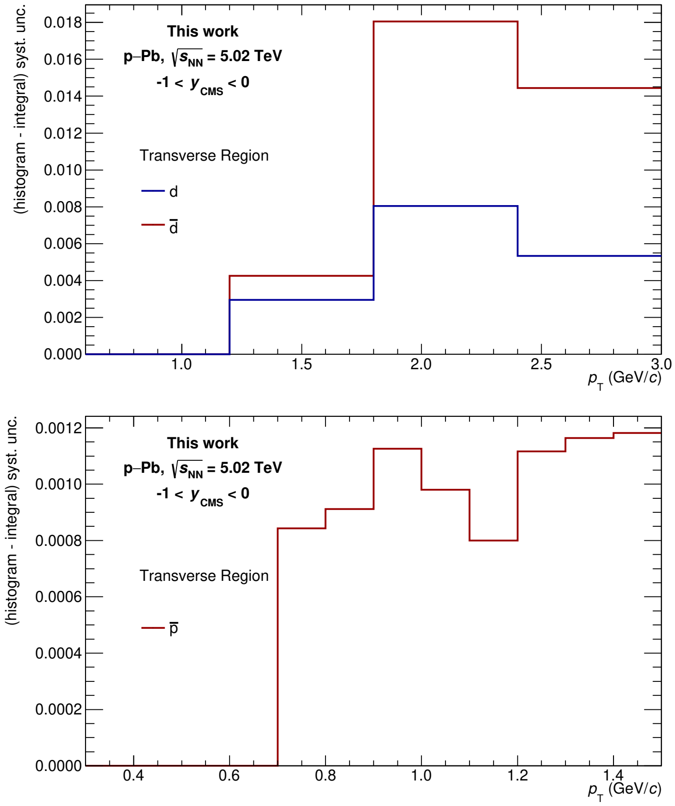

Figure A.20: Systematic uncertainty due to the different integration methods for (anti)deuterons (top) and antiprotons (bottom) in the Transverse region as a function of the transverse momentum.

Bibliography

[1] J. Chadwick, “The existence of a neutron”, *Proceedings of the Royal Society of London. Series A, Containing Papers of a Mathematical and Physical Character* **136** (1932) 692–708. `http://www.jstor.org/stable/95816`.

[2] M. Gell-Mann, “The Eightfold Way: A Theory of strong interaction symmetry”,. `CTSL-20,TID-12608,1961`.

[3] Y. Ne’eman, “Derivation of strong interactions from a gauge invariance”, *Nucl. Phys.* **26** (1961) 222–229.

[4] B. Martin and G. Shaw, *Particle Physics*. Wiley, Manchester Physics Series, 2008. `https://books.google.it/books?id=whIbrWJdEJQC`.

[5] M. Gell-Mann, “A Schematic Model of Baryons and Mesons”, *Phys. Lett.* **8** (1964) 214–215.

[6] G. Zweig, “An SU(3) model for strong interaction symmetry and its breaking. Version 2”, *Developments in the Quark Theory of Hadrons* (1964) 22–101.

[7] E. D. Bloom *et al.*, “High-Energy Inelastic e-p Scattering at 6° and 10°”, *Phys. Rev. Lett.* **23** (1969) 930–934.

[8] M. Breidenbach, J. I. Friedman, H. W. Kendall, E. D. Bloom, D. H. Coward, H. C. DeStaebler, J. Drees, L. W. Mo, and R. E. Taylor,

"Observed behavior of highly inelastic electron-proton scattering", *Phys. Rev. Lett.* **23** (1969) 935–939.

[9] O. W. Greenberg, "Spin and Unitary-Spin Independence in a Paraquark Model of Baryons and Mesons", *Phys. Rev. Lett.* **13** (Nov, 1964) 598–602.

[10] K. Chetyrkin, R. Harlander, and J. Kühn, "Quartic mass corrections to R at α", *Nuclear Physics B* **586** (2000) 56–72. [Erratum: Nucl. Phys. B **634** (2002) 413].

[11] **Particle Data Group** Collaboration, S. Navas *et al.*, "Review of Particle Physics", *Phys. Rev. D* **110** (2024) 030001.

[12] M. E. Peskin and D. V. Schroeder, *An Introduction to quantum field theory*. Addison-Wesley, Reading, USA, 1995.

[13] K. G. Wilson, "Confinement of Quarks", *Phys. Rev. D* **10** (1974) 2445–2459.

[14] O. Philipsen, "Lattice QCD at finite temperature and density", *Eur. Phys. J. ST* **152** (2007) 29–60, `arXiv:0708.1293 [hep-lat]`.

[15] Z. Fodor and C. Hoelbling, "Light Hadron Masses from Lattice QCD", *Rev. Mod. Phys.* **84** (2012) 449, `arXiv:1203.4789 [hep-lat]`.

[16] G. 't Hooft, "A Planar Diagram Theory for Strong Interactions", *Nucl. Phys. B* **72** (1974) 461.

[17] P. Kovtun, D. T. Son, and A. O. Starinets, "Viscosity in strongly interacting quantum field theories from black hole physics", *Phys. Rev. Lett.* **94** (2005) 111601, `arXiv:hep-th/0405231`.

[18] R. Machleidt and D. R. Entem, "Chiral effective field theory and nuclear forces", *Phys. Rept.* **503** (2011) 1–75, `arXiv:1105.2919 [nucl-th]`.

[19] A. G. Grozin, *Heavy quark effective theory*, vol. 201. Springer Tracts Mod. Phys., 2004.

[20] E. Eichten, K. Gottfried, T. Kinoshita, J. B. Kogut, K. D. Lane, and T.-M. Yan, "The Spectrum of Charmonium", *Phys. Rev. Lett.* **34** (1975) 369–372. [Erratum: Phys.Rev.Lett. 36, 1276 (1976)].

[21] G. Parisi, R. Petronzio, and F. Rapuano, "A Measurement of the String Tension Near the Continuum Limit", *Phys. Lett. B* **128** (1983) 418–420.

[22] **MILC** Collaboration, A. Bazavov *et al.*, "Nonperturbative QCD Simulations with 2+1 Flavors of Improved Staggered Quarks", *Rev. Mod. Phys.* **82** (2010) 1349–1417, `arXiv:0903.3598 [hep-lat]`.

[23] R. S. Bhalerao, "Relativistic heavy-ion collisions", in *1st Asia-Europe-Pacific School of High-Energy Physics*, pp. 219–239. 2014. `arXiv:1404.3294 [nucl-th]`.

[24] M. Baldo, M. Buballa, F. Burgio, F. Neumann, M. Oertel, and H. J. Schulze, "Neutron stars and the transition to color superconducting quark matter", *Phys. Lett. B* **562** (2003) 153–160, `arXiv:nucl-th/0212096`.

[25] **ALICE** Collaboration, S. Acharya *et al.*, "Measurements of Chemical Potentials in Pb-Pb Collisions at $\sqrt{s_{\rm NN}} = 5.02$ TeV", *Phys. Rev. Lett.* **133** (2024) 092301, `arXiv:2311.13332 [nucl-ex]`.

[26] J. Rafelski, "Connecting QGP-Heavy Ion Physics to the Early Universe", *Nucl. Phys. B Proc. Suppl.* **243-244** (2013) 155–162, `arXiv:1306.2471 [astro-ph.CO]`.

[27] U. W. Heinz and M. Jacob, "Evidence for a new state of matter: An Assessment of the results from the CERN lead beam program", `arXiv:nucl-th/0002042`.

[28] C. A. Ogilvie, "Review of nuclear reactions at the AGS", *Nucl. Phys. A* **698** (2002) 3–12, `arXiv:nucl-ex/0104010`.

[29] S. Basu, S. Thakur, T. K. Nayak, and C. A. Pruneau, "Multiplicity and pseudorapidity density distributions of charged particles produced in pp, pA and AA collisions at RHIC & LHC energies", *J. Phys. G* **48** (2020) 025103, `arXiv:2008.07802 [nucl-ex]`.

[30] **LHCb** Collaboration, R. Aaij *et al.*, “Centrality determination in heavy-ion collisions with the LHCb detector”, *JINST* **17** (2022) P05009, `arXiv:2111.01607 [nucl-ex]`.

[31] **ALICE** Collaboration, B. Abelev *et al.*, “Centrality determination of Pb-Pb collisions at $\sqrt{s_{\rm NN}}$ = 2.76 TeV with ALICE”, *Phys. Rev. C* **88** (2013) 044909, `arXiv:1301.4361 [nucl-ex]`.

[32] M. L. Miller, K. Reygers, S. J. Sanders, and P. Steinberg, “Glauber modeling in high energy nuclear collisions”, *Ann. Rev. Nucl. Part. Sci.* **57** (2007) 205–243, `arXiv:nucl-ex/0701025`.

[33] H. De Vries, C. W. De Jager, and C. De Vries, “Nuclear charge and magnetization density distribution parameters from elastic electron scattering”, *Atom. Data Nucl. Data Tabl.* **36** (1987) 495–536.

[34] D. Kharzeev, E. Levin, and M. Nardi, “Color glass condensate at the LHC: Hadron multiplicities in pp, pA and AA collisions”, *Nucl. Phys. A* **747** (2005) 609–629, `arXiv:hep-ph/0408050`.

[35] W. T. Deng, X. N. Wang, and R. Xu, “Hadron production in p+p, p+Pb, and Pb+Pb collisions with the HIJING 2.0 model at energies available at the CERN Large Hadron Collider”, *Phys. Rev. C* **83** (2011) 014915, `arXiv:1008.1841 [hep-ph]`.

[36] **ALICE** Collaboration, B. Abelev *et al.*, “Performance of the ALICE experiment at the CERN LHC”, *Int. J. Mod. Phys. A* **29** (2014) 1430044, `arXiv:1402.4476 [nucl-ex]`.

[37] **ALICE** Collaboration, S. Acharya *et al.*, “The ALICE experiment: a journey through QCD”, *Eur. Phys. J. C* **84** (2024) 813, `arXiv:2211.04384 [nucl-ex]`.

[38] C. Gale, S. Jeon, and B. Schenke, “Hydrodynamic Modeling of Heavy-Ion Collisions”, *Int. J. Mod. Phys. A* **28** (2013) 1340011, `arXiv:1301.5893 [nucl-th]`.

[39] **ALICE** Collaboration, K. Aamodt *et al.*, “Two-pion Bose-Einstein correlations in central Pb-Pb collisions at $\sqrt{s_{\rm NN}} = 2.76$ TeV”, *Phys. Lett. B* **696** (2011) 328–337, `arXiv:1012.4035 [nucl-ex]`.

[40] **ALICE** Collaboration, J. Adam *et al.*, "Centrality dependence of pion freeze-out radii in Pb-Pb collisions at $\sqrt{s_{\mathrm{NN}}} = 2.76$ TeV", *Phys. Rev. C* **93** (2016) 024905, `arXiv:1507.06842 [nucl-ex]`.

[41] **ALICE** Collaboration, J. Adam *et al.*, "Direct photon production in Pb-Pb collisions at $\sqrt{s_{\mathrm{NN}}} = 2.76$ TeV", *Phys. Lett. B* **754** (2016) 235–248, `arXiv:1509.07324 [nucl-ex]`.

[42] **ALICE** Collaboration, S. Acharya *et al.*, "Prompt D^0, D^+, and D^{*+} production in Pb–Pb collisions at $\sqrt{s_{\mathrm{NN}}}$ = 5.02 TeV", *JHEP* **01** (2022) 174, `arXiv:2110.09420 [nucl-ex]`.

[43] **STAR** Collaboration, J. Adams *et al.*, "Evidence from d + Au measurements for final state suppression of high p_{T} hadrons in Au+Au collisions at RHIC", *Phys. Rev. Lett.* **91** (2003) 072304, `arXiv:nucl-ex/0306024`.

[44] **ALICE** Collaboration, S. Acharya *et al.*, "Transverse momentum spectra and nuclear modification factors of charged particles in pp, p-Pb and Pb-Pb collisions at the LHC", *JHEP* **11** (2018) 013, `arXiv:1802.09145 [nucl-ex]`.

[45] **ALICE** Collaboration, J. Adam *et al.*, "Measurement of jet quenching with semi-inclusive hadron-jet distributions in central Pb-Pb collisions at $\sqrt{s_{\mathrm{NN}}} = 2.76$ TeV", *JHEP* **09** (2015) 170, `arXiv:1506.03984 [nucl-ex]`.

[46] **ALICE** Collaboration, S. Acharya *et al.*, "Measurement of the groomed jet radius and momentum splitting fraction in pp and Pb$-$Pb collisions at $\sqrt{s_{\mathrm{NN}}} = 5.02$ TeV", *Phys. Rev. Lett.* **128** (2022) 102001, `arXiv:2107.12984 [nucl-ex]`.

[47] **ALICE** Collaboration, S. Acharya *et al.*, "Medium modification of the shape of small-radius jets in central Pb-Pb collisions at $\sqrt{s_{\mathrm{NN}}} = 2.76\,\mathrm{TeV}$", *JHEP* **10** (2018) 139, `arXiv:1807.06854 [nucl-ex]`.

[48] **ALICE** Collaboration, J. Adam *et al.*, "Measurement of jet quenching with semi-inclusive hadron-jet distributions in central

Pb-Pb collisions at $\sqrt{s_{\rm NN}} = 2.76$ TeV", *JHEP* **09** (2015) 170, `arXiv:1506.03984 [nucl-ex]`.

[49] T. Matsui and H. Satz, "J/ψ Suppression by Quark-Gluon Plasma Formation", *Phys. Lett. B* **178** (1986) 416–422.

[50] **NA50** Collaboration, M. C. Abreu *et al.*, "Evidence for deconfinement of quarks and gluons from the J/Ψ suppression pattern measured in Pb + Pb collisions at the CERN SPS", *Phys. Lett. B* **477** (2000) 28–36.

[51] **NA50** Collaboration, B. Alessandro *et al.*, "A New measurement of J/Ψ suppression in Pb-Pb collisions at 158-GeV per nucleon", *Eur. Phys. J. C* **39** (2005) 335–345, `arXiv:hep-ex/0412036`.

[52] **PHENIX** Collaboration, A. Adare *et al.*, "J/ψ Production vs Centrality, Transverse Momentum, and Rapidity in Au+Au Collisions at $\sqrt{s_{\rm NN}} = 200$ GeV", *Phys. Rev. Lett.* **98** (2007) 232301, `arXiv:nucl-ex/0611020`.

[53] **PHENIX** Collaboration, A. Adare *et al.*, "Measurement of $\Upsilon(1S + 2S + 3S)$ production in $p + p$ and Au+Au collisions at $\sqrt{s_{\rm NN}} = 200$ GeV", *Phys. Rev. C* **91** (2015) 024913, `arXiv:1404.2246 [nucl-ex]`.

[54] **STAR** Collaboration, L. Adamczyk *et al.*, "J/ψ production at high transverse momenta in $p + p$ and Au+Au collisions at $\sqrt{s_{\rm NN}} = 200$ GeV", *Phys. Lett. B* **722** (2013) 55–62, `arXiv:1208.2736 [nucl-ex]`.

[55] **STAR** Collaboration, L. Adamczyk *et al.*, "J/ψ production at low p_T in Au + Au and Cu + Cu collisions at $\sqrt{s_{\rm NN}} = 200$ GeV with the STAR detector", *Phys. Rev. C* **90** (2014) 024906, `arXiv:1310.3563 [nucl-ex]`.

[56] **STAR** Collaboration, J. Adam *et al.*, "Measurement of inclusive J/ψ suppression in Au+Au collisions at $\sqrt{s_{\rm NN}}$ = 200 GeV through the dimuon channel at STAR", *Phys. Lett. B* **797** (2019) 134917, `arXiv:1905.13669 [nucl-ex]`.

[57] **ALICE** Collaboration, S. Acharya *et al.*, "Measurements of inclusive J/ψ production at midrapidity and forward rapidity in Pb–Pb collisions at $\sqrt{s_{\mathrm{NN}}} = 5.02$ TeV", *Phys. Lett. B* **849** (2024) 138451, `arXiv:2303.13361 [nucl-ex]`.

[58] S. Digal, P. Petreczky, and H. Satz, "Quarkonium feed down and sequential suppression", *Phys. Rev. D* **64** (2001) 094015, `arXiv:hep-ph/0106017`.

[59] **CMS** Collaboration, S. Chatrchyan *et al.*, "Observation of Sequential Y Suppression in Pb-Pb Collisions", *Phys. Rev. Lett.* **109** (2012) 222301, `arXiv:1208.2826 [nucl-ex]`. [Erratum: Phys. Rev. Lett. **120**, (2018) 199903].

[60] **ALICE** Collaboration, B. B. Abelev *et al.*, "Suppression of $\Upsilon(1S)$ at forward rapidity in Pb-Pb collisions at $\sqrt{s_{\mathrm{NN}}} = 2.76$ TeV", *Phys. Lett. B* **738** (2014) 361–372, `arXiv:1405.4493 [nucl-ex]`.

[61] **ALICE** Collaboration, S. Acharya *et al.*, "Y production and nuclear modification at forward rapidity in Pb–Pb collisions at $\sqrt{s_{\mathrm{NN}}} = 5.02$ TeV", *Phys. Lett. B* **822** (2021) 136579, `arXiv:2011.05758 [nucl-ex]`.

[62] H. Song, S. A. Bass, U. Heinz, T. Hirano, and C. Shen, "Hadron spectra and elliptic flow for 200 A GeV Au+Au collisions from viscous hydrodynamics coupled to a Boltzmann cascade", *Phys. Rev. C* **83** (2011) 054910, `arXiv:1101.4638 [nucl-th]`. [Erratum: Phys. Rev. C **86**, (2012) 059903].

[63] **ALICE** Collaboration, B. Abelev *et al.*, "Pion, Kaon, and Proton Production in Central Pb–Pb Collisions at $\sqrt{s_{\mathrm{NN}}} = 2.76$ TeV", *Phys. Rev. Lett.* **109** (2012) 252301, `arXiv:1208.1974 [hep-ex]`.

[64] **ALICE** Collaboration, S. Acharya *et al.*, "Production of charged pions, kaons, and (anti-)protons in Pb-Pb and inelastic pp collisions at $\sqrt{s_{\mathrm{NN}}} = 5.02$ TeV", *Phys. Rev. C* **101** (2020) 044907, `arXiv:1910.07678 [nucl-ex]`.

[65] V. Y. Naboka, I. A. Karpenko, and Y. M. Sinyukov, "Thermalization, evolution, and observables at energies available at the CERN Large Hadron Collider in an integrated hydrokinetic model of A+A collisions", *Phys. Rev. C* **93** (2016) 024902, `arXiv:1508.07204 [hep-ph]`.

[66] G. Denicol, A. Monnai, S. Ryu, and B. Schenke, "New insights from 3D simulations of heavy ion collisions", *Nucl. Phys. A* **956** (2016) 288–291, `arXiv:1512.08231 [nucl-th]`.

[67] **ALICE** Collaboration, J. Adam *et al.*, "Anisotropic flow of charged particles in Pb-Pb collisions at $\sqrt{s_{\mathrm{NN}}} = 5.02$ TeV", *Phys. Rev. Lett.* **116** (2016) 132302, `arXiv:1602.01119 [nucl-ex]`.

[68] J. Rafelski and B. Muller, "Strangeness Production in the Quark - Gluon Plasma", *Phys. Rev. Lett.* **48** (1982) 1066. [Erratum: Phys. Rev. Lett. **56**, (1986) 2334].

[69] **ALICE** Collaboration, S. Acharya *et al.*, "Multiplicity dependence of π, K, and p production in pp collisions at $\sqrt{s} = 13$ TeV", *Eur. Phys. J. C* **80** (2020) 693, `arXiv:2003.02394 [nucl-ex]`.

[70] **ALICE** Collaboration, J. Adam *et al.*, "Enhanced production of multi-strange hadrons in high-multiplicity proton-proton collisions", *Nature Phys.* **13** (2017) 535–539, `arXiv:1606.07424 [nucl-ex]`.

[71] A. Andronic, P. Braun-Munzinger, and J. Stachel, "Hadron production in central nucleus-nucleus collisions at chemical freeze-out", *Nucl. Phys. A* **772** (2006) 167–199, `arXiv:nucl-th/0511071`.

[72] R. Hanbury Brown and R. Q. Twiss, "A Test of a new type of stellar interferometer on Sirius", *Nature* **178** (1956) 1046–1048.

[73] F. Bellini and A. P. Kalweit, "Testing production scenarios for (anti-)(hyper-)nuclei and exotica at energies available at the CERN Large Hadron Collider", *Phys. Rev. C* **99** (2019) 054905, `arXiv:1807.05894 [hep-ph]`.

[74] **ALICE** Collaboration, B. Abelev *et al.*, "Charged kaon femtoscopic correlations in pp collisions at $\sqrt{s} = 7$ TeV", *Phys. Rev. D* **87** (2013) 052016, `arXiv:1212.5958 [hep-ex]`.

[75] **ALICE** Collaboration, J. Adam *et al.*, "Two-pion femtoscopy in p-Pb collisions at $\sqrt{s_{\mathrm{NN}}} = 5.02$ TeV", *Phys. Rev. C* **91** (2015) 034906, `arXiv:1502.00559 [nucl-ex]`.

[76] K.-J. Sun, C. M. Ko, and B. Dönigus, "Suppression of light nuclei production in collisions of small systems at the Large Hadron Collider", *Phys. Lett. B* **792** (2019) 132–137, `arXiv:1812.05175 [nucl-th]`.

[77] E. G. Kessler, Jr., "The Deuteron Binding Energy and the Neutron Mass", *Phys. Lett. A* **255** (1999) 221.

[78] **E878** Collaboration, M. J. Bennett *et al.*, "Light nuclei production in relativistic Au + nucleus collisions", *Phys. Rev. C* **58** (1998) 1155–1164.

[79] **E802** Collaboration, L. Ahle *et al.*, "Proton and deuteron production in Au+Au reactions at 11.6 AGeV/c", *Phys. Rev. C* **60** (1999) 064901.

[80] **E864** Collaboration, T. A. Armstrong *et al.*, "Measurements of light nuclei production in 11.5 AGeV/c Au+Pb heavy-ion collisions", *Phys. Rev. C* **61** (2000) 064908.

[81] **E864** Collaboration, T. A. Armstrong *et al.*, "Antideuteron Yield at the AGS and Coalescence Implications", *Phys. Rev. Lett.* **85** (2000) 2685–2688.

[82] **NA52 (Newmass)** Collaboration, G. Ambrosini *et al.*, "Baryon and antibaryon production in lead-lead collisions at 158 A GeV/c", *Phys. Lett. B* **417** (1998) 202–210.

[83] **STAR** Collaboration, C. Adler *et al.*, "Measurement of Inclusive Antiprotons from Au+Au Collisions at $\sqrt{s_{\mathrm{NN}}} = 130\,\mathrm{GeV}$", *Phys. Rev. Lett.* **87** (2001) 262302.

[84] **PHENIX** Collaboration, S. S. Adler *et al.*, "Deuteron and Antideuteron Production in Au + Au Collisions at $\sqrt{s_{\mathrm{NN}}} = 200$ GeV", *Phys. Rev. Lett.* **94** (2005) 122302.

[85] **BRAHMS** Collaboration, I. Arsene *et al.*, "Rapidity dependence of deuteron production in central Au + Au collisions at $\sqrt{s_{\mathrm{NN}}} = 200$ GeV", *Phys. Rev. C* **83** (2011) 044906, `arXiv:1005.5427 [nucl-ex]`.

[86] **STAR** Collaboration, H. Agakishiev *et al.*, "Observation of the antimatter helium-4 nucleus", *Nature* **473** (2011) 353–356, `arXiv:1103.3312 [nucl-ex]`. Erratum: Nature 475 (2011) 412.

[87] **STAR** Collaboration, L. Adamczyk *et al.*, "Measurement of elliptic flow of light nuclei at $\sqrt{s_{\mathrm{NN}}} = 200$, 62.4, 39, 27, 19.6, 11.5, and 7.7 GeV at the BNL Relativistic Heavy Ion Collider", *Phys. Rev. C* **94** (2016) 034908, `arXiv:1601.07052 [nucl-ex]`.

[88] **STAR** Collaboration, J. Adam *et al.*, "Beam energy dependence of (anti-)deuteron production in Au + Au collisions at the BNL Relativistic Heavy Ion Collider", *Phys. Rev. C* **99** (2019) 064905, `arXiv:1903.11778 [nucl-ex]`.

[89] **ALICE** Collaboration, J. Adam *et al.*, "Precision measurement of the mass difference between light nuclei and anti-nuclei", *Nature Physics* **11** (2015) 811–814, `arXiv:1508.03986 [nucl-ex]`.

[90] **ALICE** Collaboration, J. Adam *et al.*, "Production of light nuclei and anti-nuclei in pp and Pb-Pb collisions at energies available at the CERN Large Hadron Collider", *Phys. Rev. C* **93** (2016) 024917, `arXiv:1506.08951 [nucl-ex]`.

[91] **ALICE** Collaboration, S. Acharya *et al.*, "Multiplicity dependence of (anti-)deuteron production in pp collisions at $\sqrt{s}$ = 7 TeV", *Phys. Lett. B* **794** (2019) 50–63, `arXiv:1902.09290 [nucl-ex]`.

[92] **ALICE** Collaboration, S. Acharya *et al.*, "Measurement of deuteron spectra and elliptic flow in Pb–Pb collisions at $\sqrt{s_{\mathrm{NN}}}$ = 2.76 TeV at the LHC", *Eur. Phys. J. C* **77** (2017) 658, `arXiv:1707.07304 [nucl-ex]`.

[93] **ALICE** Collaboration, S. Acharya *et al.*, "Production of deuterons, tritons, ^{3}He nuclei, and their antinuclei in pp collisions at $\sqrt{s} = 0.9$, 2.76, and 7 TeV", *Phys. Rev. C* **97** (2018) 024615, `arXiv:1709.08522 [nucl-ex]`.

[94] **ALICE** Collaboration, S. Acharya *et al.*, "Production of ^{4}He and $^4\overline{\text{He}}$ in Pb–Pb collisions at $\sqrt{s_{\text{NN}}}$ = 2.76 TeV at the LHC", *Nucl. Phys. A* **971** (2018) 1–20, `arXiv:1710.07531 [nucl-ex]`.

[95] **ALICE** Collaboration, S. Acharya *et al.*, "Multiplicity dependence of light (anti-)nuclei production in p–Pb collisions at $\sqrt{s_{\text{NN}}}$ = 5.02 TeV", *Phys. Lett. B* **800** (2020) 135043, `arXiv:1906.03136 [nucl-ex]`.

[96] **ALICE** Collaboration, S. Acharya *et al.*, "Production of (anti-)^{3}He and (anti-)^{3}H in p-Pbcollisions at $\sqrt{s_{\text{NN}}} = 5.02$ TeV", *Phys. Rev. C* **101** (2020) 044906, `arXiv:1910.14401 [nucl-ex]`.

[97] **ALICE** Collaboration, S. Acharya *et al.*, "(Anti-)deuteron production in pp collisions at $\sqrt{s} = 13$ TeV", *Eur. Phys. J. C* **80** (2020) 889, `arXiv:2003.03184 [nucl-ex]`.

[98] **ALICE** Collaboration, S. Acharya *et al.*, "Production of light (anti)nuclei in pp collisions at $\sqrt{s}$ = 13 TeV", *JHEP* **2022** (2022) 106, `arXiv:2109.13026 [nucl-ex]`.

[99] **ALICE** Collaboration, S. Acharya *et al.*, "Jet-associated deuteron production in pp collisions at $\sqrt{s}$ = 13 TeV", *Phys. Lett. B* **819** (2021) 136440, `arXiv:2011.05898 [nucl-ex]`.

[100] **ALICE** Collaboration, S. Acharya *et al.*, "Production of light (anti)nuclei in pp collisions at $\sqrt{s} = 5.02$ TeV", *Eur. Phys. J. C* **82** (2022) 289, `arXiv:2112.00610 [nucl-ex]`.

[101] **ALICE** Collaboration, S. Acharya *et al.*, "Hypertriton Production in p–Pb collisions at $\sqrt{s_{\text{NN}}}$ = 5.02 TeV", *Phys. Rev. Lett.* **128** (2022) 252003, `arXiv:2107.10627 [nucl-ex]`.

[102] **ALICE** Collaboration, S. Acharya *et al.*, "Elliptic and triangular flow of (anti)deuterons in Pb-Pb collisions at $\sqrt{s_{\text{NN}}}$ = 5.02 TeV", *Phys. Rev. C* **102** (2020) 055203, `arXiv:2005.14639 [nucl-ex]`.

[103] **ALICE** Collaboration, S. Acharya *et al.*, "Measurement of the (anti-)^{3}He elliptic flow in Pb–Pb collisions at $\sqrt{s_{\mathrm{NN}}}$ = 5.02 TeV", *Phys. Lett. B* **805** (2020) 135414, `arXiv:1910.09718 [nucl-ex]`.

[104] **ALICE** Collaboration, S. Acharya *et al.*, "Enhanced Deuteron Coalescence Probability in Jets", *Phys. Rev. Lett.* **131** (2023) 042301, `arXiv:2211.15204 [nucl-ex]`. [Erratum: *Phys. Rev. Lett.* **132**, 109901 (2024)].

[105] **ALICE** Collaboration, S. Acharya *et al.*, "Measurement of the production of (anti)nuclei in p–Pb collisions at $\sqrt{s_{\mathrm{NN}}}$ = 8.16 TeV", *Phys. Lett. B* **846** (2023) 137795, `arXiv:2212.04777 [nucl-ex]`.

[106] **ALICE** Collaboration, S. Acharya *et al.*, "First Measurement of Antideuteron Number Fluctuations at Energies Available at the Large Hadron Collider", *Phys. Rev. Lett.* **131** (2023) 041901, `arXiv:2204.10166 [nucl-ex]`.

[107] **ALICE** Collaboration, S. Acharya *et al.*, "Light (anti)nuclei production in Pb-Pb collisions at $\sqrt{s_{\mathrm{NN}}} = 5.02$TeV", *Phys. Rev. C* **107** (2023) 064904, `arXiv:2211.14015 [nucl-ex]`.

[108] **ALICE** Collaboration, S. Acharya *et al.*, "Measurement of the production and elliptic flow of (anti)nuclei in Xe-Xe collisions at $\sqrt{s_{\mathrm{NN}}}$ = 5.44 TeV", *Phys. Rev. C* **110** (2024) 064901, `arXiv:2405.19826 [nucl-ex]`.

[109] E. Fermi, "High-energy nuclear events", *Prog. Theor. Phys.* **5** (1950) 570–583.

[110] R. Hagedorn, "Statistical thermodynamics of strong interactions at high-energies", *Nuovo Cim. Suppl.* **3** (1965) 147–186.

[111] P. Braun-Munzinger, V. Koch, T. Schäfer, and J. Stachel, "Properties of hot and dense matter from relativistic heavy ion collisions", *Phys. Rept.* **621** (2016) 76–126, `arXiv:1510.00442 [nucl-th]`.

[112] P. Braun-Munzinger, K. Redlich, and J. Stachel, "Particle production in heavy ion collisions", `arXiv:nucl-th/0304013`.

[113] V. Vovchenko and H. Stoecker, "Analysis of hadron yield data within hadron resonance gas model with multi-component eigenvolume corrections", *J. Phys. Conf. Ser.* **779** (2017) 012078, `arXiv:1610.02346 [nucl-th]`.

[114] S. Wheaton, J. Cleymans, and M. Hauer, "THERMUS", `arXiv:1108.4588 [hep-ph]`.

[115] J. Cleymans, I. Kraus, H. Oeschler, K. Redlich, and S. Wheaton, "Statistical model predictions for particle ratios at $\sqrt{s_{\mathrm{NN}}}$ = 5.5 TeV", *Phys. Rev. C* **74** (2006) 034903, `arXiv:hep-ph/0604237`.

[116] G. Torrieri, S. Steinke, W. Broniowski, W. Florkowski, J. Letessier, and J. Rafelski, "SHARE: Statistical hadronization with resonances", *Comput. Phys. Commun.* **167** (2005) 229–251, `arXiv:nucl-th/0404083`.

[117] G. Torrieri, S. Jeon, J. Letessier, and J. Rafelski, "SHAREv2: Fluctuations and a comprehensive treatment of decay feed-down", *Comput. Phys. Commun.* **175** (2006) 635–649, `arXiv:nucl-th/0603026`.

[118] M. Petran, J. Letessier, J. Rafelski, and G. Torrieri, "SHARE with CHARM", *Comput. Phys. Commun.* **185** (2014) 2056–2079, `arXiv:1310.5108 [hep-ph]`.

[119] M. Petrán, J. Letessier, V. Petráček, and J. Rafelski, "Hadron production and quark-gluon plasma hadronization in Pb-Pb collisions at $\sqrt{s_{\mathrm{NN}}} = 2.76$ TeV", *Phys. Rev. C* **88** (2013) 034907, `arXiv:1303.2098 [hep-ph]`.

[120] V. Vovchenko, M. I. Gorenstein, and H. Stoecker, "Finite resonance widths influence the thermal-model description of hadron yields", *Phys. Rev. C* **98** (2018) 034906, `arXiv:1807.02079 [nucl-th]`.

[121] V. Vovchenko and H. Stoecker, "Thermal-FIST: A package for heavy-ion collisions and hadronic equation of state", *Comput. Phys. Commun.* **244** (2019) 295–310, `arXiv:1901.05249 [nucl-th]`.

[122] A. Andronic, P. Braun-Munzinger, and J. Stachel, "Hadron production in central nucleus-nucleus collisions at chemical freeze-out", *Nucl. Phys. A* **772** (2006) 167–199, `arXiv:nucl-th/0511071`.

[123] A. Andronic, P. Braun-Munzinger, B. Friman, P. M. Lo, K. Redlich, and J. Stachel, "The thermal proton yield anomaly in Pb-Pb collisions at the LHC and its resolution", *Phys. Lett. B* **792** (2019) 304–309, `arXiv:1808.03102 [hep-ph]`.

[124] A. Andronic, F. Beutler, P. Braun-Munzinger, K. Redlich, and J. Stachel, "Thermal description of hadron production in e^+e^- collisions revisited", *Phys. Lett. B* **675** (2009) 312–318, `arXiv:0804.4132 [hep-ph]`.

[125] F. Becattini, P. Castorina, A. Milov, and H. Satz, "A Comparative analysis of statistical hadron production", *Eur. Phys. J. C* **66** (2010) 377–386, `arXiv:0911.3026 [hep-ph]`.

[126] V. Vovchenko, B. Dönigus, and H. Stoecker, "Multiplicity dependence of light nuclei production at LHC energies in the canonical statistical model", *Phys. Lett. B* **785** (2018) 171–174, `arXiv:1808.05245 [hep-ph]`.

[127] **ALICE** Collaboration, J. Adam *et al.*, "$^3_\Lambda$H and $^3_{\overline{\Lambda}}\overline{\mathrm{H}}$ production in Pb-Pb collisions at $\sqrt{s_{\mathrm{NN}}} = 2.76$ TeV", *Phys. Lett. B* **754** (2016) 360–372, `arXiv:1506.08453 [nucl-ex]`.

[128] A. Andronic, P. Braun-Munzinger, K. Redlich, and J. Stachel, "Decoding the phase structure of QCD via particle production at high energy", *Nature* **561** (2018) 321–330, `arXiv:1710.09425 [nucl-th]`.

[129] S. T. Butler and C. A. Pearson, "Deuterons from High-Energy Proton Bombardment of Matter", *Phys. Rev.* **129** (1963) 836–842.

[130] J. I. Kapusta, "Mechanisms for deuteron production in relativistic nuclear collisions", *Phys. Rev. C* **21** (1980) 1301–1310.

[131] R. Scheibl and U. Heinz, "Coalescence and flow in ultrarelativistic heavy ion collisions", *Phys. Rev. C* **59** (1999) 1585–1602, `arXiv:nucl-th/9809092 [nucl-th]`.

[132] **ALICE** Collaboration, E. Abbas *et al.*, "Mid-rapidity anti-baryon to baryon ratios in pp collisions at $\sqrt{s}$ = 0.9, 2.76 and 7 TeV measured by ALICE", *Eur. Phys. J. C* **73** (2013) 2496, `arXiv:1305.1562 [nucl-ex]`.

[133] M. Mahlein, L. Barioglio, F. Bellini, L. Fabbietti, C. Pinto, B. Singh, and S. Tripathy, "A realistic coalescence model for deuteron production", *Eur. Phys. J. C* **83** (2023) 804, `arXiv:2302.12696 [hep-ex]`.

[134] G. Ropke, "Light nuclei quasiparticle energy shift in hot and dense nuclear matter", *Phys. Rev. C* **79** (2009) 014002, `arXiv:0810.4645 [nucl-th]`.

[135] **ALICE** Collaboration, B. Abelev *et al.*, "Centrality dependence of π, K, p production in Pb-Pb collisions at $\sqrt{s_{\mathrm{NN}}}$ = 2.76 TeV", *Phys. Rev. C* **88** (2013) 044910, `arXiv:1303.0737 [hep-ex]`.

[136] **ALICE** Collaboration, J. Adam *et al.*, "Measurement of pion, kaon and proton production in proton–proton collisions at $\sqrt{s} = 7$ TeV", *Eur. Phys. J. C* **75** (2015) 226, `arXiv:1504.00024 [nucl-ex]`.

[137] U. W. Heinz and B. V. Jacak, "Two particle correlations in relativistic heavy ion collisions", *Ann. Rev. Nucl. Part. Sci.* **49** (1999) 529–579, `arXiv:nucl-th/9902020`.

[138] R. B. Wiringa, V. G. J. Stoks, and R. Schiavilla, "An Accurate nucleon-nucleon potential with charge independence breaking", *Phys. Rev. C* **51** (1995) 38–51, `arXiv:nucl-th/9408016`.

[139] D. R. Entem, R. Machleidt, and Y. Nosyk, "High-quality two-nucleon potentials up to fifth order of the chiral expansion", *Phys. Rev. C* **96** (2017) 024004, `arXiv:1703.05454 [nucl-th]`.

[140] K. Werner, B. Guiot, I. Karpenko, and T. Pierog, "Analysing radial flow features in p-Pb and p-p collisions at several TeV by studying identified particle production in EPOS3", *Phys. Rev. C* **89** (2014) 064903, `arXiv:1312.1233 [nucl-th]`.

[141] T. Sjöstrand, S. Ask, J. R. Christiansen, R. Corke, N. Desai, P. Ilten, S. Mrenna, S. Prestel, C. O. Rasmussen, and P. Z. Skands, "An introduction to PYTHIA 8.2", *Comput. Phys. Commun.* **191** (2015) 159–177, `arXiv:1410.3012 [hep-ph]`.

[142] P. Skands, S. Carrazza, and J. Rojo, "Tuning PYTHIA 8.1: the Monash 2013 Tune", *Eur. Phys. J. C* **74** (2014) 3024, `arXiv:1404.5630 [hep-ph]`.

[143] V. Vovchenko, K. Gallmeister, J. Schaffner-Bielich, and C. Greiner, "Nucleosynthesis in heavy-ion collisions at the LHC via the Saha equation", *Phys. Lett. B* **800** (2020) 135131, `arXiv:1903.10024 [hep-ph]`.

[144] V. Vovchenko and V. Koch, "Centrality dependence of proton and light nuclei yields as a consequence of baryon annihilation in the hadronic phase", *Phys. Lett. B* **835** (2022) 137577, `arXiv:2210.15641 [nucl-th]`.

[145] T. Reichert, J. Steinheimer, V. Vovchenko, B. Dönigus, and M. Bleicher, "Energy dependence of light hypernuclei production in heavy-ion collisions from a coalescence and statistical-thermal model perspective", *Phys. Rev. C* **107** (2023) 014912, `arXiv:2210.11876 [nucl-th]`.

[146] **ALICE** Collaboration, S. Acharya *et al.*, "Measurement of (anti)alpha production in central Pb–Pb collisions at $\sqrt{s_{\mathrm{NN}}} = 5.02$ TeV", *Phys. Lett. B* **858** (2024) 138943, `arXiv:2311.11758 [nucl-ex]`.

[147] **CDF** Collaboration, T. Affolder *et al.*, "Charged Jet Evolution and the Underlying Event in $p\bar{p}$ Collisions at 1.8 TeV", *Phys. Rev. D* **65** (2002) 092002.

[148] **ALICE** Collaboration, S. Acharya *et al.*, "Underlying event properties in pp collisions at $\sqrt{s}$ = 13 TeV", *JHEP* **4** (2020) 192, `arXiv:1910.14400 [nucl-ex]`.

[149] **ALICE** Collaboration, S. Acharya *et al.*, "Underlying-event properties in pp and p–Pb collisions at $\sqrt{s_{\mathrm{NN}}}$ = 5.02 TeV", *JHEP* **06** (2023) 023, `arXiv:2204.10389 [nucl-ex]`.

[150] E. Tiesinga, P. J. Mohr, D. B. Newell, and B. N. Taylor, "The 2022 CODATA Recommended Values of the Fundamental Physical Constants." `https://physics.nist.gov/constants`.

[151] A. Kounine, "The Alpha Magnetic Spectometrer on the International Space Station", *Int. J. of Mod. Phys. E* **21** (2012) 1230005.

[152] C. J. Hailey, "An indirect search for dark matter using antideuterons: the GAPS experiment", *New J. Phys.* **11** (2009) 105022.

[153] **ALICE** Collaboration, S. Acharya *et al.*, "Measurement of anti-3He nuclei absorption in matter and impact on their propagation in the Galaxy", *Nature Physics* **19** (2022) 61–71, `arXiv:2202.01549 [nucl-ex]`.

[154] A. Ibarra and S. Wild, "Prospects of antideuteron detection from dark matter annihilations or decays at AMS-02 and GAPS", *JCAP* **02** (2013) 021, `arXiv:1209.5539 [hep-ph]`.

[155] E. Carlson, A. Coogan, T. Linden, S. Profumo, A. Ibarra, and S. Wild, "Antihelium from Dark Matter", *Phys. Rev. D* **89** (2014) 076005, `arXiv:1401.2461 [hep-ph]`.

[156] M. Korsmeier, F. Donato, and N. Fornengo, "Prospects to verify a possible dark matter hint in cosmic antiprotons with antideuterons and antihelium", *Phys. Rev, D* **97** (2018) 103011, `arXiv:1711.08465 [astro-ph.HE]`.

[157] M. W. Winkler and T. Linden, "Dark Matter Annihilation Can Produce a Detectable Antihelium Flux through $\bar{\Lambda}_b$ Decays", *Phys. Rev. Lett.* **126** (2021) 101101, `arXiv:2006.16251 [hep-ph]`.

[158] **ALICE** Collaboration, S. Acharya *et al.*, "Measurement of the Low-Energy Antideuteron Inelastic Cross Section", *Phys. Rev. Lett.* **125** (2020) 162001, `arXiv:2005.11122 [nucl-ex]`.

[159] **ALICE** Collaboration, S. Acharya *et al.*, "Measurement of the low-energy antitriton inelastic cross section", *Physics Letters B* **848** (2024) 138337, `arXiv:2307.03603 [nucl-ex]`.

[160] S. Ting, "Latest Results from the AMS Experiment on the International Space Station." CERN Colloquium, 24 May 2018, `https://indico.cern.ch/event/729900/`.

[161] S. Ting, "Latest Results from AMS on the International Space Station." CERN Colloquium, 8 June 2023, `https://indico.cern.ch/event/1275785/`.

[162] **ATLAS** Collaboration, G. Aad *et al.*, "Observation of a new particle in the search for the Standard Model Higgs boson with the ATLAS detector at the LHC", *Phys. Lett. B* **716** (2012) 1–29, `arXiv:1207.7214 [hep-ex]`.

[163] **CMS** Collaboration, S. Chatrchyan *et al.*, "Observation of a New Boson at a Mass of 125 GeV with the CMS Experiment at the LHC", *Phys. Lett. B* **716** (2012) 30–61, `arXiv:1207.7235 [hep-ex]`.

[164] **LHCb** Collaboration, R. Aaij *et al.*, "Observation of structure in the J/ψ -pair mass spectrum", *Sci. Bull.* **65** (2020) 1983–1993, `arXiv:2006.16957 [hep-ex]`.

[165] **LHCb** Collaboration, R. Aaij *et al.*, "Observation of $J/\psi p$ Resonances Consistent with Pentaquark States in $\Lambda_b^0 \to J/\psi K^- p$ Decays", *Phys. Rev. Lett.* **115** (2015) 072001, `arXiv:1507.03414 [hep-ex]`.

[166] **D0, TOTEM** Collaboration, V. M. Abazov *et al.*, "Odderon Exchange from Elastic Scattering Differences between pp and $p\bar{p}$ Data at 1.96 TeV and from pp Forward Scattering Measurements", *Phys. Rev. Lett.* **127** (2021) 062003, `arXiv:2012.03981 [hep-ex]`.

[167] E. Lopienska, “The CERN accelerator complex, layout in 2022. Complexe des accélérateurs du CERN en janvier 2022.” `https://cds.cern.ch/record/2800984`.

[168] W. Herr and B. Muratori, “Concept of luminosity.” `https://cds.cern.ch/record/941318`.

[169] S. van der Meer, “Calibration of the effective beam height in the ISR.” `https://cds.cern.ch/record/296752`.

[170] “The ATLAS experiment.” `https://atlas.cern/`.

[171] “The CMS experiment.” `https://cms.cern/`.

[172] “The ALICE experiment.” `https://alice.cern/`.

[173] “The LHCb experiment.” `https://lhcb-outreach.web.cern.ch/`.

[174] “The TOTEM experiment.” `https://totem-experiment.web.cern.ch/`.

[175] “The LHCf experiment.” `https://home.cern/science/experiments/lhcf`.

[176] “The MoEDAL-MAPP experiment.” `https://moedal.web.cern.ch/`.

[177] “The FASER experiment.” `https://faser.web.cern.ch/`.

[178] “The SND@LHC experiment.” `https://snd-lhc.web.cern.ch/`.

[179] **ALICE** Collaboration, K. Aamodt *et al.*, “The ALICE experiment at the CERN LHC”, *JINST* **3** (2008) S08002.

[180] **ALICE** Collaboration, J. Alme *et al.*, “The ALICE TPC, a large 3-dimensional tracking device with fast readout for ultra-high multiplicity events”, *Nucl. Instrum. Meth. A* **622** (2010) 316–367, `arXiv:1001.1950 [physics.ins-det]`.

[181] **ALICE** Collaboration, A. Akindinov *et al.*, “Performance of the ALICE Time-Of-Flight detector at the LHC”, *Eur. Phys. J. Plus* **128** (2013) 44.

[182] **ALICE** Collaboration, S. Acharya *et al.*, “ALICE upgrades during the LHC Long Shutdown 2”, *JINST* **19** (2024) P05062, `arXiv:2302.01238 [physics.ins-det]`.

[183] **ALICE** Collaboration, B. Abelev *et al.*, “Technical Design Report for the Upgrade of the ALICE Inner Tracking System”, *J. Phys. G* **41** (2014) 087002.

[184] **ALICE** Collaboration, G. Aglieri Rinella, “The ALPIDE pixel sensor chip for the upgrade of the ALICE Inner Tracking System”, *Nucl. Instrum. Meth. A* **845** (2017) 583–587.

[185] F. Sauli, “GEM: A new concept for electron amplification in gas detectors”, *Nucl. Instrum. Meth. A* **386** (1997) 531–534.

[186] P. Buncic, M. Krzewicki, and P. Vande Vyvre, “Technical Design Report for the Upgrade of the Online-Offline Computing System”, 2015. `https://cds.cern.ch/record/2011297`.

[187] A. Alkin, G. Eulisse, J. F. Grosse-Oetringhaus, P. Hristov, and M. Kabus, “ALICE Run 3 Analysis Framework”, *EPJ Web Conf.* **251** (2021) 03063.

[188] K. Bos, *et al.*, *LHC computing Grid: Technical Design Report. Version 1.06 (20 Jun 2005)*. Technical design report. LCG. CERN, Geneva, 2005. `https://cds.cern.ch/record/840543`.

[189] S. Bagnasco, L. Betev, P. Buncic, F. Carminati, C. Cirstoiu, C. Grigoras, A. Hayrapetyan, A. Harutyunyan, A. J. Peters, and P. Saiz, “AliEn: ALICE Environment on the GRID”, *J. Phys. Conf. Ser.* **119** (2008) 062012.

[190] “AliPhysics: the ALICE software repository.” `https://github.com/alisw/AliPhysics`.

[191] P. Billoir, “Progressive track recognition with a Kalman like fitting procedure”, *Comput. Phys. Commun.* **57** (1989) 390–394.

[192] Y. Belikov, M. Ivanov, K. Safarik, and J. Bracinik, "TPC tracking and particle identification in high density environment", *eConf* **C0303241** (2003) TULT011, `arXiv:physics/0306108`.

[193] X.-N. Wang and M. Gyulassy, "HIJING: A Monte Carlo model for multiple jet production in pp, pA and AA collisions", *Phys. Rev. D* **44** (1991) 3501–3516.

[194] S. Roesler, R. Engel, and J. Ranft, "The Monte Carlo event generator DPMJET-III", in *International Conference on Advanced Monte Carlo for Radiation Physics, Particle Transport Simulation and Applications (MC 2000)*, pp. 1033–1038. 12, 2000. `arXiv:hep-ph/0012252`.

[195] `https://twiki.cern.ch/twiki/bin/viewauth/ALICE/AliDPGtoolsTrackSystematicUncertainty.`.

[196] **ALICE** Collaboration, S. Acharya *et al.*, "$p-p, p-\Lambda$, and $\Lambda-\Lambda$ correlations studied via femtoscopy in pp reactions at $\sqrt{s} = 7\,\mathrm{TeV}$", *Phys. Rev. C* **99** (2019) 024001, `arXiv:1805.12455 [nucl-ex]`.

[197] **ALICE** Collaboration, S. Acharya *et al.*, "First Observation of an Attractive Interaction between a Proton and a Cascade Baryon", *Phys. Rev. Lett.* **123** (2019) 112002, `arXiv:1904.12198 [nucl-ex]`.

[198] C. Bierlich *et al.*, "A comprehensive guide to the physics and usage of PYTHIA 8.3", *SciPost Phys. Codeb.* **2022** (2022) 8, `arXiv:2203.11601 [hep-ph]`.

[199] C. Bierlich, G. Gustafson, L. Lönnblad, and H. Shah, "The Angantyr model for Heavy-Ion Collisions in PYTHIA8", *JHEP* **10** (2018) 134, `arXiv:1806.10820 [hep-ph]`.

[200] S. Mrowczynski, "Enhancement of Deuteron Production in Jets", *Acta Phys. Polon. B* **55** (2024) 6–A2, `arXiv:2312.17695 [nucl-th]`.

[201] Y.-H. Feng, C. M. Ko, Y.-G. Ma, K.-J. Sun, X.-N. Wang, Z. Yang, and S. Zhang, "Jet-induced enhancement of deuteron production in pp and p-Pb collisions at the LHC", *Phys. Lett. B* **859** (2024) 139102, `arXiv:2408.01634 [nucl-th]`.

[202] Y. Bailung, N. Shah, and A. Roy, "Searching for enhancement in coalescence of in-jet (anti-)deuterons in proton-proton collisions", *Phys. Rev. C* **109** (2024) 044908, `arXiv:2404.01244 [hep-ph]`.

[203] S. Mrowczynski, "On the neutron proton correlations and deuteron production", *Phys. Lett. B* **277** (1992) 43–48.

[204] Z.-W. Lin, C. M. Ko, B.-A. Li, B. Zhang, and S. Pal, "A Multi-phase transport model for relativistic heavy ion collisions", *Phys. Rev. C* **72** (2005) 064901, `arXiv:nucl-th/0411110`.

[205] Z.-W. Lin and L. Zheng, "Further developments of a multi-phase transport model for relativistic nuclear collisions", *Nucl. Sci. Tech.* **32** (2021) 113, `arXiv:2110.02989 [nucl-th]`.

Acknowledgments

When I started the Ph.D. programme, more than three years ago, I never imagined how deeply this journey would change me, in so many different aspects. I would like to spend a few words to thank all the people that, in a way or another, shared this incredible experience with me. I apologise in advance if these words may fall short, but I am not the best writer.

First and foremost, I would like to thank my Ph.D. supervisor, Prof. Paola La Rocca, for always believing in me, even when sometimes I did not. Your guidance in this adventure was fundamental, from both a scientific and personal point of view. Always present and available to answer all my questions, guiding me in difficult paths, providing so many opportunities to challenge myself and constantly grow. I am deeply grateful for everything you have done, and for trusting me one more time, giving me the opportunity to continue to work with you.

I would also like to thank Dr. Chiara Pinto, that was my reference point in everything I have done during the last years: your confidence, your skills, your achievement constantly pushed me, even when it seems not. I admire your scientific career, and I hope someday to achieve even a fraction of what you have done.

I am deeply grateful to Prof. Alberto Calivà: when we started working together, I had no idea of what to expect, and now I feel very lucky for all the experiences lived together. Also, I am deeply grateful for all the motivational talks I received: I do not know yet what to expect, but I hope to be on stage one of *that* train right now, even if now it seems not.

I also would like to thank Prof. Francesco Riggi: it is thanks to him that I started this journey, and it is also thanks to him that I'm here right now. I really do not know what my career would be if, a long time ago, I chose a different bachelor (and master) thesis advisor. Thank you for inspiring the little me.

I would like to extend my gratitude to the Department of Physics and Astronomy "Ettore Majorana" of the University of Catania, that not only trained me in my academic formation, but was like a second home in these last years. Also, I would like to thank the Istituto Nazionale di Fisica Nucleare, especially the Catania section, that allowed me to have wonderful experiences during my Ph.D..

I am deeply grateful to the whole ALICE Collaboration. Everyone that I met, from the nights in the control room to the conferences in exotic places, shaped these last years in a very important way. I want to especially thank the ALICE-CERN team, that welcomed me in the last period of my Ph.D., in a very special (but strange) year that taught me a lot, both personally and scientifically. A special thanks to all the ALICE member that crossed a little bit of their path with mine, like Francesca, Nicolò, Sara, Daniela, Gudda, Simone and Rebecca, my podcast companion.

I would like to thank all my fellow Ph.D. colleagues, that shared with me the experiences of these last years. In particular, I am deeply grateful to Stefano, Valentina, Gisella and Alessandro for everything we have lived together.

A special thanks to Giacometta, Melissa and Noemi. Every time that I see where we are now I am amazed. We started together, as simple colleagues, and now we are proper scientists, like we never imagined. Sharing all these years with you was a privilege.

I would like to thank Dott. Valentina Caneddu, that was here in a very difficult period and helped me not only to find myself back, but to shape a new version of myself. We are a good team, indeed.

I am deeply grateful to my dearest friend Cristina. It is impossible to summarize in a few words what you have done to me in the last years. Your presence completely changed my friendship perspective. Before you, I thought that I was not good enough to have a friend, but with you everything is easy. Thanks for always been there, in the good and in the bad days, giving the best hugs I can hope for. Citing something you may recognize, *thank you for not envying me, but for admiring me.*

A special thanks to my parents, Nino and Angela, to my sister Deborak and her partner Vincenzo. Always there to cover my back in these long years, silently helping to manage things bigger than me. Your constant support was one of the cornerstone that allowed me to finish this journey.

Finally, I would like to thank all the people that crossed my path and, even for a couple of minutes, stopped to listen me talking about some strange physics concepts. It is also thank to you that what what started as a passion is now much more.